

# 3D bioprinting of biomimetic skeletal muscle tissue model

Zhuang, Pei

2019

Zhuang, P. (2019). 3D bioprinting of biomimetic skeletal muscle tissue model. Doctoral thesis, Nanyang Technological University, Singapore.

<https://hdl.handle.net/10356/136968>

<https://doi.org/10.32657/10356/136968>

---

This work is licensed under a Creative Commons Attribution-NonCommercial 4.0 International License (CC BY-NC 4.0).

*Downloaded on 13 Mar 2024 14:43:25 SGT*

# **3D BIOPRINTING OF BIOMIMETIC SKELETAL MUSCLE TISSUE MODEL**

**ZHUANG PEI**

**SCHOOL OF MECHANICAL AND AEROSPACE  
ENGINEERING**

**2019**

# **3D BIOPRINTING OF BIOMIMETIC SKELETAL MUSCLE TISSUE MODEL**

by

ZHUANG PEI

Supervisor: Assistant Professor Zhang Yi

Co-supervisors: Professor Chua Chee Kai

Associate Professor Tan Lay Poh

School of Mechanical and Aerospace Engineering

A thesis submitted to  
the Nanyang Technological University  
in partial fulfilment of the requirement for the degree of  
Doctor of Philosophy

*August 2019*

## Statement of Originality

I hereby certify that the work embodied in this thesis is the result of original research, is free of plagiarised materials, and has not been submitted for a higher degree to any other University or Institution.

July-30-2019

Zhuang Pei



.....

Date

.....

[Input Name Here]

## Supervisor Declaration Statement

I have reviewed the content and presentation style of this thesis and declare it is free of plagiarism and of sufficient grammatical clarity to be examined. To the best of my knowledge, the research and writing are those of the candidate except as acknowledged in the Author Attribution Statement. I confirm that the investigations were conducted in accord with the ethics policies and integrity standards of Nanyang Technological University and that the research data are presented honestly and without prejudice.

July-30-2019

Prof Zhang Yi



.....  
Date

.....  
[Input Supervisor Name Here]

## Authorship Attribution Statement

\*(B) This thesis contains material from 1 paper published in the following peer-reviewed journal(s) / from papers accepted at conferences in which I am listed as an author.

Chapter 3 is published as Zhuang P, Ng W L, An J, et al. Layer-by-layer ultraviolet assisted extrusion-based (UAE) bioprinting of hydrogel constructs with high aspect ratio for soft tissue engineering applications[J]. PloS one, 2019, 14(6): e0216776. <https://doi.org/10.1371/journal.pone.0216776>

The contributions of the co-authors are as follows:

- Prof Chua Chee Kai and Assoc Prof Tan Lay Poh provided the initial project direction and edited the manuscript drafts.
- I prepared the manuscript drafts. The manuscript was revised by Dr An Jia and Dr. Ng Wei Long.
- I co-designed part of the experiments with Dr Ng Wei Long.
- I performed all the laboratory work at the School of Mechanical and Aerospace Engineering and School of Material Science. I also analyzed the data.
- All microscopy, including sample preparation, was conducted by me in the Facility for Analysis, Characterization, Testing and Simulation.

July-30-2019

Zhuang Pei



.....

Date

.....

[Input Name Here]

## Abstract

Skeletal muscle has remarkable self-regeneration capability for minor injuries, yet massive muscle damage cannot be regenerated spontaneously and usually requires surgical interventions. The advances in tissue engineering technology has provided alternatives to build tissues with well-aligned muscle cells in both 2D and 3D. However, most strategies could only generate tissue models in micron scale or with limited thickness, which are not suitable for volumetric muscle loss (VML). As a proof of concept, an integration of 3D bioprinting technology and capillary action was performed to fabricate large 3D constructs for skeletal muscle tissue engineering.

Firstly, a layer-by-layer ultraviolet assisted extrusion-based bioprinting technology was established to fabricate complex constructs with high aspect ratio using the gelatin methacryloyl-gellan gum (GelMA-GG) bio-inks. The results suggested that bio-inks with viscosity lower than 0.124 Pa·s at 37°C were suitable for cell encapsulation and viscosity of 0.2 - 1.0 Pa·s at 25°C were bioprintable for complex constructs using layer-by-layer UV-assisted bioprinting strategy.

The second part involved the development of suitable bio-inks and the investigation of the cell viability over the entire bioprinting process. Gelatin was introduced into the GelMA-GG composite bio-ink to endow the bio-ink with dynamic mechanical properties. The newly formulated bio-ink was recognized to be initially printable and subsequently cell favorable. This hydrogel can serve as a new bio-ink for cells that require stiff surroundings for attachment and softer substrates for growth. In addition, thick and complex tissue models may require a prolonged printing process. To better understand the cell behavior during printing process, cell viability over the whole printing process was analyzed. Both C2C12 and human umbilical vein

endothelial cells (HUVECs) were examined. The results provided a deep insight into the cell damage induced by shear stress and UV crosslinking.

Lastly, the feasibility of fabricating large 3D skeletal muscle constructs with well organized cells through the combination of 3D bioprinting and capillary action was demonstrated. Dual bio-inks (GMGAGG and gelatin) and co-culture (C2C12 and HUVECs) were incorporated. Parametric study including effects of varied line spacing and different seeding density on cell alignment was performed. Suitable co-culture medium was optimized to maintain and support the growth of both C2C12 and HUVECs. The results of co-culture study have identified that 30% HUVECs suffice to support the growth of C2C12. The immunofluorescence analysis has revealed the longitudinal myofiber formation in both constructs with C2C12 only and the co-cultured constructs. The results demonstrated the feasibility and efficacy of constructing 3D thick tissues in a mild and efficient manner.



## Acknowledgements

First and foremost, I would like to express my sincere gratitude towards my supervisors Assistant Professor Zhang Yi, Professor Chua Chee Kai and Associate Professor Tan Lay Poh, for their kind patience, valuable advice and clear guidance. Their support and encouragement have always been inspiring.

I would also like to express my heartfelt gratitude to Associate Professor Yeong Wai Yee, who has been generous and supportive in sharing research facilities and consumables.

I would like to convey my highest appreciation to my project mentor, Dr An Jia and Dr Ng Wei Long for all the insightful advice that I have received from them. Furthermore, my sincere thanks also go to Dr Tan Yu Jun, Dr Ratima Suntornnond, Dr Li Hui Jun, Dr Sun Wen, Ms Zhou Miao Miao and fellow graduate students in SC3DP, for their continued motivation and assistance throughout the project.

I would like to give my special thanks to Ms Heng Chee Hoon, the technician at the Biological and Chemical Laboratory, for her kind assistance in machine operation and materials preparation.

I would like to thank my friends for their kind support in my work and life. Special thanks to Mr Yin Rui for his kindness, patience and encouragement. Last but not the least, I would like to thank my parents, who unselfishly support me with love and encouragement throughout the tough but rewarding PhD journey.



# Contents

<b>Abstract</b>	<b>ii</b>
<b>Acknowledgements</b>	<b>iv</b>
<b>List of Tables</b>	<b>xi</b>
<b>List of Figures</b>	<b>xii</b>
<b>1 Introduction</b>	<b>1</b>
1.1 Background . . . . .	1
1.2 Objectives . . . . .	4
1.3 Scope . . . . .	4
1.4 Organisation of report . . . . .	5
<b>2 Literature Review</b>	<b>7</b>
2.1 3D skeletal muscle constructs context . . . . .	7
2.1.1 Physiology . . . . .	7
2.1.2 Design criteria . . . . .	8
2.1.2.1 Matrix composition and structure . . . . .	8
2.1.2.2 Multi-cellular environment . . . . .	9
2.1.2.3 Matrix stiffness . . . . .	16
2.1.2.4 Geometrical confinement-2D topology . . . . .	16
2.1.2.5 Geometrical confinement-2D surface pattern- ing . . . . .	18
2.1.2.6 Mechanical stimuli . . . . .	24
2.1.2.7 Electrical stimuli . . . . .	26
2.2 Spatial exploration of constructing skeletal muscle tissue . . . . .	32
2.2.1 3D geometrical confinement . . . . .	32
2.2.2 Electrospun fibers . . . . .	33
2.2.3 Porous hydrogel . . . . .	39

2.2.4	Combinatorial effects of fibers and hydrogels . . . . .	44
2.2.5	3D bioprinted skeletal muscle tissue . . . . .	47
2.3	Temporal control of skeletal muscle regeneration . . . . .	57
2.4	Challenges and perspectives . . . . .	62
2.5	Summary . . . . .	64
<b>3</b>	<b>Layer-by-Layer Ultraviolet Assisted Extrusion-based Bio-printing of Hydrogel Constructs with High Aspect Ratio</b>	<b>65</b>
3.1	Introduction . . . . .	65
3.2	Materials and methods . . . . .	67
3.2.1	Preparation of GelMA-GG bio-inks . . . . .	68
3.2.2	$^1\text{H}$ NMR of GelMA . . . . .	70
3.2.3	Evaluation of rheological properties of the GelMA-GG bio-ink . . . . .	70
3.2.4	Cell encapsulation and sedimentation . . . . .	71
3.2.5	Evaluation of bio-ink's mechanical properties (Cyclic Compression Test) . . . . .	71
3.2.6	Evaluation of bio-ink's microstructure (FE-SEM imaging) . . . . .	72
3.2.7	Manual casting of cell-laden bio-inks . . . . .	72
3.2.8	3D bioprinting of cell-laden bio-inks . . . . .	73
3.2.9	Statistical analysis . . . . .	74
3.3	Results and discussion . . . . .	75
3.3.1	Determination of degree of methacrylation . . . . .	76
3.3.2	Bio-ink preparation . . . . .	77
3.3.3	Printing phase . . . . .	83
3.3.4	Post-printing phase . . . . .	85

3.3.4.1	Material property (mechanical stiffness and microstructure) . . . . .	85
3.3.4.2	Influence of bio-ink on cells: Manual casting of cell-laden bio-inks . . . . .	88
3.3.4.3	Influence of bio-ink on cells: 3D bioprinting of cell-laden bio-inks . . . . .	89
3.4	Summary . . . . .	92
<b>4</b>	<b>Development of Suitable Bio-inks and the Influence of UV Radiation on Cell Behavior</b>	<b>94</b>
4.1	Introduction . . . . .	94
4.2	Material and method . . . . .	96
4.2.1	Material preparation . . . . .	96
4.2.2	Rheological property . . . . .	97
4.2.3	Evaluation of gelatin release . . . . .	97
4.2.4	Structural integrity of GMGAGG hydrogel . . . . .	98
4.2.5	Enzymatic degradation study . . . . .	98
4.2.6	Biocompatibility characterization . . . . .	99
4.2.7	Cell culture . . . . .	99
4.2.8	Evaluation of <i>in vitro</i> cell viability over time (prior to printing) . . . . .	99
4.2.9	Evaluation of shear stress effect on cell viability over time (during printing) . . . . .	100
4.2.10	Evaluation of UV duration effect on cell survival rate (post-printing) . . . . .	102
4.2.11	Statistical analysis . . . . .	103
4.3	Results and discussion . . . . .	105
4.3.1	Evaluation of rheological property of the bio-ink . . .	105

4.3.2	Gelatin release (TNBSA) . . . . .	106
4.3.3	Structure integrity of the printed GMGAGG constructs	107
4.3.4	Enzymatic degradation study . . . . .	108
4.3.5	Biocompatibility of GMGAGG . . . . .	109
4.3.6	<i>In vitro</i> cell viability in printing syringe over time (before printing) . . . . .	111
4.3.7	Evaluation of shear stress effects on cell viability over time (during printing) . . . . .	113
4.3.8	UV duration effects on cell survival rate (single layer)	116
4.3.9	UV duration effects on cell survival rate (multiple layer)	118
4.4	Summary . . . . .	123

## 5 3D Bioprinted Constructs with Highly Efficient Capillary

	<b>Force Assisted Cell seeding</b>	<b>125</b>
5.1	Introduction . . . . .	125
5.2	Material and method . . . . .	127
5.2.1	Bio-ink preparation . . . . .	127
5.2.2	Printing process (Prior to cell seeding) . . . . .	128
5.2.3	Capillary action assisted cell seeding . . . . .	128
5.2.4	Cell culture and differentiation . . . . .	130
5.2.5	Co-culture medium optimization . . . . .	130
5.2.6	Optimization of co-culture ratio . . . . .	131
5.2.7	Immunostaining . . . . .	131
5.2.8	Statistical analysis . . . . .	132
5.3	Results . . . . .	132
5.3.1	Printed constructs . . . . .	132
5.3.2	Evaluation of varied line spacing effect on cell orientation . . . . .	134

5.3.3	Effect of cell density on cell orientation . . . . .	135
5.3.4	Formulation of co-culture medium . . . . .	137
5.3.5	Evaluation of ratio of co-cultured cells . . . . .	140
5.3.6	Immunofluorescence analysis of co-cultured constructs	140
5.4	Discussion . . . . .	143
<b>6</b>	<b>Conclusions and Future work</b>	<b>145</b>
6.1	Conclusions . . . . .	145
6.1.1	Layer-by-layer ultraviolet assisted extrusion-based bio- printing of hydrogel constructs with high aspect ratio	146
6.1.2	Development of suitable bio-inks and the influence of UV radiation on cell behavior . . . . .	147
6.1.3	3D bioprinted constructs with highly efficient capil- lary force assisted cell seeding . . . . .	148
6.2	Future research directions . . . . .	149
6.2.1	Development of novel bio-ink . . . . .	149
6.2.2	Generation of multicellular constructs . . . . .	149
6.2.3	Evaluation of capillary action on cell alignment . . .	150
	<b>List of Publications</b>	<b>151</b>
	<b>Appendix A</b>	<b>152</b>
	<b>Appendix B</b>	<b>153</b>
	<b>Appendix C</b>	<b>154</b>
	<b>Appendix D</b>	<b>155</b>
	<b>References</b>	<b>156</b>

## List of Tables

2.1	Overview of 2D geometrical confinement on skeletal muscle.	22
2.2	Overview of mechanical stimuli on skeletal muscle. . . . .	29
2.3	Hydrogels in skeletal muscle tissue engineering. . . . .	41
2.4	Overview of 3D printed skeletal muscle. . . . .	59
3.1	Porosity and average pore size of GelMA-GG with different concentrations. . . . .	89
4.1	Optimum printing pressures for hydrogels and computed flow rate of the GMGAGG bio-ink. . . . .	114
4.2	The power-law index (n), and the shear rate in 25G, 27G, 30G.	114
4.3	The total UV exposure time for each configuration. . . . .	116



## List of Figures

2.1	Structure of skeletal muscle tissues. . . . .	8
2.2	2D geometry confinement on skeletal muscle tissue engineering.	21
2.3	Electrospun fibers for skeletal muscle regeneration. . . . .	36
2.4	3D bioprinting in skeletal muscle tissue engineering. . . . .	49
3.1	Low acyl gellan gum [1]. . . . .	68
3.2	Synthesis of methacrylated gelatin and UV crosslinking of GelMA hydrogel [2]. A. Gelatin was reacted with MA to introduce a methacryloyl substitution group on the reactive amine and hydroxyl groups of the amino acid residues. (B) GelMA photocrosslinking to form hydrogel under UV irradiation. The free radicals generated by the photoinitiator I2959 initiated chain polymerization with methacryloyl substitution.	69
3.3	Schematic drawing of layer-by-layer UV-assisted bioprinting strategy. . . . .	76
3.4	<sup>1</sup> H-NMR spectra of Gelatin and GelMA. . . . .	77
3.5	Viscosity as a function of shear rate of 30 different GelMA-GG bio-inks at 37°C. a. Viscosity of GelMA-based bio-inks with GelMA concentration at 5%, 2.5% and 1%. b. Viscosity of GelMA-based bio-inks with GelMA concentration at 7.5%. c. Viscosity of GelMA-based bio-inks with GelMA concentration at 10%. d. Viscosity of GelMA-based bio-inks with GelMA concentration at 15% . . . . .	78
3.6	Bio-ink formulation involves characterization of rheological properties, ease of cell encapsulation and influence of cell sedimentation within bio-inks. . . . .	79

3.7	Viscosity as a function of shear rate of 30 different GelMA-GG bio-inks at 25°C. a. Viscosity of GelMA-based bio-inks with GelMA concentration at 1%. b. Viscosity of GelMA-based bio-inks with GelMA concentration at 2.5%. c. Viscosity of GelMA-based bio-inks with GelMA concentration at 5%. d. Viscosity of GelMA-based bio-inks with GelMA concentration at 7.5%. e. Viscosity of GelMA-based bio-inks with GelMA concentration at 10%. f. Viscosity of GelMA-based bio-inks with GelMA concentration at 15%. . . . .	81
3.8	The bioprinting phase involves characterization of rheological properties, determination of suitable UV scanning speed and selection of suitable bio-inks. . . . .	82
3.9	Printed constructs with different patterns. . . . .	85
3.10	Bio-ink properties (mechanical stiffness and microstructure).	87
3.11	Live/dead staining of C2C12 in manual-cast cell-laden bio-inks with varied concentrations on Days 0, 7 and 14, with pink arrows showing cell elongation and spreading. . . . .	90
3.12	C2C12 cell viability and proliferation study of cell printing on Day 1,4 and 7; scale bar is 500 $\mu\text{m}$ .* - $p < 0.05$ , ** - $p < 0.001$ . . . . .	92
4.1	Schematic of extrusion-based bioprinting. . . . .	102
4.2	Schematic of three printing stages. a. Cells in printing syringe over time. b. Cells under shear stress in the needle tips. c Cells under UV irradiation. c1. cells in single layer filament exposed to UV irradiation. c2. cells printed in multi-layer constructs under layer-by-layer UV curing. . . . .	104

4.3	Rheological behavior of GMGAGG and GelMA-GG composite bio-ink. . . . .	106
4.4	A. Quantitative analysis of gelatin release with TNBS. B. The zoom in view of amino acid concentration from 38-38.6 $\mu\text{g/ml}$	107
4.5	Structural integrity of printed constructs at varied time point in dPBS. . . . .	108
4.6	Degradation profile of composite bio-inks for 28 days. A. Degradation of GelMA 10%, GelMA-GG (5-0.5, 7.5-0.1/0.2/0.5 and 10-0.1/0.2) and GMAGAGG 2.5-5-0.2. B. Degradation of 5% and 7.5% GelMA. C. Zoom-in view of the degradation from day 7 to day 28. . . . .	110
4.7	Biocompatibility of GMGAGG for 10-days culture. . . . .	111
4.8	Cell viability of both C2C12 and HUVECs over 150 min (prior to printing). . . . .	113
4.9	Cell viability of C2C12 and HUVECs printed with different needle sizes. . . . .	115
4.10	Cell survival rate with varied UV scanning times and UV scanning speed. . . . .	117
4.11	Analysis of cell viability in multi-layer printed GMGAGG constructs. . . . .	120
4.12	Filament width of printed of constructs. . . . .	122
5.1	Schematic of capillary force assisted cell seeding in 3D printed constructs. . . . .	129
5.2	Printed of GMGAGG constructs. . . . .	133
5.3	Capillary action assisted cell seeding in 3D printed GMGAGG constructs. . . . .	134
5.4	The influence of line spacing on cell orientation. . . . .	135

5.5	The influence of cell seeding density on cell orientation. . . .	136
5.6	Morphology of C2C12 and HUVECs in co-cultured medium with varied combination. . . . .	138
5.7	Proliferation study of C2C12 in co-culture medium with var- ied combination over 4 days. . . . .	139
5.8	Proliferation study of HUVECs in co-culture medium with varied combination over 4 days. . . . .	139
5.9	Co-cultured cells with varied ratio of C2C12:HUVECs=5:5 and 7:3. A. Microscope imgaing of the co-cultured C2C12/HUVECs in different ratios and cell numbers. B. Proliferation study of the co-cultured C2C12/HUVECs over 7 days. . . . .	141
5.10	Immunostaining of co-cultured constructs, constructs with C2C12 alone and 2D casting (C2C12/HUVECs) were run in parallel as control, . . . . .	142
A	UV effect on C2C12 viability with varied exposure time. . .	152
B	UV effect on HUVEC viability with varied exposure time. .	153
C	Cell survival rate of printed C2C12 in GMGAGG multilayer constructs. . . . .	154
D	Cell survival rate of printed HUVECs in GMGAGG multi- layer constructs. . . . .	155

# Chapter1

## Introduction

### 1.1 Background

Skeletal muscle, which accounts for 40-45% of an adult human body mass, is innervated by somatic nerves system and controls voluntary movement and locomotion such as walking or running [3]. Contusions and lacerations during sports, trauma and tumor ablation frequently cause skeletal muscle injuries. Although skeletal muscle has the intrinsic remarkable self-regeneration capability for minor injuries, under some compromised conditions, such as severe traumatic injuries and volumetric muscle loss (VML) with muscle loss over 20%, the regeneration process is significantly restrained by fibrous scar tissue formation and therefore, causing muscle dysfunction [4, 5].

By grafting the healthy muscle tissues adjacent to the injury sites, autologous muscle transfer is frequently performed clinically and is regarded as the current gold standard. These transferred muscle tissues with the dense vascular network and nerve-muscle junction facilitate the muscle regeneration [6]. Another alternative is free functional muscle transfer when no muscle is in the vicinity of the injured tissue, yet sacrifice of healthy muscles is inevitable in these strategies. Frequently occurred donor site morbidity, insufficient innervation and complications lead to the failure of full muscle function recovery. Besides surgical interventions, physical therapy is commonly suggested to strengthen the remaining muscles and assist the muscle repair after injury. Through regular exercise or massage, physical therapy promotes vascularization and new muscle formation. However, this non invasive/minimally invasive method is less effective in VML.

Other strategies such as the transplantation of muscle precursor cells have been widely explored [7, 8, 9, 10]. The transplantation of satellite cells

to the muscle of dystrophin-deficient mdx mice has been observed with remarkable muscle fiber regeneration and contractile functional recovery [8]. However, the low expansion capacity of satellite cells, low cell survival rate potentially caused by poor localization or immune rejection and limited integration with host tissues await to be addressed.

Decellularized extracellular matrix (dECM) has been an attractive scaffold platform. dECM scaffolds preserve native structures which could guide fiber alignment and the vascular networks that could possibly facilitate nutrients transportation and waste removal [11, 12, 13]. However, the effect of the cell removal process on biochemical and mechanical properties of dECM is not completely understood, and the poor understanding of the composition and batch to batch variation resulted in inconsistent outcomes. Moreover, study on cell migration in large scaffolds is still limited.

Tissue engineering has made remarkable progress in skeletal muscle regeneration. By incorporating the exogenous factors (physical, chemical and electrical cues), tissue engineering scaffolds have been designed to be mechanically compliant and biocompatible to induce cell adhesion, proliferation and differentiation, and thus elicit desired cellular response and functional recovery. A number of bioengineering strategies including geometrical confinement, electrospun fibers, porous hydrogel with anisotropic microchannels or with other assisted strategies such as mechanical stimulation, have been implemented to construct *in vitro* skeletal muscle tissues with high fidelity through spatial or temporal control over materials, cells or other exogenous cues to accelerate the regeneration process. Each method has their own merits and disadvantages. Nevertheless, most of the skeletal muscle tissue models are fabricated with relatively small sizes which are inadequate for VML.

In recent years, 3D bioprinting has developed into a promising tool to construct reproducible and complex models that are highly automated. 3D bioprinting allows the fabrication of constructs with various materials, multiple cell types and instructive biomolecules based on pre-designed patterns. Exquisite control over the incorporated elements may better imitate the intricacies of natural physiological environment. One of the major dilemmas that hinders the development of 3D bioprinting is the lack of suitable bio-inks, especially for soft tissues. It is often difficult to find a printable material with compliant mechanical property and yet, still be able to generate large tissue constructs during 3D bioprinting without structural collapse. Hydrogels with dynamic mechanical property are of great interest. Bio-inks transitioned from stiff to soft yield highly desirable property that is initially bioprintable and subsequently cell-responsive.

Despite the superior structural feasibility offered by 3D bioprinting, the printing process can be tedious for large and complex constructs. Long duration of printing process may compromise the cell viability, especially cells such as primary cells, induced pluripotent stem cells (iPSCs), embryonic stem cells (ESCs) and so forth. Integration with other strategies that could possibly alleviate cell damage is highly desirable.

Capillary action, which enables a liquid to flow within sufficient small spaces without the assistance of external forces, has been broadly used in hard materials. Recent studies have also demonstrated the feasibility of capillary action on cell delivery in tissue engineered scaffolds [14]. Thus, by applying capillary action into appropriate 3D bioprinting constructs, we have demonstrated the potential and feasibility of fabricating large 3D bioprinted muscle constructs with unidirectional channels and high cell density for volumetric muscle loss.

## 1.2 Objectives

The overall objective of this research is to develop a bioink and subsequently construct *in vitro* skeletal muscle tissue models with anisotropic cell organization in 3D hydrogels for VML. This work has the following research objectives:

- To develop a suitable bio-ink and to establish a robust layer-by-layer UV crosslinking printing process.
- To investigate the influence of UV radiation on cell survival rate over the bioprinting process.
- To develop 3D *in vitro* skeletal muscle tissue constructs and achieve anisotropic cell organization in 3D hydrogels using 3D printing technology with the assistance of capillary force.

## 1.3 Scope

The scope of this project includes:

- Selecting a suitable bio-ink and establishing a material selection framework and layer-by-layer UV assisted extrusion-based bioprinting strategy.
- Understanding the UV radiation effects on printing resolution and cell survival rate.
- Construction of long-term culture of the 3D bioprinting skeletal muscle tissue models with an integrated capillary action-assisted bioprinting strategy.



## 1.4 Organisation of report

The thesis is organized as follows:

Chapter 1 introduces the background of skeletal muscle tissue engineering, bioprinting, capillary action application. The motivations, objectives and scope of this research are also listed.

Chapter 2 covers literature review of the efforts on skeletal muscle tissue engineering. Specifically, design criterion in engineering skeletal tissues are highlighted. State-of-the-art bioengineering technologies including geometrical confinement, electrospun fibers, porous hydrogel, and 3D bioprinting are elaborated. Limitations and future directions of tissue-engineered muscle constructs are discussed.

Chapter 3 introduces a facile bioprinting strategy that combines the rapid extrusion-based bioprinting technique with an in-built ultraviolet (UV) curing system. Bio-ink selection framework is also devised.

Chapter 4 describes the development of suitable bio-ink and investigates the UV radiation effects in the three stages of bioprinting in terms of cell viability using C2C12 and HUVECs.

Chapter 5 presents the proof-of-concept for bioprinting 3D skeletal muscle tissue constructs using 3D bioprinting. Capillary action is employed to achieve homogeneous cell seeding in a highly efficient manner. The characterization of 3D skeletal muscle constructs in term of immunofluorescence

analysis will also been included.

Chapter 6 presents the conclusions of the project as well as recommendations for future work.

# Chapter2

## Literature Review

### 2.1 3D skeletal muscle constructs context

#### 2.1.1 Physiology

Skeletal muscle consists of highly organized, densely packed myofibers (each represents the single cell), abundant blood vessels, nerve and connective tissue. Individual myofibers are covered by a basement membrane, which is continuous with the endomysium connective tissue layer. Myofibrils, derived from the fusion of myoblasts, agglomerate to form myofibers within 20 to 100  $\mu\text{m}$  [15]. Myofibrils consist of many adjacent sarcomeres that are connected end to end. The smallest functional unit of skeletal muscle is sarcomere, which consists of thick filament made of a protein known as myosin and thin filament made of a protein known as actin (Figure 2.1).

Capillaries run along the muscle fibers, which basically carry blood and supply cells with oxygen and nutrients. Many of the muscle fibers are stacked together, along with the neurons and blood vessels to form a cylindrical bundle, which is known as fascicle. Fascicles are bundled together to form a real muscle. There are two types of skeletal muscles, type I and type II. Type I basically contains a high concentration of myoglobin, a special protein that carries oxygen. Type I muscle breaks down ATP at a slow rate and thus are called slow-twitch muscle. Therefore, they are slow to fatigue and contract slowly and mainly responsible for less intense but prolonged activities such as long-distance running. Whereas the type II muscle breaks ATP at a high rate, contract quickly and are called fast-twitch fibers. They are primarily in charge of high-intensity activities such as sprinting [4].

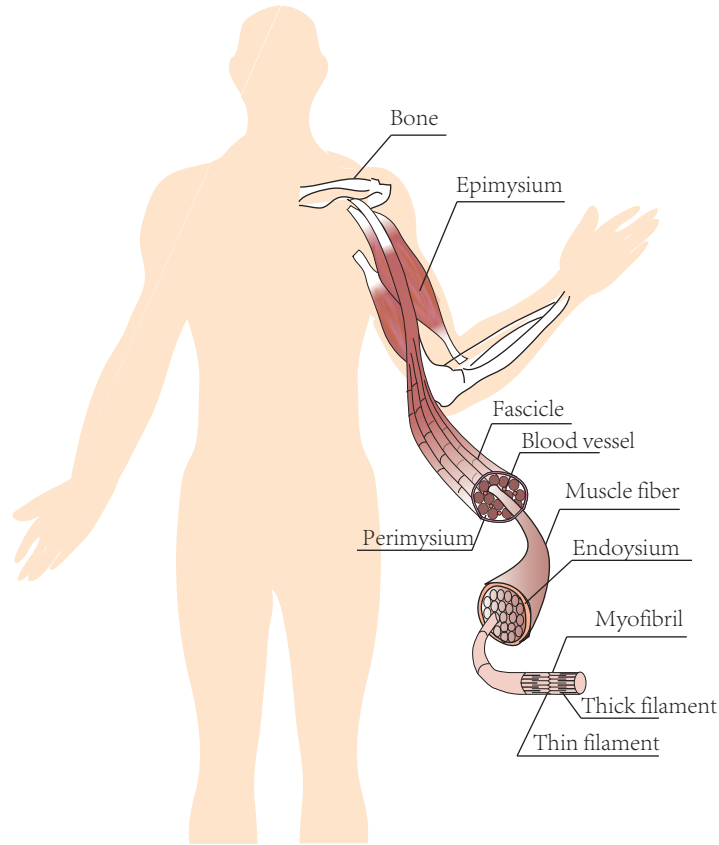


Figure 2.1: Structure of skeletal muscle tissues.

## 2.1.2 Design criteria

To better recapitulate the structure and function of the native skeletal muscle, a myriad of studies have been carried out to identify the critical factors that modulate myogenesis. Here we elaborate on these factors and their effects on myogenesis with specific examples to provide some insights into the design considerations of engineered skeletal muscle tissues.

### 2.1.2.1 Matrix composition and structure

The increasing awareness of the importance of cell-ECM interaction has fueled growing interests in decoding matrix components. ECM functions not only as mechanical support, but also imparts instructive signaling to steer cell behaviors [16]. A clear understanding of matrix components could ben-

efit material-based therapies. Generally, skeletal muscle composed of two parts of matrices, the basal lamina and intramuscular connective tissues. The basal lamina is a sheet-like structure and mostly comprises laminin, collagen IV, nidogen, and perlecan [17]. Connective tissue, with a highly organized structure, can be divided into three layers: epimysium, perimysium and endomysium. Endomysium encloses myofibers and is mainly made of aligned collagen fibers [18]. Muscle fibers bundled together and ensheathed by type I collagen enriched perimysium [19]. These fascicles, interspersed with blood vessels and axons, are wrapped by epimysium, which comprises two wavy sheets of collagen fibrils. Collagen is the major component in skeletal muscles that maintain the structural integrity [20], particularly type I and type III fibrillar collagen. Meanwhile, a minor fraction of type II, V, VI, IX, XII and XIV have been detected in some specific muscle and species [21]. Additionally, for tissues such as the smooth muscle, skeletal muscle and cardiac muscle, cell organisation dictates the tissue function. Controlling the structure of the matrix to induce cell alignment represents the first and foremost step in the myogenic process.

#### **2.1.2.2 Multi-cellular environment**

Satellite cells make up approximately 2-7% of the total nuclear content of skeletal muscle. They locate between the basal lamina and the plasma membrane that surrounds each fiber, and function as putative stem cells in skeletal muscle. These cells are quiescent in mature, healthy tissues and are specified by expression of paired box 7 (Pax7) [15]. Satellite cells play a pivotal role in muscle fiber repair. They react upon injuries, switching from quiescent to active. Satellite cells migrate to the injured site, proliferate, undergo myogenic differentiation, fuse to form new myofibers and integrate

with the muscle. Seminal studies have demonstrated the efficacy of satellite cells transplantation [22, 23]. The transplantation of single intact myofiber with seven satellite cells into radiation-ablated muscles produced over a hundred new muscle fibers with thousands of nucleus [22]. Robust self-renewal and expansion have been observed. Given the myogenic potential, satellite cell is a suitable source for muscle regeneration. However, they are identified to be highly heterogeneous in function and thus with varied efficacy in regeneration [22, 24, 25, 10, 26]. Moreover, the difficulty in isolation and purification of the cells and the low expansion capacity *ex vivo* awaits to be addressed [10, 27]. This has greatly intrigued the interests in exploring various cell types with comparable regeneration capability. Myoblasts [28], mesoangioblasts [29, 30], pericytes [31, 32], embryonic stem cells (ESCs) [33], induced pluripotent stem cells (iPSCs) [34], mesenchymal stem cells (MSCs) [35, 36], muscle-derived stem cells (MDSC) and adipose-derived stem cells (ADSCs) have been extensively explored for their myogenic capability [37, 38]. Some detailed reviews have summarized the cell sources and types for skeletal muscle regeneration [39, 40].

Muscle contraction is regulated by the intimate collaboration of muscle tissues, capillaries, nervous tissue and connective tissues, suggesting that in addition to muscle cells, fibroblasts, neurons and endothelial cells are indispensable when constructing *in vitro* muscle tissues. The interaction between muscle cells and fibroblast is essential as the collagen and other ECM proteins and some growth factors are mainly secreted by interstitial fibroblasts. Cooper et al. have clarified the possible role of fibroblast as an elastic substratum to support contractility and as a facilitator for the development and maturation of C2C12 [41]. Specifically, cells cultured on collagen- or laminin-coated substrates detached massively after 5-6 days differentiation,

whereas for C2C12 cultured on fibroblast substratum, extended contractile myotube culture period has been observed. Highly matured sarcomeric structure has been confirmed by immunostaining. Electrical stimulation at 10V was applied and the occurred reproducible calcium transients revealed the functional maturation in terms of calcium handling proteins. The potential of fibroblasts on promoting the C2C12 proliferation and spontaneous myoblast differentiation and stabilizing the tissue integrity by secreting the ECM proteins were further confirmed in subsequent studies [42, 43, 44, 45]. In a recently published study, Rao et al. conducted a co-delivery of myoblasts and fibroblasts using decellularized skeletal muscle extracellular matrix (SkECM) hydrogel to tibialis anterior (TA) of C57BL/6 mice models [44]. Myoblast or co-delivery with PBS was run as control. Cell viability was remarkably increased in skECM with fibroblasts on day 7 compare to control groups. As demonstrated by Perimed laser speckle contrast analysis, better perfusion was found compared to the saline group. It is noteworthy that co-delivery with better recapitulating of native environment yielded more desirable results.

Skeletal muscle is a highly vascularized tissue. Capillaries interspersed in the muscle fibers to facilitate the nutrients and oxygen transportation and waste removal. Particularly, for thick engineered tissues, the absence of vascular network frequently induces tissue necrosis in the central zone and finally leads to the failure of fully functional recovery. To overcome this, myoblasts co-culture with endothelial cells to vascularize the tissue has been widely investigated [46, 47, 48, 49, 50, 51, 52, 53, 54]. Notably, Levenberg et al. reported a tri-culture by seeding myoblast, embryonic fibroblast and endothelial cells (ECs) on 3D highly porous scaffold (PLGA-PLLA) [49]. Medium (myoblast medium and EGM-2) effect was examined. The results

showed that EGM-2 was not very supportive for myoblast differentiation whereas myoblast medium promoted myoblast differentiation and endothelial network formation. The increased VEGF expression highlighted the pivotal role of fibroblasts on promoting the formation and stabilization of the endothelial vessels. To analyze the therapeutic potential, the constructs were implanted into three different models. Continuous cell differentiation *in vivo* and host integration were observed in all three models. The quantitative analysis of the perfused vessels revealed that constructs with muscle cells only have  $21 \pm 2$  vessels, while constructs with endothelial cells had  $30 \pm 2$  vessels. This indicated that prevascularization could possibly improve blood perfusion and survival. In a lateral study, Koffler et al. conducted the tri-culture on a biodegradable, acellular scaffold to analyze the degree of *in vitro* vascularization [54]. The constructs were cultured *in vitro* and observed at different incubation periods (1 day, 1, 2 and 3 weeks). ECs and myoblasts spread toward the perimeter of the scaffold within one day of culture. The vessel-like structure appeared at the peripheral of scaffold 1 week in culture. Two and three weeks later, the open vessel-like structures were observed at the center of the scaffold and almost covered the entire construct. The constructs with varied maturity (1 day, 1, 2 and 3 weeks) were then transplanted to the abdominal wall of nude mice to investigate the tissue integration. Muscle formation was observed in all the groups, and increase with incubation time, fibers tend to be more organized and closely packed. This technology was further extended and applied to repair large soft tissue defects [51]. The triple-cultured constructs were cultured *in vitro* to form the small capillary network and then implanted to femoral artery and veins for prevascularization for 1 week. The extensive vascular density and perfusion indicated that the scaffolds were highly vascularized,



therefore was transferred to abdominal viscera for a full-thickness abdominal wall repair. The engineered constructs remained viable and vascularized and integrated with the surrounding tissues. The tri-culture system has exhibited great potential in enhancing muscle regeneration, maturation, and integration. However, constructs in these studies were lack of anisotropic structures. Chen et al. introduced a co-culture of L6 skeletal myoblast and HUVECs in 3D micropatterned collagen scaffold with parallel and concave microgrooves [50]. The ratio of myoblast to HUVECs varied from 1:0 (mono-culture), 3:1 to 1:1 (co-culture), and the total seeding concentration ranged from  $1 \times 10^6$ ,  $4 \times 10^6$  to  $6 \times 10^6$  cells/mL. The results showed that lower seeding concentration ( $1 \times 10^6$  cells/mL) resulted in the formation of cellular spheroids rather than cell bundles in the scaffolds. Muscle bundle tissues were observed in all the seeding ratio, however, the group with a lower ratio of HUVEC yielded the formation of intermittent tubule-like structure.

Co-culture system is very attractive as it provides a more authentic scenario for cells, therefore better recapitulate the native condition. The optimal medium to support various cell types for sustained culture should be sorted out. Gholobova et al. have carried out a systematic study by a co-culture of human muscle progenitor cells (myoblast 92% and fibroblast 8%) with HUVECs in a fibrin ECM [48]. Total cell seeding density ( $1 \times 10^6$  or  $2 \times 10^6$ ), cell ratio (muscle cell: HUVECs= 60:40, 50:50, 70:30) and culture medium have been examined in both 2D and 3D to optimize the culture condition. The results suggested that EGM-2 allowed the growth of HUVECs and myofiber formation in comparison to SkGM (skeletal muscle growth medium). In co-culture with a total of  $1 \times 10^6$  cells, 30% and 40% HUVECs showed apparently better endothelial network formation compared with co-culture bioartificial muscles (BAMs) with a 50:50 ratio. When a total cell

number of  $2 \times 10^6$  was used, no significant difference regarding the improvement of myofiber formation was observed. The results indicated that cell number is a dominant factor over cell ratio.

Muscle contraction begins when the nervous system generates an electrical signal, which is known as an action potential, travels through the motor neuron. The neuromuscular junction is where the motor neuron reaches a muscle cell. When the signal reaches the neuromuscular junction, a neurotransmitter called acetylcholine (ACh) is released by motor neurons, binds to receptors on the outside of the muscle fiber. That initiates a chemical reaction within the muscle, causing muscle contraction. Given that neuronal input is essential for muscle development, maturation and function, electrical stimulation is frequently used to mimic the neuronal stimulation to induce muscle contraction in a laboratory environment. However, the electrical stimulation is not conducive for long-term culture, which makes the neural stimulation necessary when constructing the *in vitro* muscle tissues. Both 2D monolayer and 3D co-culture have been explored for constructing neuromuscular junction [55, 56, 57, 58, 59, 60].

Larkin et al. co-cultured skeletal muscle construct with fetal nerve explants [56]. The co-culture constructs were observed to exhibit spontaneous contraction while monoculture did not. The presence of ACh at the junctions between nerve extensions and the muscle constructs was confirmed with immunohistochemical labeling. Morimoto et al. generated 3D free-standing neuron-muscle constructs with highly aligned and matured muscle fibers from the co-culture of skeletal muscle fibers and motor neurons [57]. They have developed free-standing muscle fiber constructs with C2C12-laden matrigel, followed by mNSC differentiation on the muscle constructs. The neurospheres were in tight connection with muscle fiber bundle, stable adher-

ence without slipping. The AChRs were formed at the connection between the muscle fibers and the neurons. Strikingly, with the chemical stimulation of glutamic acid on motor neurons, the muscle-neuron constructs contracted synchronously with a contractile displacement ( $37.7\mu\text{m}$ ) larger than that of spontaneous contractions ( $0.9\mu\text{m}$ ). Taken together, co-culture of muscle cells with neurons has greatly improved the muscle contractility. This was also confirmed by a lateral study performed by Smith et al. in 3D collagen-based skeletal constructs with primary cells (primary muscle-derived cells (MDCs) and ventral horn motor neurons) [58]. Similarly, the co-culture system was applied to a fibrin-based 3D matrix by Martin et al [60]. Immunohistochemical analysis confirmed the uniaxial alignment myotube formation and the attachment of neurons to the fibrin gel. Immunostaining of SV-2 and AChR suggested the presence of putative NMJ formation within the fibrin gel. With the electrical stimulation, constructs cultured for 18 days exhibited 145% greater twitch force and augmented by 143% tetanic force in comparison to the control group (with no neurons). This highlighted the critical role of neurons on muscle contraction. Moreover, the co-cultured constructs showed more consistent striations ( $84.42\% \pm 7.85\%$  of myotubes) than aneural constructs ( $13.9\% \pm 4.47\%$ ).

Overall, the co-culture systems, including fibroblast, HUVECs and neurons, have provided profound insight into the cell-cell interactions and effective platforms to better recapitulate actual muscle tissues. They would be of considerable benefits to the study of pathology and pharmacokinetics of relevant degenerative diseases.

### 2.1.2.3 Matrix stiffness

It is well known that mechanical property of substrates exerts significant effects on cell behavior. As documented that the differentiation of MSCs is highly modulated by substrate stiffness. They could adopt neuronal phenotype on softer substrate (0.1-1 kPa) [61], and tend to be myogenic on matrices with 10-fold stiffness (8-17 kPa) [62, 63]. On a rigid substrate (25-40 kPa), they are likely to be osteogenic [64]. Similarly, skeletal muscle cells are regulated by substrate elasticity as well. The elastic modulus of healthy muscle is 12 kPa, while aging, degenerated and injured muscles possess a higher elastic modulus over 18 kPa [65]. PM Gilbert et al. has highlighted the importance of satellite niche rigidity by growing freshly isolated muscle stem cells on laminin-coated PEG hydrogel (12 kPa) and rigid plastic dishes (10<sup>6</sup> kPa). Notably, muscle stem cells on softer substrates exhibit superior self-renewal capability *in vitro* and regeneration capacity when subsequently injected into mice [66]. In addition to cell differentiation, matrix stiffness has a great impact on myofiber formation and maturation [67, 68]. Engler et al. introduced collagen strips that attached to glass or polyacrylamide gels with varied elasticity (1, 8, 11, 17 kPa). The results indicated that C2C12 cells aligned and fused into myotubes regardless of substrate stiffness, whereas myosin/actin striation was stiffness-dependent. Striations were only observed on gels (8 and 11 kPa) with similar stiffness to normal muscle tissues. With human myoblast, Serena et al. have further verified the critical role of substrate stiffness in governing striated myotube formation.

### 2.1.2.4 Geometrical confinement-2D topology

Skeletal muscle consists of nanofibrils where organisation determines functionality. As demonstrated, myoblasts grow randomly in the absence of

contact guidance and this is not conducive to generate contractile tissues. Therefore, it is advantageous to design scaffolds with appropriate topographical support to align the muscle cells and elicit a desirable cellular response. With this in mind, early studies have devoted enormous efforts to evaluate the effects of various micro- or nano-scale surface topology and patterning on directing cell behavior and attempt to screen out the optimum feature [69, 70]. Hitherto, a plethora of techniques enable the generation of nano-/micro-scale features, including but not limited to photolithography [71, 72], soft lithography [73, 74, 75], hot embossing [76], stretching [77], micro-contact printing [78, 79, 80] and abrasion [81], etching [82, 83], UV embossing [84], direct laser writing [62, 85, 86].

Correspondingly, a number of patterns such as groove/ridges/channels [87, 71, 78], holes [76], square, circle and diamond posts [75], cantilever [88] and continuous wavy micropatterns [89, 90, 91, 81, 92], with feature sizes spanning a wide range have been evaluated (Table 2.1). As revealed in table 2.1, groove/ridge pattern in nano or microscale has been the focus of the research.

Groove/ridge pattern with size up to 100  $\mu\text{m}$  allows the myoblast alignment and elongation, but with limited effect on cell differentiation. An outstanding study has been conducted by Charest et al.[76]. They analyzed the primary and C2C12 myoblast alignment and differentiation by a series of micro-topological patterns, including groove/ridges and an array of holes, with various sizes (width or diameter) ranging from 5 to 75  $\mu\text{m}$  and depth around 5.1  $\mu\text{m}$  (Figure 2.2a). Notably, cell alignment has been observed in all the groove patterns but selectively aligned along the rows of holes. The alignment is modulated by the groove width, increased alignment was observed on narrower groove widths. Evidenced by sarcomeric myosin and

Ach receptor expression, cell density and differentiation was not significantly affected by the topography (Figure 2.2b). In addition, groove/ridge pattern in nanoscale facilitate myoblast alignment as well [82, 93]. Clark et al. suggested that ultrafine gratings (130 nm wide grooves separated by 130 nm wide ridges and 210 nm deep) allows cell alignment, but inhibit myotube formation. Wang et al. also observed cell alignment and enhanced differentiation on substrates with widths of 450 nm and 900 nm, and varied depth in 100, 350 and 550 nm [82].

Aside from groove/ridge pattern, continuous wavy pattern and posts enable cell alignment as well. Lam et al. demonstrated that wavy pattern with  $6\mu\text{m}$  periodicity gives rises to the most healthy and robust myoblast and optimum alignment (as shown in Figure 2.2g and 2.2h)[92]. Through the comparison between grooves with sharp edges and sinusoidal wavy patterns with round edges, Jiang et al. has declared the negligible role of sharp edges for eliciting contact guidance [90]. Besides linear patterns, surface roughness encompasses the capability to align myoblasts as well [81].

#### **2.1.2.5 Geometrical confinement-2D surface patterning**

Similarly, surface patterning has been frequently utilized to modify material surface chemically or physically, thus impart surface topology as contact guidance. ECM proteins such as collagen, fibronectin and laminin are commonly used to induce cell adhesion and direct cell alignment [79, 94, 95, 96]. Other cell repulsive materials such as PEG and PEO-PPO are employed independently as well to confine the area for cell mobility or work with cell-adhesive protein synergistically [97].

By patterning fibronectin, Bajaj et al. have explored the influence of diverse geometrical constraints on myogenic differentiation process [98]. The

geometries include lines with various widths (300  $\mu\text{m}$ , 150  $\mu\text{m}$ , 80  $\mu\text{m}$ , 40  $\mu\text{m}$ , 20  $\mu\text{m}$ , 10  $\mu\text{m}$ ), torus with different inner diameters (40  $\mu\text{m}$ , 100  $\mu\text{m}$ , 200  $\mu\text{m}$ ) and hybrid pattern (linear and circular feature with varied arc degrees: 30°, 60° and 90°) (Figure 2.2c). Fusion index, degree of maturation, cell alignment, and the response to electrical pulse stimulation (EPS) were evaluated to quantitatively study the differentiation of C2C12. Cells conformed uniformly to the micropattern within 24h-culture. Through immunostaining of MHC, fusion index (regions with  $\geq 2$  nuclei) and maturation index (regions with  $\geq 5$  nuclei) were calculated (Figure 2.2d). Surprisingly, hybrid 30° pattern exhibited a 2-fold and 3-fold increase in terms of fusion index in comparison to linear patterns and circular patterns, respectively. A higher maturation index has been observed in hybrid 30° pattern than all the rest patterns. Taken together, the results suggested that including a small degree of circularity hybrid 30° pattern to a linear structure promotes cells differentiation and myotube maturation.

A simple but systematic study has been conducted by Duffy et al. [79]. The authors evaluated the role of ECM protein and geometrical patterning in modulating myotube formation and alignment. They have compared fibronectin(FN), laminin, collagen type I and collagen type IV with the anisotropically coated substrate and micro-contact printed line patterns with spacing at 10, 15, 20, or 30  $\mu\text{m}$  and width at 20, 50, 100, or 200  $\mu\text{m}$ . Both C2C12 and human skeletal muscle-derived cells (SkMDCs) have been examined. After 6-d differentiation, C2C12 delamination was observed on lines patterned with Col I and IV and isotropic Col I substrate, while myotube formation was observed on FN and laminin regardless of patterns. As evaluated by MHC, laminin coated substrates was found to be superior to FN- and Collagen-coated regarding myotube numbers, myotube length

and fusion index. These results suggested that cell adhesion and differentiation is protein-dependent. Further investigation of geometrical effect was carried out on laminin-coated substrates with varied patterns. The results showed that 10  $\mu\text{m}$  line spacing with considerable myotube area and myotubes bridged across laminin lines, whereas 20, or 30  $\mu\text{m}$  spacing allows cells to grow to conform to the line patterns (Figure 2.2e). With the increased line width, the myotubes began to orient off axis to the pattern. To determine the influence of cell types and species, protein screening was repeated with SkMDCs. Similarly, laminin outperformed FN and collagen in terms of cell attachment and differentiation. Strikingly, cell alignment and differentiation of human SkMDCs were similar in all the patterns, independent of line width and spacing (Figure 2.2f). The disparate trends highlighted the importance of cell selection when designing tissue constructs.

Taken together, these 2D features function as tools to identify the potential of physical cues to induce cell alignment, promote myotube maturation and massively contribute to our understanding of the mechanism of how cells sense their surrounding environment. However, cells only sense the substrate topology when they are in direct contact with the substrates. Moreover, topology plays a critical role in cell alignment, but negligible effects on cell proliferation or myogenic differentiation.



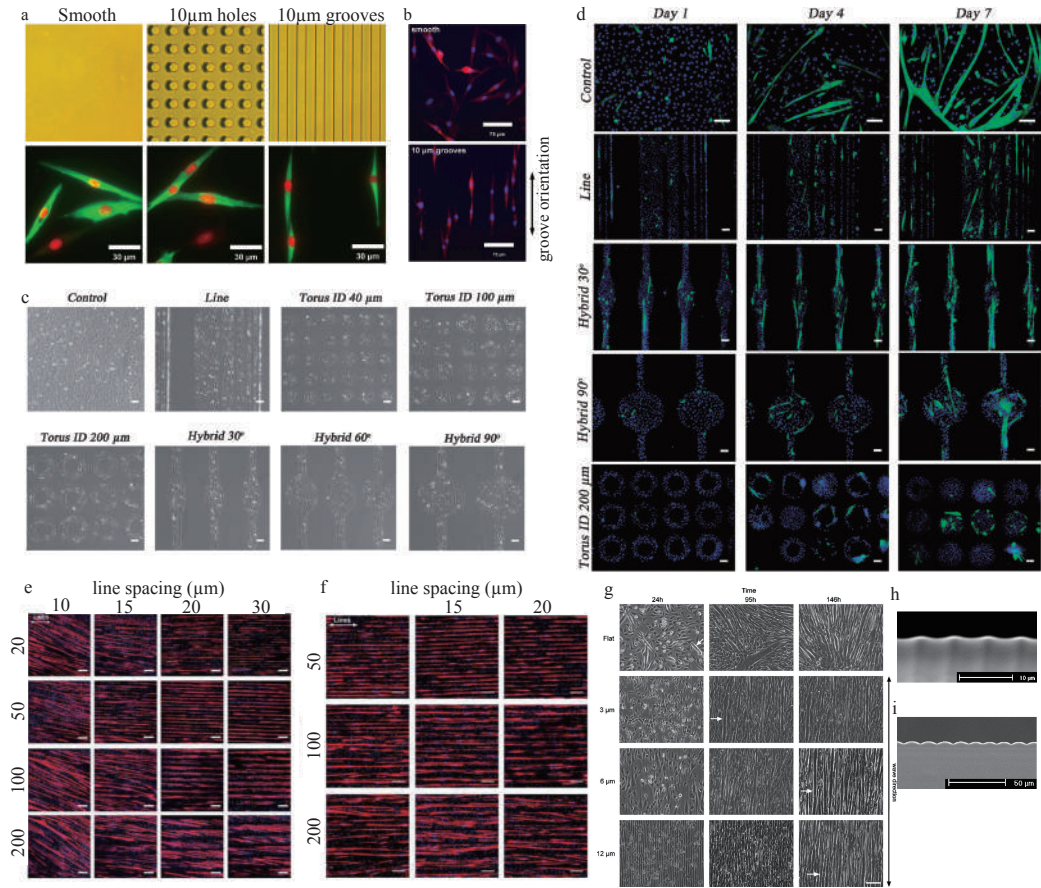


Figure 2.2: 2D geometry confinement on skeletal muscle tissue engineering. a) Cellular orientation is influenced by surface topography and immunostaining of sarcomeric myosin and nuclei. b) AchR expression is not influenced by topography (reproduced with permission from Ref. [76]. Copyright © 2007 Elsevier Ltd). c) Phase contrast images of the different micropatterned cell islands used in the study—lines of different widths (300, 150, 80, 40, 20, and 10  $\mu\text{m}$ ), tori of different inner diameters (40, 100, and 200  $\mu\text{m}$ ), and hybrid patterns of different arc degrees (30, 60 and 90°). d) DAPI and MHC staining of the C2C12 cells on the different patterns (reproduced with permission from Ref. [98]. Copyright © 2011, Oxford University Press). e) Representative images of C2C12 cells differentiated on 16 different line patterns of LAM f) Representative images of MHC and DAPI staining of human myotube formation on  $100 \times 20$  lines (reproduced with permission from Ref. [79]. Copyright © 2016, Biomedical Engineering Society). g) Micrographs of muscle cells on different wave sizes. h) SEM images of 6 and 12 mm sized wavy PDMS substrate (reproduced with permission from Ref. [92]. Copyright © 2006 Elsevier Ltd).

Table 2.1: Overview of 2D geometrical confinement on skeletal muscle.

Fabrication method	Cells	Materials	Pattern/Size	Key feature	Ref
Hot embossing	Primary and C2C12 myoblasts	Self-assemble monolayers presenting CH <sub>3</sub>	Ridges/grooves(equal width) holes (pitch $d = 2$ fold hole $d$ ) ranges from $5\text{-}75\mu\text{m}$ depth $5.1\mu\text{m}$	<ul style="list-style-type: none"> <li>• Myoblast alginment</li> <li>• No significant effect on cell density or differentiation</li> </ul>	[76]
Microcontact printing	C2C12, human primary myoblasts	PA, ave thickness : $100\mu\text{m}$	Lane-interspacing: 100-100; 300-300; 500-500; 100-50; 100-200 $\mu\text{m}$	<ul style="list-style-type: none"> <li>• Wider lanes showed a decrease in C2C12 proliferation</li> <li>• Human primary myoblast proliferation is not affected by patterning width</li> </ul>	[99]
Plasma oxidized with air	C2C12	PDMS, laminin coating	Continuous wavy micropattern: 3, 6, $12\mu\text{m}$ in periodicity, amplitudes of 400, 670, and 1700 nm	<ul style="list-style-type: none"> <li>• Wave features with <math>6\mu\text{m}</math> periodicity produced myoblasts and myotubes with the optimum alignment</li> </ul>	[92]
Electron beam lithography and dry etching	C2C12	Polystyrene	Groove/ridge: width/depth: $450/100$ , $450/350$ , $900/100$ and $900/550$ nm	<ul style="list-style-type: none"> <li>• Cell alignment</li> </ul>	[82]
UV-Embossing	C2C12	Polyurethane diacrylate	wall/channel width combinations: $10/40$ , $10/80$ , $10/120$ , $10/160$ , $25/40$ , $25/80$ , $25/120$ , and $25/160\mu\text{m}$ , 2-cm long, 65 to 70 $\mu\text{m}$ deep/high.	<ul style="list-style-type: none"> <li>• Cells in <math>40\mu\text{m}</math> channel exhibited better elongation</li> </ul>	[84]
Photolithography	C2C12	PLLA-TMC	groove widths (5, 10, 25, 50, $100\mu\text{m}$ ) depths (0.5, 1, 2.5, $5\mu\text{m}$ )	<ul style="list-style-type: none"> <li>• 2.5 and 1 <math>\mu\text{m}</math> in depth 50 and <math>25\mu\text{m}</math> in width showed the best results</li> </ul>	[71]
Grinding with abrasives	C2C12	PDMS	Mean roughness (Ra) type I: $0.03\mu\text{m}$ type II: $0.16\mu\text{m}$ type III: $0.56\mu\text{m}$	<ul style="list-style-type: none"> <li>• Myoblasts alignment on type II and III;</li> <li>• Differentiation was not significantly influenced by linear microscale features</li> </ul>	[81]

Fabrication method	Cells	Materials	Pattern/Size	Key feature	Ref
Soft lithography	C2C12	PDMS	Patterned lines (20 $\mu$ m width 20 $\mu$ m gaps);square posts (20 $\mu$ m edge length, 20 $\mu$ m gaps)		[75]
UV lithography	C2C12	glass coverslips	6.7 $\mu$ m-deep channels with widths ranging from 5 to 120 $\mu$ m	<ul style="list-style-type: none"> <li>•optimal width 20 <math>\mu</math>m, the cells neatly arranged in parallel arrays</li> </ul>	[83]
Replication molding	C2C12	PDMS	A series of wavy patterns: $\lambda < 500\text{nm}$ , $500 < \lambda < 1000$ , $1000 < \lambda < 2000$	<ul style="list-style-type: none"> <li>•Large waviness: cells immediately align</li> <li>•Very small patterns: no global alignment</li> <li>•Intermediate pattern sizes: cell align upon confluency</li> </ul>	[89]
Soft lithography	C2C12	PDMS membrane laminin coating	Line, square, hexagonal lattices, square, circular, and diamond posts	<ul style="list-style-type: none"> <li>•Micropatterned substrates influence cell alignment, localization of focal adhesions, accumulation of ACh receptors.</li> </ul>	[75]
Micro-contact printing	C2C12	Fibronectin coated petri dish	lines with varied widths (10-300 $\mu$ m) tori with different inner dia (40-200 $\mu$ m) hybrid pattern with varied arc degrees: 30°, 60° and 90°	<ul style="list-style-type: none"> <li>•Adding a small degree of circularity to a linear structure promotes cells differentiation and myotube maturation.</li> </ul>	[98]
Micro contact printing	C2C12 SkMDCs	FN, laminin, collagen type I and IV	Line patterns: spacing at 10, 15, 20, or 30 $\mu$ m; width at 20, 50, 100, or 200 $\mu$ m	<ul style="list-style-type: none"> <li>•Cell adhesion and differentiation is protein-dependent Cell orientation and differentiation is species-dependent</li> </ul>	[79]

### 2.1.2.6 Mechanical stimuli

Skeletal muscle is in charge of voluntary movement in the body and subjected to cyclic stretch and relaxation constantly. Mechanotransduction is of critical importance in skeletal muscle tissue [100]. A growing body of research has demonstrated that the crucial effect of mechanical stimulation on regulating skeletal muscle cell behavior (as shown in Table 2.2) [101, 102, 103, 104], yet the underlying mechanisms of mechanical loading on cell behavior is not completely understood. Pioneer study conducted by Vandenberg et al. has revealed that embryonic chicken myoblasts on a collagen-coated substrate aligned parallel to the strain direction under a slowly increasing uniaxial strain rate 0.35mm/h for 3 days [105]. Muscle hypertrophy and increased protein expression and DNA content were observed. Thereafter, a vast majority of studies have been attempting to optimize the strain parameters including direction, duration and frequency to elicit a desirable cellular response (as shown in Table 2.2).

A systematic study has been carried out by Ahmed et al. [97]. They investigated the synergistic effect of geometrical confined surface and cyclic tensile strain (CTS) on myoblast behavior. Briefly, they have configured six different kinds of substrates: homogeneous FN functionalized substrates (1MPa) with or without the presence of cyclic tensile strain; substrates with 0° line pattern (30μm wide parallel lines with 40μm line spacing) in CTS-free state; and 0°, 45°, 90° micro-patterned substrates under CTS. Actin fiber orientation, nuclei aspect ratio and nuclei orientation have been examined. For homogeneous patterned substrates, cells in strain-free condition showed no specific orientation and actin fibers extended to all directions randomly, while cells subjected to CTS tend to reorient their stress fibers around 71.5° with regard to strain direction. In the micro-patterned surface under CTS,

the stress fiber orientation is demonstrated to be dependent on the line direction. In  $0^\circ$  patterned substrates, stress fibers were observed with  $47.9^\circ$   $19.5^\circ$  relative to strain direction; in  $45^\circ$  lines, cells aligned roughly along the patterned lines; and in vertically patterned substrates, cells were highly elongated and aligned along the patterned lines. With respect to nuclei orientation, nuclei elongated along with the direction of line pattern in all the micro-patterned substrates but randomly orientated in homogeneous ones. This revealed that geometrical constraint is the dominant factor in nuclei orientation in comparison to CTS. Strikingly, striations were only observed in  $45^\circ$  patterned substrates. Given the difficulty of actin striation on stiff substrates, the results emphasized the importance of certain strain condition on myogenesis could shield the negative effect of stiff substrates.

Moon et al. have generated 3D collagen-based acellular tissue scaffolds with human MPCs [103]. The scaffolds ( $1.5 \times 0.3 \times 0.3 \text{ cm}^3$ ) were subjected to stretch and relaxation of 10% of their initial length and were stretched 3 times/min for the first 5 min of every hour from day 5 to 3 weeks *in vitro*. Scaffolds under static culture were run in parallel as control and were analyzed on 5 days, 1, 2 and 3 weeks. As indicated by histological studies, unidirectional cell alignment was observed in the constructs with mechanical stimulation within 1 week, while which was absent in static culture. After 3 weeks of mechanical stimulation, the scaffolds were able to generate contractile forces, but not statically cultured control tissues. The MPCs-seeded scaffolds were subsequently implanted onto the latissimus dorsi muscle of mice after 1-week mechanical stimulation. The scaffolds were retrieved on week 1 to 4. As illustrated by immunostaining and H&E, scaffolds with mechanical stimulation displayed superior cell alignment in comparison to control group. The scaffolds generated tetanic and twitch contractile re-

sponses with a specific force of 1% and 10%, respectively, of that observed on native latissimus dorsi after 4 weeks. In a recently published study, Aguilar-Agon et al. has investigated the effect of mechanical loading on mediating skeletal muscle hypertrophy of 3D collagen-based skeletal muscle model using C2C12 cell line [101]. A continuous increasing load was applied to the engineered construct to achieve 15% stretch in 1h, thereafter the construct was left under tension (15% stretch) for another 2hs. The mRNA expression of IGF-1, matrix metalloprotease 2 and 9 (MMP-2, 9), MuRF-1 and MAFbx after mechanical overload 0, 21, 45h were examined. IGF-1 mRNA was significantly upregulated after 21h and 45h mechanical loading. Similarly, MMP-2 mRNA was observed with increased expression 21 hr after loading. However, MMP-9 mRNA was remained unaltered. A significant decrease in ubiquitin ligase MAFbx was spotted 45 hr after mechanical loading, while MuRF-1 mRNA expression remained relatively stable. The results of immunoblotting reported the increased in phosphorylation of Akt, p70S6K, and 4EBP-1 of mechanically loaded scaffold. In addition, the immunostaining demonstrated the increased in myotube size and fusion, which was indicative of the myotube hypertrophy. Furthermore, the functionality of the muscle was assessed by measuring the tetanic force. The force production increased in a step-wise manner after 21h (140%) and 45 hr (265%) mechanical loading in comparison to the unloaded ones. Taken together, these studies demonstrated the efficacy of mechanical stimuli on promoting myogenesis and force production. However, the strain regimen should be further considered.

### 2.1.2.7 Electrical stimuli

Neuronal stimulation is essential for skeletal muscle maturation and contraction. Using electrical pulse stimulation as a surrogate to elicit desired muscle contraction has been widely investigated. Tremendous efforts have been devoted to optimizing the electrical stimuli (ES) protocol to better facilitate skeletal muscle activity and ameliorate muscle damage during the chronic stimulation period. A plethora of different ES protocols has been applied in 2D monolayer culture, which can be referred to [106]. High-voltage stimulation (2–2.5V/mm) or frequencies over 3Hz was detrimental to 2D C2C12 muscle cells [107]. A multitude of studies both 2D [108, 109] and 3D [110, 111, 107] have demonstrated that electrical stimulation advances the differentiation and maturation of muscle cells, promotes force production [112].

A pioneering study carried out by Brevet et al. [113] reported that ES (14h-48h, 0.6s train of 10- to 25-ms biphasic pulses delivered every 4s for 7 hours in total) rendered an increase in myosin accumulation and contractile protein synthesis in comparison to non-electrical stimulated control group. Langelaan et al. investigated the ES effects (4 V/cm, 6 ms pulses at a frequency of 2 Hz) in 2D and 3D culture with long-standing cell lines C2C12 and primary cell source: muscle progenitor cells (MPCs) [114]. The remarkable difference in maturation level between the two cell types was identified by cross-striations and expression levels of mature myosin heavy chain (MHC) isoforms, indicated that MPCs constructs were more susceptible to ES.

A notable study published recently by Khodabukus et al. has investigated the effects of electrical stimulation on human engineered muscle structure, function and metabolism [115]. The model was electrically stimulated with intermittent stimulation at 1Hz and 10Hz after 1-week differentiation.

Notably, the 7-day electrical stimulation significantly increased nuclei numbers, muscle bundle size, as well as glucose and fatty acid metabolic independent of frequency. Moreover, a 3-fold higher twitch and tetanic force were found with electrical stimulation in comparison to the non-stimulated controls. Strikingly, the specific force was increased to 19.3 mN/mm<sup>2</sup> (1 Hz), yielded the highest value reported hitherto for human engineered tissues. Upregulation of several sarcomeric proteins including dystrophin, myosin heavy chain, and sarcomeric  $\alpha$ -actinin indicated the maturity of the myotubes, which is consistent with previous studies.



Table 2.2: Overview of mechanical stimuli on skeletal muscle.

	Strain type	Materials	Cells	Amplitude, frequency, duration	Key feature	Ref
2D	Uniaxial stretch	Laminin collagen I proNectin coated membrane	MPC C2C12	0-2% (2d) followed by a uniaxial intermittent stretch regime of 2-6% (3 h on, 3 h off)	<ul style="list-style-type: none"> <li>No cell alignment</li> <li>Maturation inhibited</li> </ul>	[116]
	Uniaxial or equibiaxial CTS	Collagen I	C2C12	15%, 0.5Hz, 1s strain and 1s rest for 48h, then 3d rest	<ul style="list-style-type: none"> <li>Equibiaxial: no cell alignment;</li> <li>Uniaxial: cell aligned perpendicular to the strain direction</li> <li>Increased myoblast differentiation and myotube formation</li> </ul>	[105]
	Equibiaxial stretch	Collagen-coated plates	C2C12	12%, 0.7 Hz, 1 h/d for 2d or 5d	<ul style="list-style-type: none"> <li>2d: no significant change in myotube area and diameter</li> <li>5d: increase in myotube diameter and area (&gt;2 fold)</li> </ul>	[117]
	Uniaxial CTS	Silicone membrane precoated with collagen type I	ASCs	10%, 1Hz for 24h	<ul style="list-style-type: none"> <li>Cell alignment perpendicular to strain direction.</li> <li>Compare to chemical treatment, mechanical factor has less effect on myogenic differentiation</li> <li>The addition of mechanical stimuli upregulated MyoD, MyHC2, MyoG expression.</li> </ul>	[117]
	Uniaxial CTS	Silicone sheets coated with fibronectin	Mouse BMSCs C2C12 human gingival fibroblasts rBMSCs	10%, (0.08, 0.17, 0.33, and 0.50 Hz) up to 7d	<ul style="list-style-type: none"> <li>0.17Hz resulted good cell alignment</li> <li>mBMSCs aligned parallel to strain vector while other cell types aligned perpendicular to strain direction</li> <li>Upregulation of Myf5 and MRF4, myosin- and myogenin-positive myotube formation</li> </ul>	[118]
2D	Uniaxial CTS	Collagen I coated substrate	Adipose-derived stem/stromal cell	11%, 0.5 Hz, 1 h/day, 18 days (from d3- d21)	<ul style="list-style-type: none"> <li>Cell aligned at almost 45° to the direction of strain</li> <li>Increased expression of desmin, myoD and MHC</li> </ul>	[119]

	Strain type	Materials	Cells	Amplitude, frequency, duration	Key feature	Ref
	Uniaxial CTS	Collagen-coated silicone rubber membranes"	C2C12	20% elongation for 24 h 0.1Hz 2s on-time, 4s off-time	<ul style="list-style-type: none"> <li>Decreased MyoD and MNF-a</li> <li>No expression of myogenin and MNF-b</li> </ul>	[119]
	Uniaxial CTS	Collagen-coated BioFlex plates	C2C12	17% strain, 1 Hz, 1 h of cyclic strain every 24 h for 5 days	<ul style="list-style-type: none"> <li>Enhanced proliferation</li> <li>Inhibit differentiation into myotubes</li> </ul>	[120]
	Uniaxial CTS	BioFlex plates	C2C12	10%, 0.25Hz, 2s strain and 2s rest for 1h/day for 5 days	<ul style="list-style-type: none"> <li>Cyclic stretch induces C2C12 proliferation</li> <li>Inhibits MHC, MRFs expression and myotube formation</li> </ul>	[121]
3D	Uniaxial CTS	Collagen-coated plates	bovine satellite cells	10%, 0.25Hz, 2s strain and 2s rest for 1h/day for 5 days	<ul style="list-style-type: none"> <li>Induces the proliferation of bovine satellite cells</li> <li>Suppresses their myogenic differentiation through the activation of ERK</li> </ul>	[121]
	Uniaxial CTS	NCO-sP(EO-stat-PO) hydrogel, fibronectin	C2C12	7%, 0.5 Hz, for 4 days (24 h/day)	<ul style="list-style-type: none"> <li>Geometrical constraint result fiber alignment but no influence on proliferation or differentiation</li> <li>Geometric constraint is the dominant factor in determining nucleus shape and orientation</li> </ul>	[97]
	Static strain	Collagen/ Matrigel	Primary human skeletal muscle cells	3.5um/10min (10d) to reach 10% strain then hold for 3d 5% strain (2d) 10% strain (2d) 15% strain (4d).	<ul style="list-style-type: none"> <li>Cell alignment due to internal longitudinal tension</li> <li>Increased myofiber diameter by 12% and area percentage by 40%</li> </ul>	[122]

Strain type	Materials	Cells	Amplitude, frequency, duration	Key feature	Ref
Cyclic strain	Collagen-based acellular tissue scaffolds	Primary human muscle precursor cells	10%, 3 times/min for the first 5 min of every hour from 5 days to 3 weeks	<ul style="list-style-type: none"> <li>• Unidirectional orientation</li> <li>• Analysis of tissue constructs retrieved 1 to 4 weeks post-implantation showed that constructs generated tetanic and twitch contractile responses with a specific force of 1% and 10%</li> </ul>	[103]
Cyclic strain	Fibrin	MPC, C2C12	a 2-day uniaxial ramp stretch of 0–2%, followed by a uniaxial intermittent stretch regime of 2–6% dynamic stretch (3 h on, 3 h off)	<ul style="list-style-type: none"> <li>• Maturation inhibited</li> </ul>	[116]
Static strain	Fibrin	C2C12	10% static strain for 6h, 18h rest at 3% static strain, 7days	<ul style="list-style-type: none"> <li>• Cell alignment</li> <li>• Enhanced muscle maturity</li> </ul>	[104]
Continuous strain	Fibrin	C2C12	25% and 50% strain	<ul style="list-style-type: none"> <li>• Cell alignment under continuous strain</li> </ul>	[123]
Continuous strain	Collagen	C2C12	Continuous increasing load to 15% strain in 1h and remained tension for 2hs	<ul style="list-style-type: none"> <li>• Increase expression in IGF1 and MMP-2, decrease in MAFbx</li> <li>• Increased myotube fusion and size, force production</li> </ul>	[101]

## 2.2 Spatial exploration of constructing skeletal muscle tissue

The efforts in the 2D study have greatly helped to establish the fundamental understanding of muscle regeneration mechanism and to analyze and identify the influential parameters such as pattern size and shape on myogenesis. However, with the absence of cell-cell interaction, cells in 2D culture are inadequate to reflect the 3D culture conditions. Given its deficiency in thickness and shape flexibility, it is challenging for direct clinical application, and it is impractical to achieve functional tissue from 2D culture. Thus, recent studies experienced a dramatic paradigm shift from 2D to 3D platform.

### 2.2.1 3D geometrical confinement

Through precise control over geometry, Aubin et al. have generated 3D cell alignment within gelMA hydrogel [124]. NIH 3T3-laden gelMA (5%) solution was micropatterned onto PEG-coated glass slides and followed by UV crosslinking for 20s, resulting micropatterned gelMA hydrogel with a thickness of 150  $\mu\text{m}$  and varied width from 50  $\mu\text{m}$  to 200  $\mu\text{m}$ . Consistent with previous findings, the narrower width produces better cell alignment. To better assess the influence of cell types, they further extend the study to C2C12, HUVEC and rodent cardiac side population cells (CSP), all of which form aligned, highly organized tissue *in vivo*. Human liver carcinoma cells (Hep-G2), which does not form unidirectional organized tissue, was utilized as control. As revealed by F-actin staining, HUVEC, C2C12 and CSP cells aligned longitudinally to the patterned hydrogels, whereas Hep-G2 fail to organize into aligned constructs. The study suggested that

given appropriate geometrical features, cells with the intrinsic potential to align *in vivo* will spontaneously form aligned, elongated constructs *in vitro*. With a larger geometry, Costantini et al. have investigated the influence of geometrical confinement and mechanical stiffness on the 3D GelMA hydrogels regarding myogenesis. Through varying the polymer concentration (3%, 4%, 6%, 8%) and crosslinking degree (4 min UV or 5 min UV), they have formulated a set of GelMA with varied mechanical properties ranging from 1 to 17kPa. GelMA hydrogel with three different cross-section:  $2000 \times 2000 \mu\text{m}$ ,  $1000 \times 1000 \mu\text{m}$ ,  $500 \times 500 \mu\text{m}$  was fabricated with PDMS mold and  $2 \times 10^7$  cells/ml of C2C12 were encapsulated. The results revealed that cells underwent rapid spread at the lower concentration of GelMA (3%, 4%), while limited spreading was observed at higher concentration (6%, 8%). In terms of geometry confinement, smaller cross-section resulted in better cell alignment and more homogeneous myotube distribution. Cell-mediated gel compaction along with the decreased cross-section was observed in all the groups. The study underlined the crucial role of mechanical property and geometrical features in constructing 3D muscle tissues.

### 2.2.2 Electrospun fibers

By presenting the cells with micro- or nano-scale topological cues, aligned fibers enable the mimicking of native anisotropic structure to align myoblasts in a highly efficient manner, thus gain great attention for skeletal muscle regeneration [125, 126, 127]. Huang et al. have examined the effect of nanoscale and microscale substrates on regulating cell behavior and myogenesis [128]. They fabricated the PLLA nanofiber scaffolds and stretched uniaxially to 200% deformation in length at 60 °C to achieve aligned nanofibers (Figure 2.3b). 2% gelatin or fibronectin was coated on the surface of the

scaffold to facilitate cell attachment. The randomly oriented nanofibrous scaffold was employed as control. Moreover, patterned PDMS membranes with parallel microgrooves (10  $\mu\text{m}$  wide and apart, 2.8  $\mu\text{m}$  deep, 1cm in length) and non-patterned membranes were prepared to determine the effect of micro-scale features (Figure 2.3a). The PDMS substrates were oxygen plasma treated, followed by 2% gelatin coating. Similarly, cells on both patterned PDMS substrate and aligned nanofibrous scaffold yielded myoblast alignment and enhanced myotube maturation in comparison to the non-patterned and randomly oriented ones. Notably, the myotube length on aligned nanofibers ( $1.8 \pm 0.3$  mm) was more than twice the length on micropatterned substrates ( $0.7 \pm 0.1$  mm), which suggested that nano-scale feature is more efficient than micro-scale in promoting myotube assembly.

In terms of the nanofibrous scaffold, technologies such as drawing, phase separation, templating, self-assembly allow the production of fibers as well. Details discussion over these technologies could be found in the literature [40]. Here, we confine the scope to electrospun fibers. The electrospinning technology has been well established and has been discussed in detail by several prominent reviews with respect to fundamental principles, compatible materials, effects of influential processing parameters among other variables [129, 130, 131, 132]. Fine adjustment over flow rate, needle size, collector type and electric field allows the generation of fibers with varied size-scale (from nano- to micro-) and shapes including randomly oriented fiber mesh [133, 134, 135], tubes [136], arrays [137, 138], and cylinders [139]. It is well acknowledged that aligned fibers are superior to randomly orientated ones in promoting cell alignment [140, 141, 142, 143, 144], which represents the essential and fundamental step of skeletal muscle regeneration. Guex et al. has prepared aligned and randomly oriented micron ( $3.3 \pm 0.8$   $\mu\text{m}$ ,) or nano

( $237 \pm 98$  nm) featured fibrous poly( $\epsilon$ -caprolactone) non-wovens through electrospinning [145]. Plasma coating (nanometer thick) was applied to modify the surface. The results revealed that both aligned nano- and micro-scale fibers induced myoblast alignment, highlighted the dominant role of fiber orientation rather than fiber size over the cellular arrangement. Moreover, evidenced by DNA quantification on day 3, 5 and 7, cell numbers on plasma-coated substrates were significantly elevated on all three days in comparison to the non-treated, which suggested that chemical modification is effective on promoting cell adhesion.

In order to improve the muscle tissue regeneration, surface coating was utilized to improve the biocompatibility with several ECM-proteins, such as gelatin [128, 148, 149], Matrigel [135], collagen [150, 135, 151], laminin [150] and fibronectin [128, 148, 135]. Zahari et al. electrospun PMMA nanofibers and coated with laminin or collagen, in the presence or absence of genipin. A mixture of myoblasts and fibroblasts were seeded on the surface of the scaffold. The results demonstrated the remarkable myoblast proliferation and migration on the laminin-coated scaffold, while the collagen-coated surface was more supportive for fibroblasts. The results underscored the critical importance of the chemical environment for promoting cell attachment and proliferation. Riboldi et al. discovered that coating types modulate cell behaviors [135]. The author investigated the difference on coated collagen, fibronectin, Matrigel with varied concentration and uncoated DegraPols slides with immortal cell lines (C2C12 and L6) and primary human satellite cells (HSCs) in terms of cell viability, adhesion and differentiation. Surprisingly, C2C12 and L6 are more favorable of Matrigel ( $130 \mu\text{g}/\text{ml}$ ) coated membranes, while uncoated DegraPols tend to be more HSCs-permissive. Different chemical affinities between integrin receptors and the ligand bind-

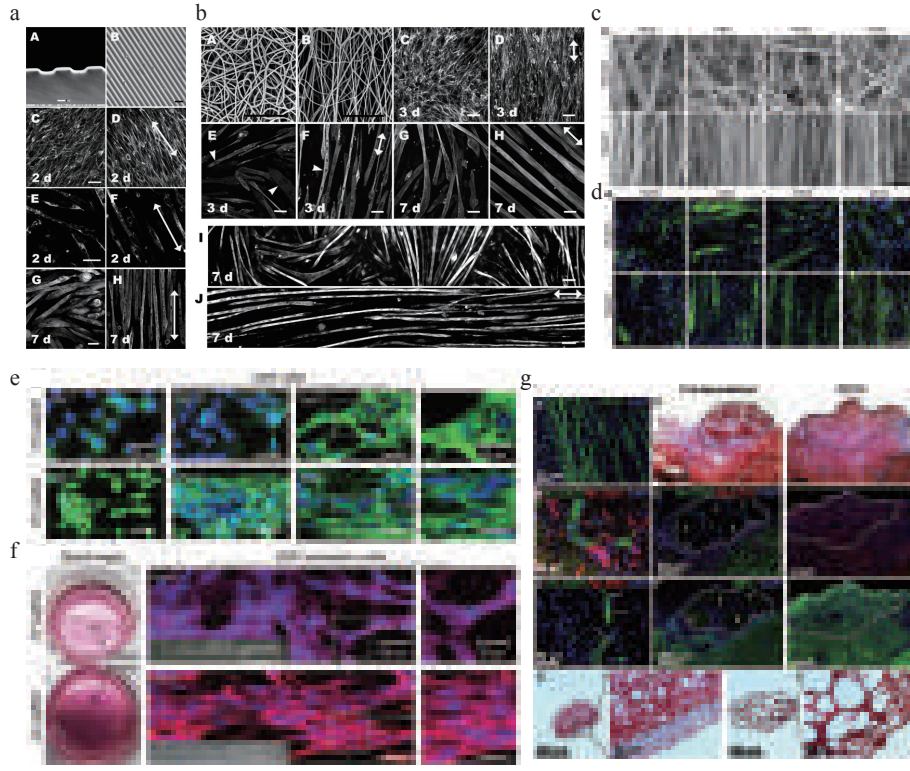


Figure 2.3: Electrospun fibers for skeletal muscle regeneration. a) Myoblast alignment and myotube organisation on a micropatterned PDMS substrate. b) Myoblast alignment and myotube assembly on an aligned PLLA nanofibrous scaffold (Reprinted with permission from Ref. [128]. Copyright (2006) American Chemical Society). c) SEM images of PCL/PANi nanofibers with varied PANi concentration. d) Immunofluorescence staining for MHC of PCL/PANi nanofibers with varied PANi concentration (Reprinted with permission from Ref. [146]. Copyright © 2012 Elsevier Ltd). e) Fluorescence images of DAPI/MHC staining at days 7, 14, and 21. f) Optical and DAPI/sarcomeric  $\alpha$ -actin staining images after 21 d of culture (reproduced with permission from Ref. [147]. © WILEY-VCH Verlag GmbH & Co. KGaA, Weinheim). g) Immunostaining of pre-vascularized scaffolds in VML defect (reproduced with permission from Ref. [46]. © 2018 Elsevier Ltd).

ing domains of different protein coatings may be the explanation for the disparate cell behaviors.

Both natural and synthetic polymers can be processed into fibers [152, 153, 154], collagen [134, 155, 156, 157], chitosan [158, 139], gelatin [159, 160, 161, 162] and fibrin [46, 163], silk fibroin [164, 126] have been electrospun independently or co-electrospun with synthetic polymers such as PCL, PLA, PLLA and so forth [165, 166, 167, 158, 168]. The incorporation of natural



polymers greatly enhanced cell adhesion.

As revealed by many researchers that electrical stimulation is conducive for promoting myotube formation and maturation, conductive materials such as carbon nanotubes, silver nanoparticles, gold nanoparticles, graphene oxide (GO), polyaniline and Poly(3,4-ethylene dioxythiophene) (PEDOT) are frequently incorporated to endow the scaffolds with electrical properties [169, 170, 171, 127, 172, 173, 174, 175]. Ku et al. has incorporated PANi into PCL polymer (200mg/ml) to fabricate conductive nanofibrous scaffold [146], and investigated the synergistic effects of topological and electrical cues on myoblast behavior. PANi with varied concentration from 0-3mg/ml was added and randomly orienteud fibers were used as control (Figure 2.3c). The results demonstrated that cellular organisation has been steered by fiber orientation, and thus myotube direction, which is in good accordance with the previous research. Moreover, cell growth and proliferation were similar in all the groups, independent of fiber orientation and PANi concentration. While reflected by MHC expression and gene expression, fiber orientation and PANi concentration has shown significant impact on myoblast differentiation (Figure 2.3d). Chen et al. have also investigated the combined effects of topological guidance and electrical cues on myoblast behavior systematically [141]. The results added more evidence to the effectiveness of eliciting the desired cellular response of incorporating electrical cues.

A great deal of studies have reported the great potential of electrospun fibers on skeletal muscle regeneration. However, in most cases, densely packed fiber scaffolds lead to slow cell infiltration rate, which precludes the further application of the technology and render the fibrous scaffolds most likely to function as 2D surfaces. A growing body of studies have reported the cell migration inside fibrous scaffolds [176, 163, 177, 178, 179]. Jin Nam

et al. [180] married salted leaching with electrospinning to induce engineered delamination into 3D engineered scaffold. Cells infiltrated into the electrospun fiber through the salt generated pores. Over a 3-week culture, up to 4 mm of cellular infiltration was observed. Another strategy utilized sacrificial fibers to increase porosity and therefore cell infiltration. Through the involvement of PEO with varied content from 5% to 80%, Baker et al. have introduced a composite fibrous scaffold using dual-polymer electrospinning process[177]. Individual PEO fibers were interspersed within the composite fibrous scaffold. The mechanical property can be adjusted by varying the PEO ratio. Cells infiltration occurred along with the removal of sacrificial fibers. This method has demonstrated the feasibility of controlling cell infiltration into PCL fibrous scaffold, yet the cell distribution still remains to be challenging. Regarding this problem, Yeo et al. fabricated the cell-laden nanofibrous bundle via cell electrospinning with alginate/PEO [147]. Weight fractions, processing parameters have been optimized to achieve an electrospinnable material and highly aligned structure with homogeneous cell distribution. In comparison to cell printing strategy, cell electrospinning has greatly improved the cell elongation, alignment and differentiation, highlighted the massive potential application of cell-electrospun scaffold (Figure 2.3e,f).

Vascularization has been a long-standing challenge in engineered thick tissues. The absence of proper vascular networks would eventually lead to necrosis in the central part of the tissues. Gilbert et al. generated electrospun fibrin scaffolds with 15% alginate owing to its similar stiffness to native tissue and functioned as a sacrificial polymer to induce porosity for better cell infiltration [46]. Two types of scaffolds include “spread” and “bulk” were prepared. C2C12 was used to examine the *in vitro* perfor-

mance of the scaffolds. Surprisingly, in both types, densely aligned MHC<sup>+</sup> myotubes, multinucleation and sarcomeric striations were confirmed with immunostaining. Notably, spontaneous contraction was also observed. The C2C12-seeded scaffolds were subsequently transplanted into TA muscle defect in mice for 2 or 4 weeks. After 2 weeks, both bulk and spread scaffolds yielded significant regeneration, evidenced by the densely populated MHC<sup>+</sup> myofibers and abundant network at the graft area. Myofiber density experienced dramatic increase while capillary network density remained steady. Myofiber showed an average diameter of 23 $\mu$ m, which is roughly half of native myofiber. To better serve large muscle defect, the pre-vascularized scaffolds were prepared by co-cultured human endothelial cells and human adipose-derived stem cells on the C2C12-seeded scaffolds for 11 days. The scaffolds were therefore transplanted into VML defects and harvested after 10 days. Notably, as demonstrated by Ms-CD31 and DAPI, implanted electrospun scaffolds successfully anastomosed with host vessels and exhibited perfusion by host red blood cells (Figure 2.3g).

### 2.2.3 Porous hydrogel

In order to maximize the potential therapeutic effects of cells, a proper matrix for cell delivery is appealing. An engineered matrix is supposed to locate the cells to the injury site and improve the cell retention, offer instructive cues to enhance integration with host tissues, promote myogenesis, angiogenesis and neurogenesis, and degrade in a controlled manner to allow the new tissue ingrowth [181].

Owing to their high water content, biocompatibility, tunable chemical and mechanical properties, hydrogels have been widely explored for regenerative medicine and tissue engineering applications [182]. Over the past

decades, researchers have sought to maximize the potential therapeutic utility of cells and signaling factors by developing biomaterial-based strategies that support and guide skeletal muscle repair processes. Numerous materials such as dECM hydrogel [11, 183, 184, 44], collagen [185, 186, 101], gelatin methacryloyl (gelMA) [187, 68], chitosan-based [188, 189], hyaluronic acid (HA) [190], fibrin [34, 37, 191], PEG-based [192, 193], Keratin [194, 195], have been investigated (as listed in Table 3).

Although hydrogels exhibited great potential in tissue engineering applications, the disorganized and isotropic network structure has precluded their widespread adoption in engineering oriented tissues. Most of the hydrogel scaffold is assisted with external stimuli to elicit a desired cellular response and cellular arrangement. Plenty of strategies have been employed to form biomimetic fascicle-like structures with hydrogels resembling that of native muscle tissue. Anchoring is broadly used. By applying passive tension on the hydrogel scaffold, myoblasts within the 3D matrix are promoted to fuse into multinucleated myotubes, ultimately form a uniaxially, aligned fiber bundles [111, 28, 213]. In addition, mechanical stimulation [101], magnetic stimulation [228] and geometrical confinement [210], are recognized to be effective in facilitating myoblast alignment within hydrogel.

Fibrin has been identified to be one of the best matrices for skeletal muscle cells embedding. Huang et al. developed a self-organized myoblast-encapsulated 3D fibrin scaffold [111]. The fibrin gel was fixed with two silk sutures pinned at each end of the plate. Myoblasts were seeded and differentiated on top of the fibrin gel. Cell-mediated contraction of the gel culminates 10 days after plating. The contractility was measured after 14 days.

The engineered tissue generated a maximum twitch force of  $329 \pm 26.3 \mu\text{N}$

and a maximal tetanic force of  $805.8 \pm 55 \mu\text{N}$  when electrically stimulated. Interestingly, the addition of IGF-I with the varied amount (25, 50, or 75

Table 2.3: Hydrogels in skeletal muscle tissue engineering.

Materials	Cells	Ref
Alginate-based	C2C12	[196, 197, 198]
	Primary myoblasts	[199, 200]
	Satellite cells	[201]
dECM	RASMC and C2C12	[184]
	C2C12, NIH-3T3	[202, 203]
	C2C12	[183]
	HUVEC, human skeletal muscle cells	[204]
Fibrin-based	Primary myoblasts	[111, 205, 186]
	C2C12, hMPCs	[206]
	Human muscle cells	[207]
	Human myoblast	[208, 28]
	Neonatal rat myoblast	[209, 191]
	C2C12, primary myoblasts	[210]
	C2C12	[104, 211]
	Human muscle progenitor cells, HUVEC	[48]
	Human skeletal myocyte cell line	[212]
Collagen-based	C2C12	[101]
	Primary rat muscle cells	[213, 186]
GelMA	C2C12	[187, 68, 214, 215, 216, 217]
PEG-based	MuSC	[66]
	C2C12	[218, 219, 220, 221, 222]
	Pericytes	[32]
	Mesoangioblasts	[223]
	SCs	[193]
Gelatin-based	H9c2 myoblasts	[224]
	C2C12	[225]
HA-based	Primary myoblasts	[190, 226]
	SCs, MPCs	[227]
Chitosan	C2C12	[188, 189]
POEGMA	C2C12	[228]
Keratin	MPCs	[194, 195]

<sup>1</sup> POEGMA: Poly(oligoethylene glycol methacrylate).

<sup>2</sup> RASMC: Primary rat aortic smooth muscle cells

ng) in the fibrin gel resulted in 50, 36, and 31% increases in force production compared to untreated 3D tissue. Although the diameter of myotubes formed did not exceed 10  $\mu\text{m}$ , the study has shed light on the development of *in vitro* 3D skeletal muscle tissue.

Gholobova et al. have generated endothelial network within a fibrin-based bioartificial muscle (BAM) which has been discussed above [48]. In a recent study, they have applied the model to drug testing [28]. The engineered muscle was fabricated based on the well-established protocol by encapsulating C2C12 mouse myoblasts, human myoblasts or human mixed muscle cells in fibrin gel in a silicone mold containing 2 attachment points respectively. The engineered tissues were maintained in growth medium for 2 days and subsequently switch to differentiation medium, and kept for 7 days before the injection. Multiple compounds including a dye (Trypan blue), a hydrolysable compound CDFDA, a reducible substrate (*pro* – *NanoLuc*) and a wasp venom toxin (mastoparan) were selected. Direct reflux, release and metabolism were characterized in BAM comparison to 2D cell culture and isolated human muscle strips. The authors started with the parameter optimization of the BAM (1mg/ml fibrin with a thickness just below 2mm) to enable up to 1  $\mu\text{l}$  per injection site, the concentration of the injected compound to ensure they were detectable, and direct reflux when removing the needle with Trypan blue. Creatine kinase (CK) is an intracellular enzyme which releases upon cell damage. Mastoparan (1 $\mu\text{l}$ , 1mg/ml), a wasp venom peptide was injected once or four times to BAM. HBSS was injected as a control group. CK release in BAM was in a dose-dependent manner. With regard to CDFDA and pro-NanoLuc, 80% of CDFDA was released after 1.5h, while only 40% of pro-NanoLuc release was detected. The disparate release profile between BAM and 2D cell culture has highlighted the benefits

of the 3D BAM in drug release and toxicity testing.

Aside from passive tension, mechanical stimulation or geometrical restriction, thermally induced phase separation followed by freeze-drying is an alternative to creating anisotropic microporous scaffolds that enable myoblasts alignment and thus oriented myotube formation [188, 229, 230, 231, 232]. Leveraging on directional freezing technique, Jana et al. has developed the 3D uniaxial tubular porous scaffolds made of chitosan [188]. Briefly, chitosan solution was poured into a cylindrical Teflon mold which has a metal cap on one end and a Teflon cap on the other. During lyophilization, the Teflon cap was maintained at 25 °C, and the other was kept in low temperature to establish a temperature gradient that allows the formation of tubular porous microstructure within the scaffold. The effect of the polymer concentration (4, 6, 8, and 12 wt%) and freeze-drying temperature (metal cap temp: -20 °C, -70 °C and -180 °C) on the scaffold properties (structural and mechanical) were investigated. The results demonstrated that the pore sizes range from 200 to 500  $\mu\text{m}$ , 30 to 250  $\mu\text{m}$ , and 10 to 50  $\mu\text{m}$  under -20 °C, -70 °C and -180 °C, respectively. A similar trend has been observed between pore size and polymer concentration. The pore size decreases with increasing polymer concentration. The mechanical property increased when increasing the temperature gradients. Notably, polymer concentration had a significant effect on myotube diameter rather than myotube length. Taken together, the study has introduced a strategy to create unidirectional pores within the 3D matrix with tunable properties to facilitate the engineering of oriented tissues.

Taking advantage of shear force, shear-induced alignment is prevalent in injectable hydrogels. Injectable hydrogels are advantageous owing to the ease of manipulation, the good shape conformity to the defect site and min-

imally invasive and is very attractive in controlled delivery. Utilizing pH-dependent collagen fibrillogenesis, Nakayama et al. introduced a nanofibrillar collagen scaffold with shear-based extrusion to form aligned fibrils [47]. SEM confirmed that the nanofibrils with a diameter range from 30-50 nm aligned along a uniaxial direction. C2C12 were cultured on both randomly oriented scaffolds and aligned scaffolds and went through a 5-day differentiation. Human endothelial cells were used for co-culture with the myotubes for another 4 days. As demonstrated by the immunostaining of MHC, the aligned scaffolds gave rise to the formation of longer myotubes in comparison to the randomly oriented scaffolds. Notably, the average length of myotubes was further promoted from  $510 \pm 60 \mu\text{m}$  to  $760 \pm 10 \mu\text{m}$  in the presence of endothelial cells. Additionally, the aligned endothelialized engineered scaffolds exhibited more striated myotubes than randomly oriented scaffolds. Notably, aligned endothelialized engineered scaffolds demonstrated greater contractile magnitudes and more highly synchronized movement. Increased secretion of angiogenic and myogenic cytokines by endothelial cells were observed in engineered skeletal muscle formed from aligned scaffolds. To evaluate the therapeutic efficacy, the scaffolds were implanted to mice for regenerating TA muscle defect.

Similarly, in extrusion-based bioprinting technology, it capitalizes on shear force to promote cell alignment and have been reported to be effective. This will be discussed separately in the later sections.

#### **2.2.4 Combinatorial effects of fibers and hydrogels**

Fibers and hydrogel matrices have been broadly exploited individually to regenerate muscle tissue due to their ability to mimic the native tissue properties. However, the low cell infiltration rate in fibrous scaffold and poor



mechanical property of hydrogel scaffold have impeded further application. This intrigued the interests in investigating the combined multiscale effects by integrating the fibrous structure and porous hydrogels into one single platform [233, 234, 235, 222, 236, 237]. The hybrid constructs enable the incorporation of nano- or micro-scale features to guide cell alignment and reinforce the mechanical property simultaneously. Several configurations of fiber/hydrogel scaffolds have been delineated by [234]. Generally, laminated sandwich structures by stacking fiber sheets between hydrogel layers [235, 238], or the core-shell structure by encapsulating fibers in hydrogels are most commonly used [222, 237]. One simple study has been reported by Jana et al.[235]. They have introduced a laminated structure with chitosan scaffold bands placed on top of aligned chitosan/PCL nanofibers. The chitosan scaffold band width is  $20\text{ }\mu\text{m}$ , spacing between two bands range from  $50\text{-}100\text{ }\mu\text{m}$ . Fiber diameter lies between  $100\text{ and }150\text{ nm}$ . Over a 6-day culture, control group with chitosan-PCL film substrate showed an unorganized cell distribution. Both C2C12 cells on the pure nanofiber substrate and on the substrate with nano- and micro- topology were observed with remarkable cell alignments, while the lateral has been demonstrated with better MHC expression. The results signified that nano-scale feature is dominant in promoting myoblast alignment and elongation, while the combination of nano- and micro-scale feature induces late stage myogenic maturation. Similar study was published by Cha et al [219]. Taken together the PEG patterning and electrospinning technology, they have developed a dual-scale cell culture system which is composed of aligned PCL nanofiber sheet with micro-patterned surface. The PEG hydrogel pattern was set at  $100\text{ and }200\text{ }\mu\text{m}$  with pattern interval fixed at  $200\text{ }\mu\text{m}$ . The fiber substrates were fabricated in three different orientations: random, perpendicular and

parallel to the PEG line pattern. C2C12 cells were then seeded on the scaffold. Notably, on the perpendicularly oriented fibers, over 70% of cells were dispersed  $\pm 10^\circ$  of the fiber orientation; while on the paralleled fiber substrate, cells are observed with more than 90% aligned to the fiber direction. The nuclei orientations were more likely to be affected by nanofiber direction, which confirmed that nano-scale feature is dominant in comparison to micro-scaled one. Further, MHC expression was quantitatively examined by relative intensity of MHC expression against the cell number. On randomly oriented fiber substrates, negligible difference of MHC expression was spotted between  $200\mu\text{m}$  and  $100\mu\text{m}$ . On patterned fibers, higher expression was observed on  $100\mu\text{m}$  than  $200\mu\text{m}$ , indicated the importance of narrower patterns on myogenesis.

These studies have highlighted the benefits of the co-existence of nano- and micro-scale features. However, they failed to create a real 3D structure and lack of cell-cell interactions.

Also modeling native skeletal muscle structure, Ling Wang et al. developed a 3D core-shell composite scaffold [222]. Specifically, the core-shell composite scaffolds, in which the aligned nanofiber PCL/SF/PANi yarn (NFY) core was ensheathed by poly(ethylene glycol)-co-poly(glycerol sebacate) (PEGS-M) hydrogel. By adjusting the drawing speed, a series of NFY with varied diameters (50, 100,  $165\mu\text{m}$ ) have been fabricated. The PGS-M hydrogel column possesses a diameter of  $550\mu\text{m}$  and stiffness around  $11 \pm 3\text{ kPa}$ . C2C12 cells were seeded on NFY for cell attachment for 24h, then coated with the hydrogel. The results demonstrated significant cell attachment and elongation after 24h. Evidenced by the increased aspect ratio of cells from 5.8 on the NFY to 8.5 after a 2-day culture in the hydrogel. The results highlighted the synergistic effects of nano- and micro-features.

To better recapitulate the native structures, the author has extended the core-shell structure with two orthogonal layers of parallel aligned NFYs encapsulated in the hydrogel sheet. As revealed by the optical images, cells were fully filled the peripheral surfaces of these NFYs within the 3D hydrogel sheet over 3 days culture. Taken together, the results suggested the feasibility and potential of constructing 3D environment for directing cell alignment with core-shell scaffolds that encompass both nano- and micro-scale features.

Generally, taken together fibrous structure and water-enriched hydrogels, the fiber/hydrogel scaffolds endow the cells with topological cues and present a 3D cell favorable environment with improved mechanical property. However, most of the studies made no reference to the cell infiltration problem which still remains to be one of the critical challenges of such culture systems.

### **2.2.5 3D bioprinted skeletal muscle tissue**

3D bioprinting had rapidly developed into a flexible tool in recent years. Exquisite spatial control over materials, cells and exogenous signaling render 3D bioprinting particularly attractive to generate 3D *in vitro* hierarchical functional tissues. Incorporating specific cell types, growth factors and permissive materials, 3D bioprinting has achieved some remarkable progress in cartilage [239], eye [240], bone [241], cardiac[242], nerve [243], vascular networks [244, 245], and muscles [246], in terms of structural heterogeneity and multi-cellular environment. The layer-by-layer printing manner endows great flexibility to the constructs. 3D bioprinting allows the precise position of cells, materials and functional molecules at the desired place in a pre-designed structure, and thus enables the construction of reproducible and scalable heterogeneous tissues which could possibly recapitulate the com-

plexity of native tissues. The frequently used extrusion-, droplet- and laser-based technologies have been reviewed by loads of experienced researchers [247, 248]. Among all the techniques, extrusion-based bioprinting has been frequently employed due to the ease of manipulation, cost-effectiveness and broad material choices. The selection of bio-ink plays a pivotal role in bioprinting. Basically, the bio-ink is supposed to be printable, biocompatible, compliant mechanical property and degradation rate that could match the speed of tissue growth [249, 250]. Both natural and synthetic materials have been widely explored and adapted to meet the requirement of bioprinting. Herein, we critically review the state-of-art progress of bioprinted muscle tissues in terms of materials, cells, structures and functional recovery.

Choi et al. have developed skeletal muscle tissue model using dECM-based bio-ink with bioprinting to control the cellular organisation [183]. PCL was deposited at the end of the constructs as geometrical constraints, applying passive tension to the cells within the constructs. Cellular orientation was analyzed with varied linewidth (500  $\mu\text{m}$ , 1500  $\mu\text{m}$ , 5000  $\mu\text{m}$ ). The results demonstrated that linewidth of 500  $\mu\text{m}$  yielded the best cellular alignment and cell alignment was significantly increased over time (as shown in Figure 2.4a). Particularly, cells were initially randomly organized in the linewidth of 5000  $\mu\text{m}$ , after 7-d differentiation, nearly 60% cells were elongated and aligned (Figure 2.4b). In comparison to constructs printed with collagen, a higher level expression of *Myo5*, *MyoG*, *MyoD* and *MHC* was observed in dECM-based bio-ink printed constructs. Moreover, striation spotted in dECM-based bio-ink printed constructs was indicative of the maturation of the constructs. Notably, Agrin, which is a functional ECM molecule participating in NMJ development, was detected in dECM bio-ink, gave rise to a remarkable number of  $\alpha\text{-BTX}^+$  cells in dECM-based bio-ink printed

constructs. Together with the bioprinting presented topological cues, the dECM bio-ink maybe advantageous in promoting skeletal muscle regeneration. Given the outstanding performance of dECM bio-ink, the authors have further evaluated the therapeutic effect on VML model in a recently published study [204]. The skeletal muscle dECM (mdECM) and vascular dECM (vdECM) bioinks were derived from porcine tibialis anterior (TA) muscle muscles and descending aortas, respectively.

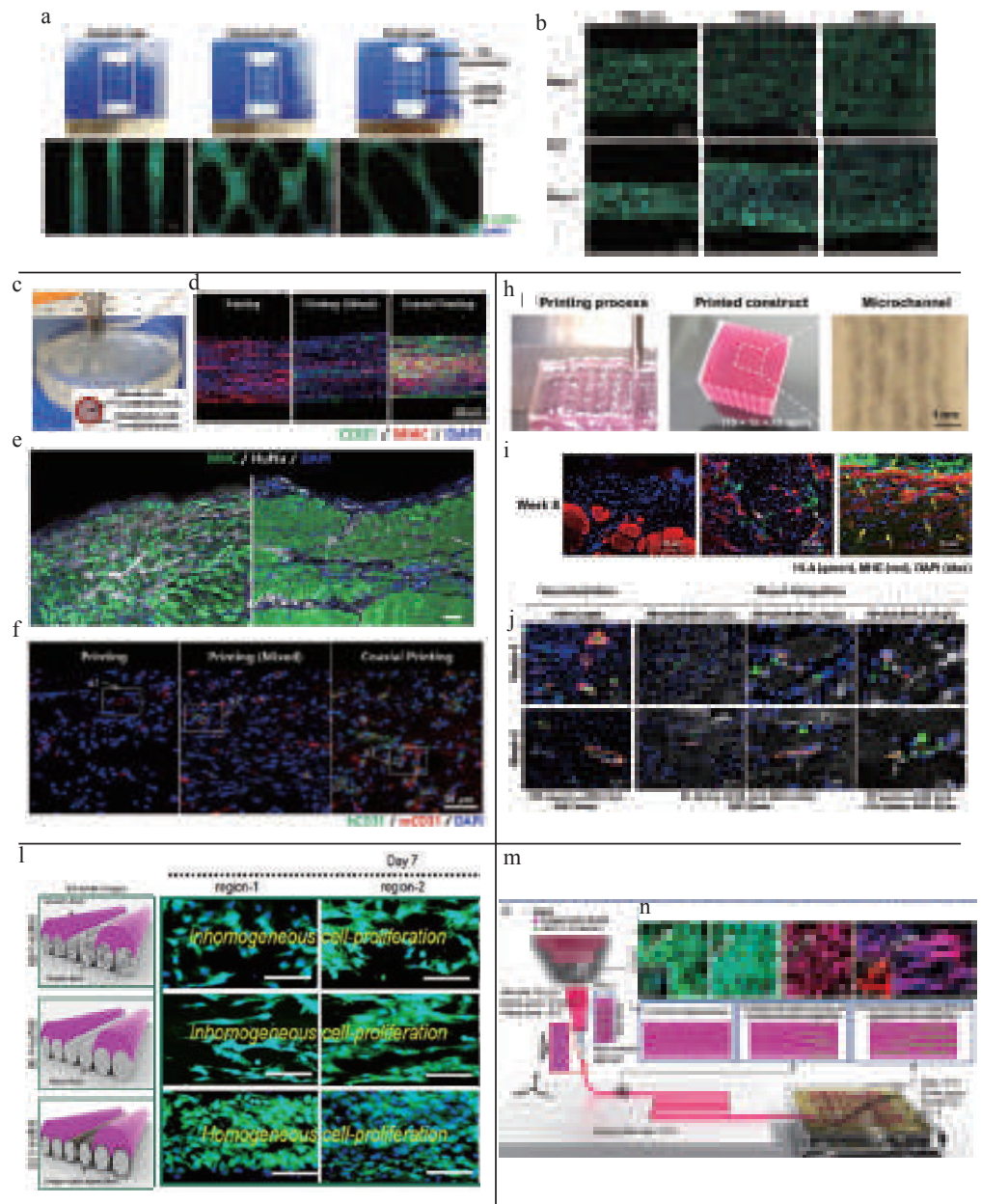


Figure 2.4: 3D bioprinting in skeletal muscle tissue engineering. a) 3D printing of dsECM bio-ink to promote myoblast alignment. b) Cellular orientation in muscle construct with varied linewidth on day 1 and day 7 (Reprinted with permission from Ref. [183]. *copyright* WILEY-VCH Verlag GmbH & Co. KGaA, Weinheim). c) 3D cell printed prevascularized muscle construct with dsECM and dvECM bio-ink through co-axial printing. d) Immunostaining of different muscle constructs. e) Immunostaining of prevascularized constructs retrieved from VML injured TA muscle model. f. Immunostaining showing the vascularization of TA muscles treated with different muscle constructs (Reprinted with permission from Ref. [204]. *copyright* 2019 Elsevier Ltd). h. The bio-printed constructs with dimension up to  $15 \times 15 \times 15$  printed with ITOP system. i) Double immunofluorescence analysis of bioprinted muscle constructs on newly formed muscle. j) Immunofluorescence of vascularization and neural integration of the implanted constructs (Reprinted with permission from Ref. [251]. Copyright *copyright* 2018, Springer Nature). l. Microfibrous Bundle Structure Fabricated Using an Electric Field-Assisted/Cell Printing. Adapted with permission [252]. Copyright (2018) American Chemical Society). m) 3D cell printing process using the Gly/KCl buffer solution. n) Immunofluorescence staining of DAPI (blue)/MHC (green) after 7, 14 and DAPI(blue)/sarcomeric  $\alpha$ -actinin (red) images after 14 and 21 days of cell culture. Adapted with permission [253]. *copyright* 2019 Elsevier B.V.).

Due to the low viscosity and weak mechanical property of the dECM bioink, gelatin granule-based ( $181.21 \pm 73.38 \mu\text{m}$ ) printing reservoir was used as supporting bath and as sacrificial materials to generate microchannels. PVA was added into the gelatin granules as a coagent to rapidly polymerize the dECM bioink to facilitate 3D stacking. A well-organized 3D skeletal muscle tissue in a dimension of  $15 \times 6 \times 4\text{mm}$  using human skeletal muscle cells was printed. dECM sponge and bulk dECM hydrogel with same dimension were prepared in parallel as control. *In vitro* study with pimonidazole showed that significant hypoxia occurred in bulk dECM hydrogel. The three types of constructs were then implanted into VML (40%) mice models for regeneration capacity assessment. The 3D printed constructed yielded 71%

recovery compared to uninjured tissue. In order to maximize the therapeutic efficacy, vdECM bio-ink and HUVECs were incorporated to fabricate the prevascularized muscle constructs (Figure 2.4c). The two different cell-laden bio-inks were deposited simultaneously with a coaxial nozzle to create core-shell structure as shown in Figure 2.4c. Constructs with muscle cells only and constructs that were made of simply mixing of both cell types and both bio-inks. MHC and CD31 confirmed the formation of myotube and endothelial network. Specifically, in co-axial printing, myotubes were present inside and endothelial networks were surrounded in the outer layer, indicating the compartmentalized constructs were achieved (Figure 2.4d). H&E staining of the constructs retrieved from VML models demonstrated the reduced fibrosis in co-axial printed constructs. MHC staining showed that the densely packed muscle fibers were more extensively distributed in coaxial printing group in comparison to others (Figure 2.4e). Furthermore, in coaxial printed group, a remarkable higher number of co-localized hCD31<sup>+</sup> and mCD31<sup>+</sup> structures was observed, implying anastomoses with host vasculatures (Figure 2.4f). In situ force measurement indicated 85% recovery in coaxial printed constructs. Taken together, the results suggested that by presenting spatially inductive cues, printing with dECM bio-ink could promote de novo muscle formation and functional recovery.

Merceron et al. engineered a muscle-tendon unit with integrated organ printing (IOP) technology [254]. A customized bio-ink consists of hyaluronic acid, gelatin and fibrinogen were used to encapsulating cells (C2C12 and NIH/3T3). Thermoplastic PU and PCL were printed as the scaffolding of muscle-side and tendon side, respectively, with a 10% overlap to create an interface. C2C12-laden bio-inks were deposited within the gap of PU and NIH/3T3-laden bio-inks were localized within the gap of PCL, the printed

construct (20 mm long  $\times$  5mm wide  $\times$  1mm high) was further crosslinked using thrombin for 30min. The mechanical characterization revealed that the PU side with elastic modulus  $0.39 \pm 0.05$  MPa is more like elastomeric materials, while the PCL side with young modulus  $46.67 \pm 2.67$  MPa is much stiffer. The cells were able to survive the printing process and exhibited overall viability over 80% after 1-day culture. After 7 days, the cell viability slightly increased. Notably, C2C12 aligned anisotropically and expressed desmin and MHC, indicating their differentiation into myotubes. On the tendon side, collagen type I deposition was detected. This study has demonstrated the versatility of the IOP system and the feasibility of constructing tissues with heterogeneous properties. With this IOP system, Kang et al. have generated 3D anisotropic muscle tissue constructs (15mm  $\times$  5mm  $\times$  1mm) [255]. PCL pillars are printed as scaffolding. C2C12 cells were printed with bio-ink consists of gelatin, fibrinogen, HA and glycerol. Pluronic 127 was deposited as support and sacrificial material. After crosslinking with thrombin, the uncrosslinked components including gelatin, HA, glycerol and Pluronic were washed away. Interestingly, high cell viability and cell alignment were observed in the construct with PCL pillars, while the constructs without PCL support were not. As demonstrated by MHC expression, myotubes formation was observed after 7-d differentiation. To further evaluate the muscle tissue development, the 7-d differentiated constructs were implanted in nude rats subcutaneously, with a common peroneal nerve embedded to promote integration. Well-organized muscle fibers were observed in the retrieved constructs after 2 weeks. The presence of acetylcholine receptor (AChR) clusters was confirmed by immunostaining of MHC and  $\alpha$ -BTX. The double staining of  $\alpha$ -BTX and neurofilament (NF) demonstrated the nerve integration *in vivo*. vWF expression revealed the vascu-



larization throughout the constructs. Electromyography was performed to assess muscle function. Compound muscle action potential was 3.6 mV, indicating that the muscle was responsive to electrical stimulation, yet still immature. To determine the therapeutic potential, Kim et al. used the IOP system to develop 3D muscle constructs with human primary muscle progenitor cells [251]. The 3D bioprinted constructs (up to 15mm  $\times$  15mm  $\times$  15mm) composed of fibrin gel as bio-ink ((Figure 2.4h), PCL pillar as scaffolding and gelatin as a sacrificial material to create microchannels with a diameter of 300-400 $\mu$ m. The constructs were cultured for 1 day in growth medium and 9 days in differentiation medium. *In vitro* results showed that the printed constructs maintained high viability throughout the culture period, while cells in non-printed constructs (10 mm  $\times$  10mm  $\times$  3mm,  $30 \times 10^6$  cells/ml) mostly died at 5 days. Scaffolds maturation was confirmed by MHC expression. Double-immunostaining of  $\alpha$ -sarcomeric actin ( $\alpha$ -SA) and laminin confirmed the presence of cross-striated myofibers, implied the muscle contractile properties. To optimize the cell density in bioprinted constructs, bioprinted constructs with varied cell densities (10, 20, 30, and  $50 \times 10^6$  cells/ml) were implanted subcutaneously in mice. H&E staining confirmed the presence of constructs for up to 4 weeks. The retrieved constructs were characterized by MHC and human leukocyte antigen A (HLA) expression. Double staining identified that tissue formation increased with increased cell density, but the negligible difference was found between 30 million and 50 million. As more cells will increase the oxygen and nutrient consumption, the result suggested that  $30 \times 10^6$  cells/ml was the optimal cell density in bioprinted constructs. To determine the therapeutic potential, the bioprinted constructs with a dimension of 10  $\times$  7mm  $\times$  3.6mm were further applied to TA muscle defect. Strikingly, muscle force was re-

covered by up to 82% of normal muscle force by 8 weeks. H&E analysis showed superior myofiber formation and organisation in bioprinted group and double staining of MHC/HLA confirmed the new myofiber formation (Figure 2.4i). As evidenced by vWF/ $\alpha$ -smooth muscle actin staining, the bioprinted constructs were well-vascularized at 4 weeks. Furthermore, the result of triple-staining of NF/AChR/MHC and NF/AChR/HLA indicated the innervation of the constructs and the integration of the newly formed myofibers in the bioprinted constructs with the host nerve system (Figure 2.4j). Taken together, the study highlighted the potential of the bioprinted constructs with the cellular organisation for skeletal muscle regeneration.

Topological cues presented by electrospun fibers have shown great efficacy in promoting cell alignment. Intrigued by this, Yeo et al. have integrated electrospinning and cell printing to fabricate hierarchical scaffolds with micro/nano features [256]. Through melt-plotting, PCL was printed into a grid pattern to provide physical support. An adapted electrospinning approach was subsequently used to generate aligned PCL micro/nanofibers (AF) onto the plotted struts. This was followed by depositing C2C12-encapsulated alginate/PEO bio-ink. PEO was used as leaching material to release cells and enable cell migration. Constructs with randomly oriented fibers (RF) and no fibers (NF) were taken as control. The constructs were rolled up to create 3D free-standing tissues and cultured for 7 days. The live/dead assay demonstrated that cells survived the printing process and remained high cell viability over 94% for all types of scaffolds. Over a 7-d culture, cell number in AF and RF scaffolds underwent a dramatic increase, which indicated the fibers within the scaffolds largely enhanced cell proliferation. MHC staining on day 3 and 7 demonstrated a better alignment, higher myotube number and length in AF scaffolds in comparison to RF scaffolds.

The higher gene expression level of MyoD, myogenin and troponin T in AF scaffolds than the rest underscored the critical role of fiber alignment in promoting muscle maturation. Similar results were obtained in a later study, Yeo and Kim [252] generated microfibrinous bundle structure with electrohydrodynamic (ETH) process and cell printing using myoblast-laden collagen bio-ink (Figure 2.4m). 3D PCL fibrous structures were produced with ETH printing with wet electrospinning. The 3D fibrous bundle was then subjected to uniaxial stretch with varied stretching percentage (0, 20, 40, 60, 80, and 100%) to achieve anisotropic structures, thereafter C2C12-laden collagen/PEO bio-ink was deposited on the fibrous bundle. Similarly, PEO concentration (1, 2, and 3 wt %) was optimized to facilitate cell release, stable cell attachment and maintain structural integrity. Three different configurations were designed: aligned, randomly oriented, collagen-coated. The results indicated similar viability in all the groups, but with varied differentiation. Reflected by MHC staining, cell alignment has been observed in both aligned scaffolds (Figure 2.4n). Notably, more homogeneous cell proliferation was achieved on the collagen-coated scaffold. The results indicated that the combination of topological effect and the biochemical effect is of considerable benefit to promote muscle development and maturation [77, 252, 256].

Bioprinting allows the generation of 3D constructs with the good cellular organisation due to the intrinsic strain imposed to the molecules or fibers when the bio-ink flow through the nozzle. However, the printed filaments dimension mainly depends on the nozzle size with an average diameter of a hundred microns. To better recapitulate the native muscle structure, some other strategies such as microfluidics, material fibrillation, stretching were engaged to generate more authentic constructs [257, 253, 258, 77]. Kim et

al. have developed a micropatterned PCL microfiber strut using the microfibrillation/leaching process of PVA from a printed PCL/PVA structure [257]. Varied PCL/PVA ratio (1:9, 3:7, 5:5, 7:3, 9:1), processing temperature (70, 85 and 100 °C) and applied pneumatic pressure (150kPa, 350kPa) were examined in order to achieve fibrillated structure. Collagen-coating was employed to improve the bioactivity. Similarly, leveraging on collagen fibrillation, Kim's group has recently developed a microfibrinous collagen construct through direct cell printing to induce orientation of collagen molecules, followed by collagen fibrillation to generate the topographical cue [253]. Processing parameters including applied shear stress, moving speed, collagen weight fraction and a fibrillating buffer solution (KCl and L-glycine) were optimized to produce a highly aligned cell-laden collagen structure without compromising cell viability. To determine the effect of surface topology on cellular activity, C2C12 cells were printed. Printed collagen constructs with the random surface pattern were used as control. MTT assay and live/dead staining showed similar cell proliferation rates and high cell survival rate in both groups. Phalloidin staining identified the unidirectional alignment in collagen constructs with surface topology, while no cell alignment was observed in the control group. As demonstrated by MHC and sarcomeric  $\alpha$ -actinin staining and RT-PCR, the collagen structure with aligned morphology outperformed the unaligned collagen in terms of cell alignment, myotube formation, maturity and the level of myogenic gene expression. These could be due to the synergistic effect of topological cues and biochemical cues presented by collagen constructs. To further demonstrate the feasibility of this approach for various tissues, H9C2, hASCs and MC3T3-E1 were investigated. Collagen fiber-induced alignment was demonstrated in all the group. The results suggested that the technique of cell alignment using

aligned collagen fibrils can be a new complementary method for regenerating various tissue systems.

## 2.3 Temporal control of skeletal muscle regeneration

A major stumbling block that hinders the development of cell delivery is that cells can hardly survive the harsh environment including the host immune response and the enzymatic process [181]. Besides cells, a cascade of growth factors and cytokines are recognized in regulating the different aspects of the muscle regeneration process [259]. The most effective regulating factors in the myogenic process are growth factor IGF-1 and angiogenic growth factor VEGF; they both have been reported to positively influence muscle generation [260, 261, 262, 263]. HGF and FGF2 are shown to be potent angiogenic factors [264]. Borseli et al. have systematically investigated the interplay of VEGF and IGF1 within alginate hydrogels for ischemic muscle regeneration. [261]. Five different configurations including alginate hydrogel alone, alginate with VEGF or IGF1 or both and bolus delivery of VEGF and IGF1 (3  $\mu$ g each) in PBS have been studied. VEGF was released in a sustained manner, while IGF with a smaller size released faster *in vitro*. The results revealed that alginate/VEGF and alginate/VEGF/IGF both increased muscle blood densities compare to untreated and the bolus injection, IGF delivery showed moderate effect on vascularization in gracilis and negligible effect in tibialis. Moreover, alginate/VEGF and alginate/VEGF/IGF delivery resulted in 80% and 95% of tissue perfusion, respectively. The results suggested the crucial role of VEGF delivery from alginate on angiogenesis. IGF delivery exhibited moderate effect in this study, this may due

to the burst release of IGF. The co-delivery of VEGF/IGF with alginate has shown the remarkable effect on muscle regeneration, angiogenesis and functional recovery. Taken together, the study stressed out the crucial role of instructive cues in steering muscle regeneration and provided profound insight into growth factors delivery to treat muscle damage. Along this line, the author has extended the research and incorporated satellite cells to create dual delivery of cell/bioactive molecules(VEGF/IGF) within alginate gels to a more severe ischemia injury [265]. Cells delivered within alginate showed more robust engraftment at 3 days post-treatment in comparison to bolus injection, accompanied with increase size and mass of regenerating muscles. The cell/growth factors group also exhibited enhanced angiogenesis and tissue perfusion, while reduced inflammation and fibrosis compared to other conditions. Notably, the increased contractile force suggested the great efficacy of the dual delivery of cells and growth factors could help to further ameliorate the muscle damage.

Table 2.4: Overview of 3D printed skeletal muscle.

Printing strategy	Material	Cell	Printing parameter	Structure	Size	Mechanical property	Key feature	Ref
Extrusion-based	mdECM PCL constraints	C2C12	Printing T: 18 °C	Parallel type diamond type chain type	Filament width 500, 1500, 5000 $\mu\text{m}$	$12 \pm 3 \text{ kPa}$	<ul style="list-style-type: none"> <li>• dECM bioink and 3D printing enable the mimicking of functional and structural properties of native muscle</li> </ul>	[183]
Extrusion-based	mdECM vdECM PCL constraints gelatin granule bath	HUVEC human skeletal muscle cell	Printing T: 18 °C	Fiber bundle	$15 \times 6 \times 4 \text{ mm}$	\	<ul style="list-style-type: none"> <li>• Prevascularization promotes muscle regeneration</li> </ul>	[204]
Extrusion-based	PCL-Collagen coated	C2C12	Nozzle dia: $350 \mu\text{m}$	Microbril structure	$4 \sim 30 \mu\text{m}$	20MPa	<ul style="list-style-type: none"> <li>• Cell alignment</li> </ul>	[257]
Extrusion-based	CMCMA, alginate-MA	C2C12	Nozzle dia: $200 \mu\text{m}$	Two layers	Height: $250 \mu\text{m}$ filament width: $200 \mu\text{m}$	GelMA-CMCMA: $1.96 \pm 0.16 \text{ kPa}$ GelMA-AlgMA: $5.53 \pm 2.01 \text{ kPa}$	<ul style="list-style-type: none"> <li>• Composite bioink with tunable mechanical property</li> </ul>	[266]
IOP	Polyurethane PCL, HA, gelatin fibrinogen	C2C12	PCL: $200 \mu\text{m}$ PU: $300 \mu\text{m}$	Lattice structure	L×W×H: $20 \times 5 \times 1 \text{ mm}$	PU-C2C12 $0.39 \pm 0.05 \text{ MPa}$ ; PCL-NIH/3T3 $46.67 \pm 2.67 \text{ MPa}$ ; interface $1.03 \pm 0.14 \text{ MPa}$	<ul style="list-style-type: none"> <li>• Integrated tissue constructs with region specific biological and mechanical characteristics</li> </ul>	[254]

Printing strategy	Material	Cell	Printing parameter	Structure	Size	Mechanical property	Key feature	Ref
ITOP	Fibrinogen gelatin HA, glycerol, PCL pillar Pluronic F-127	C2C12	$\sim 400\ \mu\text{m}$ width	Fiber bundle structure	L×W×H: 15×5×1mm	/	<ul style="list-style-type: none"> <li>•Nerve integration and vascularization throughout the construct was observed <i>in vivo</i>.</li> </ul>	[255]
ITOP	Fibrin, gelatin	hMPCs	$\sim 400\ \mu\text{m}$ width	Fiber bundle structure	L×W×H: 15×15×15mm	/	<ul style="list-style-type: none"> <li>•82% Functional recovery of TA defect</li> <li>•Nerve integration and vascularization was observed <i>in vivo</i>.</li> </ul>	[251]
Microfluidic printing co-axial needle	PEG- Fibrinogen, alginate	C2C12	Hydrogel fibers $\sim 250\ \mu\text{m}$	aligned hydrogel fibers	7 layers thickness $\sim 350\ \mu\text{m}$	/	<ul style="list-style-type: none"> <li>•Multi-cellular</li> <li>•Enable the printing of non-easily manipulated materials</li> </ul>	[258]
Extrusion -based	Tetramer self-assembling peptides CH-01 and CH-02	C2C12	Nozzle dia: 400 $\mu\text{m}$	Circle, square	Circle dia: 8 mm square : $6 \times 6\ \text{mm}^2$ , 3 layers	/	<ul style="list-style-type: none"> <li>•Cell alignment</li> </ul>	[267]
Three-axis printing system with a dispensing system	Collagen	C2C12 H9C2 MC3T3-E1 hASC	Nozzle dia: 150 $\mu\text{m}$ Printing cartridge T: 25°C Working stage T: 37°C	Grid pattern	$12 \times 6 \times 0.8\ \text{mm}^3$	/	<ul style="list-style-type: none"> <li>•High degree of cell alignment and high myogenic gene expression</li> </ul>	[253]



Printing strategy	Material	Cell	Printing parameter	Structure	Size	Mechanical property	Key feature	Ref
Extrusion-based	PCL alginate/PEO	C2C12	PCL nozzle dia: 400 $\mu\text{m}$ alginate/PEO: 150 $\mu\text{m}$	Grid pattern	PCL strut dia: $\sim 400\text{ }\mu\text{m}$ Fiber dia: $\sim 1\text{ }\mu\text{m}$	43-48MPa	<ul style="list-style-type: none"> <li>• Hierarchical scaffold consists of topological cues to direct cell alignment</li> </ul>	[256]
Extrusion-based	PCL collagen/PEO	C2C12	PCL nozzle dia: 180 $\mu\text{m}$ collagen/PEO: 150 $\mu\text{m}$	aligned fibers with collagen/PEO printed on the top	10mm $\times$ 15mm $\times$ 90 $\mu\text{m}$ PCL fibrous bundle dia: $\sim 100\text{ }\mu\text{m}$	\	<ul style="list-style-type: none"> <li>• Scaffold with topological cues and protein to induce myotube formation</li> </ul>	[252]
Extrusion-based	PCL	C2C12	PCL nozzle dia: 300 $\mu\text{m}$	Grid pattern	9mm $\times$ 3mm $\times$ 0.2mm struct dia: 263.7 $\pm$ 6.7 $\mu\text{m}$	\	<ul style="list-style-type: none"> <li>• Uni-axially aligned patterns on the surface of 3D printed PCL scaffold achieved by stretching</li> <li>• Myoblast alignment</li> </ul>	[77]
Inkjet-printing	Suspension of C2C12 cells in sterile PBS solution	C2C12	dia: 85 $\mu\text{m}$	Cantilever	800 $\times$ 100 $\times$ 5 $\mu\text{m}$	\	<ul style="list-style-type: none"> <li>• High resolution</li> <li>• Myotube formation</li> </ul>	[268]
FDM with surface coating	Printing: PVA coating: PLA, agarose, SOEA	hMSCs	nozzle dia: 300 $\mu\text{m}$	Cantilever	layer height: 200, 100, 50 $\mu\text{m}$	\	<ul style="list-style-type: none"> <li>• Staircase morphology</li> <li>• Cell alignment</li> </ul>	[268]

## 2.4 Challenges and perspectives

Current research focus of skeletal muscle engineering is to achieve 3D tissue structure with highly organized and densely packed myofibers, and thereafter, generates matured myotubes with sufficient contractility. Plenty of strategies have been implemented to induce anisotropic cellular arrangement by imposing spatial or temporal control over cells, materials and instructive signaling and considerable progress have been achieved. Evidence of physiological studies have demonstrated that 3D *in vitro* constructs enable the regeneration of VML injuries to some extent. However, currently the animal models in use are mostly immunodeficient or immunocompromised, which are inadequate to reflect the harsh physiological environment. Moreover, to replicate the native muscle tissue more faithfully, the artificial construct is supposed to be comparative of native muscles structurally and functionally. The myotube diameter and contractile force are reported to be 50-100  $\mu\text{m}$  and about 200  $\text{mN}/\text{mm}^2$ , respectively. However, the myofiber size and contractile properties of *in vitro* constructs are still inferior to those of native adult muscle, which implies the incomplete muscle maturation. Given the complexity in structure and functionality, it is still a daunting task to engineer a functional skeletal muscle tissue *in vitro*. To better mimick the native skeletal muscle tissues, some of the limitations have to be addressed.

1. Current engineering muscle tissues are mainly based on immortal cell lines such as C2C12, these cell lines are typically modified to proliferate indefinitely, making them convenient to biological experiments. However, they cannot fully respond in the same way as primary cells. Nevertheless, it is difficult to obtain primary cells from aged donors or patients, and their limited proliferative capability has greatly hindered the widespread applica-

tion. A robust human cell source with myogenic potential and can support long-term culture should be sorted out. The new development on iPSCs have highlighted the great potential in iPSC cells. iPSCs possess indefinite propagation potential, and can be derived from the patient directly, therefore with preserved pathologic phenotypes. This makes the iPSCs highly attractive to pathological studies, drug screening and as well as regenerative therapy.

2. Skeletal muscle tissue consists of several support cells including but not limited to fibroblast, vascular endothelial cells (ECs) and motor neurons, which enable blood flow and innervation of the tissue. Therefore, it is highly desirable to incorporate multiple cell types in order to capture the cell-cell interactions *in vivo*. Particularly, for large tissue defect, not only restricted to muscle, vascular network is indispensable to avoid necrosis and support long-term culture. More importantly, achieving *de novo* innervation of regenerated myofibres remains a stumbling block for functional restoration of VML injuries. Nevertheless, it is challenging to co-culture and differentiate multiple cell types as each cell type requires distinct surrounding environment and culture medium. Vascularization has been the long-standing issue for almost all the tissues.

3. In addition, constructs that only offer structural support are insufficient to restore functionality. Materials that provide instructive cues that could elicit desired cellular response should be formulated. A large amount of materials has been explored for their capability of muscle regeneration. Among them, the use of collagen and fibrin gel for generating muscle constructs have been well established. However, the batch to batch variation and intrinsic weak mechanical property have impeded the further application of these natural materials. Synthetic materials have been proposed to

be promising alternatives [193]. These materials with controllable property could better support multiple cell types and functional integrity.

4. The increased awareness of the critical role of bioactive molecules has intrigued some interests in integrating growth factor into the skeletal muscle constructs to promote myogenesis. However, the insufficient understanding of how the endogenous cues function led to inconsistent and undesirable results.

## 2.5 Summary

Tremendous efforts have been devoted to develop physiologically relevant *in vitro* models in the past years. Considerable progress has been achieved through a number of bioengineering technologies with tight spatial and temporal control, as reviewed in this paper. Geometrical confinement, nanofibers, porous hydrogels and bioprinting have provided great insight into the mechanism of how cells behave in a 3D environment. Nevertheless, an engineered construct that could support multiple cells types with compliant mechanical property, necessary molecules and capable of restoring muscle function with interspersed vascular networks and adequate innervation has yet to be achieved. Particularly, further development of materials, more robust cell technology and a deeper understanding of molecular gradients in native tissue are in desperate need. We envision that with the advances in biological science, material science and burgeoning engineering technologies, better and more realistic *in vitro* models could be developed

# Chapter3

## Layer-by-Layer Ultraviolet Assisted Extrusion-based Bioprinting of Hydrogel Constructs with High Aspect Ratio

**Note:** This chapter has been reproduced in its entirety (with some modifications to the experiment) with permission as an academic work from the following publication [269]:

Zhuang, P., Ng, W. L., An, J., Chua, C. K., and Tan, L. P. (2019). Layer-by-layer ultraviolet assisted extrusion-based (UAE) bioprinting of hydrogel constructs with high aspect ratio for soft tissue engineering applications. PloS one, 14(6), e0216776.

### 3.1 Introduction

The emerging 3D bioprinting approaches have offered a great potential in fabricating highly-complex, biomimetic tissue constructs by simultaneously depositing cells and biomaterials in a highly-specific arrangement [270, 271]. The precise deposition of cells and biomaterials facilitates the important cell-cell [272, 243, 273] and cell-biomaterial interactions [274, 275, 276] for tissue maturation. Notably, designing a suitable microenvironment is highly critical for regulating cellular behavior [277, 278, 279, 280]. Extracellular matrix (ECM) presents a plethora of physical and chemical cues to regulate the cell behaviors. Engler et al. has demonstrated that myosin/actin striation were only observed on gels (8 and 11 kPa) with similar stiffness to normal muscle tissues, highlighted the importance of mechanical cues on tissue maturation [67]. Duffy et al. has demonstrated the role of ECM protein and geometrical patterning in modulating myotube formation and alignment [79].

One of the major challenges in the field of soft tissue engineering is

fabricating complex tissue constructs with compliant mechanical property and suitable structure integrity to avoid structural collapse [281]. Most of the reported works incorporated reinforcement materials such as poly( $\epsilon$ -caprolactone) (PCL) polymer within the 3D bioprinted constructs to improve the mechanical stability [282, 255]. However, the long period of degradation makes it less desirable for soft tissue engineering applications.

The different bioprinting approaches include extrusion-based [283, 284, 285, 286], inkjet-based [287, 288], microvalve-based [248, 289], and laser-based systems [290, 291]. Among these different approaches, extrusion-based bioprinting is the most prevalent approach due to its fast fabrication speed, ease of operation and compatibility with various bio-inks [284]. An ideal bio-ink should exhibit good printability, biocompatibility and compliant tissue stiffness [292, 293, 294, 295]. Most of the existing bio-inks are modified from natural biomaterials such as gelatin [296, 297, 298, 250, 299] and collagen [300, 301, 302] to form new composite bio-inks with tunable properties. Particularly, gelatin methacryloyl (GelMA) has been identified as a promising bio-ink owing to its excellent biological properties and tunable physical properties [2, 16]. GelMA-based bio-inks have been utilized in the field of tissue engineering and regenerative medicine, such as cartilage [303], neural tissues [304], cardiac tissues [305, 306] and even musculoskeletal tissues [214]. However, it is important to note that high GelMA concentrations ( $\geq 10\%$ ) usually result in limited cell activity due to the relatively high crosslinking density and stiffness of the photo-crosslinked constructs [307], while low GelMA concentrations lead to poor printability with low printing resolution and poor shape fidelity. Moreover, the GelMA-based bio-ink has a narrow printing process window which is highly dependent on the printing temperature. Hence, further optimization is required to improve the stabil-

ity and printability of GelMA bio-inks. A plethora of methods have been explored to improve the rheological behavior of GelMA, such as the addition of various materials like nanosilicates [308], partial crosslinking GelMA with enzymes [250], or through cooling process [307]. Among these methods, gellan gum, which is a non-toxic polysaccharide, has been discovered as a promising rheological modifier to improve the rheological property of the bio-ink [303, 309, 310, 311].

Although GelMA-gellan gum (GelMA-GG) bio-ink has exhibited great potential in improving the printability of GelMA-based bioink, the excessive addition of gellan gum may in turn compromise the biocompatibility. Hence, minimum ideal amount of gellan gum in GelMA-based bioinks was selected to endow the enhanced printability of GelMA-GG and balanced biocompatibility. Meanwhile, layer-by-layer UAE bioprinting was implemented to reinforce the structure stability and printing resolution when constructing thick cell-laden tissue constructs. As such, we have demonstrated the ability to fabricate bioprinted constructs with high aspect ratio via a layer-by-layer UAE bioprinting strategy in this Chapter. This section serves as a platform in identifying printing strategies that produce constructs with high aspect ratio.

## 3.2 Materials and methods

Gellan gum (GG) is a biocompatible anionic polysaccharide produced by bacterial fermentation. GG is a linear polysaccharide that consists of glucose (Glc), rhamnose (Rha) and glucuronic acid (GlcA) (Figure 3.1). GG is endotoxin free and has been widely used in food industry and FDA approved since 1992 [1]. The gelation of GG is an ionotropic process, which means that the presence of cations is necessary for the formation of a stable gel. In

this ionic crosslinking process, cations with different quantity and different chemical nature exhibit diverse effect on gelation. Divalent cations such as  $\text{Ca}^{2+}$  and  $\text{Mg}^{2+}$  promote a more efficient gelation than monovalent  $\text{Na}^+$  and  $\text{K}^+$ . Gellan gum is widely used in tissue engineering (TE), such as cartilage and intervertebral disc repair [1].

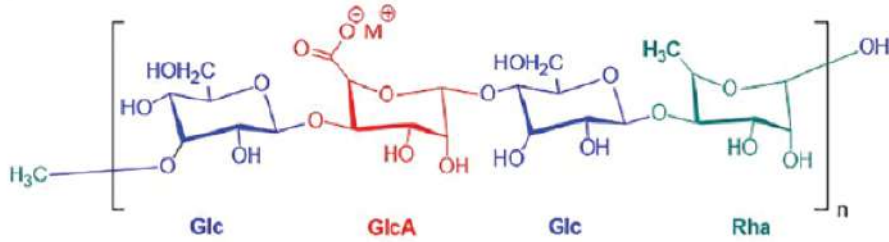


Figure 3.1: Low acyl gellan gum [1].

Gelatin methacryloyl (GelMA) is synthesized by the reaction of gelatin with methacrylic anhydride (MA) at  $50^{\circ}\text{C}$ . The reaction introduces methacryloyl substitution groups on the reactive amine and hydroxyl groups of the amino acid residues (Figure 3.2A) [2], which allows further crosslinking under UV light irradiation to form more stable structure through the covalent bonding (Figure 3.2B). As gelatin is a denatured collagen, GelMA preserves the cell binding motifs. The degree of methacrylation and UV exposure time has all been found to influence the physical and biological properties.

### 3.2.1 Preparation of GelMA-GG bio-inks

GelMA was prepared by reacting 10% (w/v) gelatin (Sigma Aldrich, type A from porcine skin, 300g Bloom, Singapore) with methacrylic anhydride (Sigma Aldrich) at  $50^{\circ}\text{C}$  as previous research described ([312]). The solution was dialyzed in 12-14kDa dialysis tubing (Sigma Aldrich) against distilled water at  $40^{\circ}\text{C}$  for 7 days, followed by 7-day lyophilization. It was then stored at  $-30^{\circ}\text{C}$  for future use. Irgacure 2959 (Sigma Aldrich) was dissolved



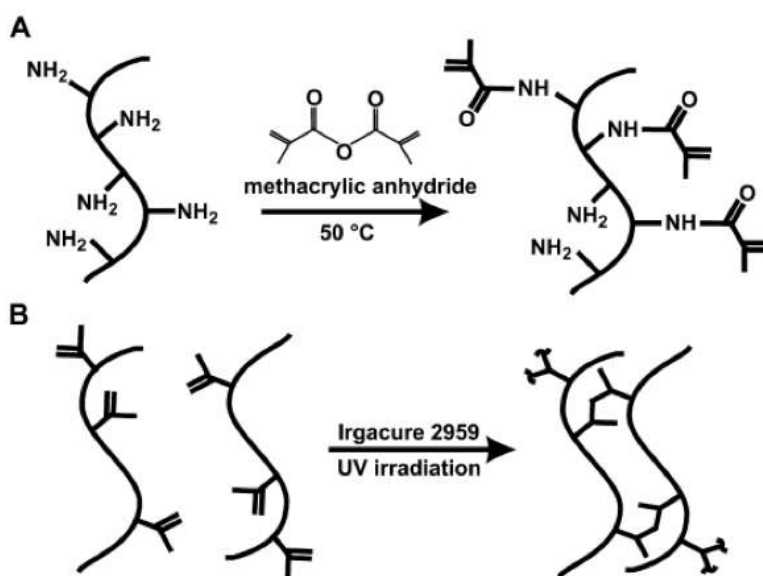


Figure 3.2: Synthesis of methacrylated gelatin and UV crosslinking of GelMA hydrogel [2]. A. Gelatin was reacted with MA to introduce a methacryloyl substitution group on the reactive amine and hydroxyl groups of the amino acid residues. (B) GelMA photocrosslinking to form hydrogel under UV irradiation. The free radicals generated by the photoinitiator I2959 initiated chain polymerization with methacryloyl substitution.

in 10% PBS (v/v) at  $70^\circ\text{C}$  to achieve the final concentration 0.1% (w/v) as described before ([310]). Sucrose (Sigma Aldrich) was added to generate an isotonic solution. GelMA was added into the PBS-based reagent at room temperature in varying quantities to achieve the concentrations at 2%, 4%, 10%, 15%, 20%, 30% (w/v) stored in  $37^\circ\text{C}$  incubator for future use. Low acyl gellan gum (Gelzan<sup>TM</sup> CM, *Gelrite*<sup>(c)</sup>) was purchased from Sigma Aldrich. Gellan gum solution was prepared by dissolving gellan gum powder in the PBS-based solution to concentrations at 0%, 0.2%, 0.4%, 1%, 1.5% (w/v). The GelMA-GG composite bio-inks were formed by mixing GelMA and gellan gum solution at  $45^\circ\text{C}$  in 1:1 ratio for 1h to achieve 30 different combinations of GelMA-GG composite bio-inks.

### 3.2.2 $^1\text{H}$ NMR of GelMA

The methacrylation of gelatin was measured by  $^1\text{H}$  NMR (Proton nuclear magnetic resonance) spectroscopy.  $^1\text{H}$  NMR utilizes nuclear magnetic resonance in NMR spectroscopy with respect to hydrogen-1 (protium) nuclei within the molecules of a substance, in order to determine the structure of its molecules [313].  $^1\text{H}$  NMR is commonly used to identify the replacement of free amino groups on gelatin by methacrylate groups. Typically, both gelatin and the lyophilized GelMA was dissolved in  $\text{D}_2\text{O}$  at a concentration of 50 mg/mL and  $^1\text{H}$  NMR spectra were repetitively collected for three times at room temperature. Purely absorptive signals were achieved by phase correction. The areas of the peaks were integrated after baseline correction. The degree of methacrylation was defined by Equation 3.1 where the percentage of  $\epsilon$ -amino groups of gelatin modified with methacryloyl groups was calculated.

$$DM(\%) = \left(1 - \frac{A(\text{LysinemethyleneofGelMA})}{A(\text{Lysinemetheyleneofunmodifiedgelatin})}\right) \times 100 \quad (3.1)$$

### 3.2.3 Evaluation of rheological properties of the GelMA-GG bio-ink

The rheological properties of the different composite bio-inks were tested using a rheometer (MCR 501, Anton Paar Germany GmbH, Ostfildern, Germany). The viscosity and the shear thinning properties of the different composite bio-inks were evaluated by using a cone plate (angle:  $1^\circ$ ) with 25 mm diameter. The bio-ink viscosities were evaluated for shear rates ranging from 0.1 to 500  $\text{s}^{-1}$  at both  $37^\circ\text{C}$  (cell encapsulation temperature) and  $25^\circ\text{C}$  (printing temperature) to evaluate the suitable range of bio-ink viscosities for cell encapsulation and bioprinting process respectively. All measurements

were performed in triplicate.

### **3.2.4 Cell encapsulation and sedimentation**

For the ease of vision, C2C12 cells were labeled fluorescently with CellTracker<sup>TM</sup> Green CMFDA (Thermo Fisher), which is a fluorescent dye suitable for monitoring cell movement or location. The fluorescent dye is stable and designed to display fluorescence for over 72 hours. It is nontoxic at working concentrations and well retained in cells. Briefly, 50  $\mu$ g dry powder of CellTracker<sup>TM</sup> Green CMFDA was initially dissolved in DMSO to a final concentration of 10 mM. Thereafter, the solution was further diluted with serum-free medium to achieve final working concentration of 1  $\mu$ M. The labeled C2C12 cells were then gently mixed with GelMA-GG bio-inks at 37°C to achieve a final cell density of  $4 \times 10^6$  cells/ml. The cell-laden bio-inks were loaded into printing cartridges (the cartridges were cut into ring patterns to provide flat bases) and then were kept at 25°C (emulating printing temperature) for 1.5 hours to evaluate the effect of cell sedimentation. The GelMA-GG composite bio-inks were then frozen in 4°C for 20 mins after 1.5 hours of encapsulation to fix the cells under physical crosslinking for imaging. The cell-laden hydrogels were then cut in half to expose the cross-section, which were then put on glass slides for imaging. The cell-laden bio-inks were observed using an inverted microscope (Carl Zeiss Axio Vert. A1).

### **3.2.5 Evaluation of bio-ink's mechanical properties (Cyclic Compression Test)**

The mechanical properties of the printed GelMA-GG bio-inks were tested with a uniaxial compression tester (Instron 5569, UK) at room temperature with 100 N load cell. All the samples were prepared into a cylindrical shape

with a diameter of 12 mm and 5 mm height. The cyclic tests were recorded over 5 cycles at 30% strains, followed by continual compression at a rate of 2 mm/min until failure. The Young's modulus was calculated as the slope of the linear region of the stress-strain curve in the 0-10% of the strain range.

### **3.2.6 Evaluation of bio-ink's microstructure (FE-SEM imaging)**

Field Emission Scanning Electron Microscope (FE-SEM) imaging was carried out to analyze the microstructures of the printed GelMA-GG constructs. GelMA-GG constructs were printed in a rectangular shape (10 mm  $\times$  10 mm  $\times$  2 mm) and were dehydrated using graded ethanol (starting from 25, 50, 75, 90, 95 to 100% v/v). The samples were then dried using a critical point dryer (Leica EM CPD030, Germany) to retain the microstructure within the printed GelMA-GG constructs. The dried samples were then carefully sectioned using a sterile surgical blade to expose the cross-section before coating the samples with platinum (Pt) using a sputtering machine (Polaron SC7640 Sputter Coater from Quorum Technologies, United Kingdom). Representative images of GelMA-GG microstructure ( $n = 6$ ) were taken at a 30,000x magnification using Ultra-Plus FE-SEM (Carl Zeiss, Germany). ImageJ was used to analyze the FE-SEM images to determine the pore sizes and porosity within the GelMA-GG microstructures at varying concentrations.

### **3.2.7 Manual casting of cell-laden bio-inks**

Immortalized C2C12 mouse myoblast cells were cultured in DMEM with 10% fetal bovine serum, 1% antibiotic-antimycotic in 37 °C, 5% CO<sub>2</sub> environment. The culture medium was changed every 2~3 days and the cells were harvested at 60-70% confluency. C2C12 cells were gently mixed with

GelMA-GG bio-inks (5-0.5, 7.5-0.1, 7.5-0.2, 7.5-0.5, 10-0.1, 10-0.2) to a final cell density of  $4 \times 10^6$  cells/ml. The cell-encapsulated bio-inks were then casted into pre-designed square PDMS mold with a dimension of  $10 \times 10 \times 1$  mm, followed by UV crosslinking. Live/Dead staining was performed on Day 0, 7 and 14. Live/dead staining was performed using Molecular Probes. Live/Dead staining kits (Life-Technologies). The calcein AM will stain the viable cells green, while the ethidium homodimer-1 will stain the dead cells red. The samples were washed thrice with  $1 \times$  PBS and 1 mL of staining solution was added to each of the 12-well plates containing the GelMA-GG bio-inks and was incubated for 30 mins at room temperature before observation under Inverted Microscopy (Carl Zeiss Axio Vert. A1). This study allowed us to identify suitable bio-inks for cell proliferation and spreading prior to actual printing.

### **3.2.8 3D bioprinting of cell-laden bio-inks**

C2C12 cells were printed using a bioprinter (Regenhu, Villaz-St-Pierre, Switzerland) to study the influence of material stiffness and microstructure on the cell behaviour. Based on the earlier study of manual casting cell-laden bio-inks, we have selected a single bio-ink from each group to represent bio-inks of different material stiffness. The bio-inks were first printed using the extrusion-based print-heads, followed by curing each subsequent layer of printed bio-ink with a built-in UV-lamp (150mW, 365 nm wavelength). All the printing cartridges, needle tips, pyrex bottles and sucrose solution were fully autoclaved before use. C2C12 cells were first suspended in an isotonic sucrose solution at  $37^\circ\text{C}$ , followed by gently mixing with GelMA-GG bio-inks at  $37^\circ\text{C}$  using a pipette (Gilson) before transferring the cell-laden bio-inks into the sterilized Nordson printing cartridge. The 3D constructs

were printed at  $25 \pm 1^\circ\text{C}$  using a 27G needle tip (inner diameter:  $210\ \mu\text{m}$ ). The printed constructs were cultured over a week; live/dead staining and Prestoblu<sup>e</sup> proliferative assay were performed on Day 1, 3, 7 to evaluate the cell viability and proliferation rates. Live/Dead staining was performed using Molecular Probes Live/Dead staining kits (Life-Technologies). The calcein AM will stain the viable cells green, while the ethidium homodimer-1 will stain the dead cells red. The samples were washed three times with PBS and 1 mL of staining solution was added to each of the 12-well plates containing the samples and incubated for 30 min at room temperature before observation under Inverted Microscopy (Carl Zeiss Axio Vert. A1). Briefly, at each time point, sample in each well was cultured with  $360\ \mu\text{l}$  medium plus  $40\ \mu\text{l}$  presto blue added for 2hrs at  $37^\circ\text{C}$ . Thereafter, aliquots were pipetted into a new 96-well plate. The 96-well plates were then placed into a microplate reader and fluorescent mode was used to measure. The excitation at 560 nm and emission at 590 nm of the content of each well was measured, control group, with no cell seeded, was used to determine their corresponding background absorbance and these values were subtracted from the measurements.

### 3.2.9 Statistical analysis

All results were expressed as (*mean value  $\pm$  standard deviation(SD)*). The results were evaluated by one-way ANOVA analysis coupled with the Tukey test. Differences are considered statistically significant when  $p \leq 0.05$  and greatly significant when  $p \leq 0.001$ . All experiments were performed in triplicate.

### 3.3 Results and discussion

The stringent requirements of bio-inks have resulted in the limited choice of printable cell-laden bio-inks. Some biocompatible materials (e.g collagen and hyaluronic acid) have exhibited poor printing resolution and weak mechanical property that constantly lead to structural collapse. Particularly, for soft tissues, it is difficult to find a suitable material with compliant mechanical property of native tissues while maintaining good structural integrity after several layers of printing. In contrast, GelMA is a thermo-sensitive material with highly tunable mechanical stiffness and has been commonly used for various biomedical applications due to its suitable biological properties and tunable physical characteristics. GelMA-based bio-inks possess important properties of native extracellular matrix (ECM) due to the presence of arginylglycylaspartic acid (RGD) peptide motifs that favor cell attachment, spreading and proliferation. However, the poor rheological properties of GelMA bio-inks at low concentrations ( $<10\%$ ) have resulted in poor printability and instable structures. Previous studies have reported GelMA or gelatin printing through bioprinters that are equipped with a temperature control system ([314]). However, most commercial bioprinters do not usually include such a temperature control system, hence posing a challenge to maintain a consistent printability of GelMA-based bio-inks due to fluctuations in temperature during printing process. Gellan gum is a thermo-reversible water-soluble anionic polysaccharide which has been used to improve the bio-ink printability by modifying the viscosity ([311]). Gellan gum (GG) is used to reinforce GelMA, leading to a more robust composite hydrogel. However, the printability of GelMA-GG is still limited to simple and relatively thin structures. Herein, we introduce a bioprinting strategy that enables the fab-

rication of tissue constructs with high aspect ratio via a layer-by-layer UAE bioprinting strategy (Figure 3.3). GelMA-based bio-ink with low amount of

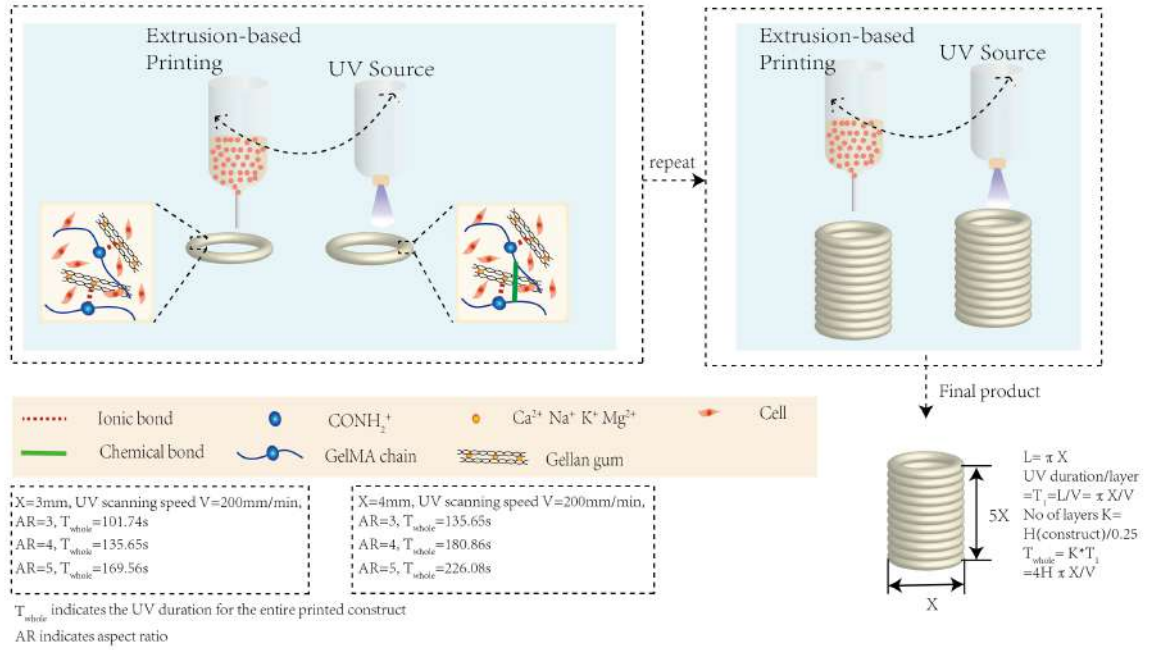


Figure 3.3: Schematic drawing of layer-by-layer UV-assisted bioprinting strategy. The gellan gum in the bio-ink serves as a viscosity enhancer to improve the bio-ink printability (via formation of ionic bonds between GelMA chain and gellan gum) during the extrusion printing process prior to further UV crosslinking (to form chemical bond between adjacent GelMA chains) of each individual printed layer. This layer-by-layer UV-assisted bioprinting strategy is repeated to eventually achieve fabrication of complex 3D structures with high aspect ratio.

### 3.3.1 Determination of degree of methacrylation

Compared with the spectrum of unmodified gelatin, GelMA sample showed new functional groups, indicated by the two black arrows in Figure 3.4. The peaks at around chemical shifts ( $\delta$ ) of 5.4 and 5.6 ppm were assigned to the acrylic protons (2H) of the grafted methacryloyl group, and another peak at ( $\delta$ ) = 1.8 ppm could be attributed to the methyl group (3H) of the grafted



methacryloyl group. Meanwhile, there was a decrease of the intensity at 2.9 ppm, which was assigned to the lysine methylene (2H) and highlighted with blue stripe. As lysine is the reaction site, this trend could be used to quantify degree of methacrylation, which was  $55.4\% \pm 0.5\%$ .

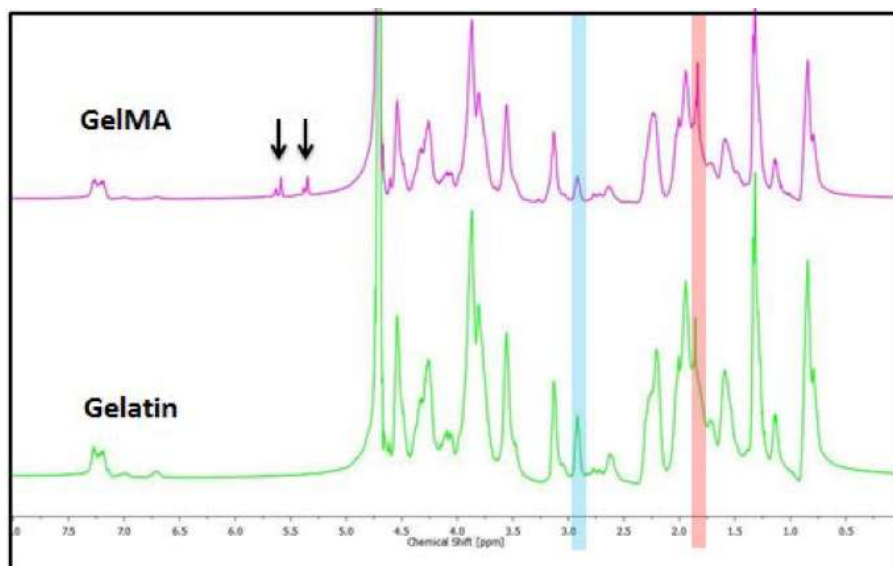


Figure 3.4:  $^1\text{H}$ -NMR spectra of Gelatin and GelMA.

### 3.3.2 Bio-ink preparation

Bio-ink viscosity plays an important factor influencing cell encapsulation within bio-inks. To evaluate the quality of cell encapsulation, rheological behavior of GelMA-GG was investigated at  $37^\circ\text{C}$  (incubation temperature) (Figure 3.5). The rheological behavior of the bio-ink was manipulated by varying the concentrations of GelMA and gellan gum.

A significant increase in the bio-ink viscosity (as shown in Figure 3.5A) at a constant shear rate of  $100\text{s}^{-1}$  at  $37^\circ\text{C}$  (emulating encapsulation process) was observed across all GelMA concentrations with increasing gellan gum concentration from 0.1 to 0.75%. In contrast, a less significant increase in

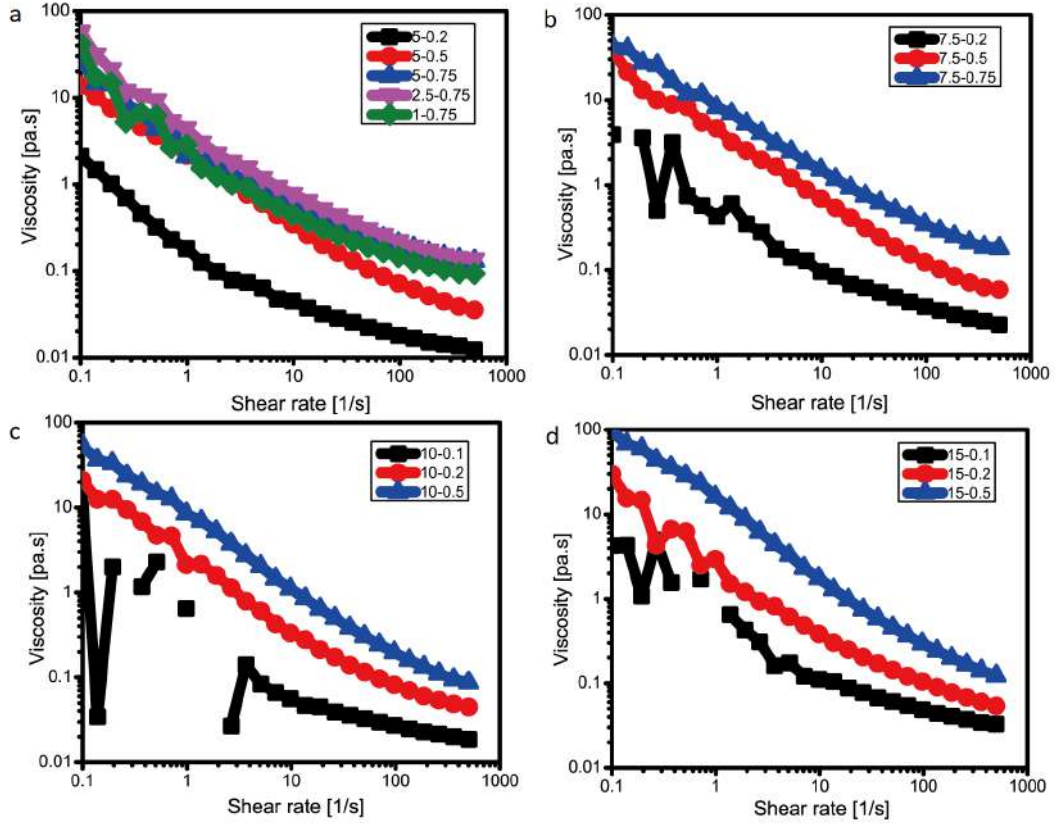


Figure 3.5: Viscosity as a function of shear rate of 30 different GelMA-GG bio-inks at 37°C. a. Viscosity of GelMA-based bio-inks with GelMA concentration at 5%, 2.5% and 1%. b. Viscosity of GelMA-based bio-inks with GelMA concentration at 7.5%. c. Viscosity of GelMA-based bio-inks with GelMA concentration at 10%. d. Viscosity of GelMA-based bio-inks with GelMA concentration at 15%

the bio-ink viscosity was observed when the GelMA concentration was varied from 1 to 15%. During the cell encapsulation process, cell pellets of desired cell density were pipetted into the bio-inks and mixed manually. Generally, homogenous cell distribution was observed in most of the GelMA-GG bio-inks in this study. However, the results have shown that the addition of

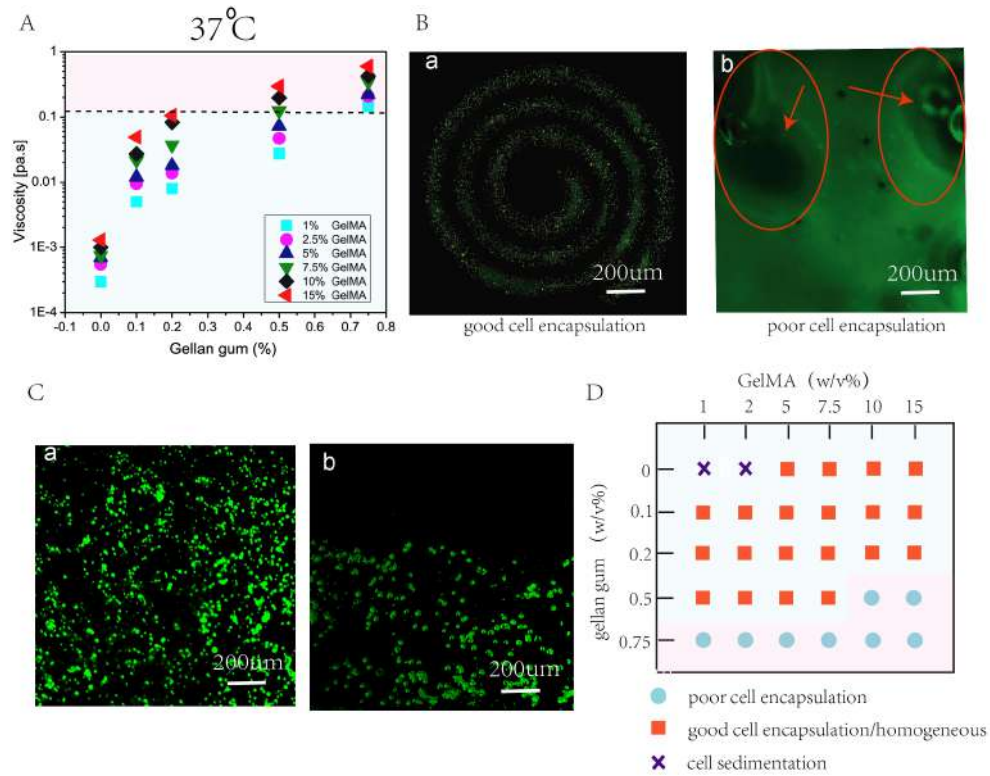


Figure 3.6: Bio-ink formulation involves characterization of rheological properties, ease of cell encapsulation and influence of cell sedimentation within bio-inks. A) Viscosities of 30 different GelMA-GG bio-inks at a constant shear rate of  $100\text{s}^{-1}$  at  $37^\circ\text{C}$  indicate higher bio-ink viscosity with increasing polymer concentrations. B) Representative images to highlight the influence of bio-ink viscosity on cell encapsulation; a low viscous bio-ink facilitates good cell encapsulation (in spiral pattern) whereas a highly viscous bio-inks results in poor cell encapsulation. C) Representative images to highlight the influence of bio-ink viscosity and density on cell sedimentation; a low polymer concentration (low viscosity and density) and without gellan gum leads to cell sedimentation whereas a high polymer concentration (high viscosity and density) results in a homogeneous cell distribution with negligible cell sedimentation. D) An overview of the different GelMA-GG bio-inks in terms of cell encapsulation and cell distribution.

0.75% GG in all GelMA-GG bio-inks resulted in the formation of highly viscous bio-inks at 37°C which was inappropriate for cell encapsulation. Furthermore, GelMA-GG bio-inks of 10-0.5% w/v ( $\sim 0.2 \text{ Pa} \cdot \text{s}$ ) and 15-0.5% w/v ( $\sim 0.3 \text{ Pa} \cdot \text{s}$ ) also exhibited poor cell encapsulation. The representative images of the encapsulated cells in the GelMA-GG bio-inks are shown in Figure 3.5B; homogeneous cell encapsulation was observed in low viscous bio-inks, spiral pattern was printed to show the homogeneous cell distribution (Figure 3.5B a) while non-homogeneous cell distribution with trapped air bubbles was spotted in highly viscous bio-inks (Figure 3.5B b). The low viscous bio-inks (less than 124 mPa·s) facilitated easy cell encapsulation and resulted in homogeneous cell distribution within the cell-encapsulated bio-inks (left of Fig 2B), whereas the highly viscous bio-inks (over 124 mPa·s) are generally considered to be unsuitable for cell encapsulation due to the relatively higher bio-ink viscosities that led to non-homogeneous cell distribution and trapped air bubbles (Figure 3.5B b). As such, our study has shown that a bio-ink viscosity of  $\sim 0.15 \text{ Pa} \cdot \text{s}$  could be the threshold bio-ink viscosity for homogeneous cell encapsulation at 37°C.

Another important consideration is the cell sedimentation effect within the bio-inks over time. An ideal cell-laden bio-ink should result in a homogeneous cell output over time by mitigating the effect of cell sedimentation during the printing process. As such, we further investigated the effect of cell sedimentation in the cell-laden bio-inks with homogeneous cell distribution over a period of 1.5 hours (typical printing duration for large tissue constructs). All the selected GelMA-GG bio-inks were mixed with fluorescently-labelled cells and were evaluated over a period of 1.5 hours to study the effect of cell sedimentation which is caused by the gravitational forces acting upon the encapsulated cells within the bio-inks. The GelMA-

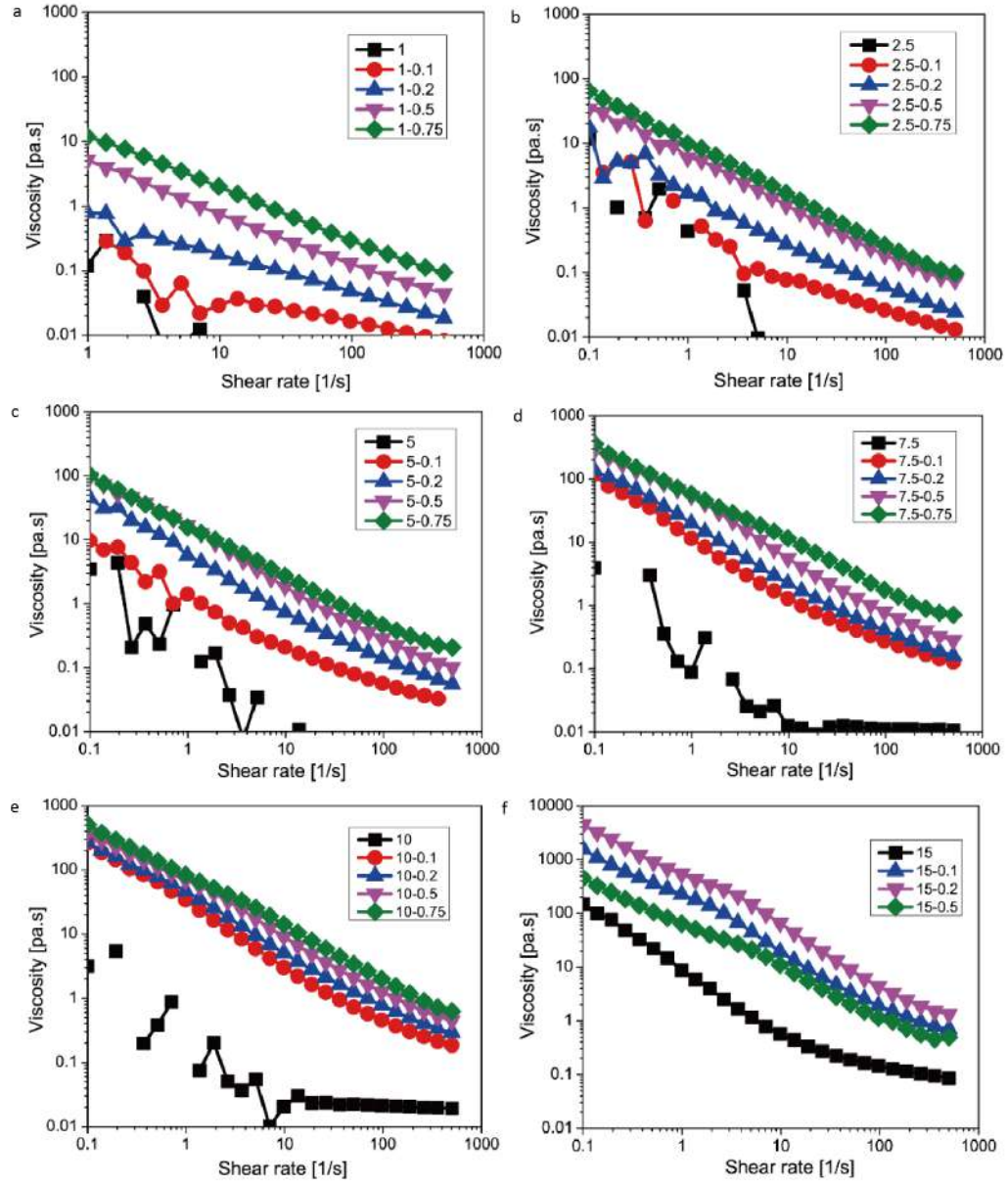


Figure 3.7: Viscosity as a function of shear rate of 30 different GelMA-GG bio-inks at 25°C. a. Viscosity of GelMA-based bio-inks with GelMA concentration at 1%. b. Viscosity of GelMA-based bio-inks with GelMA concentration at 2.5%. c. Viscosity of GelMA-based bio-inks with GelMA concentration at 5%. d. Viscosity of GelMA-based bio-inks with GelMA concentration at 7.5%. e. Viscosity of GelMA-based bio-inks with GelMA concentration at 10%. f. Viscosity of GelMA-based bio-inks with GelMA concentration at 15%.

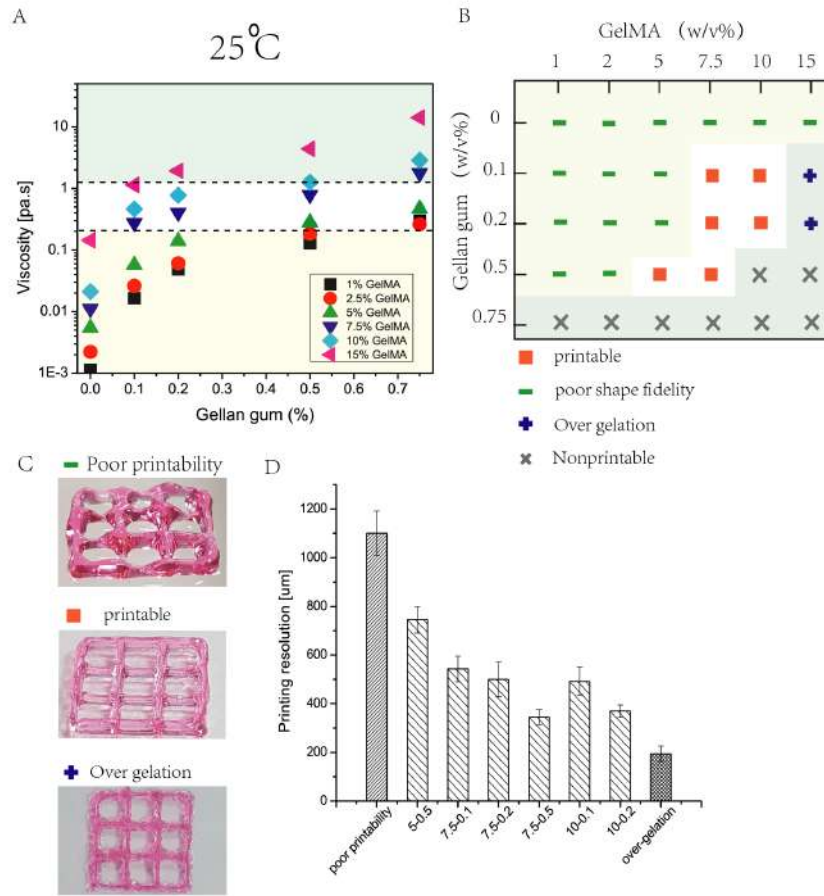


Figure 3.8: The bioprinting phase involves characterization of rheological properties, determination of suitable UV scanning speed and selection of suitable bio-inks. A) Rheological properties of 30 different GelMA-GG bio-inks at a constant shear rate of  $100\text{s}^{-1}$  at  $25^{\circ}\text{C}$  indicated higher bio-ink viscosity with increasing polymer concentrations. B) An overview of the different GelMA-GG bio-inks in terms of printability and cell encapsulation. C) Representative images of printed constructs to distinguish among the three different classifications; (Top) poor printability, (Middle) good printability, (Bottom) over-gelation. D) Influence of bio-ink on printing resolution, a more viscous bio-ink results in higher printing resolution due to significantly less spreading of the shear-thinning bio-inks upon contact with the substrate surface.

GG composite bio-inks were frozen in 4°C for 20 mins after 1.5 hours of encapsulation to fix the cells under physical crosslinking at 4°C for imaging and are carefully observed using an inverted microscope (Carl Zeiss Axio Vert. A1). It was observed that there was negligible cell sedimentation effect in most of the GelMA-GG bio-inks over a period of 1.5 hours. The density and viscosity of the bio-inks increase with increasing polymer concentration; which explains the negligible cell sedimentation effect found in most of the GelMA-GG bio-inks (Figure 3.5C a). In contrast, significant cell sedimentation effect was observed in 1-0% w/v and 2-0% w/v bio-inks (low GelMA concentration and without gellan gum) (Figure 3.5C b). Particularly, the 1-0% w/v and 2-0% w/v GelMA-GG bio-inks still remained in liquid state whereas the other bio-inks have transited into a gel state after 1.5 hours of encapsulation. The low viscosity and density of 1-0% w/v and 2-0% w/v bio-inks led to significant cell sedimentation, hence they were not suitable to be used as cell-laden bio-inks (Figure 3.5D).

### 3.3.3 Printing phase

Shear thinning behavior, the non-Newtonian behavior of fluids whose viscosity decreases under shear strain, is highly desirable for the printing process. As illustrated in Figure 3.7, over a range shear rates, the GelMA-GG bio-inks exhibited shear thinning behavior independent of the concentrations. As in this study, the printing was conducted under room temperature, which is around 25°C, and the rheological properties of the bio-inks were also examined at 25°C. Further, Figure 3.6A presented the bio-ink viscosities at a fixed shear rate of 100 s<sup>-1</sup> for all the groups. Generally, the bio-ink viscosity increased with increasing polymer concentration. As the GG concentration increased up to 0.75%, the viscosity increased significantly across all the



GelMA concentration groups. Similarly, the effect of GelMA concentration on bio-ink viscosity also exhibited the same trend albeit less dramatically as GG. A high viscosity within the printable range helped to reduce bio-ink spreading upon contact with the substrate surface prior to UV crosslinking.

3D grid and tubular constructs were printed to demonstrate the ability to print complex structures with high aspect ratio (AR) using the proposed layer-by-layer UV-assisted bioprinting approach (printing speed 100mm/min, UV scanning speed 400mm/min) (Figure 3.9). Both grid pattern ( $W \times L = 9\text{mm} \times 9\text{mm}$ ) with a height of 10mm (Figure 3.9A b-g) and a height of 30mm (Figure 3.9B a and b) can be printed with all the selected groups of materials using the layer-by-layer UV curing strategy. Conversely, printing without using the layer-by-layer UV curing method yielded constructs with poor resolution and building up taller structures were challenging. Furthermore, it is to be noted that the difficulty of printing high aspect ratio structures increases as the diameter of the printed constructs decreases. The smallest tubular structure that can be successfully printed with high repeatability is of 3 mm diameter with a high AR of 5 (as shown in Figure 3.9B d). As a proof-of-concept, multi-material printing was performed in the transverse and longitudinal directions to demonstrate the ability to print multi-material constructs with high aspect ratio (Figure 3.9B f-h). Firstly, multi-material printing in the transverse direction was demonstrated by fabricating concentric tubular structures of different diameters in Figure 3.9B f and Figure 3.9B g. Next, multi-material printing in the longitudinal direction was demonstrated by fabricating tubular structures of different distinct regions as shown in Figure 3.9B h. As clearly demonstrated by the printed grid and tubular structures, the layer-by-layer UV curing strategy has shown great improvement in constructing taller structures ( $AR \geq 5$ ) and better resolution



than those printed with post curing strategy.

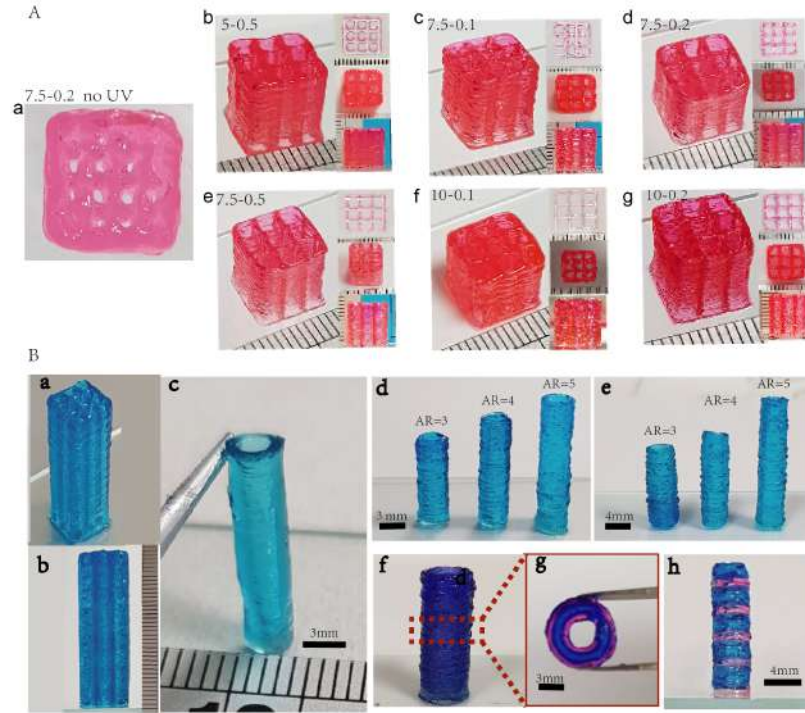


Figure 3.9: Printed constructs with different patterns. A) a. Printed grid construct with no layer-by-layer UV curing using 7.5-0.2 group. b-g. Printed grid pattern ( $W \times L \times H = 9\text{mm} \times 9\text{mm} \times 10\text{mm}$ ) with the 6 selected GelMA-GG bio-inks. B) a. Printed grid construct ( $W \times L \times H = 9\text{mm} \times 9\text{mm} \times 30\text{mm}$ ). b. Side view of the printed construct ( $W \times L \times H = 9\text{mm} \times 9\text{mm} \times 30\text{mm}$ ). c-e. Tubular structures printed with GelMA-GG bio-ink (7.5-0.2) with different AR which is bioprintable and cell permissive. f-h. Multiple materials deposition with the layer-by-layer UV curing strategy.

### 3.3.4 Post-printing phase

#### 3.3.4.1 Material property (mechanical stiffness and microstructure)

The matrix stiffness is one of the critical factors that regulates cell behaviors; therefore, it is crucial to consider the matrix stiffness of the printing

material when designing such in vitro tissue constructs ([315, 316]). The material stiffness influences cell migration, differentiation and proliferation. Driven by this, we have measured the material stiffness of the selected composite hydrogel with good printability (5-0.5%, 7.5-0.1%, 7.5-0.2%, 7.5-0.5%, 10-0.1%, 10-0.2% w/v). These printed constructs were subjected to 5 times pre-cyclic under 30% strain. The cyclic compression curves of all the groups exhibited similar cyclic recovery performance, which indicated excellent recovery capability of the bio-inks (Figure 3.9A). As revealed by Figure 3.9B, the composite bio-inks exhibited a large range of compressive modulus. The results suggest that higher polymer concentration leads to higher compressive modulus, since a range of compressive modulus from 9kPa to 16kPa could be achieved by tuning the polymer concentration. It is important to note that the modulus could be further adjusted by UV intensity and exposure time. With the increased UV intensity and exposure time, the hydrogel stiffness can be increased to the scale of a hundred kPa ([317]).

Further in-depth characterization of the material stiffness was performed by evaluating the micro-structure of the bio-inks using Field-emission scanning electron microscope (FE-SEM), as shown in Figure 3.9C. The different printed GelMA-GG bio-ink constructs were subjected to critical point drying to carefully preserve the native micro-structure found in the GelMA-GG bio-ink. FE-SEM imaging of the different bio-inks at 30,000x magnifications indicated a porous 3D microenvironment and highly-interconnected pores within the GelMA-GG printed constructs. ImageJ was used to analyse the FE-SEM images to determine the pore sizes and porosity within the GelMA-GG microstructures at varying concentrations. The FE-SEM images reveal that a 5-0.5% w/v GelMA-GG printed construct showed the largest pore size ( $172.7 \pm 63.9$  nm), whereas 10-0.2% w/v GelMA-GG printed

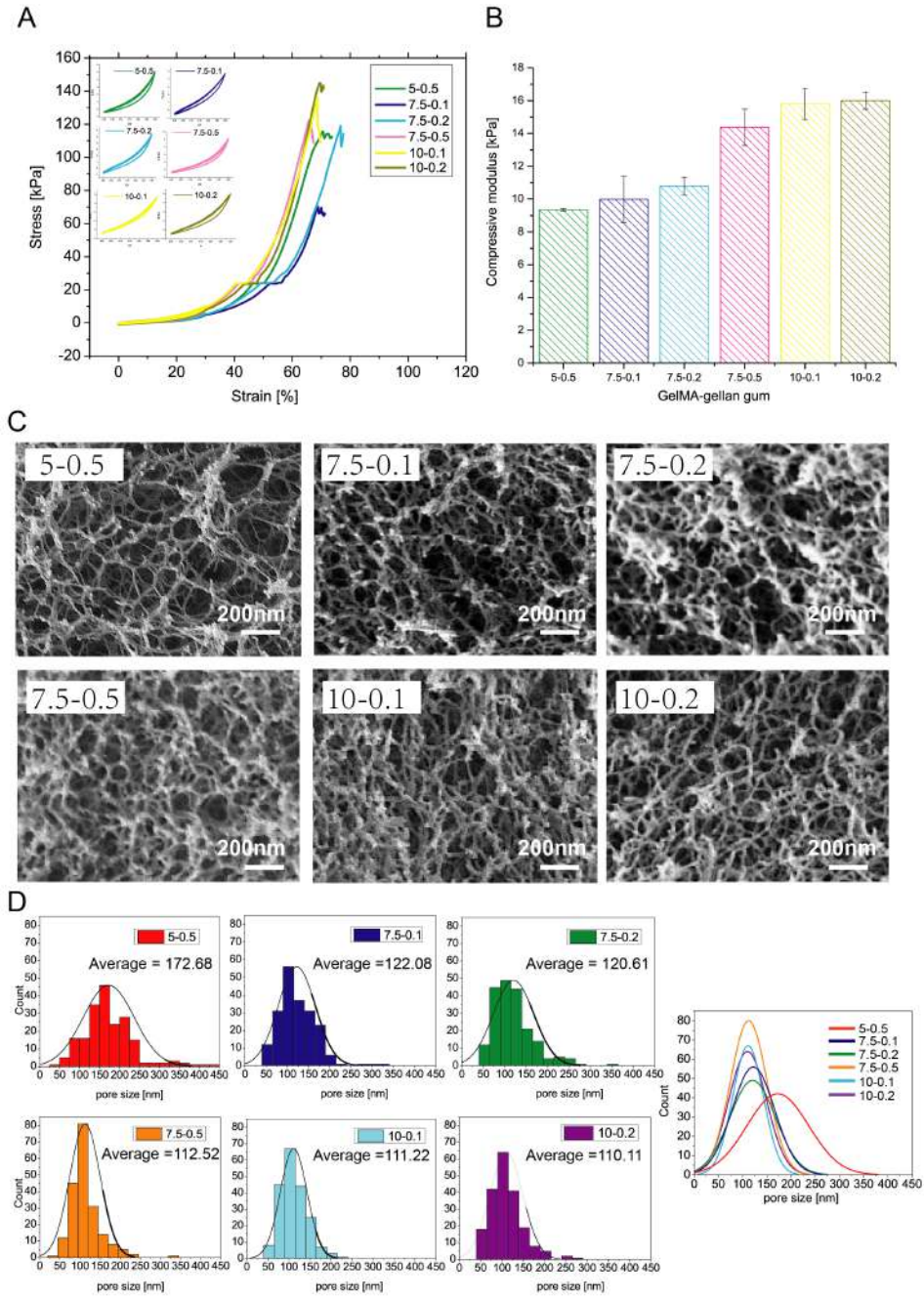


Figure 3.10: Bio-ink properties (mechanical stiffness and microstructure). A) Cyclic compression test. B) Compressive modulus of GelMA-GG bio-inks with different concentrations. C) FE-SEM imaging of GelMA-GG with varied concentrations; scale bar = 200 nm. D) Pore size distribution of GelMA-GG hydrogel bio-inks.

construct showed the smallest pore size ( $110.1 \pm 38.9$  nm). The pore size of the 3D GelMA-GG printed constructs generally decreased with increasing polymer concentration but the influence of GelMA concentration is more significant than that of GG. For a constant 2.5% increase in GelMA concentration; a significant 34.8% reduction in pore size was observed when comparing between 5-0.5% w/v ( $172.7 \pm 63.9$  nm pore size) and 7.5-0.5% w/v ( $112.5 \pm 37.9$  nm pore size), whereas only a small reduction of 1.2% in pore size was observed when comparing between 7.5-0.1% w/v ( $122.1 \pm 43.8$  nm pore size) and 7.5-0.2% w/v ( $120.6 \pm 47.3$  nm pore size). Further change in GG concentration did not result in significant changes in pore size (6.7% difference between 7.5-0.2% w/v and 7.5-0.5% w/v). In conclusion, pore size is shown to be more dramatically affected by GelMA than GG concentration with pore size decreasing with increase of polymer concentration as summarized in Table 3.1. Taken together the compressive modulus and average pore size distribution, the decreasing pore sizes corresponded to increased mechanical stiffness. In addition, negligible pore size changes were observed for GelMA with the concentration of 7.5%, while with the increasing gelatin gum concentration, the mechanical properties of these three composite hydrogels increased by nearly 50%.

#### **3.3.4.2 Influence of bio-ink on cells: Manual casting of cell-laden bio-inks**

To evaluate the biocompatibility of the hydrogel blends, C2C12 cells were encapsulated inside the 3D GelMA-GG constructs over a period of 14-day culture. Live/dead staining was used to characterize the cell behavior at Days 0, 7 and 14. The presence of living cells ( $\geq 95\%$  of total encapsulated cells) within all the composite GelMA-GG constructs indicated high cell vi-

Table 3.1: Porosity and average pore size of GelMA-GG with different concentrations.

	Porosity (%)	Average pore size (nm)
5-0.5	65.33	$172.7 \pm 63.9$
7.5-0.1	53.08	$122.1 \pm 43.89$
7.5-0.2	52.17	$120.6 \pm 47.3$
7.5-0.5	43.11	$112.5 \pm 37.9$
10-0.1	42.38	$111.2 \pm 31.8$
10-0.2	41.11	$110.1 \pm 38.9$

ability at all time points (Day 0, 7 and 14) as shown in Figure 3.11. Furthermore, cell elongation and spreading (as depicted in Figure 3.11) in 5-0.5%, 7.5-0.1% and 7.5-0.2% w/v GelMA-GG constructs on Day 7 indicated that the bio-ink micro-structure and stiffness were supportive of C2C12 differentiation. Notably, 5-0.5 % w/v GelMA-GG bio-ink showed a much better cell spreading and elongation than the 7.5-0.1 and 7.5-0.2% w/v GelMA-GG bio-inks. In contrast, the C2C12 cells in the 7.5-0.5, 10-0.1 and 10-0.2% w/v GelMA-GG bio-inks mostly remained round in shape within the 3D bio-ink constructs over a 14-days culture (After 14 days, cells remained alive but still in round shape). 3D matrix with lower mechanical stiffness and larger pore size are more favorable to cell elongation and spread. The results demonstrated that pore size and mechanical stiffness of the bio-ink have critical influence in regulating cell behavior.

#### 3.3.4.3 Influence of bio-ink on cells: 3D bioprinting of cell-laden bio-inks

By performing the manual casting approach, we can easily select the suitable composite bio-inks for our desired tissue engineering applications (specifi-

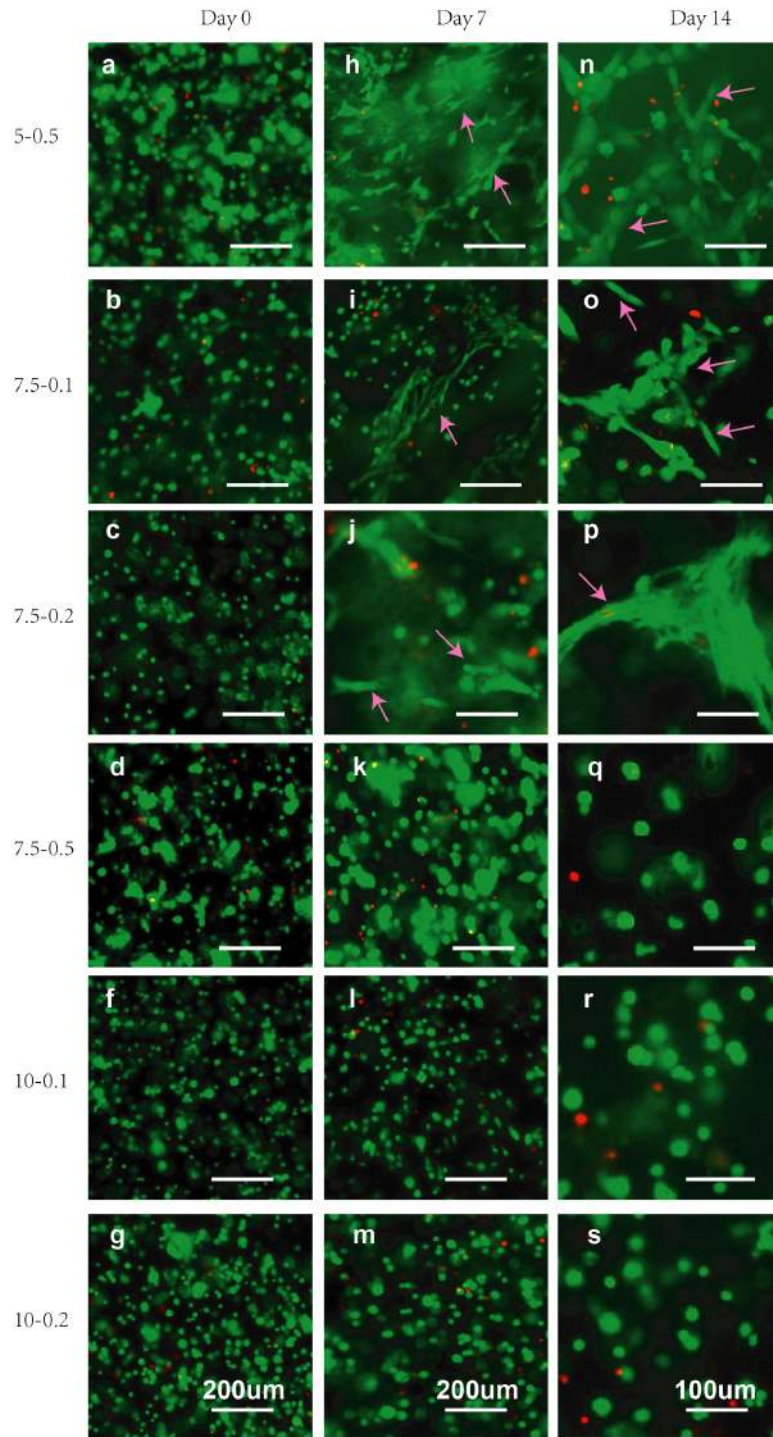


Figure 3.11: Live/dead staining of C2C12 in manual-cast cell-laden bio-inks with varied concentrations on Days 0, 7 and 14, with pink arrows showing cell elongation and spreading.



cally for soft tissue engineering in this work). The C2C12 cells in 5-0.5%, 7.5-0.1% and 7.5-0.2% w/v GelMA-GG constructs were able to spread and proliferate well due to the more favorable material micro-structures and stiffness, whereas the C2C12 cells in 7.5-0.5%, 10-0.1% and 10-0.2% w/v GelMA-GG constructs remained round. To further verify that the results in the manual-casting approach could be reproduced in the printed constructs, we chose 1 type of bio-ink from each group (elongated cells in the 5-0.5% w/v GelMA-GG constructs and round cells in the 7.5-0.5% w/v GelMA-GG constructs) for further experiments. The C2C12 cells were printed using the 5-0.5% and 7.5-0.5% w/v GelMA-GG bio-inks into 3D lattice structure. The cell viability was evaluated at Days 1, 4 and 7 post-printing, as shown in Figure 3.12. The high viability of printed cells indicated that the bioprinting process had insignificant effect on the viability of cells. Similarly, cell elongation was clearly observed in 5-0.5% GelMA-GG bioprinted constructs on Day 7. The cell proliferation was characterized using a PrestoBlue assay by measuring the relative fluorescence units and comparing with the standardized cell density curve in Figure 3.12. Overall, the printed C2C12 cells in 5-0.5% w/v GelMA-GG bioprinted constructs showed a faster proliferation rate relative to the printed C2C12 cells in the 7.5-0.5% w/v GelMA-GG bioprinted constructs as indicated by the faster increase in cell number over 7 days of study (Figure 3.12). The results were in good agreement with the manual-casting study, which proved that our bioprinting process does not have adverse effects on cells survival and differentiation.

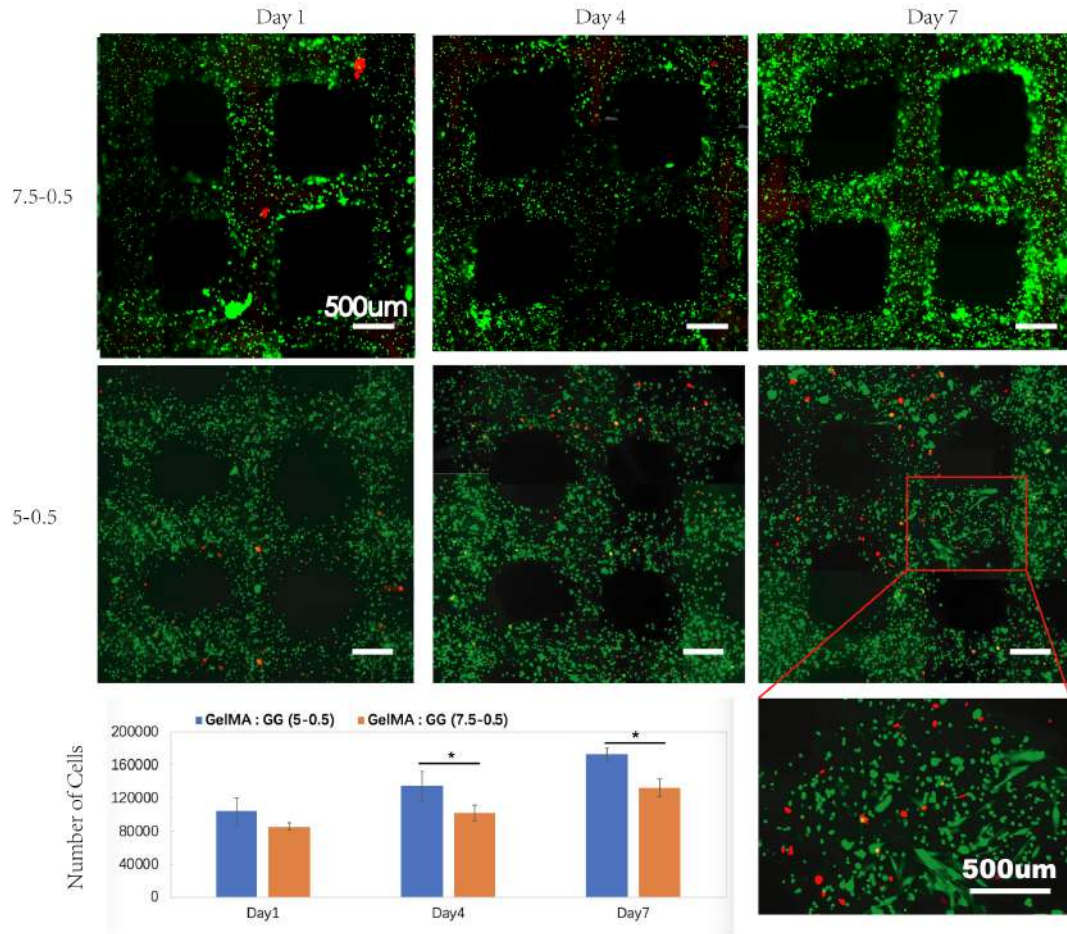


Figure 3.12: C2C12 cell viability and proliferation study of cell printing on Day 1,4 and 7; scale bar is 500  $\mu\text{m}$ .\* -  $p < 0.05$ , \*\* -  $p < 0.001$ .

### 3.4 Summary

The GelMA-based bio-inks have exhibited great biocompatibility for cells due to the presence of RGD peptides. However, challenges in using GelMA as bio-ink remain especially in printability and poor structure integrity. In this chapter, we have presented a layer-by-layer UV-assisted bioprinting strategy to fabricate complex 3D bioprinted constructs with high aspect ratio for tissue engineering of soft tissues using the GelMA-GG bio-inks. To strike a



balance between printability and biocompatibility, a minimum ideal amount of gellan gum was added to enforce the printability of the bioinks without compromising the biocompatibility. In-depth characterization and evaluation on the different composite GelMA-GG bio-inks have been performed to select a suitable range of GelMA-GG bio-inks through our proposed parametric study. The three main phases of bio-ink development involved were 1) bio-ink preparation phase, 2) printing phase and 3) post-printing phase. From our work, a suitable range of bio-ink viscosity lower than 0.124 Pa·s at 37°C was found to be suitable for cell encapsulation and to achieve a homogeneous cell-laden bio-inks. Material viscosity of 0.2-1.0 Pa·s at a printing temperature of 25°C was recommended for printing of complex 3D cell-laden constructs with high aspect ratio using our layer-by-layer UV-assisted bioprinting strategy. In addition, a strong correlation between material microstructure and stiffness has been shown and their synergistic influence on cell behavior has been investigated. In conclusion, this chapter has presented an effective approach to fabricate complex 3D structures with great structure integrity, high aspect ratio, good shape fidelity and mechanical stability of soft materials and in this case GelMA-GG composite bio-ink. This method could be easily adapted for all light curable materials and would find great potential in scaffold/bioprinting for tissue engineering of soft tissues.

# Chapter 4

## Development of Suitable Bio-inks and the Influence of UV Radiation on Cell Behavior

### 4.1 Introduction

The past few decades have witnessed the rapid development of 3D bioprinting technology. The major platforms for bioprinting include droplet-, extrusion and laser-based printers based on different driving forces. Droplet-based printing consists of inkjet printing (thermal, piezoelectric, electro hydrodynamic jetting and electro static bioprinting), acoustic droplet ejection and micro-valve printing [243]. Droplet-based printing allows the deposition of discrete droplet, while extrusion-based bioprinting (pneumatic-driven and mechanical-driven) can only print continuous filaments. Various materials have been tailored to meet the requirements of specific printing technology. Generally, droplet-based printing allows the printing of materials with low viscosities ranging from 3.5 to 70 mPa.s, while extrusion-based bioprinting is able to print materials with a broader range of higher viscosities (30 mPa.s to  $6 \times 10^7$  mPa.s) [247]. One of the key challenges in bioprinting is the lack of suitable bio-inks which are printable, able to build thick and complex structures without structural collapse, and biocompatible to support various cell types. Both natural and synthetic biomaterials including but not limited to fibrin, collagen, chitosan, hyaluronic acid, gelatin, alginate and Poly(ethylene glycol) (PEG) have been extensively investigated. Among them, GelMA has been widely utilized due to the ease of manipulation, cost-effectiveness and tunable mechanical properties. A great deal of studies have demonstrated the good biocompatibility of GelMA with lower concentrations [301, 318, 319], but with relatively poor printability. As demonstrated in Chapter 3, in combination with layer-by-layer UV curing

bioprinting, a small addition of gellan gum into GelMA could improve the printability, therefore achieve stable 3D constructs with high aspect ratio and structural fidelity [269]. Nevertheless, it is inadequate for an ideal bio-ink to just provide structural support. Rather, the bio-ink should also be smart enough to deliver instructive cues to elicit desired cellular response. From our work, the microstructure analysis revealed the dense network of the GelMA-GG constructs printed with layer-by-layer UV crosslinking. The small pore sizes range from 110-170 nm, which is conducive for cell ingrowth and migration. To tackle this, materials that possess dynamic mechanical property, which can provide initial support and subsequently offer proper space for cells to grow and migration is highly desirable.

In addition, cell viability is the fundamental indicator to determine whether the fabrication process is cell friendly. Generally, the bioprinting process could be divided into three different stages: a) Resting, the cells were resting in printing syringe prior to printing. b) Extrusion, cell-laden bio-inks were extruded out of the printing needle (during printing). c) Crosslinking, cell-laden bio-inks were printed onto the building platform and waiting for crosslinking, in our case, UV crosslinking. UV source has been commonly used for photocurable bio-inks. However, the effect of UV influence on cell viability has not yet been examined systematically. It is of critical importance to elucidate the effect of printing process on cell survival rate to better control the printing parameters and thus, the property of the constructs.

In this chapter, a composite GelMA-based bio-ink with dynamic mechanical property was formulated. Based on GelMA-gellan gum composite hydrogel, gelatin was further introduced to improve the biological property. Material characterization including rheological property, structure integrity, degradation and biocompatibility were performed. In addition, cell viability

over the entire printing process was analyzed. Specifically, cell survival rate in the printing syringe over time was assessed. Moreover, the effect of shear stress on cell viability when the cells were extruded from the needle tip was investigated. Lastly, the influence of UV radiation on cell viability (C2C12 and HUVECs) was evaluated. This study will provide insight into bio-ink selection and the understanding of UV radiation effect on cells to achieve mechanically stable and cell-favorable constructs.

## 4.2 Material and method

### 4.2.1 Material preparation

GelMA was prepared by reacting 10% (w/v) gelatin (Sigma Aldrich, type A from porcine skin, 300g Bloom, Singapore) with methacrylic anhydride (Sigma Aldrich) at 50 °C based on previous study [312]. The solution was dialyzed in 12-14 kDa dialysis tubing (Sigma Aldrich) against distilled water at 40°C for 1 week, followed by 1-week lyophilization. It was then stored at -30°C for future use. Irgacure 2959 (Sigma Aldrich) was dissolved in 10% PBS (v/v) at 70°C to achieve the final concentration 0.1% (w/v) as described before [310]. 6% sucrose (Sigma Aldrich) was added to generate an isotonic solution. GelMA was added into the PBS-based reagent at room temperature to achieve the concentrations at 7.5% (w/v). Gelatin and Gellan gum solution were prepared by dissolving gelatin and gellan gum (Sigma Aldrich, Gelzan<sup>TM</sup> CM, Gelrite) powder in the PBS-based solution to a concentration of 15% and 0.6%(w/v) respectively. The GelMA-gelatin-gellan gum composite bio-inks were generated by mixing GelMA, gelatin and gellan gum solution at 45°C in 1:1:1 ratio for 1h to achieve homogeneous GelMA-based composite bio-inks. As a control, GelMA-gelatin hydrogel was

prepared by mixing 6% GelMA and 10% gelatin solution in 1:1 ratio, GelMA-gellan hydrogel was formulated by mixing 15% GelMA and 0.2%, 0.4% gellan gum. The GelMA-gelatin-gellan gum composite hydrogel was recorded as GMGAGG, GelMA-gelatin hydrogel as GMGA and GelMA-gellan gum as GelMA-GG in the following study.

#### **4.2.2 Rheological property**

The rheological properties of the composite bio-inks were tested using a rheometer (MCR 501, Anton Paar Germany GmbH, Ostfildern, Germany). The viscosity and the shear thinning properties of the composite bio-inks were evaluated by using a cone plate (angle:1°) geometry with 25 mm diameter. The bio-ink viscosity was evaluated for shear rates ranging from 0.1 to 500s<sup>-1</sup> at 25°C (printing temperature). All measurements were performed in triplicate.

#### **4.2.3 Evaluation of gelatin release**

As gelatin was introduced into the bioink without crosslinking, it is expected that gelatin leaching will take place during incubation. The release of gelatin could offer extra space for cell spreading, migration and ingrowth, which, however, may in turn compromise the mechanical property of the scaffold or even lead to structural collapse. Therefore, the gelatin release profile has to be considered. To quantify the gelatin release of GMGAGG bio-ink during incubation, 2,4,6-trinitrobenzene-sulfonic acid (TNBS) assay was performed as previously described [320]. Briefly, printed hydrogel constructs (9 mm × 9 mm × 2.5 mm) were soaked in 3 ml dPBS in a 12-well plate for varied time intervals (day 1, day 3, day 5). Supernatant of each time point was dialyzed in 0.1 M sodium bicarbonate solution (pH=8.5) for 7 days. Then, 0.5 ml of

each sample solution was mixed with 0.25 ml 0.01% TNBS solution (in 0.1 M sodium bicarbonate buffer) and then incubated for 2h at 37 °C. Next, 0.25 mL of 10 w/v% sodium dodecyl sulfate and 0.125 mL of 1 N hydrochloric acid were added to cease the reaction. The absorbance of each sample was measured at 335 nm. The glycine standard curve was then generated to determine the amino group concentration, with sample solutions prepared at 0, 15, 20, 30, 36, 45, 90 and 180  $\mu\text{g/ml}$ . The experiment was conducted in sets of three ( $N = 3$ ) under identical conditions.

#### **4.2.4 Structural integrity of GMGAGG hydrogel**

An ideal bio-ink should provide initial mechanical support, and sufficient structural integrity to support long-term culture. In this study, structural integrity of hydrogel over time was studied for 21 days in dPBS at 37 °C. 3D printed rectangular samples (9 mm  $\times$  9 mm ) were prepared. The constructs were printed with different number of layers, namely, 10 layers and 20 layers. The hydrogels were stained with a food dye for ease of visualization. 7.5-0.2 GelMA-GG composite hydrogel was run in parallel as a control.

#### **4.2.5 Enzymatic degradation study**

0.02 %(w/v) Collagenase (Sigma-Aldrich, USA) in PBS was prepared for enzymatic degradation test of bio-inks over 28 days. Hydrogel samples including GMGAGG (2.5-5-0.2) and GelMA-GG (5-0.5, 7.5-0.1, 7.5-0.2, 7.5-0.5, 10-0.1, 10-0.2) were freeze-dried and weight loss was recorded every two or three days. Pure GelMA 5%, 7.5% and 10% were prepared as control group. Collagenase solution was changed every 2-3 days over the entire experimental period.

#### 4.2.6 Biocompatibility characterization

Biocompatibility of GMGAGG hydrogel was performed with C2C12. C2C12 were trypsinized and resuspended in GMGAGG hydrogel at a concentration  $5 \times 10^6$  cells/ml using a pipette (Gilson) to gently mix and transfer to a 5cc syringe (Nordson) for printing. Constructs were printed into a grid pattern with a dimension of  $9 \times 9 \times 2.5$  mm. The printed constructs were cultured for 1 week and cell viability was examined with live/dead staining assay. Live/dead staining was performed using Molecular Probes, Live/Dead staining kits (Life-Technologies). The calcein AM would stain the viable cells green, while the ethidium homodimer-1 would stain the dead cells red.

#### 4.2.7 Cell culture

Murine C2C12 myoblasts (American Type Culture Collection) were maintained in growth medium containing DMEM, 10% fetal bovine serum (Gibco, Carlsbad, CA) and 1% penicillin-streptomycin (Gibco) at below 70% confluence. Human umbilical vein endothelial cells (HUVECs) were cultured with EndoGRO-LS Complete Culture Media kit (Sigma-Aldrich). All cells were incubated in an atmosphere with 5% of CO<sub>2</sub> at 37°C. Cells were trypsinized upon 70% confluence and replated. Media was replaced every 2-3 days.

#### 4.2.8 Evaluation of *in vitro* cell viability over time (prior to printing)

C2C12 and HUVECs were gently mixed with GMGAGG and GMGA composite hydrogel at 37°C to achieve a final cell density of  $5 \times 10^6$  cells/ml respectively. Thereafter the cell-laden hydrogel was casted into 24 well plate, with 200  $\mu$ l/well (N=4). The cell-laden hydrogel was kept at room tem-

perature without any further crosslinking. Cell viability was examined at varied incubation duration: 0 min, 30 min, 60 min, 90 min, 120 min, 150 min. At each time point, 100  $\mu$ l live/dead staining reagent was added to each well and incubated for 30 min. The samples were then imaged with Inverted Microscopy (Carl Zeiss Axio Vert. A1). Image J software was used to calculate the cell viability.

#### **4.2.9 Evaluation of shear stress effect on cell viability over time (during printing)**

3D bioprinting was performed with bioprinter from Regenhu (Villaz-St-Pierre, Switzerland) at  $25 \pm 1$  °C. The printer is equipped with a built-in UV lamp (500 mW, 365 nm wavelength) to crosslink the photocurable materials. C2C12 and HUVECs were gently mixed with GMGAGG hydrogel at 37°C to achieve a final cell density of  $5 \times 10^6$  and  $1 \times 10^6$  cells/ml, respectively. All the printing syringes, needle tips, forceps, pyrex bottles were fully sterilized before use. Cell-laden bio-inks were loaded to the sterilized Nordson printing syringe. To evaluate the effect of shear stress on cell viability, 25G (inner diameter=260  $\mu$ m), 27G (inner diameter=210  $\mu$ m) and 30G (inner diameter=160  $\mu$ m) needle tips were adopted. Single layer circular pattern with a diameter of 12 mm was printed at varied time point 0 min, 30 min, 60 min, 90 min, 120 min, 150 min without further crosslinking. Cell viability was investigated with live/dead staining immediately after printing. The samples were then imaged with Inverted Microscopy (Carl Zeiss Axio Vert. A1). Image J software was used to calculate the cell viability.

Shear stress plays a pivotal role in bioprinting. It is inevitable in any form of bioprinting, therefore it has to be considered during printing. It was demonstrated that proper shear stress could modulate stem cell differ-



entiation, while excessive shear stress leads to cell rupture by damaging cell membrane [321]. Generally speaking, shear stress is affected by the applied air pressure, the material viscosity and the needle size selected.

The extrusion-based bioprinting setup is shown in Figure 4.1, for a power-law fluid in a pipe, shear stress is the function of shear rate, as shown in Equation (4.1).

$$\tau = m\dot{\gamma}^n \quad (4.1)$$

Where  $n$  and  $m$  are the power-law index and power-law consistency coefficient,  $\dot{\gamma}$  is the shear rate.

Then the viscosity can be expressed as follows,

$$\eta = m\dot{\gamma}^{(n-1)} \quad (4.2)$$

Assuming that in the syringe there is a uniform flow rate ( $V$ ), the volumetric flow rate ( $Q$ ) of a non-Newtonian fluid can be written as follows,

$$Q = \pi R^2 V = \pi \left( \frac{n}{3n+1} \right) \left( \frac{-\Delta p}{2ml} \right)^{1/n} R^{\frac{3n+1}{n}} \quad (4.3)$$

Where  $\Delta p$  is the pressure drop,  $L$  is the length of the printing syringe.  $R$  is the radius of the syringe (Figure 4.8).

Then pressure drop can be described as follows,

$$\Delta p = -2ml \left[ \frac{Q}{\pi \frac{n}{3n+1} R^{\frac{3n+1}{n}}} \right]^n \quad (4.4)$$

The shear rate can be expressed as follows,

$$\dot{\gamma}^n = \left[ \frac{Q}{\pi \frac{n}{3n+1} R^{\frac{3n+1}{n}}} \right]^n \times r \quad (4.5)$$

The shear stress during printing can be derived with the aid of shear rate-shear stress curve accordingly. The printing pressure used for each configuration need to be properly adjusted. 25G, 27G and 30G needle tip

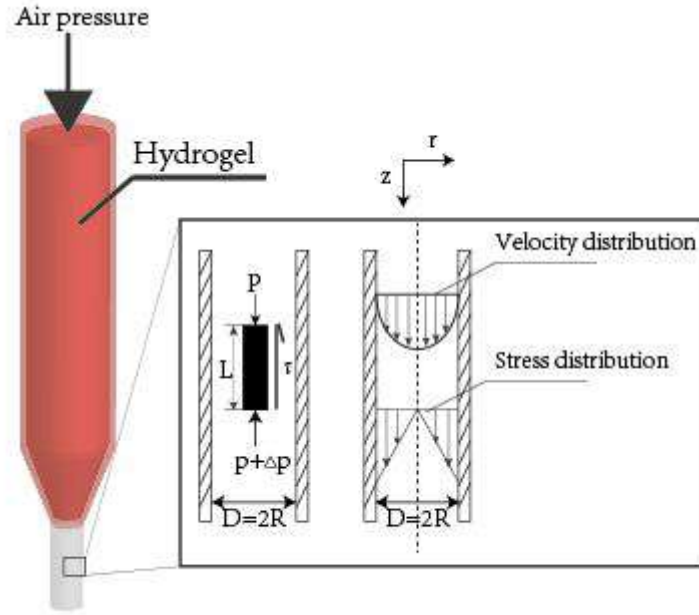


Figure 4.1: Schematic of extrusion-based bioprinting. Left: flow through a bioprinting needle. Right: stress distribution and the velocity distribution

was selected for this experiment. The extrusion time, which is the duration for the hydrogels (with a certain volume) to be fully extruded out from the nozzle under their respective optimal printing pressures, were recorded for the calculation of flow rate [322]. The shear stress can be derived as

$$\tau = m \left[ \frac{Q}{\pi \frac{n}{3n+1} R^{\frac{3n+1}{n}}} \right]^n \times r \quad (4.6)$$

#### 4.2.10 Evaluation of UV duration effect on cell survival rate (post-printing)

UV radiation reinforce mechanical stability of the constructs, while prolonged UV duration may in turn compromise the cell viability. Therefore, it is critical to balance the mechanical property and biological functions. To determine the influence of UV exposure time on cell viability, two different printing processes were designed. (i) Single layer of square pattern ( $1.4 \times$

1.4 mm) (as shown in Figure 4.2c) was printed and exposed to UV lamps with different UV scanning speed (100, 200, 400, 600, 800, 1000 mm/min) and times (1, 3, 5, 7, 9, 11), X time indicates the number of times UV pen scanned the pattern. Both C2C12 and HUVECs were examined. (ii) Cell-laden GMGAGG constructs with 1, 3, 5, 7, 9 and 11 layers were printed into circular pattern under fixed printing speed and pressure (400 mm/min, 2.8 bar) (Figure 4.2c). Layer thickness was set at 250  $\mu\text{m}$ . Cells in the bottom-most layer of the constructs were imaged by fluorescent microscope. In addition, C2C12-laden GelMA-GG was printed as control.

#### **4.2.11 Statistical analysis**

All results were expressed as (mean value  $\pm$  standard deviation (SD)). The results were evaluated by one-way ANOVA analysis coupled with the Tukey test. Differences were considered statistically significant when  $p \leq 0.05$  and greatly significant when  $p \leq 0.001$ .

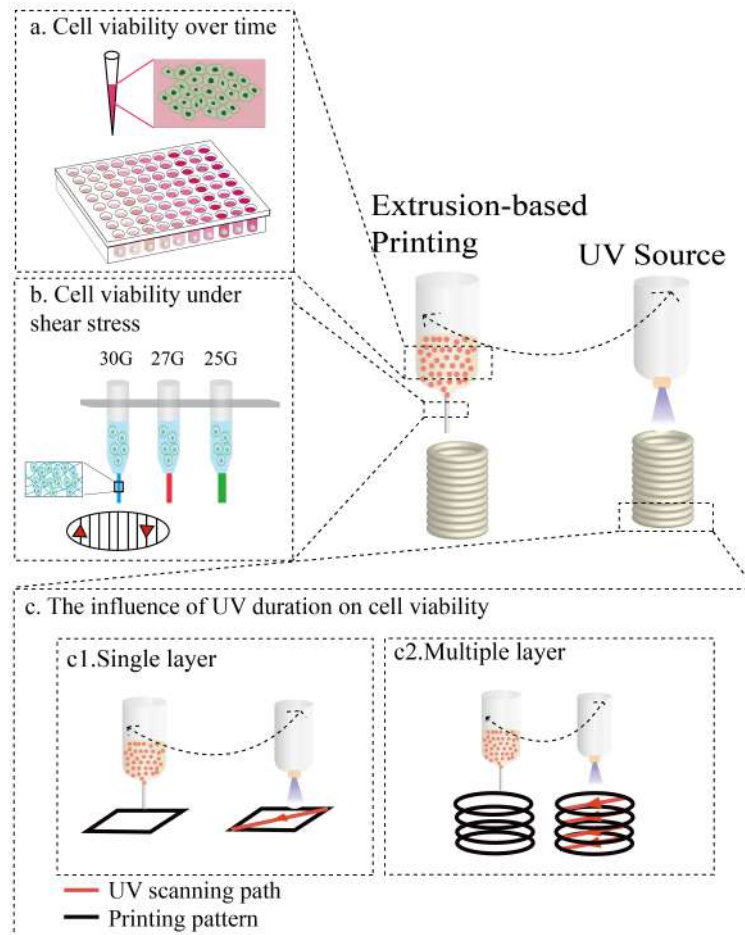


Figure 4.2: Schematic of three printing stages. a. Cells in printing syringe over time. b. Cells under shear stress in the needle tips. c Cells under UV irradiation. c1. cells in single layer filament exposed to UV irradiation. c2. cells printed in multi-layer constructs under layer-by-layer UV curing.

## 4.3 Results and discussion

Bioprinting enables the construction of complex structures by direct deposition of cells, materials or other biomolecules based on a pre-designed pattern. In comparison to other printing technologies such as metal printing or polymer printing, bioprinting is a highly demanding technology since the cells involved in the printing process require stringent surrounding environment, namely, bio-ink. In Chapter 3, a layer-by-layer UV curing bioprinting process which allows the construction of structures with high aspect ratio using low viscous GelMA-GG bio-ink was established. The UV radiation greatly improved the printing fidelity, which in turn yielded constructs with dense network. Herein, we introduce gelatin to the composite bio-ink to create a more cell friendly environment.

### 4.3.1 Evaluation of rheological property of the bio-ink

Rheological property such as shear thinning of a bioink is an important parameter for indication of printability and cell survivability during printing. Here, the rheological property of bioinks with varying composition were investigated. GMGAGG represents GelMA-gelatin-gellan gum composite hydrogel and GelMA-GG represents GelMA-gellan gum composite hydrogel. The 2.5-5-0.2 GMGAGG exhibited a decreased viscosity with increasing shear rate (as shown in Figure 4.3), which demonstrated the shear thinning behavior of the blended hydrogel. Figure 4.3 also showed that GMGAGG exhibited a relatively higher viscosity across the entire range of applied shear rates in comparison with GelMA-GG 7.5-0.1 and 7.5-0.2, indicating the improved printability of the bio-ink.

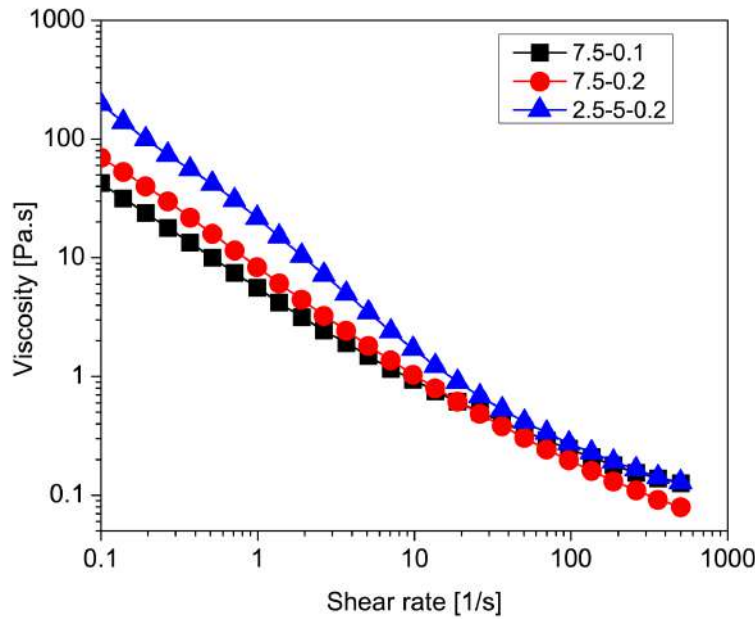


Figure 4.3: Rheological behavior of GMGAGG and GelMA-GG composite bio-ink.

### 4.3.2 Gelatin release (TNBSA)

TNBS is a highly sensitive and rapid chemical used to calculate the free amino groups. The reaction of TNBS with primary amines gives rise to a highly chromogenic product that can be readily measured at 335 nm. TNBS method is conducted for titration of free amino groups of lysine and hydroxy lysine residues in gelatin. To determine the amino group concentration, the results were compared with a standard curve. The standard curve was plotted with glycine dissolved in a series of concentrations. Gelatin exists in the composite hydrogel will gradually leach out during incubation in culture medium. As illustrated in Figure 4.4, no significant difference on the amino group concentration in the culture medium on day 1, 3 and 5 was observed. The amino group concentration was found to be 38-38.6  $\mu\text{g}/\text{ml}$ . This revealed that the uncrosslinked gelatin in the composite hydrogel mostly dis-

solved in medium in the first 24h-incubation, thus the gelatin content in the printed structure should reach stability within 24h.

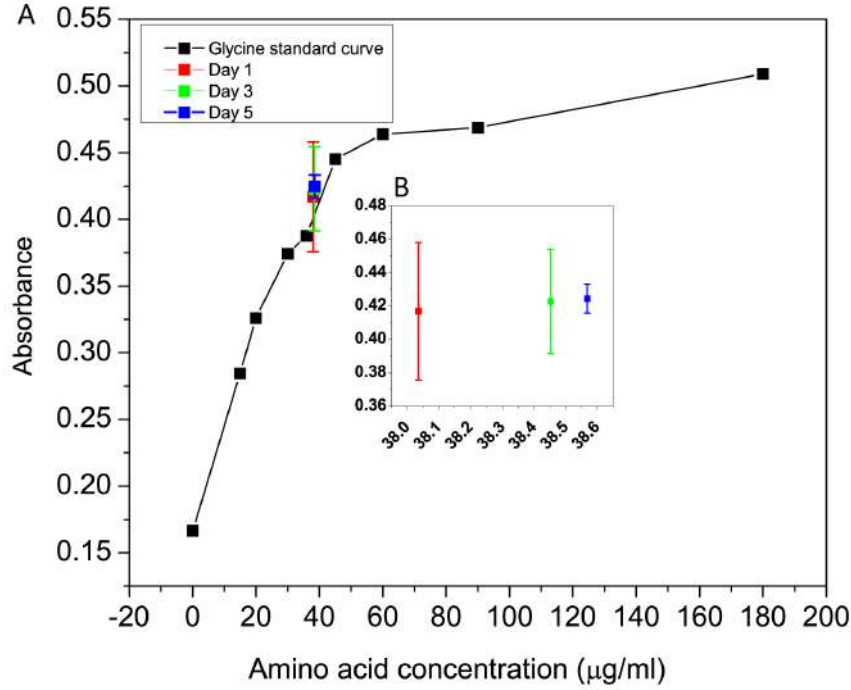


Figure 4.4: A. Quantitative analysis of gelatin release with TNBS. B. The zoom in view of amino acid concentration from 38-38.6 µg/ml

### 4.3.3 Structure integrity of the printed GMGAGG constructs

The release of gelatin from the composite hydrogel will weaken the constructs and may compromise the structural integrity. To evaluate the stability of the printed constructs, the structural integrity of the printed constructs (GMGAGG and 7.5-0.2 GelMA-GG) with different layers (10 layers and 20 layers) were investigated up to 21 days. As demonstrated in Figure 4.5, structural collapse occurred in constructs printed with GMGAGG within 21 days, while 7.5-0.2 can be maintained up to 21 days.

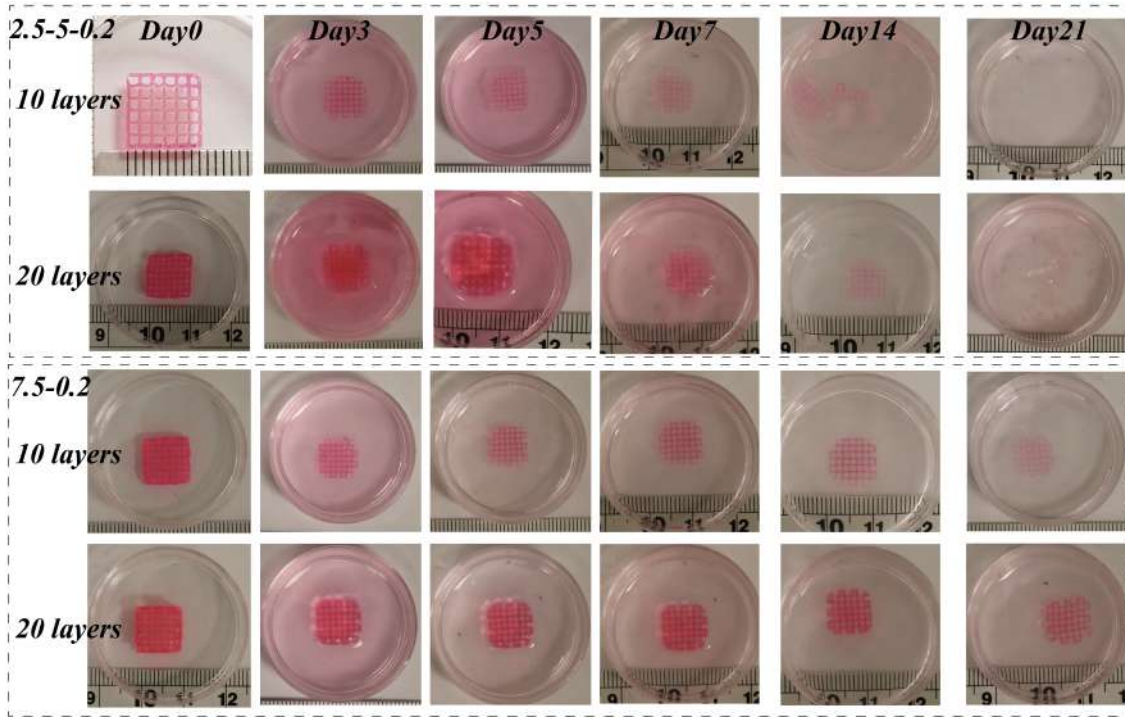


Figure 4.5: Structural integrity of printed constructs at varied time point in dPBS.

#### 4.3.4 Enzymatic degradation study

Controlling the degradation rate of the printed construct is crucial because the construct functions as a temporary supportive template that should degrade over time, ideally match the rate of tissue regeneration. Here, we investigated the degradation rate of GMGAGG hydrogel and GelMA-GG hydrogel with varied concentrations. It is reported that gellan gum and GelMA degrade quite slowly in PBS [323]. However, gellan gum and GelMA could be gradually degraded upon exposure to lysozyme and collagenase, respectively. To analyze the degradation rate of the GelMA-based bioink, the bio-ink samples were incubated in PBS solution with 0.02% collagenase. As Figure 4.6 depicted, pure GelMA (5%, 7.5%, 10%) all completely degraded within 2 days. This is in good agreement with the previous findings [324]. All the bio-inks experienced a sharp decrease in weight (less than 20% weight



remained) within the first 5 days. Generally, bio-inks with higher GelMA ratio exhibited a faster weight loss rate. Notably, with the same GelMA concentration, construct with smaller pore sizes (as shown in Chapter 3, Figure 3.10) exhibited a slower degradation rate. For instance, with fixed GelMA concentration at 7.5%, 7.5-0.5, which encompass denser network degraded slower than 7.5-0.1 and 7.5-0.2 GelMA-GG. From 10 days to 28 days, all the GelMA-GG bio-inks remained stable and no significant weight loss was observed. Notably, the remaining mass was in accordance with the gellan gum concentration. As demonstrated in the work by Xu et al. [323], gellan gum degraded to 20% of their initial weight after 16 days when immersed in PBS with 0.5 mg/mL lysozyme. As there was no lysozyme, gellan gum could barely be degraded. In comparison to GelMA-GG hydrogel, GMGAGG constructs fully degraded within 16 days. The release of gelatin resulted in looser network and obviously weaker mechanical property compared to GelMA-GG, and thus leading to significant faster degradation of the constructs. Taken together, the degradation of construct *in vivo* is highly concentration dependent and therefore could be well modulated to facilitate cell migration and ingrowth.

#### 4.3.5 Biocompatibility of GMGAGG

The C2C12 cells were printed using the 2.5-5-0.2% w/v GMGAGG bio-inks into 3D lattice structure. As revealed by the microscopic imaging, the majority of C2C12 were elongated on day 3. Live/dead staining on day 10 further confirmed the high cell viability and network formation within the printed constructs (Figure 4.7). In comparison to GelMA-GG printed constructs (5-0.5), in which cells started to elongate on day 7, GMGAGG exhibited superior biological property. This was due to the gelatin release

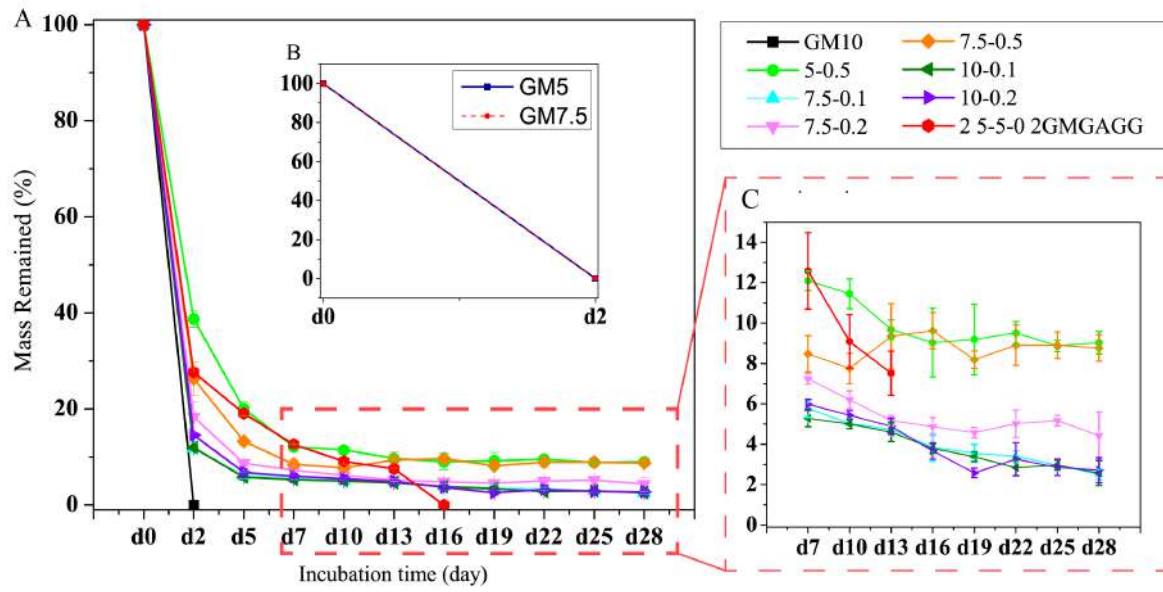


Figure 4.6: Degradation profile of composite bio-inks for 28 days. A. Degradation of GelMA 10%, GelMA-GG (5-0.5, 7.5-0.1/0.2/0.5 and 10-0.1/0.2) and GMAGAGG 2.5-5-0.2. B. Degradation of 5% and 7.5% GelMA. C. Zoom-in view of the degradation from day 7 to day 28.

during incubation which created more space for cell spreading, elongation and migration.

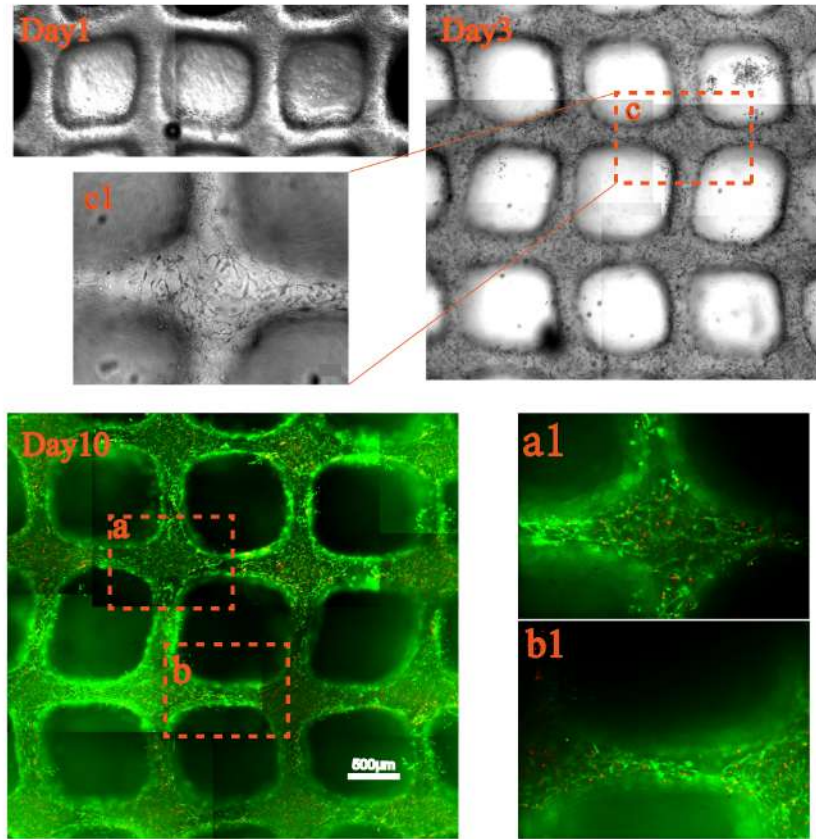


Figure 4.7: Biocompatibility of GMGAGG for 10-days culture.

#### 4.3.6 *In vitro* cell viability in printing syringe over time (before printing)

In conventional tissue engineering method, such as casting, cells are flooded with bulk of materials and biomolecules in a short period of time, while 3D bioprinting may require a longer processing time according to the thickness and complexity of the constructs. The rapid operation process reduces the risk of cell damage or death. By contrast, tedious bioprinting process poses great challenge to cells. Before printing, cell-laden bio-inks are loaded into a printing syringe and resting before printing. To examine how stable are the cells suspended in the bio-inks, cell survival rate over 150 min using C2C12

and HUVECs in GMGAGG hydrogel were investigated at room temperature (Figure 4.8a). GMGA was run as control group. The cell viability is calculated by dividing the number of viable cells by the number of total cells and multiplying by 100. The number of cells in the images were obtained by Image J software. The statistical analysis in Figure 4.8b revealed that for both cell types, the number of viable cells reduced with the increasing incubation time, yet at a different rate. Generally, both cells types maintained overall cell viability greater than 80% over a 150 min incubation (as shown in Figure 4.8b, red dash line). Significant difference in cell viability occurred after 90 min. Particularly, C2C12 exhibited higher cell survival rate (over 90%) than HUVECs in both GMGAGG and GMGA bio-inks, which was indicative of the C2C12's robustness in comparison with HUVECs.

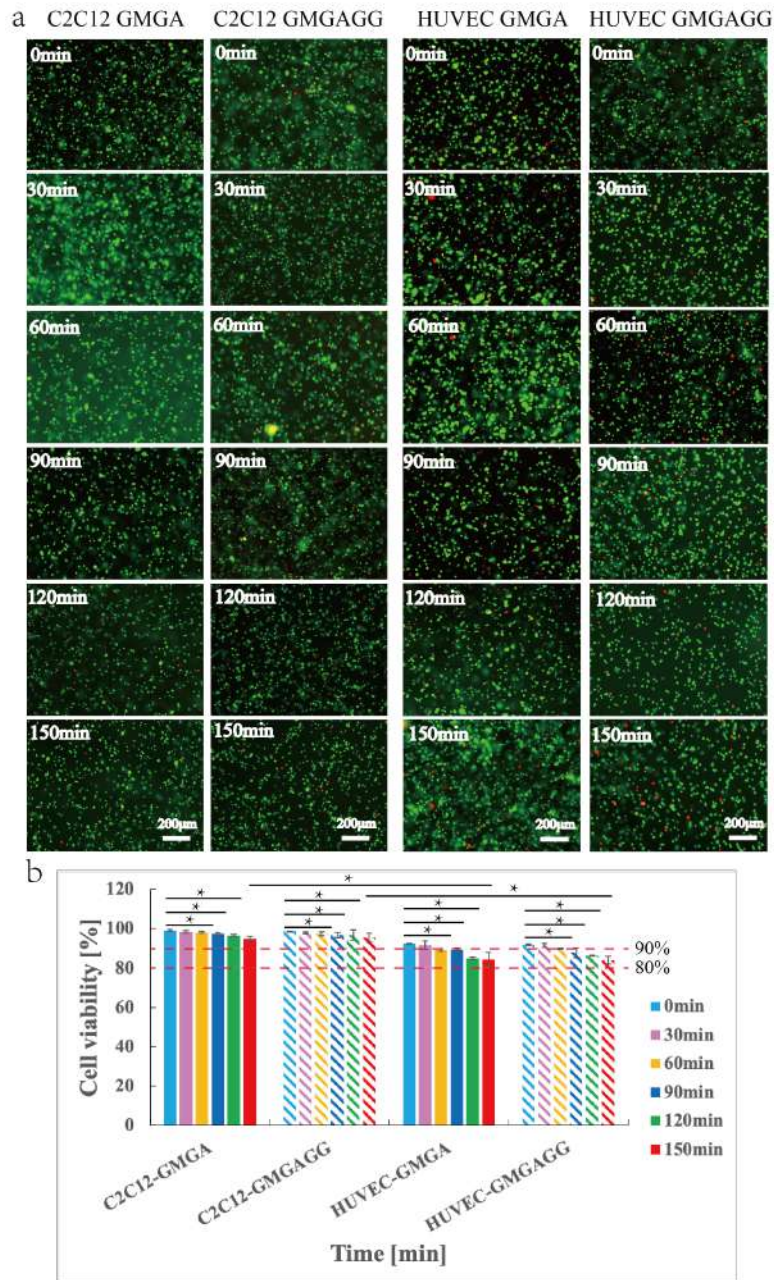


Figure 4.8: Cell viability of both C2C12 and HUVECs over 150 min (prior to printing).

#### 4.3.7 Evaluation of shear stress effects on cell viability over time (during printing)

It is reported that the major cause for cell damage and loss of overall viability is the shear forces present in the needle during printing. Here, with varied

incubation time, the coupling effect of incubation time and shear stress on cell survival rate was investigated.

The flow rate of GMGAGG 2.5-5-0.2 hydrogel in the printing nozzle 25G, 27G and 30G was obtained as shown in Table 4.1.

Table 4.1: Optimum printing pressures for hydrogels and computed flow rate of the GMGAGG bio-ink.

Parameters	25G	27G	30G
Pressure (Bar)	1.5	2.8	4
Flow rate (mm/s)	16.8	10.8	7.46

The power-law index and the shear rate was shown in Table 4.2.

Table 4.2: The power-law index (n), and the shear rate in 25G, 27G, 30G.

Parameters	25G	27G	30G
n	0.086	0.086	0.086
m	19.24	19.24	19.24
Shear rate (1/s)	947.23	755.03	682.85
Shear stress(Pa)	34.67	34.00	33.71

In comparison to non-printed cells at different time point (Figure 4.8), the number of viable cells of both C2C12 and HUVECs decreased after extruded from the printing nozzle, regardless of needle tip size. According to the results of each time point, increasing cell loss was observed along with the decreased nozzle diameter, especially after 60 min incubation. As recorded in Table 4.2, shear stress generated in the three different needles were similar. With incubation time shorted than 60 min, cells printed with three needles



yielded similar cell survival rate. While with time increased, cells in narrower needles (27G and 30G) induced greater cell damage in comparison to 25G (Figure 4.9b). Especially for HUVECs, which experienced significant drop in viable cell numbers after 90 min. Particularly, only 60% of HUVECs were found to be viable after printed with 30G needle. This highlights the coupling effect of time and shear stress on cell viability.

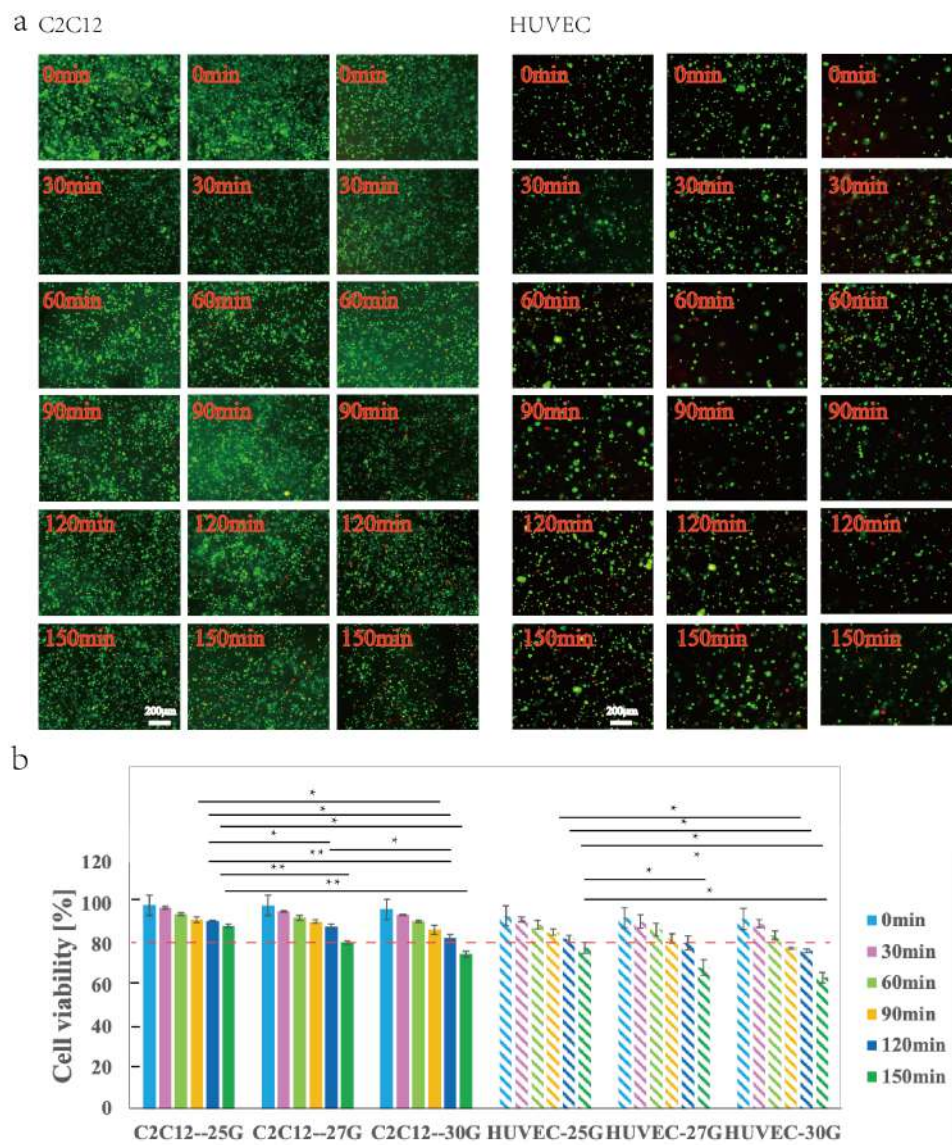


Figure 4.9: Cell viability of C2C12 and HUVECs printed with different needle sizes.

### 4.3.8 UV duration effects on cell survival rate (single layer)

As the layer-by-layer UAE bioprinting method utilizes UV source (365 nm wavelength, 500 mJ/cm<sup>2</sup>) to stabilize the printed constructs, the critical effects of UV on printing resolution and cell behaviors should be examined. Firstly, the UV radiation effect on single layer cell-laden GMGAGG using C2C12 and HUVECs (as shown in Figure 4.2c-c1) were investigated. Different UV exposure time was controlled by adjusting UV scanning speed. For each layer, UV scanning times were varied from 1 to 11 times. Control group that without UV crosslinking was printed along with the varied UV scanning times. The corresponding UV exposure time for each construct is shown in Table 4.3.

Table 4.3: The total UV exposure time for each configuration.

UV scanning speed (mm/min)	UV scanning time (s)					
	1 time	3 times	5 times	7 times	9 times	11 times
100	1.188	3.564	5.94	8.316	10.692	13.068
200	0.594	1.782	2.97	4.158	5.346	6.534
400	0.297	0.891	1.485	2.079	2.673	3.267
600	0.198	0.594	0.99	1.386	1.782	2.178
800	0.148	0.444	0.74	1.036	1.332	1.628
1000	0.118	0.354	0.59	0.826	1.062	1.298
ctrl	0	0	0	0	0	0

As shown in Figure A and Figure B (Appendix A and B), the filament width of single layer printed GMGAGG using C2C12 and HUVECs were not very consistent. This is owing to the weakened mechanical property in comparison to GelMA-GG. The rapid gelatin release may also compro-



maintain the structural integrity when immersed in live/dead staining solution. Moreover, the different cell density of C2C12 and HUVECs yielded varied viscosity of the final GMGAGG bio-ink. Lower viscosity was observed with more cells encapsulated. Filaments printed with HUVEC-laden GMGAGG bio-ink clearly showed a narrower average filament width.

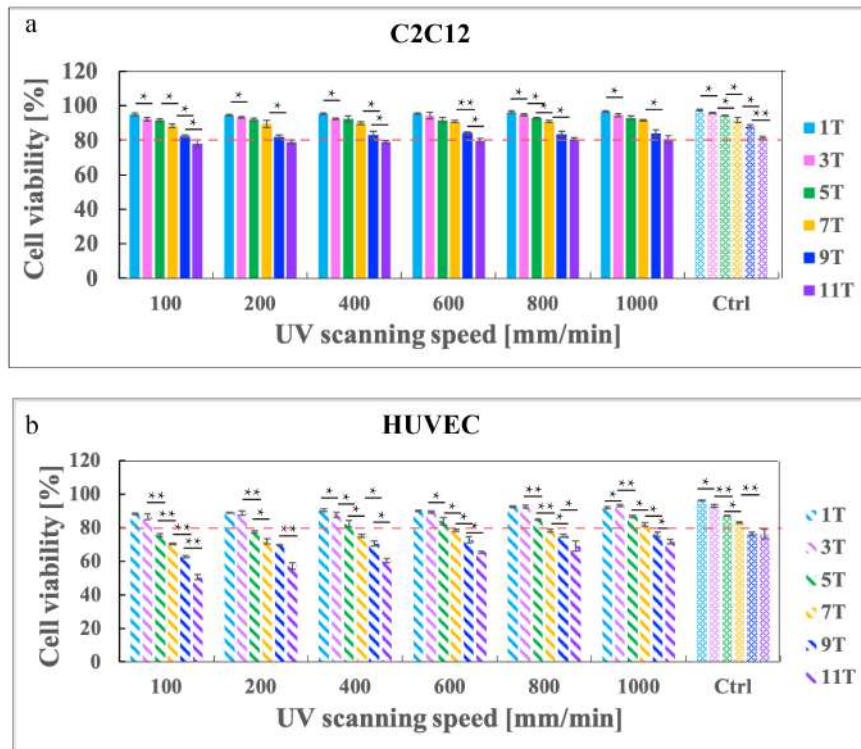


Figure 4.10: Cell survival rate with varied UV scanning times and UV scanning speed.

With regard to cell viability, the control group without UV crosslinking confirmed the cell damage induced either by prolonged incubation time or shear stress (Figure 4.10). Cell viability displayed a UV duration-dependent tendency. With the same scanning speed, increasing UV time led to increased cell death. With the fixed scanning times (1, 3, 5, 7, 9, 11), varied scanning speed has shown minor effects on cells, especially C2C12 cells. Notably, given a similar exposure time, cell under 1 time 200 mm/min scanning

exhibited higher viability than three times 1000 mm/min scanning. With increased UV exposure times, HUVECs underwent dramatic cell damage after 5 times scanning (Figure 4.10b), regardless of scanning speed. With 11 times UV exposure, HUVECs was observed with a viability of 50.6%. This revealed that HUVECs were highly susceptible to UV crosslinking.

#### **4.3.9 UV duration effects on cell survival rate (multiple layer)**

In terms of building thick constructs, materials are deposited layer-by-layer. It is critical to ensure a suitable UV radiation duration that not only achieves adequate crosslinking but also high cell viability. Motivated by this, multilayer constructs (1, 3, 5, 7, 9, 11 layers) with C2C12 and HUVECs were prepared (Appendix C and D: Figure C and D ). To investigate the influence of different materials, GelMA-GG with C2C12 cells were also printed as control group (Figure 4.11c). In this session, the influence of UV on cell viability was characterized instantly post-printing by evaluating the cells at the bottom-most layer of the constructs using live/dead staining kit. The cells at the bottom-most layer would be those that had been subjected to the longest UV exposure and most prone to cell death caused by UV exposure, if any. The results in Figure 4.11a demonstrated that for 1-layer, 3-layer, 5-layer and 7-layer constructs, cell viability of C2C12 in GMGAGG maintained above 90%. Starting from layer 9, cell viability showed a slightly drop but still remained above 80% (dash line in Figure 4.11a). While with regard to HUVECs, they were more sensitive and fragile than C2C12, which is consistent with the above findings. 1-7 layer constructs encompass cell viability over 80%, while viable cell number dropped slightly from 9-layer onwards (Figure 4.11b). Nevertheless, in comparison to single layer print-

ing with same UV exposure time, cells in multi-layer constructs displayed a higher cell viability and better stability. Similar trends has been observed in C2C12-laden GelMA-GG ( cell viability over 85%)(Figure 4.11c). Taken together, as the damages on cells s depending on the UV effective dose received by the cells, the results suggested the shield effect of materials and that varied scanning times and UV per se has significant effect on single layer printing with cells, while less significant effect on multiple layer constructs with the same exposure time.

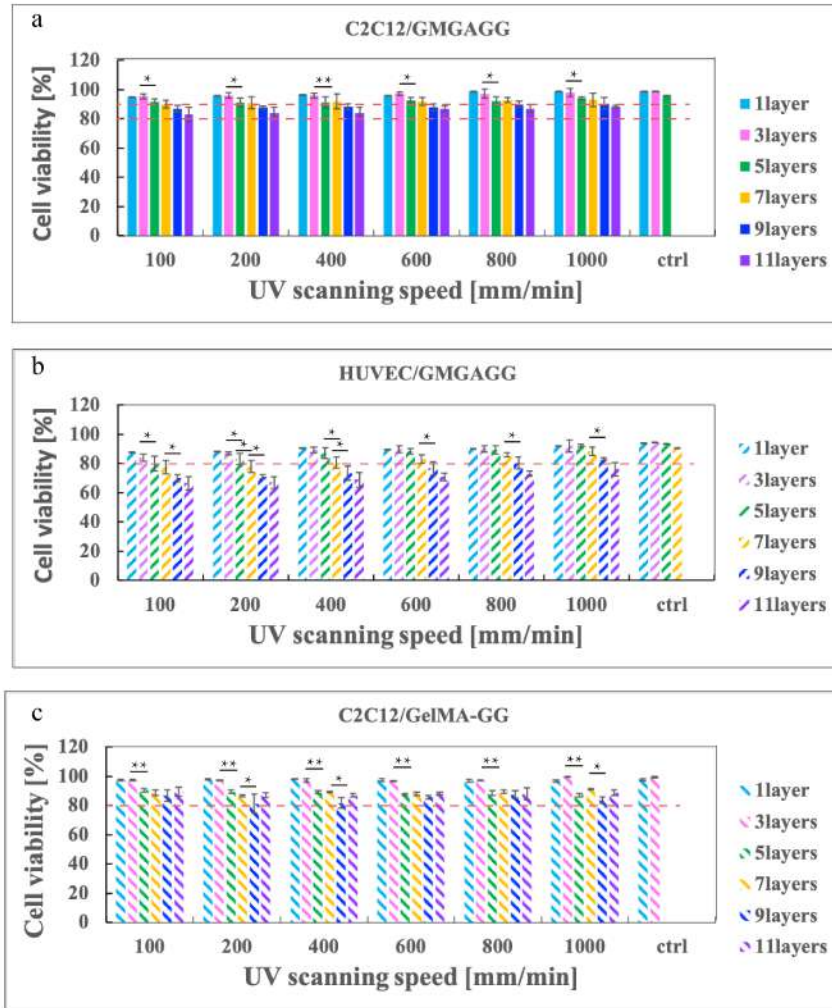


Figure 4.11: Analysis of cell viability in multi-layer printed GMGAGG constructs. a.C2C12 viability in the bottom-most layer of printed GMGAGG constructs. b.HUVECs viability in the bottom-most layer of printed GMGAGG constructs. c.C2C12 viability in the bottom-most layer of printed GelMA-GG constructs.

In addition to cell viability, printing resolution was monitored by measuring the width of the printed ring pattern (1, 3, 5, 7, 9 and 11 layers) with thinner filaments indicating higher printing resolution. As shown in Figure 4.12a, in printed C2C12 with GMGAGG, a slower UV scanning speed led to a higher printing resolution. As the number of printing layers increased, the effect of UV scanning speed on the filament width seem to diminish. It

can be seen that the increase in filament width with increasing UV scanning speed to be at the most prominent when printing 1 and 3 layers. The results indicated that under a fixed printing speed and printing pressure, a slower UV scanning speed led to a longer UV crosslinking duration which resulted in higher degree of UV crosslinking and consequently reduced bio-ink spreading when subsequent layers were printed directly over it. Hence, filament width in each layer tends to be more stable and consequently improving the overall printing resolution and structural fidelity. Structural collapse occurred in control group after deposition of 7 layers due to insufficient self-support capability without UV crosslinking. The control group using GelMA-GG has also exhibited similar trends (Figure 4.12c). While with lower viscosity, GelMA-GG allowed only 5 layers' stacking in the absence of UV radiation. However, significant difference in printing resolution was identified in HUVECs/GMGAGG (Figure 4.12b). The filament width of C2C12/GMGAGG ranged from 400  $\mu\text{m}$  to 1000  $\mu\text{m}$ , while that of HUVECs/GMGAGG ranged from 400  $\mu\text{m}$  to 600  $\mu\text{m}$ . The filament width was relatively consistent, regardless of printing layers. One of the possible reasons might be due to the difference in cell density. As demonstrated by Diamantides et al. [325], rheological property of the bio-ink is affected by cell seeding density. Higher cell seeding density resulted to lower viscosity bio-ink. Therefore, GMGAGG with HUVECs was stiffer than C2C12-laden GMGAGG. Further, for bio-inks with higher viscosities, the deposited bio-inks tend to be more stable and the UV irradiation effect is not less obvious than that in low viscous bio-inks on printing resolution.

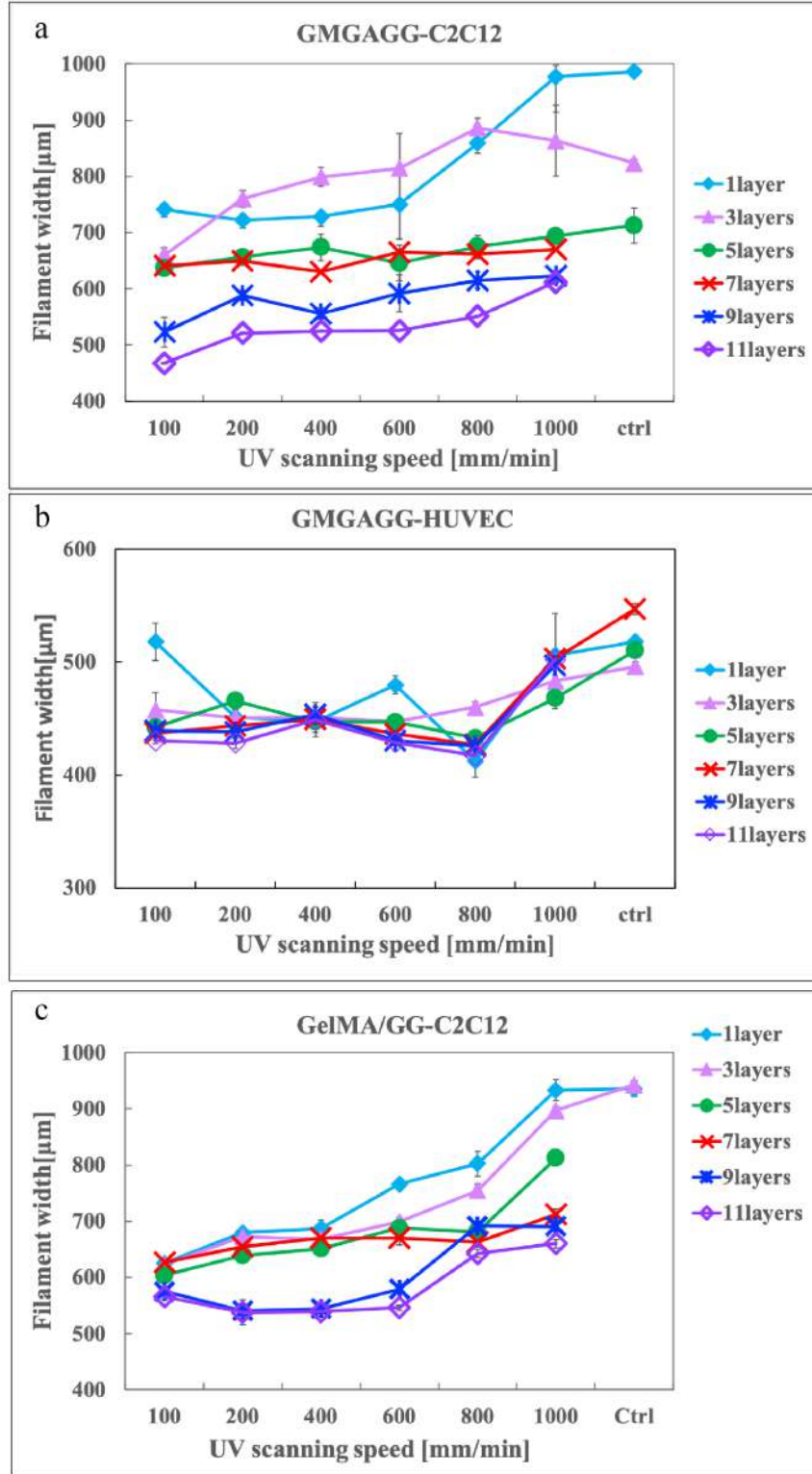


Figure 4.12: Filament width of printed constructs. a. Filament width of printed C2C12/GMGAGG. b. Filament width of printed HUVECs/GMGAGG. c. Filament width of printed C2C12/GelMA-GG.

## 4.4 Summary

In this Chapter, a suitable bio-ink was formulated by introducing gelatin into GelMA-GG composite hydrogel. Material characterizations including rheological property, gelatin release, structural integrity, degradation and biocompatibility have been conducted and compared with GelMA-GG bio-ink. The addition of gelatin endowed the bio-ink with a dynamic mechanical property. The bio-ink was found to be initially bioprintable and cell-permissive during incubation. In addition, cell viability, as a fundamental indicator, over the entire bioprinting process was analyzed. The bioprinting process could be categorized into three different stages: a. Before printing, cells were resting in printing syringe; b. During printing, cells were passing the printing needle tip; c. Crosslinking. Both C2C12 and HUVECs were examined in the three stages. Specifically, cell damage and loss were observed throughout all these three stages. Long incubation time in the printing syringe could damage the cells before printing. However, in comparison to the other two stages, the damage was minor and only applicable to those thick and complex structures. Furthermore, the shear stress in printing needle has been calculated and the coupling effects of incubation time and shear stress were investigated. A narrower needle tip exerts higher shear force on the cells, which is detrimental and should be minimized. The balance between needle diameter and cell viability could be adjusted via several parameters including pressure and printing speed. Lastly, the influence of UV duration on cell viability in terms of single layer printing and multi-layer printing was analyzed. In single layer printing, cell viability was found to be UV duration-dependent. HUVECs were more sensitive than C2C12. In addition to single layer printing, cell survival rate in the bottom-most layer of multilayer con-

structs has also been investigated. In comparison to single layer printing, cells exhibited higher viability in multi-layer printing, suggesting the shield effects of materials in multi-layer printing.



# Chapter5

## 3D Bioprinted Constructs with Highly Efficient Capillary Force Assisted Cell seeding

### 5.1 Introduction

Skeletal muscle injuries have been estimated to affect millions of people in United States. Although skeletal muscle has endogeneous self-regeneration capability for minor injuries, massive muscle damage cannot be regenerated spontaneously and usually requires surgical interventions. Autologous muscle transfer is considered to be the gold standard. The healthy tissue in vicinity with the dense vascular network and nerve-muscle junction will facilitate the muscle regeneration [6]. Yet the tissue availability, donor site morbidity and insufficient innervation still remain to be challenging. The advances in biological science have achieved some progress in restoring the muscle function through cell transplantation [7, 8, 9, 10]. However, the low expansion capacity, low cell viability potentially caused by poor localization or immune rejection and limited integration with host tissues await to be addressed.

Tissue engineering has evolved tremendously over the decades. By incorporating biomaterials, cells and functional molecules, tissue engineering strategies have been attempting to piece together instructive elements to build artificial tissue models, and therefore, achieve functional recovery. As reviewed in Chapter 2, a plethora of bioengineering methods including geometrical constraints, electrospun fibers, electrical and mechanical stimulations have been implemented to constructs *in vitro* muscle tissue models, in both 2D and 3D. In the the current research of tissue engineering of organized and aligned cells constructs, majority of the work is limited to micron scale or with relatively thin layer, which is inadequate for volumetric muscle

loss (VML).

3D bioprinting is driving the major innovations in many fields as it enables the fabrication of tissue constructs with diverse cell types, multiple materials, heterogeneous properties and relatively large and thick constructs. 3D bioprinting provides superior structural feasibility, yet the printing process can be tedious for large and complex constructs. Cells exposed to the prolonged printing process could be damaged, especially for some sensitive cells.

Capillary action is a ubiquitous phenomenon and can be found in many applications, such as wound care and absorbent textiles [326, 327, 328]. It is advantageous that capillary action could distribute the liquid within sufficient small spaces in a highly efficient manner in the absence of external pressure.

A variety of cell sources has been investigated for their myogenic potential, such as immortal cell lines C2C12 and L6, ESCs, iPSCs, and MSCs. Among them, the immortalized C2C12 myoblast cell line is widely studied [41, 67, 76, 79], and has been frequently used by many researchers to engineer 2D myotube constructs. The C2C12 cell line differentiates rapidly, forming contractile myotubes and producing characteristic muscle proteins.

Additionally, skeletal muscle tissue consists a bunch of cells. Each cell plays their specific role to support the entire tissue working in a well-organized manner. As skeletal muscle demands high oxygen, vascularization is essential and should be considered to for capillary network formation. In order to study the cell-cell interactions, endothelial cell is co-cultured with myoblasts. In this study, human umbilical vein endothelial cells (HUVECs) are utilized as they are readily available, easy to manipulate, highly proliferative, and possible to migrate and integrate with new tissues [329].

Herein, with 3D bioprinting technology and capillary action, we are able to fabricate large 3D bioprinted muscle constructs with unidirectional channels and high cell density fast and efficiently. In this research, C2C12 and human umbilical vein endothelial cells (HUVECs) were co-cultured. Parametric study including the effects of line spacing of the constructs and seeding density on cell orientation was examined. The optimal co-culture medium to support both cell types were formulated. The immunofluorescence analysis of printed constructs was performed to confirm the feasibility of applying bioprinting-based strategy and capillary action to fabricate 3D skeletal muscle constructs.

## 5.2 Material and method

### 5.2.1 Bio-ink preparation

GelMA was prepared by reacting 10% (w/v) gelatin (Sigma Aldrich, type A from porcine skin, 300g Bloom, Singapore) with methacrylic anhydride (Sigma Aldrich) at 50°C based on well-established protocol [312]. The solution was dialyzed in 12-14kDa dialysis tubing (Sigma Aldrich) against distilled water at 40 °C for 1 week, followed by 1-week lyophilization. It was then stored at -30°C for future use. Irgacure 2959 (Sigma Aldrich) was dissolved in 10% PBS (v/v) at 70 °C to achieve the final concentration 0.1% (w/v) as described before [310]. 6% sucrose (Sigma Aldrich) was added to generate an isotonic solution. GelMA was added into the PBS-based reagent at room temperature to achieve the concentrations at 7.5% (w/v). Gelatin and gellan gum solution were prepared by dissolving gelatin and gellan gum (Sigma Aldrich, Gelzan<sup>TM</sup> CM, Gelrite) powder in the PBS-based solution to a concentration of 15% and 0.6%(w/v) respectively. The GelMA-gelatin-

gellan gum composite bio-inks were generated by mixing GelMA, gelatin and gellan gum solution at 45°C in 1:1:1 ratio for 1h to achieve homogeneous GelMA-based composite bio-inks. 5% GelMA was prepared by dissolving GelMA foam in DMEM. 7% gelatin solution was prepared as sacrificial materials to create hollow channels for nutrient and oxygen supply in the constructs.

### 5.2.2 Printing process (Prior to cell seeding)

All the constructs were printed with Regenhu (Villaz-St-Pierre, Switzerland) bioprinting system. The printer is equipped with a built-in UV lamp (500 mW, 365 nm wavelength) to crosslink the photocurable materials. GM-GAGG and gelatin bioink were loaded into sterile plastic syringes and then inserted to extrusion-based cartridges. Printing schematic was shown in Figure 5.1. The constructs ( $L \times W \times H = 9 \text{ mm} \times 9 \text{ mm} \times 7 \text{ mm}$ ) with different line spacing (1.5 mm, 1.2 mm, 1.0 mm) were then kept dry in petri dish. Upon finishing the constructs, gelatin was extruded with another printhead to fill some of the hollow channels.

### 5.2.3 Capillary action assisted cell seeding

To evaluate the feasibility of capillary seeding of soft materials, scaffolds with varied line spacing (1.5 mm, 1.2 mm, 1.0 mm) were investigated using cell-laden GelMA solution. C2C12 cells suspended 5% GelMA solution was pipetted onto hydrophobic petri dish. The printed constructs were immediately placed on the top of the cell-laden GelMA solution. . It was observed that the cell-laden GelMA solution started to fill the hollow channels of the constructs through capillary force. The liquid suction process was visualized by food dye.

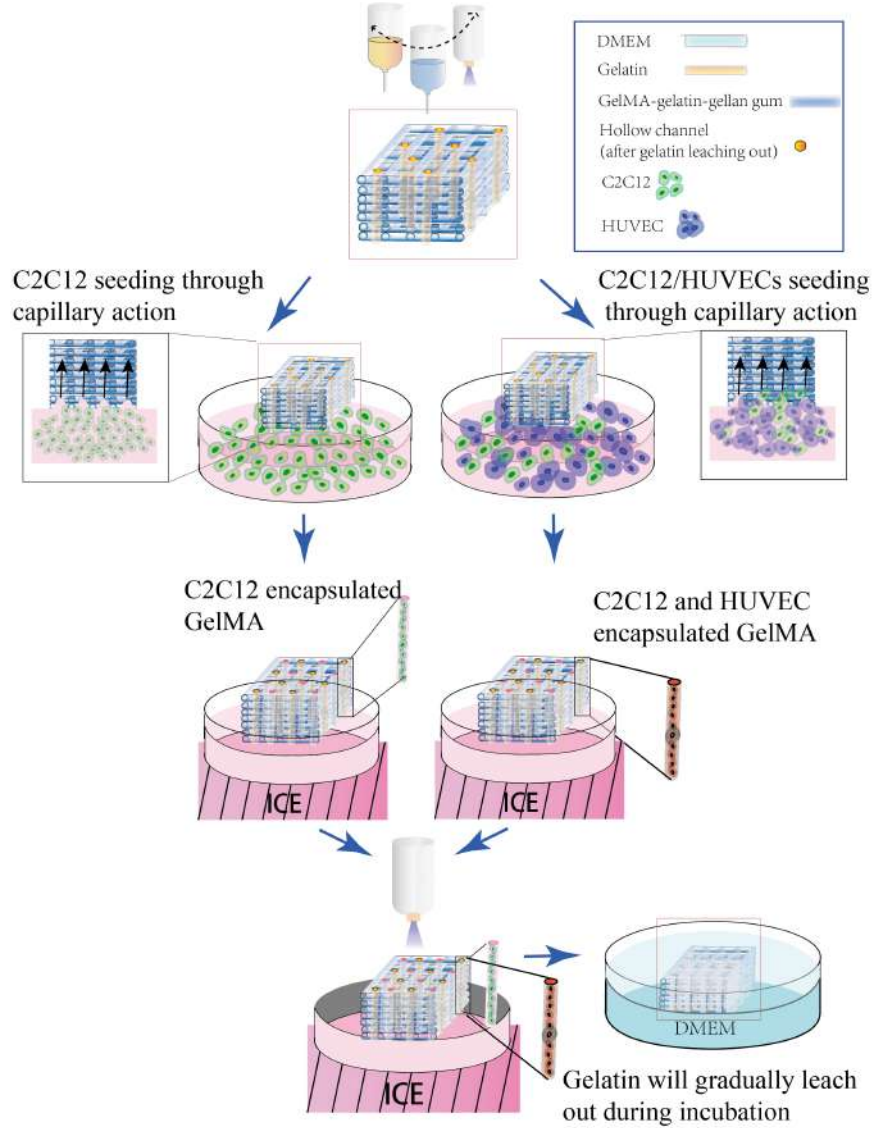


Figure 5.1: Schematic of capillary force assisted cell seeding in 3D printed constructs.

To examine the influence of cell seeding density on cell orientation,  $5 \times 10^6$ ,  $10 \times 10^6$ ,  $20 \times 10^6$  and  $50 \times 10^6$  cells/ml were prepared and scaffold with 1.2mm line spacing was utilized for capillary seeding. The seeding process was repeated and visualized by phenol red. The constructs were instantly transferred to a cold petri dish on ice to stabilize the GelMA solution for 5 min. The constructs were subsequently exposed to UV lamp to achieve

complete gelation of GelMA hydrogel. Thereafter, the constructs were incubated at 37 °C without medium for 20 min to stabilize the cells within hollow channels. Growth medium was added 20 min later. The constructs were maintained in growth medium for 5 days and differentiated for 10 days.

For co-culture constructs, HUVECs and C2C12 were mixed in a ratio of 3:7 to achieve of final seeding density of  $20 \times 10^6$  cells/ml. The cells were seeded into the hollow channels of the constructs by capillary force in the same way.

#### **5.2.4 Cell culture and differentiation**

Murine C2C12 myoblasts (American Type Culture Collection) were maintained at below 70% confluence in growth medium containing DMEM, 10% fetal bovine serum (Gibco, Carlsbad, CA) and 1% penicillin–streptomycin (Gibco). After 7 days culture, growth medium was replaced with differentiation medium, which consists of 2% FBS, 1% penicillin–streptomycin (Gibco) and DMEM. Human umbilical vein endothelial cells (HUVECs) were cultured with EndoGRO-LS Complete Culture Media kit (Sigma-Aldrich). Cells were trypsinized upon 70% confluency and replated. Culture medium was changed every 2-3 days.

#### **5.2.5 Co-culture medium optimization**

One of the critical challenges in co-culture is the lack of compatible medium for all the cell types. The co-culture medium is supposed to support the growth of both cell types for long term culture. The optimization of co-culture medium was performed by culturing C2C12 and HUVECs individually in different mixture of culture medium (SkGM (skeletal muscle growth medium), EndoGRO). Different culture medium with varied ratio (skGM:

EndoGRO) of 1:0, 2:1, 1:1, 1:2 and 0:1 were formulated. Both cells were cultured for 4 days and cell proliferation rate was analyzed as a fundamental indicator.

### **5.2.6 Optimization of co-culture ratio**

To determine the cell seeding density, C2C12 and HUVECs with varied ratio of 5:5 and 7:3 were co-cultured for 7 days with optimized co-culture medium. The initial seeding density included  $1 \times 10^6$  and  $2 \times 10^6$  cells per 24 well. Cell growth and proliferation rate were analyzed.

### **5.2.7 Immunostaining**

Constructs with C2C12 and C2C12/HUVECs were fixed with 4% (v/v) paraformaldehyde for 40 min at room temperature, rinsed 3 times in PBS, then permeabilized with 0.1% (v/v) Triton X-100 for 30 min at room temperature. Afterwards, the samples were thoroughly rinsed 3 times. 3% bovine serum albumin in PBS was used as blocking buffer. The constructs were then incubated at room temperature for 1 hour. The samples were washed thrice after the removal of blocking buffer. C2C12 samples were incubated with mouse anti-MF-20 antibody (MF20;  $1 \mu\text{g/ml}$ ; Developmental Studies Hybridoma Bank, Iowa City, IA) at  $4^\circ\text{C}$  overnight and washed with PBS. The samples were then incubated with fluorescein isothiocyanate-conjugated anti-mouse antibody (1:100 in dPBS, Sigma-Aldrich) for 1 hour at room temperature. Thereafter, Actingreen<sup>TM</sup> 488 ReadyProbe and NucBlue<sup>TM</sup> in PBS were added to each sample and incubated for 30 min away from light to stain F-actin and nuclear. C2C12/HUVEC constructs were incubated with MF20 and rabbit Anti-CD31 antibody (Abcam, ab28364). The constructs were then incubated with secondary antibodies, fluorescein isothiocyanate-

conjugated anti-mouse antibody (1:100 in dPBS, Sigma-Aldrich) and Alexa 647-conjugated anti-rabbit IgG (Abcam, 1:200 in dPBS). The staining solution were then removed and washed with PBS three times. The images were analyzed using NIH Image J software. The cells that were aligned within  $\pm 10^\circ$  of the construct direction were defined as aligned cells.

### 5.2.8 Statistical analysis

All results were expressed as (mean value  $\pm$  standard deviation (SD)). The results were evaluated by one-way ANOVA analysis coupled with the Tukey test. Differences were considered statistically significant when  $p \leq 0.05$  and greatly significant when  $p \leq 0.001$ .

## 5.3 Results

### 5.3.1 Printed constructs

The schematic of constructing skeletal muscle tissue models was illustrated in Figure 5.1. Briefly, the engineered constructs with unidirectional channels was designed and printed using layer-by-layer UV assisted bioprinting, followed by capillary-assisted cell seeding. The constructs were composed of GMGAGG scaffold, gelatin as a sacrificial material and the hollow channels for capillary seeding. GMGAGG scaffolds with varied line spacing were displayed in Figure 5.2a. The average line spacing of each scaffold was measured to be  $1035.45 \pm 54.53 \mu\text{m}$ ,  $794.73 \pm 45.28 \mu\text{m}$  and  $673.11 \pm 33.96 \mu\text{m}$ , respectively. To ensure cell viability in the constructs, we employed gelatin as sacrificial material in the printing to create hollow channels during incubation. As illustrated in Figure 5.2c, 2 selected channels were filled with gelatin solution to show the feasibility of the method. Food dye was utilized,



for the ease of visualization. Figure 5.2d showed the complete construct with gelatin in the channels and Figure 5.2e is the top view. The remaining hollow channels were used for capillary seeding. As shown in Figure 5.3, GMGAGG scaffold with line spacing 1.2 mm was investigated for capillary seeding. The 5% GelMA solution filled up the hollow channels within 25s.

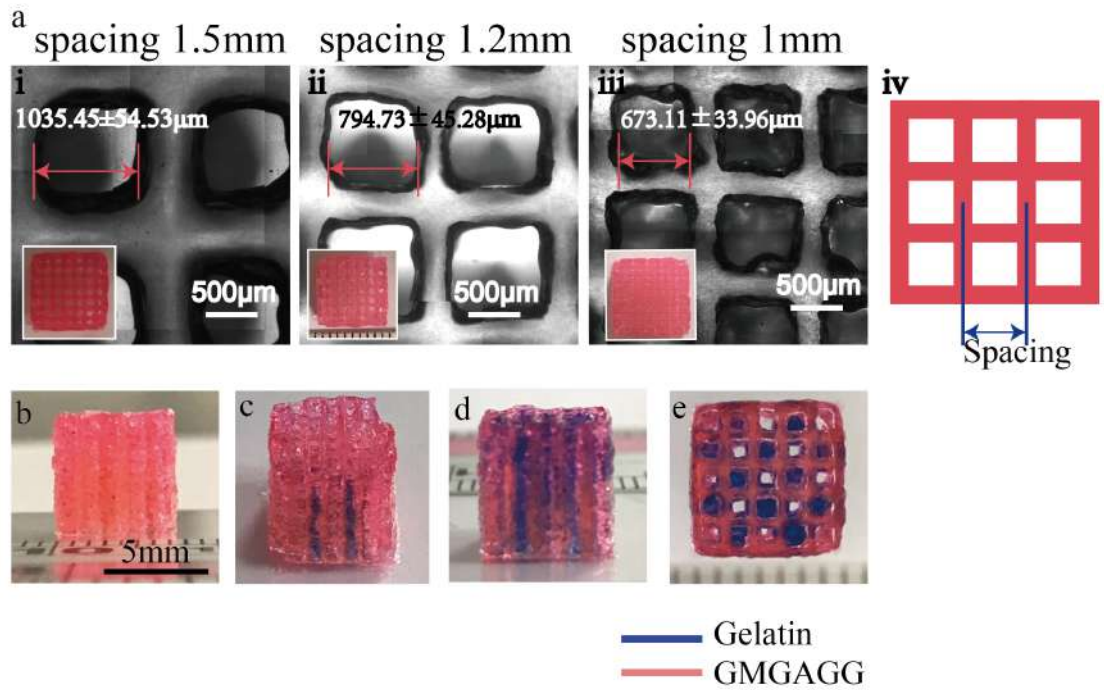


Figure 5.2: Printed of GMGAGG constructs. a. Printed scaffolds with varied line spacing (1.5 mm, 1.2 mm and 1.0 mm). b. The side view of the printed construct. c. Two channels of the printed constructs filled with gelatin solution. d. The printed construct filled with gelatin solution for capillary seeding. e. The top view of the constructs

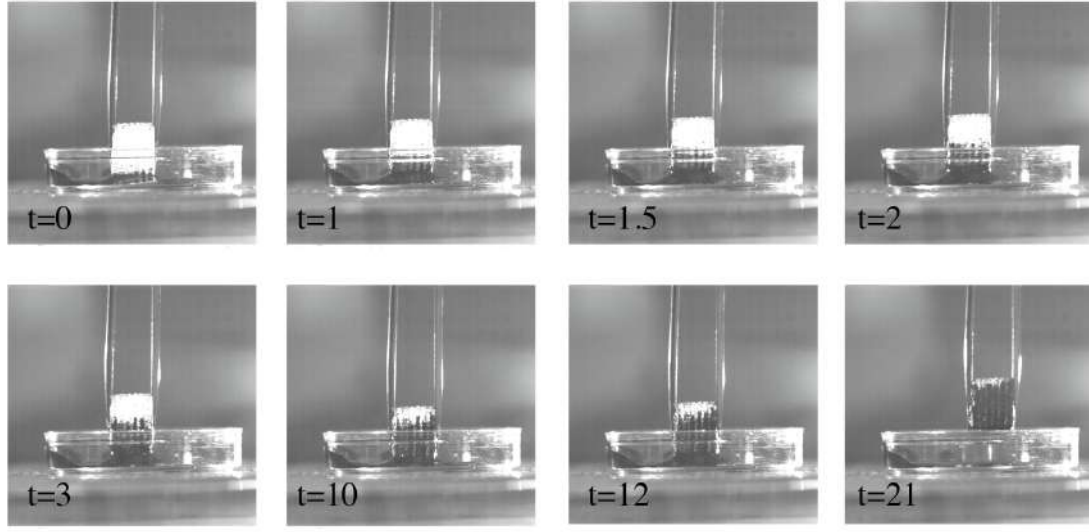


Figure 5.3: Capillary action assisted cell seeding in 3D printed GMGAGG constructs.

### 5.3.2 Evaluation of varied line spacing effect on cell orientation

The coupling effects of geometrical confinement and capillary force-assisted seeding on cell orientation were investigated by adjusting the line spacing of the 3D printed constructs. The constructs with three different line spacings (1.5 mm, 1.2 mm, 1.0 mm) were prepared. They were cultured in growth medium for 5 days and followed by 10-day differentiation. As demonstrated by immunostaining in Figure 5.4, the control group, where cell-laden GelMA was casted onto petri dish, the cells exhibited random orientation. Whereas, the cells within the constructs exhibited various degrees of alignment with the decreased line spacing inducing better alignment of cells. Particularly, line spacing at 1.5 mm showed the lowest degree of cell alignment ( $39.3\% \pm 4.6\%$ ), while line spacing at 1.2 mm and 1.0 mm had similar and relatively high cell alignment at about 70%.

### 5.3.3 Effect of cell density on cell orientation

To determine the optimal cell seeding density, four different cell densities were investigated using constructs with line spacing at 1.2 mm. Cell orientation was examined after 10-day differentiation. As depicted by DAPI and F-actin staining, seeding density at  $5 \times 10^6$  yielded random cell organization (Figure 5.5). Cell alignment was observed with seeding density over  $10 \times 10^6$  cells/ml. Notably,  $10 \times 10^6$  cells/ml seeding density showed 58% cell orientation, and  $20 \times 10^6$  cells/ml has exhibited a better cell alignment of 66%. Strikingly, with  $50 \times 10^6$  cells/ml, GelMA within the constructs was observed with significant cell mediated gel compaction. As shown in Figure 5.5, in comparison to constructs with other densities, apparent thinning gel with  $50 \times 10^6$  cells/ml were observed. The cell-laden gel width was reduced from 600-700  $\mu\text{m}$  to an average width about 50-60  $\mu\text{m}$ . Taken together, constructs with 1.2 mm line spacing and  $20 \times 10^6$  cells/ml were selected for

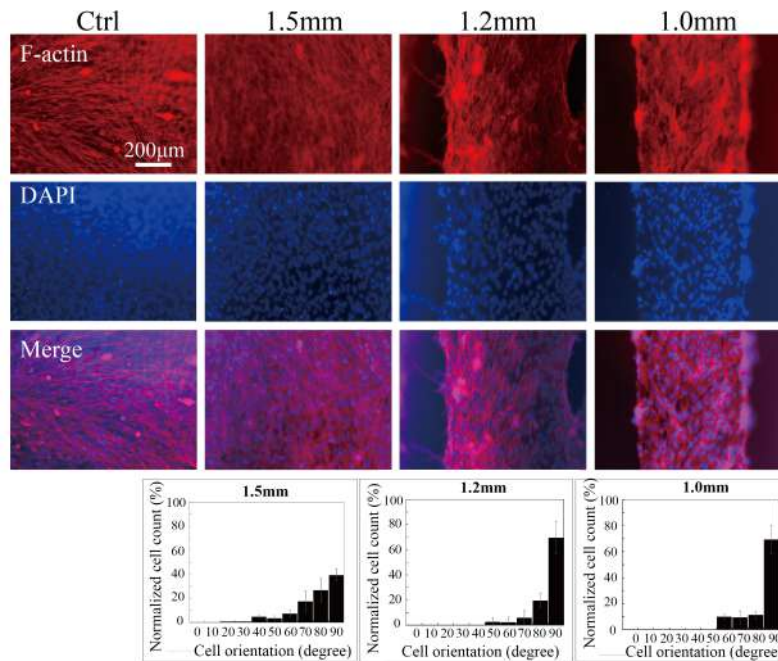


Figure 5.4: The influence of line spacing on cell orientation.

the following studies.

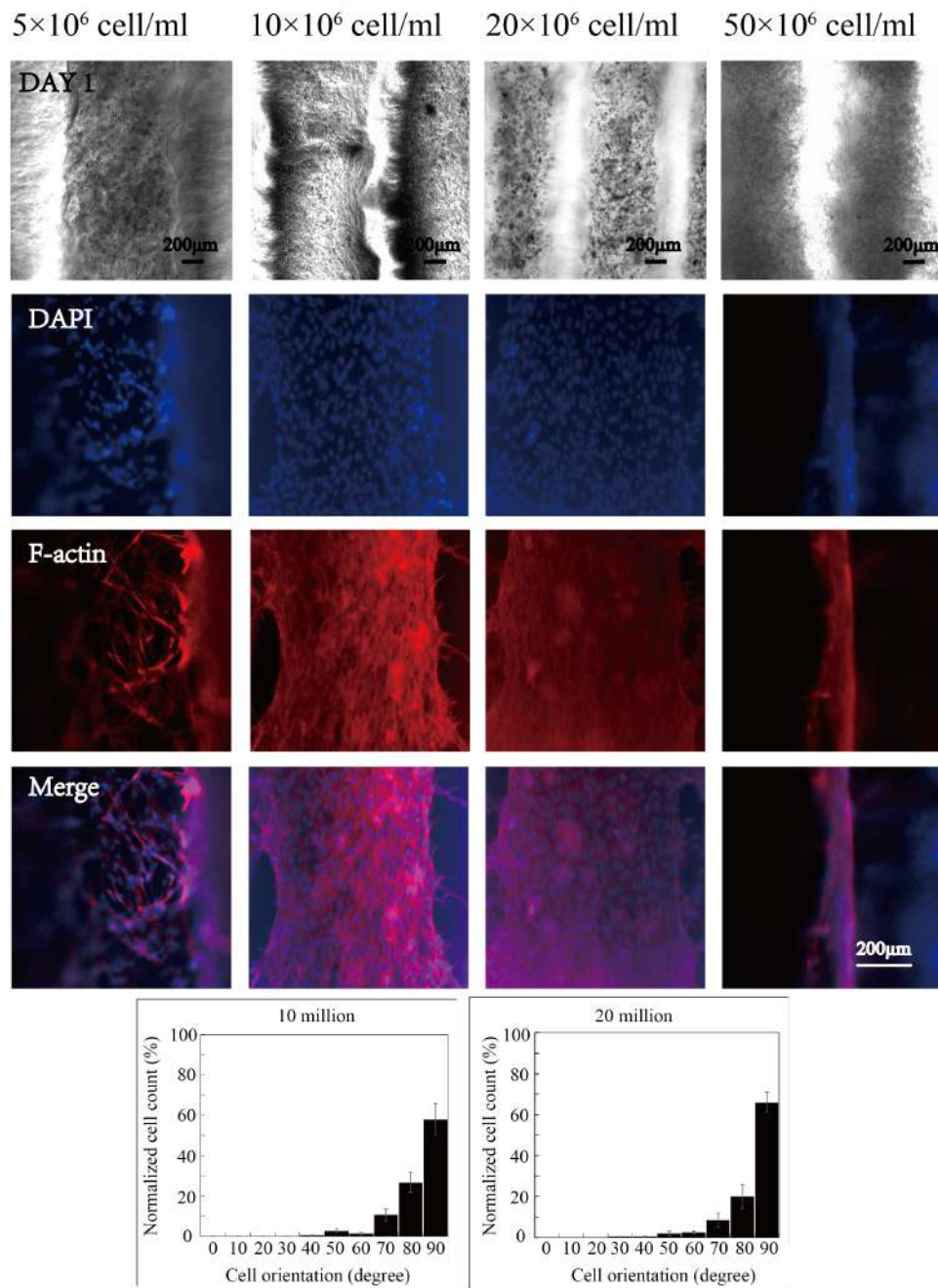


Figure 5.5: The influence of cell seeding density on cell orientation.

### 5.3.4 Formulation of co-culture medium

As shown in Figure 5.6, C2C12 was relatively robust and able to grow and proliferate in EndoGRO medium but in a slower rate in comparison to other medium with skGM. The proliferation results of C2C12 in Figure 5.7 demonstrated that the growth rate of C2C12 decreased with the increased ratio of EndoGRO. However, the results revealed that HUVECs were highly sensitive to medium change. HUVECs could hardly survive for 4 days when the medium has a ratio of EndoGRO lower than 50% (Figure 5.8). The growth rate of HUVECs increased with the increasing EndoGRO ratio. Taken together, EndoGRO allowed the growth of C2C12, while skGM was unable to support HUVECs. To ensure the growth, proliferation and achieve proper cell morphology of both cell types, skGM : EndoGRO= 1:2 was selected for co-culture study.

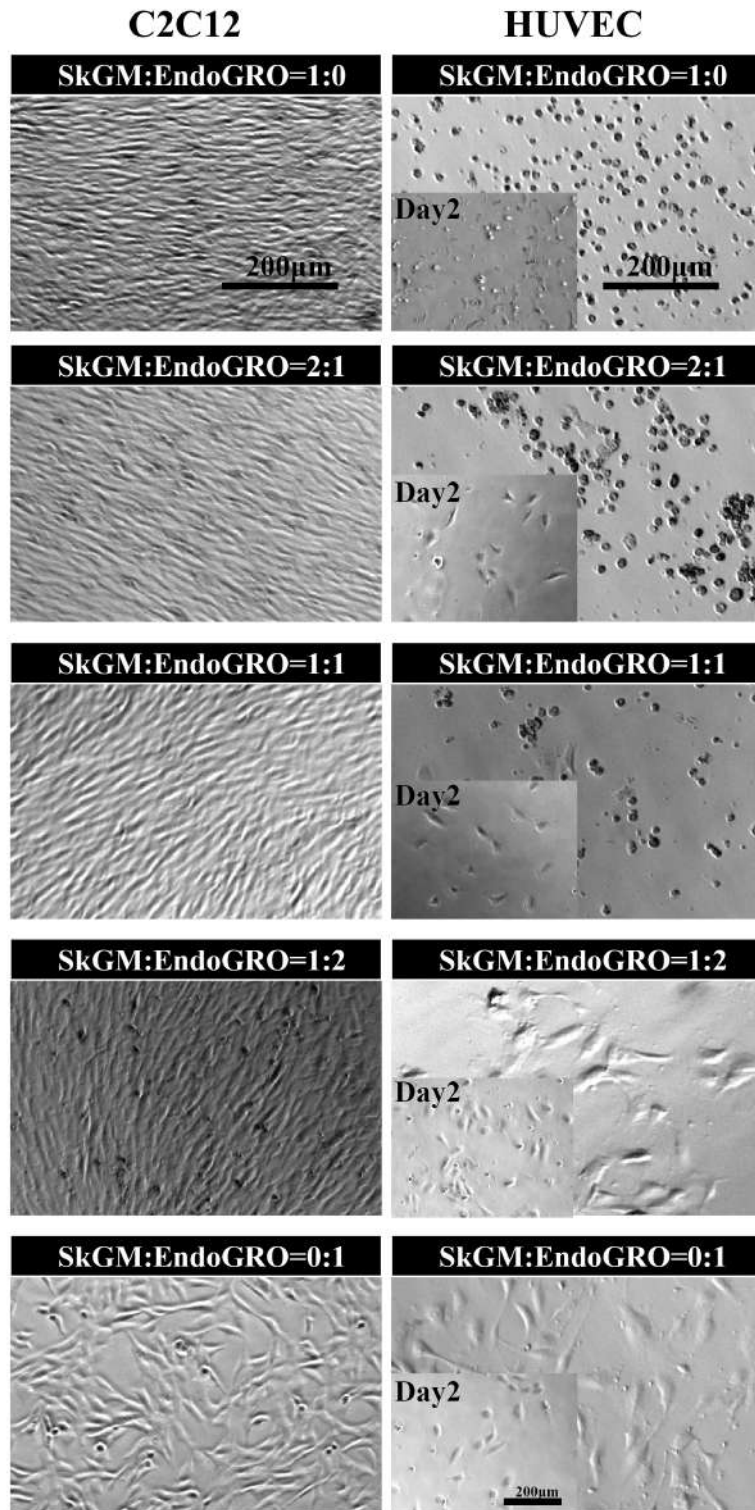


Figure 5.6: Morphology of C2C12 and HUVECs in co-cultured medium with varied combination.

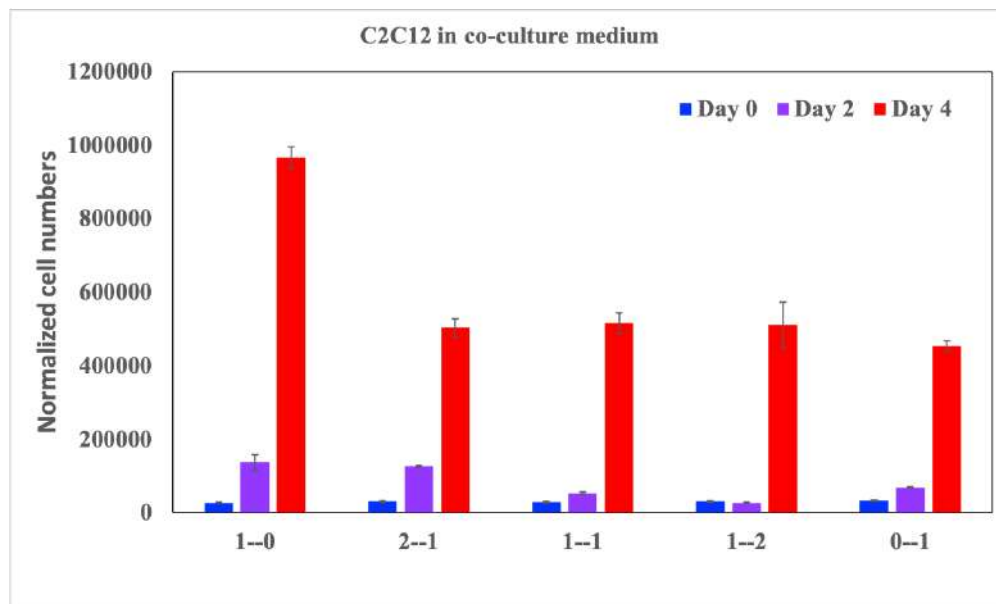


Figure 5.7: Proliferation study of C2C12 in co-culture medium with varied combination over 4 days.

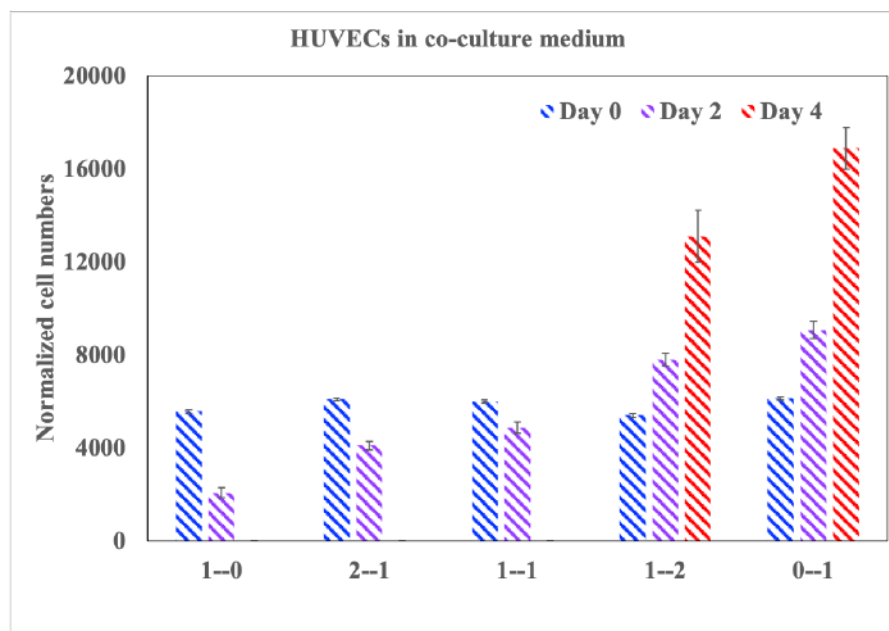


Figure 5.8: Proliferation study of HUVECs in co-culture medium with varied combination over 4 days.



### 5.3.5 Evaluation of ratio of co-cultured cells

To determine the optimal cell seeding density, cells with two different ratios (C2C12:HUVEC = 5:5 and 7:3) were analyzed. Growth condition of the cells was depicted in Figure 5.9. The proliferation study showed that (Figure 5.9) with higher ratio of C2C12, the group showed a faster growth rate from day 2 to day 5, independent of initial seeding density. All the groups achieved 90% confluence after 7 days culture. The results suggested that 30% of HUVECs was sufficient to support the growth of C2C12.

### 5.3.6 Immunofluorescence analysis of co-cultured constructs

Immunofluorescence staining of the printed constructs with both C2C12 and C2C12/HUVECs (7:3) were performed after 10-day differentiation. Casted GelMA hydrogel with C2C12/HUVECs (7:3) were run in parallel as control. The constructs were stained with myosin heavy chain (MHC), cluster of differentiation 31 (CD31) and DAPI. MHC is a differentiation marker of skeletal muscle tissue and signifies the myotube formation. CD31 is also referred to as platelet endothelial cell adhesion molecule-1 (PECAM-1) and expressed ubiquitously within the vascular compartment. CD31 is used primarily to demonstrate the presence of endothelial cells. As shown in Figure 5.10, MHC<sup>+</sup> cells indicated the formation of longitudinally aligned myofibers in both printed constructs. While in control group, MHC were barely expressed. The expression of endothelial cell marker CD31 confirmed the presence of HUVECs. The involvement of HUVECs did not interrupt the myotube alignment in the constructs.



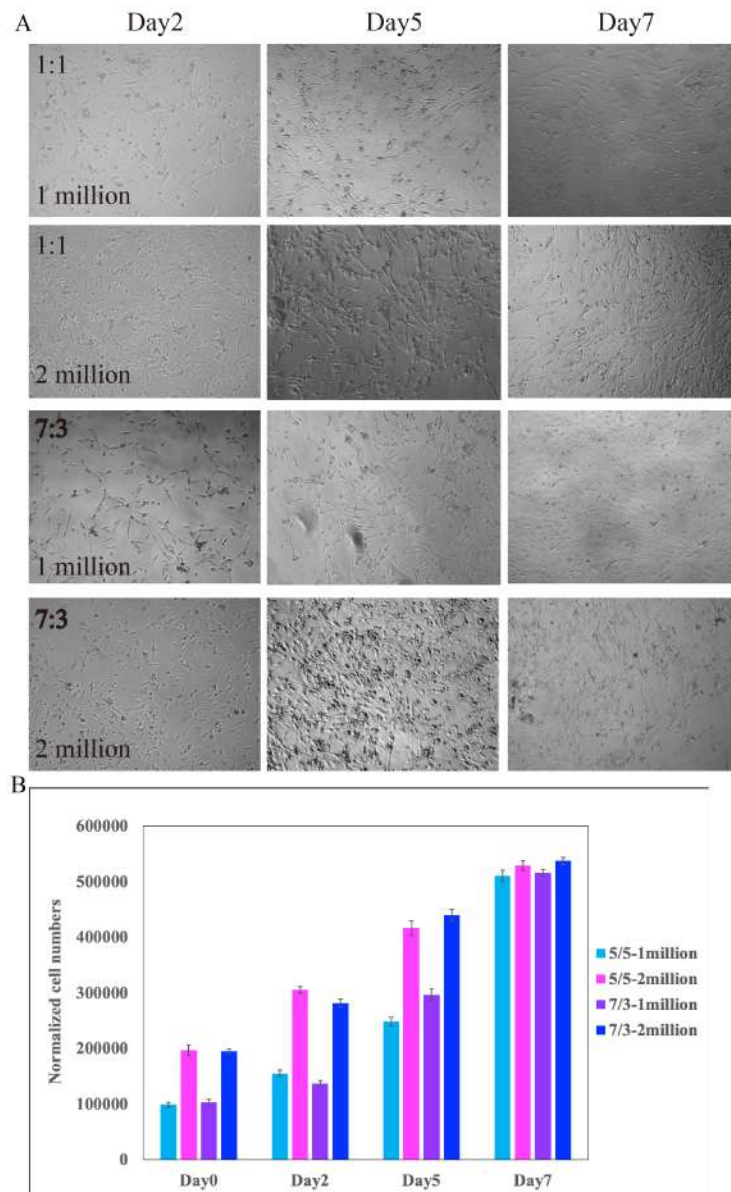


Figure 5.9: Co-cultured cells with varied ratio of C2C12:HUVECs=5:5 and 7:3. A. Microscope imaging of the co-cultured C2C12/HUVECs in different ratios and cell numbers. B. Proliferation study of the co-cultured C2C12/HUVECs over 7 days.

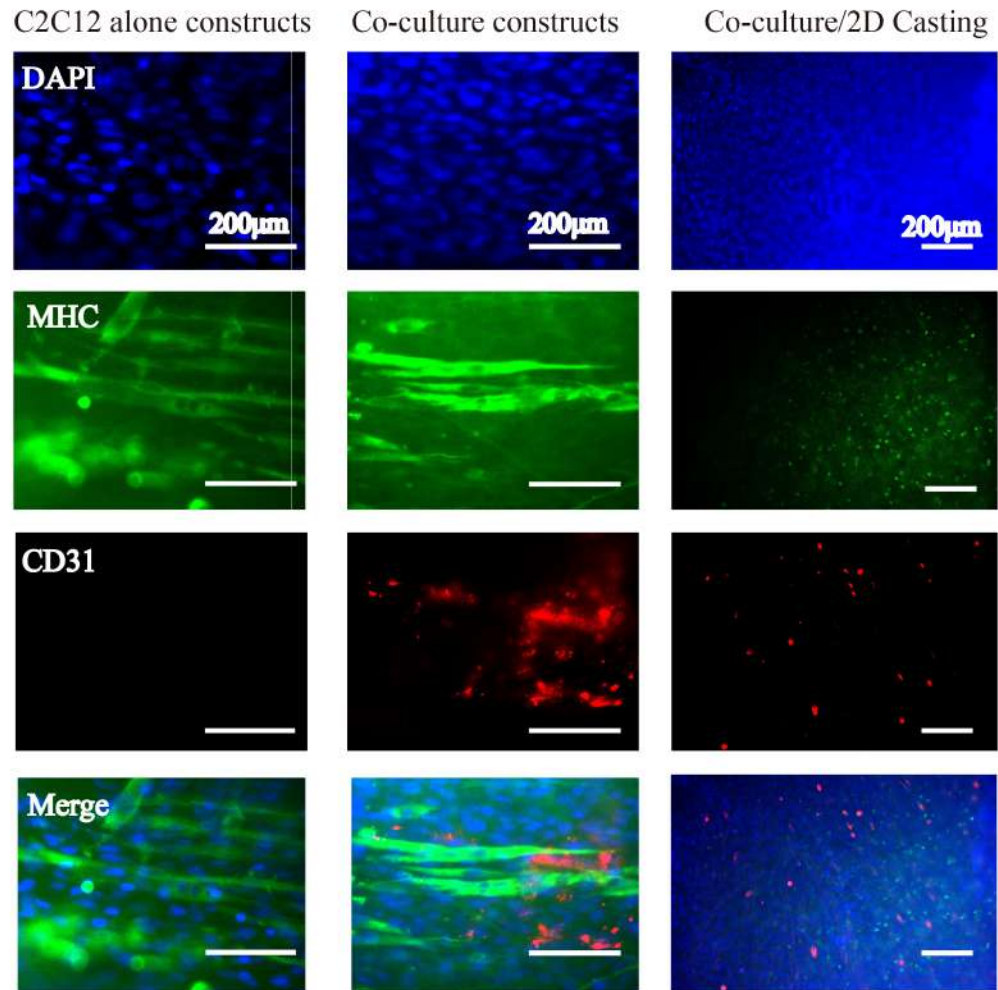


Figure 5.10: Immunostaining of co-cultured constructs, constructs with C2C12 alone and 2D casting (C2C12/HUVECs) were run in parallel as control,

## 5.4 Discussion

Numerous methods have been explored to generate engineered skeletal muscle tissue constructs, yet it is still a daunting task to recapitulate the complexity of muscles with current methods of fabrication. This research aims to fabricate 3D skeletal muscle constructs with highly aligned cells fast and efficiently through the collaboration of 3D bioprinting and capillary action. In the engineered constructs, gelatin was used as a sacrificial material to create hollow channels to facilitate the capillary action-assisted cell seeding as well as nutrient and oxygen transportation.

The constructs printed with varied line spacing have provided different channel width as geometrical confinement. In combination with capillary force, the cells could be distributed into the channels evenly and aligned, although with varied orientation degree. As demonstrated, the capillary force was correlated with the viscosity of the liquid, radius of the capillary and the traveled distance [330]. The capillary action could be controlled by adjusting the polymer concentration and the diameter of the capillary. In this case, GelMA was highly thermosensitive and the viscosity could be modulated by tuning the temperature.

The initial cell density ranging from 5 to  $50 \times 10^6$  cells/ml was considered on improving the cellular organization. The results demonstrated the cell alignment when using  $10 \times 10^6$  cells/ml and  $20 \times 10^6$  cells/ml. Interestingly, with the seeding density of  $50 \times 10^6$  cells/ml, cell-mediated gel compaction was observed. The thinning gel width experienced a significant reduction from 600-700  $\mu\text{m}$  to about 50-60  $\mu\text{m}$ . Cell-mediated gel compaction is of critical importance in tissue engineering, embryonic development, wound healing, and many disease states. Unconstrained gel compaction has been

reported by some notable research using collagen and fibrin [122, 210, 331]. In our study, unconstrained 10-15% gel compaction is in good accordance with previous research [210]. Bian et al. has investigated the gel compaction using collagen and fibrin gels with varied ratios [210]. The results demonstrated that cells encapsulated in fibrin had higher compaction than collagen gel, suggesting that one of the regulators in the cell-mediated compaction process is the gel components. In addition, cell-mediated gel compaction has been demonstrated with other cell types, such as cardiomyocytes or bovine chordal fibroblasts, indicating the dependence of the degree of gel compaction on the specific cell type.

To present a physiologically relevant environment, C2C12 and HUVECs were co-cultured in the constructs. The co-culture medium with skGM : EndoGRO = 1:2 was formulated to support and maintain the growth of C2C12 and HUVECs. The ratio of C2C12 and HUVECs was examined and 30% HUVECs were recognized to be sufficient to support the growth of C2C12. As revealed by the immunofluorescence analysis, no myofiber formation was observed in the control group with random cell orientation. The result was in good accordance with the previous finding. Further observation on the MHC staining indicated the longitudinal aligned myofiber formation and the presence of endothelial cells in both printed constructs. This further highlighted the efficacy of combining the 3D bioprinting technology and capillary action to achieve 3D cell alignment.

# Chapter6

## Conclusions and Future work

### 6.1 Conclusions

The research has fulfilled the main objective of this project: generating skeletal muscle model with unidirectionally organized cells using an integrated extrusion-based bioprinting in a highly efficient manner; established a layer-by-layer ultraviolet assisted extrusion-based bioprinting strategy with improved printing fidelity which allowed the generation of structures with high aspect ratio; developed a suitable bio-ink with dynamic mechanical property, superior biocompatibility and printability. The main contributions of this research are as follows:

1) A layer-by-layer ultraviolet assisted extrusion-based bioprinting strategy was well-established. Structures with high aspect ratio were able to be achieved using low viscosity bio-inks. A suitable threshold of viscosity for printing at room temperature was identified.

2) A novel bio-ink with dynamic mechanical properties was developed. The mechanical property switched from stiff to soft yielded bio-ink to be initially bioprintable and thereafter cell permissive. This has shed light on the bio-ink formulation according to cell-specific requirements. The cell survival rate over the entire bioprinting process were investigated.

3) A novel bioprinting technology and capillary action integrated strategy was developed to generate constructs with hollow channels mimicked skeletal muscle tissues. C2C12 and HUVECs were co-cultured within the constructs. Longitudinal myofiber-like structures and high cell density were achieved. This is the main structural feature in skeletal muscle tissue engineering.

### **6.1.1 Layer-by-layer ultraviolet assisted extrusion-based bioprinting of hydrogel constructs with high aspect ratio**

GelMA-based bio-inks has been investigated extensively in the field of tissue engineering and regenerative medicine due to their cost-effectiveness, ease of manipulation and outstanding biocompatibility. However, it is well acknowledged that GelMA with low concentration has limited printability. Some studies have introduced gellan gum to improve the printability. GelMA-gellan gum (GelMA-GG) bio-ink has exhibited great potential in improving the printability of GelMA-based bioink, yet the excessive addition of gellan gum may in turn compromise the biological properties. To balance the printability and biocompatibility, a layer-by-layer UV-assisted bioprinting strategy to fabricate complex 3D bioprinted constructs with high aspect ratio using the GelMA-GG bio-inks was introduced. A bio-ink selection framework including cell encapsulation, cell printing and further characterization has been devised. The results recommended that bio-inks with viscosity lower than 0.124 Pa·s at 37°C was suitable for cell encapsulation and to achieve great homogeneity. With printing temperature around 25°C, the results suggested that materials with viscosity of 0.2-1.0 Pa·s were suitable for printing of complex 3D cell-laden constructs with high aspect ratio using layer-by-layer UV-assisted bioprinting strategy. Unlike the previous studies that UV curing was implemented to stabilize the structure post-printing, this method could be easily adapted for all light curable materials with low viscosity and would find great potential in scaffold/bioprinting for tissue engineering of soft tissues.

### **6.1.2 Development of suitable bio-inks and the influence of UV radiation on cell behavior**

The lack of suitable bio-ink is one of the major bottlenecks that precludes the 3D bioprinting technology from further applications. In this work, a suitable bio-ink for soft tissue engineering was formulated by incorporating gelatin into GelMA-GG composite hydrogel. The bio-ink was recognized with tunable and dynamic mechanical property, which was initially bioprintable and cell favorable during incubation. The strategy is of considerable benefits due to the specific requirements of different cells. Apart from bio-ink, cells are of critical importance in bioprinting. Generally, the bioprinting process could be divided into three stages in terms of cell status. a. Resting, cells resting in printing syringe prior to printing; b. Extrusion, cells in the printing needle tip, exposed to shear stress; c. Crosslinking (UV radiation). Cell survival rate of both C2C12 and HUVECs were investigated over the three different stages. Specifically, cell damage and loss were observed throughout all these three stages. The results demonstrated that long incubation time over 90 min has significant effect on cell viability. However, in comparison to the other two stages, the damage was negligible. Furthermore, the coupling effects of shear stress in printing needle (30G, 27G and 25G) with incubation time were analyzed. Cell damage occurred regardless of the size of the needle used. Further, the results demonstrated that narrower needle diameter induced greater cell loss over time. Especially after 90 min incubation, cells were identified to be more susceptible to shear stress. Lastly, the influence of UV duration on cell viability in terms of single layer printing and multi-layer printing was assessed. In single layer printing, cells viability was found to be UV duration-dependent. HUVECs were highly sensitive

to UV radiation in comparison to C2C12. For multi-layer constructs, cell viability in the bottom-most layer has been examined and compared with single layer printing. The results revealed that given the same UV exposure time, cells in multi-layer constructs exhibited higher viability, highlighting the shield effect of the bio-inks.

### **6.1.3 3D bioprinted constructs with highly efficient capillary force assisted cell seeding**

In this chapter, engineered constructs with multiple bio-inks and multiple cell types were generated. The feasibility of applying bioprinting-based strategy and capillary action to fabricate 3D skeletal muscle constructs has been investigated. Parametric study on cell orientation was performed. Constructs with varied line spacing (1.5 mm, 1.2 mm, 1.0 mm) and initial seeding density ( $5 \times 10^6$ ,  $10 \times 10^6$ ,  $20 \times 10^6$  and  $50 \times 10^6$  cells/ml) were investigated. The immunostaining of DAPI and F-actin showed that the decreased line spacing has yielded better cell alignment. With respect to cell seeding density, the  $5 \times 10^6$  cells/ml was unable to generate aligned cell orientation, while the  $50 \times 10^6$  cells/ml induced significant cell-mediated gel compaction. Taken together,  $20 \times 10^6$  cell/ml is suitable for cell alignment. To provide a physiological relevant environment, C2C12 and HUVECs were co-cultured in the printed constructs. A suitable co-culture medium of skGM:EndoGRO (1:2) was formulated to support and maintain the growth of C2C12 and HUVECs. The immunostaining confirmed the longitudinal aligned myofiber formation and the presence of endothelial cells in the printed constructs. This further highlighted the feasibility of combining the 3D bioprinting technology and capillary action to achieve 3D cell alignment.



## 6.2 Future research directions

### 6.2.1 Development of novel bio-ink

Constructs that only offer structural support are insufficient to restore functionality. Materials that provide instructive cues that could elicit desired cellular response should be formulated. A large amount of materials have been explored for their capability of muscle regeneration. Among them, the use of collagen and fibrin gel for generating muscle constructs has been well established. However, the batch to batch variation and intrinsic weak mechanical property have impeded the further application of these natural materials. Synthetic materials have been proposed to be promising alternatives [193]. Materials with controllable property and could support multiple cell types should be formulated.

### 6.2.2 Generation of multicellular constructs

Skeletal muscle tissue consists of several support cells including but not limited to fibroblast, vascular endothelial cells (ECs) and motor neurons, which enable blood flow and innervation of the tissue. Therefore, it is highly desirable to incorporate multiple cell types in order to capture the cell-cell interactions *in vivo*. Particularly, for large tissue defect, not only restricted to muscle, vascular network is indispensable to avoid necrosis and support long-term culture. More importantly, achieving *de novo* innervation of regenerated myofibres remains a stumbling block for functional restoration of VML injuries. Nevertheless, it is challenging to co-culture and differentiate multiple cell types as each cell type requires distinct surrounding environment and culture medium. Furthermore, current engineering muscle

tissues are mainly based on immortal cell lines such as C2C12, these cell lines are modified to proliferate indefinitely to facilitate biological experiments. However, they cannot fully reflect the response of primary cells. Cell type selection has great impact on the outcomes. The rapid development of iPSC technology may facilitate the generation of personalized tissues models.

### **6.2.3 Evaluation of capillary action on cell alignment**

This study demonstrated the efficacy of distributing the cells by capillary action efficiently. Capillary action is a common phenomenon and has been investigated extensively in hard materials. However, limited study on soft materials has been discovered. The diameter of the capillary, the viscosity of the liquid and the travel length are coordinately modulating the outcome of capillary seeding. A systematic study of capillary action on cell seeding should be implemented to better facilitate the cell orientation.

## List of Publications

- [1] Zhuang, P., Sun, A. X., An, J., Chua, C. K., and Chew, S. Y. (2018). 3D neural tissue models: From spheroids to bioprinting. *Biomaterials*, 154, 113-133.
- [2] Zhuang, P., Ng, W. L., An, J., Chua, C. K., and Tan, L. P. (2019). Layer-by-layer ultraviolet assisted extrusion-based (UAE) bioprinting of hydrogel constructs with high aspect ratio for soft tissue engineering applications. *PloS one*, 14(6), e0216776.
- [3] Zhuang, P., An, J., Chua, C. K. and Tan, L. P. (2019). The spatial and temporal exploration for skeletal muscle regeneration. (Submitted)
- [4] Zhuang, P., An, J., Chua, C. K. and Tan, L. P. (2019). 3D bioprinted Constructs with Highly Efficient Capillary Force Assisted Cell seeding. (Under preparation)
- [5] Zhuang, P., An, J., Tan, L. P., and Chua, C. K. (2018). The current status of 3D bioprinting for neural tissue models. *Proceedings of the 3rd International Conference on Progress in Additive Manufacturing (Pro-AM 2018)*, 14-17 May, Singapore, Singapore.
- [6] Zhuang, P., An, J., and Chua, C. K. (2017). Printability study on Gelatin Methacryloyl(GelMA)-based hydrogel for 3D bioprinting. *2017 International Conference on Biofabrication*, 15-18 October, Beijing, China.

# Appendix A

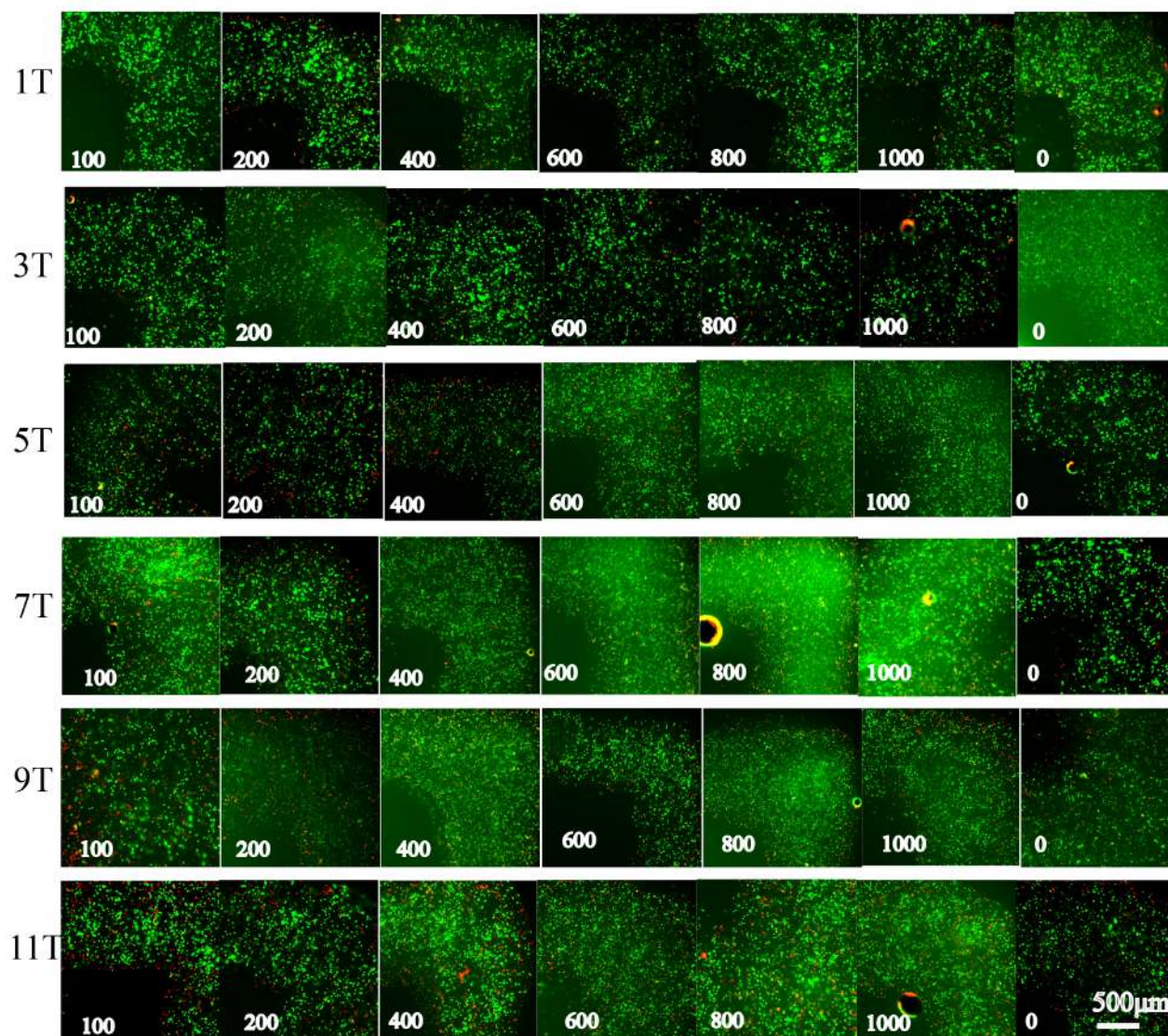


Figure A: UV effect on C2C12 viability with varied exposure time.

# Appendix B

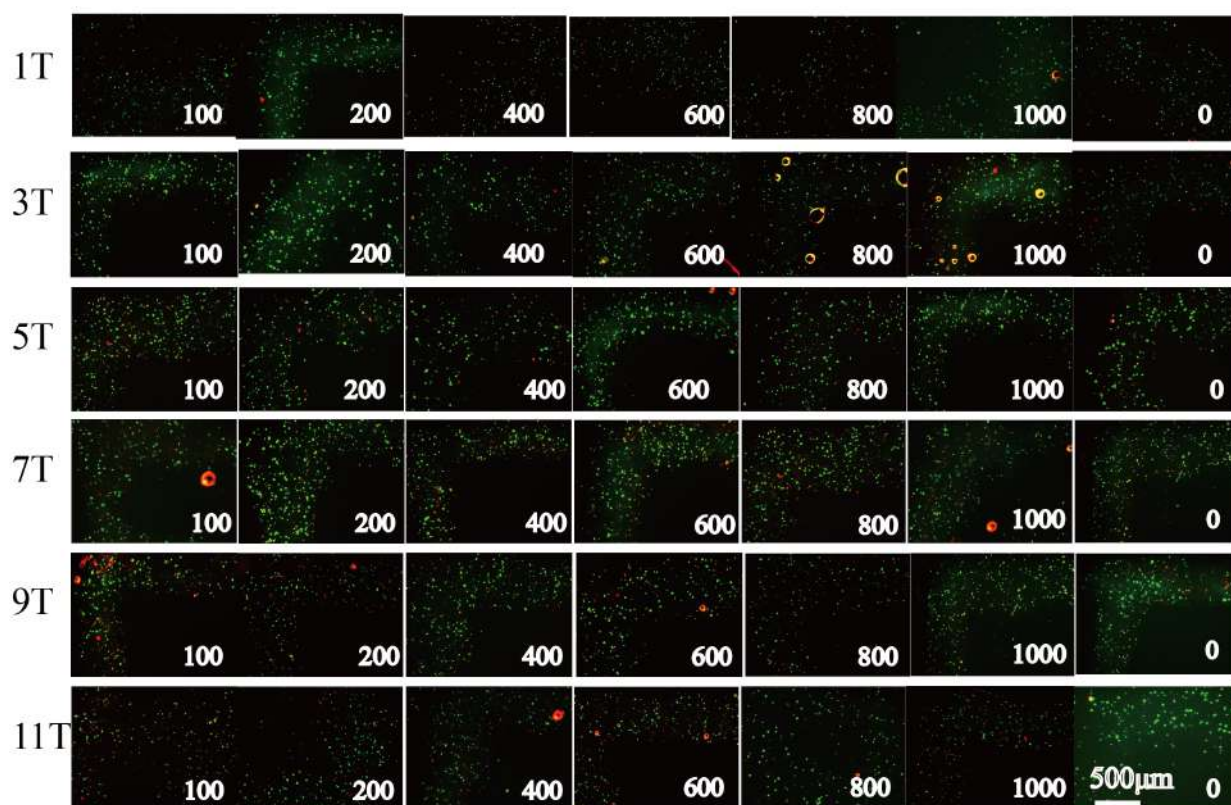


Figure B: UV effect on HUVEC viability with varied exposure time.



# Appendix C

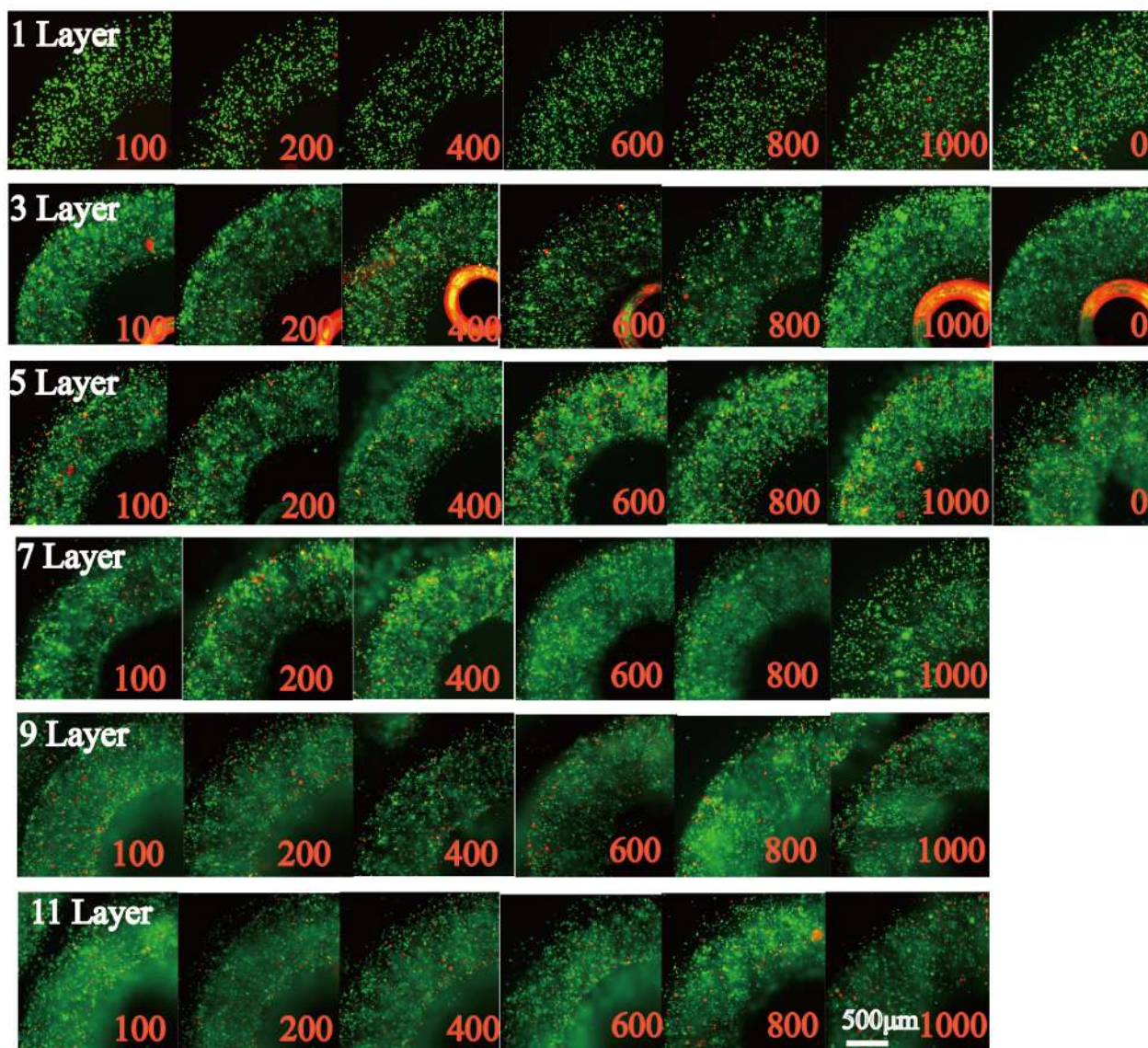


Figure C: Cell survival rate of printed C2C12 in GMGAGG multilayer constructs.

# Appendix D

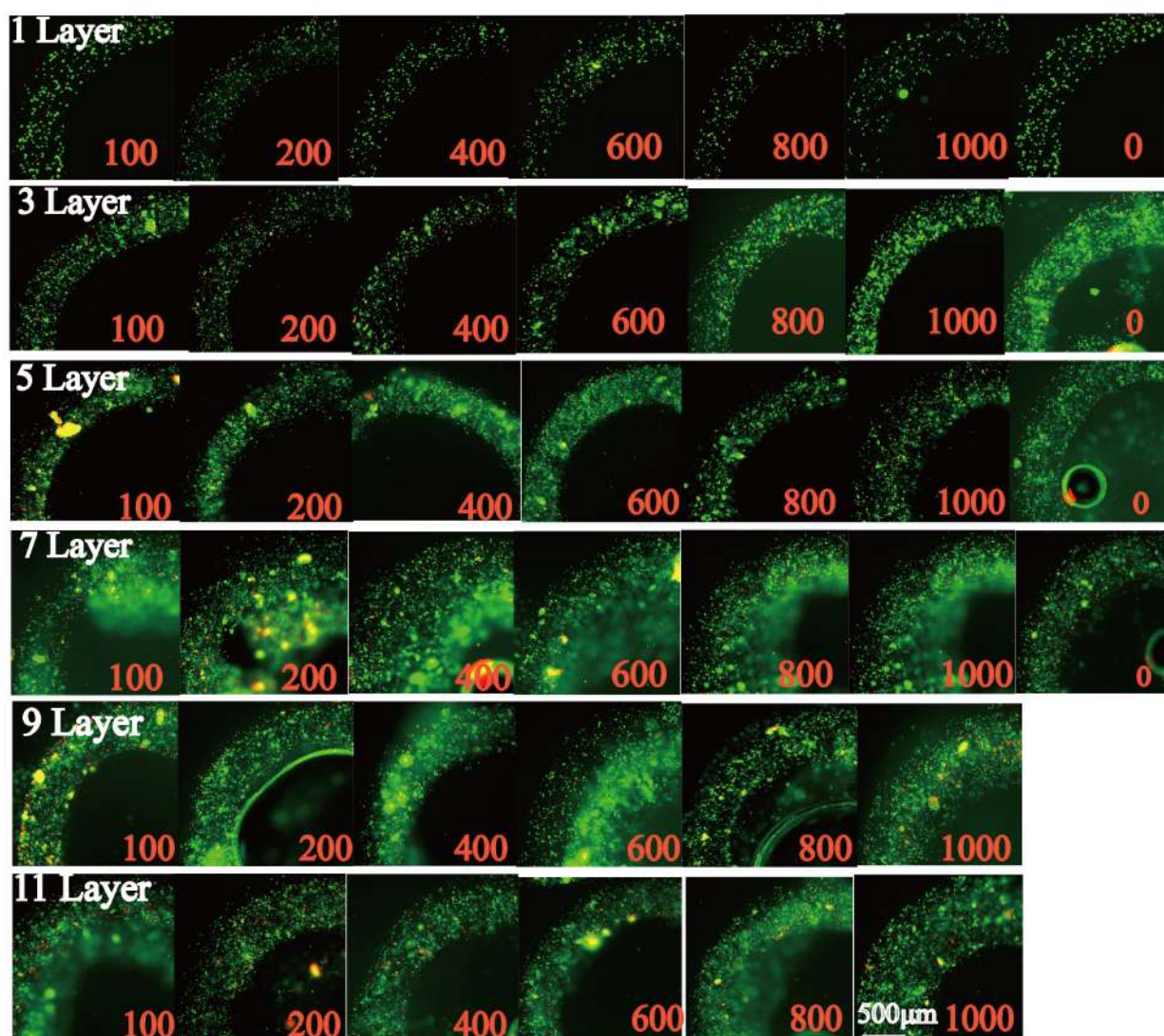


Figure D: Cell survival rate of printed HUVECs in GMGAGG multilayer constructs.

## References

- [1] Ana H Bacelar, Joana Silva-Correia, Joaquim M Oliveira, and Rui L Reis. Recent progress in gellan gum hydrogels provided by functionalization strategies. *Journal of Materials Chemistry B*, 4(37):6164–6174, 2016.
- [2] Jason W Nichol, Sandeep T Koshy, Hojae Bae, Chang M Hwang, Seda Yamanlar, and Ali Khademhosseini. Cell-laden microengineered gelatin methacrylate hydrogels. *Biomaterials*, 31(21):5536–5544, 2010.
- [3] AD Bach, JP Beier, J Stern-Staeter, and RE Horch. Skeletal muscle tissue engineering. *Journal of cellular and molecular medicine*, 8(4):413–422, 2004.
- [4] Brittany L Rodriguez and Lisa M Larkin. Functional three-dimensional scaffolds for skeletal muscle tissue engineering. In *Functional 3D Tissue Engineering Scaffolds*, pages 279–304. Elsevier, 2018.
- [5] Benjamin T Corona, Jessica C Rivera, Johnny G Owens, Joseph C Wenke, and Christopher R Rathbone. Volumetric muscle loss leads to permanent disability following extremity trauma. *Journal of Rehabilitation Research & Development*, 52(7), 2015.
- [6] Juan Liu, Dominik Saul, Kai Oliver Böker, Jennifer Ernst, Wolfgang Lehman, and Arndt F Schilling. Current methods for skeletal muscle tissue repair and regeneration. *BioMed research international*, 2018, 2018.
- [7] RG Miller, Khema R Sharma, GK Pavlath, E Gussoni, M Mynhier, P Yu, AM Lanctot, CM Greco, L Steinman, and HM Blau. Myoblast implantation in duchenne muscular dystrophy: the san francisco study. *Muscle & Nerve: Official Journal of the American Association of Electrodiagnostic Medicine*, 20(4):469–478, 1997.



- [8] Massimiliano Cerletti, Sara Jurga, Carol A Witzak, Michael F Hirshman, Jennifer L Shadrach, Laurie J Goodyear, and Amy J Wagers. Highly efficient, functional engraftment of skeletal muscle stem cells in dystrophic muscles. *Cell*, 134(1):37–47, 2008.
- [9] Cheng Zhang, HY Feng, SL Huang, JP Fang, LL Xiao, XL Yao, Chun Chen, X Ye, Yin Zeng, XL Lu, et al. Therapy of duchenne muscular dystrophy with umbilical cord blood stem cell transplantation. *Zhonghua yi xue yi chuan xue za zhi= Zhonghua yixue yichuanxue zazhi= Chinese journal of medical genetics*, 22(4):399–405, 2005.
- [10] Didier Montarras, Jennifer Morgan, Charlotte Collins, Frédéric Relaix, Stéphane Zaffran, Ana Cumano, Terence Partridge, and Margaret Buckingham. Direct isolation of satellite cells for skeletal muscle regeneration. *Science*, 309(5743):2064–2067, 2005.
- [11] Marco Quarta, Melinda Cromie, Robert Chacon, Justin Blonigan, Victor Garcia, Igor Akimenko, Mark Hamer, Patrick Paine, Merel Stok, Joseph B Shrager, et al. Bioengineered constructs combined with exercise enhance stem cell-mediated treatment of volumetric muscle loss. *Nature communications*, 8:15613, 2017.
- [12] Benjamin T Corona, Catherine L Ward, Hannah B Baker, Thomas J Walters, and George J Christ. Implantation of in vitro tissue engineered muscle repair constructs and bladder acellular matrices partially restore in vivo skeletal muscle function in a rat model of volumetric muscle loss injury. *Tissue Engineering Part A*, 20(3-4):705–715, 2013.
- [13] Amit Aurora, Janet L Roe, Benjamin T Corona, and Thomas J Walters. An acellular biologic scaffold does not regenerate appreciable

- de novo muscle tissue in rat models of volumetric muscle loss injury. *Biomaterials*, 67:393–407, 2015.
- [14] Ravi K Garg, Robert C Rennert, Dominik Duscher, Michael Sorkin, Revanth Kosaraju, Lauren J Auerbach, James Lennon, Michael T Chung, Kevin Paik, Johannes Nimpf, et al. Capillary force seeding of hydrogels for adipose-derived stem cell delivery in wounds. *Stem cells translational medicine*, 3(9):1079–1089, 2014.
- [15] Taimoor H Qazi, David J Mooney, Matthias Pumberger, Sven Geissler, and Georg N Duda. Biomaterials based strategies for skeletal muscle tissue engineering: existing technologies and future trends. *Biomaterials*, 53:502–521, 2015.
- [16] Bae Hoon Lee, Nathaniel Lum, Li Yuan Seow, Pei Qi Lim, and Lay Poh Tan. Synthesis and characterization of types a and b gelatin methacryloyl for bioink applications. *Materials*, 9(10):797, 2016.
- [17] Sólveig Thorsteinsdóttir, Marianne Deries, Ana Sofia Cachaco, and Fernanda Bajanca. The extracellular matrix dimension of skeletal muscle development. *Developmental biology*, 354(2):191–207, 2011.
- [18] JA Trotter and PP Purslow. Functional morphology of the endomysium in series fibered muscles. *Journal of morphology*, 212(2):109–122, 1992.
- [19] Peter P Purslow and John A Trotter. The morphology and mechanical properties of endomysium in series-fibred muscles: variations with muscle length. *Journal of Muscle Research & Cell Motility*, 15(3):299–308, 1994.

- [20] Allison R Gillies and Richard L Lieber. Structure and function of the skeletal muscle extracellular matrix. *Muscle & nerve*, 44(3):318–331, 2011.
- [21] Takanori Nishimura. Role of extracellular matrix in development of skeletal muscle and postmortem aging of meat. *Meat Science*, 109:48–55, 2015.
- [22] Charlotte A Collins, Irwin Olsen, Peter S Zammit, Louise Heslop, Aviva Petrie, Terence A Partridge, and Jennifer E Morgan. Stem cell function, self-renewal, and behavioral heterogeneity of cells from the adult muscle satellite cell niche. *Cell*, 122(2):289–301, 2005.
- [23] Robert W Arpke, Radbod Darabi, Tara L Mader, Yu Zhang, Akira Toyama, Cara-lin Lonetree, Nardina Nash, Dawn A Lowe, Rita CR Perlingeiro, and Michael Kyba. A new immuno-, dystrophin-deficient model, the nsg-mdx4cv mouse, provides evidence for functional improvement following allogeneic satellite cell transplantation. *Stem cells*, 31(8):1611–1620, 2013.
- [24] Yusuke Ono, Luisa Boldrin, Paul Knopp, Jennifer E Morgan, and Peter S Zammit. Muscle satellite cells are a functionally heterogeneous population in both somite-derived and branchiomic muscles. *Developmental biology*, 337(1):29–41, 2010.
- [25] Hang Yin, Feodor Price, and Michael A Rudnicki. Satellite cells and the muscle stem cell niche. *Physiological reviews*, 93(1):23–67, 2013.
- [26] John K Hall, Glen B Banks, Jeffrey S Chamberlain, and Bradley B Olwin. Prevention of muscle aging by myofiber-associated satellite cell

- transplantation. *Science translational medicine*, 2(57):57ra83–57ra83, 2010.
- [27] Jennifer L Shadrach and Amy J Wagers. Stem cells for skeletal muscle repair. *Philosophical Transactions of the Royal Society B: Biological Sciences*, 366(1575):2297–2306, 2011.
- [28] Dacha Gholobova, Melanie Gérard, Lieselot Decroix, Linda Desender, Nico Callewaert, Pieter Annaert, and Lieven Thorrez. Human tissue-engineered skeletal muscle: a novel 3d in vitro model for drug disposition and toxicity after intramuscular injection. *Scientific reports*, 8(1):12206, 2018.
- [29] Teuta Domi, Emanuela Porrello, Daniele Velardo, Alessia Capotondo, Alessandra Biffi, Rossana Tonlorenzi, Stefano Amadio, Alessandro Ambrosi, Yuko Miyagoe-Suzuki, Shin’ichi Takeda, et al. Mesoangioblast delivery of miniagrin ameliorates murine model of merosin-deficient congenital muscular dystrophy type 1a. *Skeletal muscle*, 5(1):30, 2015.
- [30] Elena Serena, Susi Zatti, Alice Zoso, Francesca Lo Verso, F Saverio Tedesco, Giulio Cossu, and Nicola Elvassore. Skeletal muscle differentiation on a chip shows human donor mesoangioblasts’ efficiency in restoring dystrophin in a duchenne muscular dystrophy model. *Stem cells translational medicine*, 5(12):1676–1683, 2016.
- [31] Alexander Birbrair and Osvaldo Delbono. Pericytes are essential for skeletal muscle formation. *Stem Cell Reviews and Reports*, 11(4):547–548, 2015.

- [32] Claudia Fuoco, Elena Sangalli, Rosa Vono, Stefano Testa, Benedetto Sacchetti, Michael VG Latronico, Sergio Bernardini, Paolo Madeddu, Gianni Cesareni, Dror Seliktar, et al. 3d hydrogel environment rejuvenates aged pericytes for skeletal muscle tissue engineering. *Frontiers in physiology*, 5:203, 2014.
- [33] Jun Ke Zheng, Yi Wang, Aditi Karandikar, Qian Wang, Hui Gai, Ai Lian Liu, Chao Peng, and Hui Zhen Sheng. Skeletal myogenesis by human embryonic stem cells. *Cell research*, 16(8):713, 2006.
- [34] Lingjun Rao, Ying Qian, Alastair Khodabukus, Thomas Ribar, and Nenad Bursac. Engineering human pluripotent stem cells into a functional skeletal muscle tissue. *Nature communications*, 9(1):126, 2018.
- [35] Sahar Ansari, Chider Chen, Xingtian Xu, Nasim Annabi, Homayoun H Zadeh, Benjamin M Wu, Ali Khademhosseini, Songtao Shi, and Alireza Moshaverinia. Muscle tissue engineering using gingival mesenchymal stem cells encapsulated in alginate hydrogels containing multiple growth factors. *Annals of biomedical engineering*, 44(6):1908–1920, 2016.
- [36] Justus P Beier, Franz F Bitto, Claudia Lange, Dorothee Klumpp, Andreas Arkudas, Oliver Bleiziffer, Anja M Boos, Raymund E Horch, and Ulrich Kneser. Myogenic differentiation of mesenchymal stem cells co-cultured with primary myoblasts. *Cell biology international*, 35(4):397–406, 2011.
- [37] Nadine Matthias, Samuel D Hunt, Jianbo Wu, Jonathan Lo, Laura A Smith Callahan, Yong Li, Johnny Huard, and Radbod Darabi. Volumetric muscle loss injury repair using in situ fibrin gel cast seeded

- with muscle-derived stem cells (mdscs). *Stem cell research*, 27:65–73, 2018.
- [38] Min Hwan Kim, Hea Nam Hong, Joon Pio Hong, Chan Jeoung Park, Seog Woon Kwon, Soon Hee Kim, Gilson Kang, and MiJung Kim. The effect of vegf on the myogenic differentiation of adipose tissue derived stem cells within thermosensitive hydrogel matrices. *Biomaterials*, 31(6):1213–1218, 2010.
- [39] Jonathan Mark Fishman, Athanasios Tyraskis, Panagiotis Maghsoudlou, Luca Urbani, Giorgia Totonelli, Martin A Birchall, and Paolo De Coppi. Skeletal muscle tissue engineering: which cell to use? *Tissue Engineering Part B: Reviews*, 19(6):503–515, 2013.
- [40] Soumen Jana, Sheeny K Lan Levengood, and Miqin Zhang. Anisotropic materials for skeletal-muscle-tissue engineering. *Advanced Materials*, 28(48):10588–10612, 2016.
- [41] ST Cooper, AL Maxwell, E Kizana, M Ghoddusi, EC Hardeman, IE Alexander, DG Allen, and KN North. C2c12 co-culture on a fibroblast substratum enables sustained survival of contractile, highly differentiated myotubes with peripheral nuclei and adult fast myosin expression. *Cell motility and the cytoskeleton*, 58(3):200–211, 2004.
- [42] Leonardo Ricotti, Toshinori Fujie, Helena Vazão, Gianni Ciofani, Roberto Marotta, Rosaria Brescia, Carlo Filippeschi, Irene Corradini, Michela Matteoli, Virgilio Mattoli, et al. Boron nitride nanotube-mediated stimulation of cell co-culture on micro-engineered hydrogels. *PloS one*, 8(8):e71707, 2013.

- [43] B Kalman, C Monge, A Bigot, V Mouly, C Picart, and T Boudou. Engineering human 3d micromuscles with co-culture of fibroblasts and myoblasts. *Computer methods in biomechanics and biomedical engineering*, 18(sup1):1960–1961, 2015.
- [44] Nikhil Rao, Gillie Agmon, Matthew T Tierney, Jessica L Ungerleider, Rebecca L Braden, Alessandra Sacco, and Karen L Christman. Engineering an injectable muscle-specific microenvironment for improved cell delivery using a nanofibrous extracellular matrix hydrogel. *ACS nano*, 11(4):3851–3859, 2017.
- [45] Michael R Hicks, Thanh V Cao, and Paul R Standley. Biomechanical strain vehicles for fibroblast-directed skeletal myoblast differentiation and myotube functionality in a novel coculture. *American Journal of Physiology-Cell Physiology*, 307(8):C671–C683, 2014.
- [46] Jordana Gilbert-Honick, Shama R Iyer, Sarah M Somers, Richard M Lovering, Kathryn Wagner, Hai-Quan Mao, and Warren L Grayson. Engineering functional and histological regeneration of vascularized skeletal muscle. *Biomaterials*, 164:70–79, 2018.
- [47] Karina H Nakayama, Marco Quarta, Patrick Paine, Cynthia Alcazar, Ioannis Karakikes, Victor Garcia, Oscar J Abilez, Nicholas S Calvo, Chelsey S Simmons, Thomas A Rando, et al. Treatment of volumetric muscle loss in mice using nanofibrillar scaffolds enhances vascular organization and integration. *Communications biology*, 2(1):170, 2019.
- [48] Dacha Gholobova, Lieselot Decroix, Vicky Van Muylder, Linda Desender, Melanie Gerard, Gilles Carpentier, Herman Vandenburg, and Lieven Thorrez. Endothelial network formation within human

- tissue-engineered skeletal muscle. *Tissue Engineering Part A*, 21(19-20):2548–2558, 2015.
- [49] Shulamit Levenberg, Jeroen Rouwkema, Mara Macdonald, Evan S Garfein, Daniel S Kohane, Diane C Darland, Robert Marini, Clemens A Van Blitterswijk, Richard C Mulligan, Patricia A D’Amore, et al. Engineering vascularized skeletal muscle tissue. *Nature biotechnology*, 23(7):879, 2005.
- [50] Shangwu Chen, Naoki Kawazoe, and Guoping Chen. Biomimetic assembly of vascular endothelial cells and muscle cells in microgrooved collagen porous scaffolds. *Tissue Engineering Part C: Methods*, 23(6):367–376, 2017.
- [51] Yulia Shandalov, Dana Egozi, Jacob Koffler, Dekel Dado-Rosenfeld, David Ben-Shimol, Alina Freiman, Erez Shor, Aviva Kabala, and Shulamit Levenberg. An engineered muscle flap for reconstruction of large soft tissue defects. *Proceedings of the National Academy of Sciences*, 111(16):6010–6015, 2014.
- [52] Eiji Nagamori, Trung Xuan Ngo, Yasunori Takezawa, Atsuhiko Saito, Yoshiki Sawa, Tatsuya Shimizu, Teruo Okano, Masahito Taya, and Masahiro Kino-oka. Network formation through active migration of human vascular endothelial cells in a multilayered skeletal myoblast sheet. *Biomaterials*, 34(3):662–668, 2013.
- [53] Silvia Carosio, Laura Barberi, Emanuele Rizzuto, Carmine Nicoletti, Zaccaria Del Prete, and Antonio Musaro. Generation of ex vivo-vascularized muscle engineered tissue (x-met). *Scientific reports*, 3:1420, 2013.



- [54] Jacob Koffler, Keren Kaufman-Francis, Yulia Shandalov, Dana Egozi, Daria Amiad Pavlov, Amir Landesberg, and Shulamit Levenberg. Improved vascular organization enhances functional integration of engineered skeletal muscle grafts. *Proceedings of the National Academy of Sciences*, 108(36):14789–14794, 2011.
- [55] Xiufang Guo, Mainak Das, John Rumsey, Mercedes Gonzalez, Maria Stancescu, and James Hickman. Neuromuscular junction formation between human stem-cell-derived motoneurons and rat skeletal muscle in a defined system. *Tissue Engineering Part C: Methods*, 16(6):1347–1355, 2010.
- [56] Lisa M Larkin, Jack H Van Der Meulen, Robert G Dennis, and Jeffrey B Kennedy. Functional evaluation of nerve-skeletal muscle constructs engineered in vitro. *In Vitro Cellular & Developmental Biology-Animal*, 42(3-4):75–82, 2006.
- [57] Yuya Morimoto, Midori Kato-Negishi, Hiroaki Onoe, and Shoji Takeuchi. Three-dimensional neuron–muscle constructs with neuromuscular junctions. *Biomaterials*, 34(37):9413–9419, 2013.
- [58] Alec ST Smith, Samantha L Passey, Neil RW Martin, Darren J Player, Vivek Mudera, Linda Greensmith, and Mark P Lewis. Creating interactions between tissue-engineered skeletal muscle and the peripheral nervous system. *Cells Tissues Organs*, 202(3-4):143–158, 2016.
- [59] Md Arifuzzaman, Akira Ito, Kazushi Ikeda, Yoshinori Kawabe, and Masamichi Kamihira. Fabricating muscle–neuron constructs with improved contractile force generation. *Tissue Engineering Part A*, 25(7-8):563–574, 2019.

- [60] Neil RW Martin, Samantha L Passey, Darren J Player, Vivek Mudera, Keith Baar, Linda Greensmith, and Mark P Lewis. Neuromuscular junction formation in tissue-engineered skeletal muscle augments contractile function and improves cytoskeletal organization. *Tissue Engineering Part A*, 21(19-20):2595–2604, 2015.
- [61] Adam J Engler, Shamik Sen, H Lee Sweeney, and Dennis E Discher. Matrix elasticity directs stem cell lineage specification. *Cell*, 126(4):677–689, 2006.
- [62] Chenyuan Gao, Lin Tang, Jieyu Hong, Chunyong Liang, Lay Poh Tan, and Huaqiong Li. Effect of laser induced topography with moderate stiffness on human mesenchymal stem cell behavior. *Journal of Physics: Materials*, 2(3):034006, 2019.
- [63] Y Shona Pek, Andrew CA Wan, and Jackie Y Ying. The effect of matrix stiffness on mesenchymal stem cell differentiation in a 3d thixotropic gel. *Biomaterials*, 31(3):385–391, 2010.
- [64] Andrew S Rowlands, Peter A George, and Justin J Cooper-White. Directing osteogenic and myogenic differentiation of mscs: interplay of stiffness and adhesive ligand presentation. *American Journal of Physiology-Cell Physiology*, 295(4):C1037–C1044, 2008.
- [65] Karl JA McCullagh and Rita CR Perlingeiro. Coaxing stem cells for skeletal muscle repair. *Advanced drug delivery reviews*, 84:198–207, 2015.
- [66] Penney M Gilbert, Karen L Havenstrite, Klas EG Magnusson, Alessandra Sacco, Nora A Leonardi, Peggy Kraft, Nghi K Nguyen, Sebastian Thrun, Matthias P Lutolf, and Helen M Blau. Substrate elasticity

- regulates skeletal muscle stem cell self-renewal in culture. *Science*, 329(5995):1078–1081, 2010.
- [67] Adam J Engler, Maureen A Griffin, Shamik Sen, Carsten G Bönemann, H Lee Sweeney, and Dennis E Discher. Myotubes differentiate optimally on substrates with tissue-like stiffness: pathological implications for soft or stiff microenvironments. *J Cell Biol*, 166(6):877–887, 2004.
- [68] Vahid Hosseini, Samad Ahadian, Serge Ostrovidov, Gulden Camci-Unal, Song Chen, Hirokazu Kaji, Murugan Ramalingam, and Ali Khademhosseini. Engineered contractile skeletal muscle tissue on a microgrooved methacrylated gelatin substrate. *Tissue Engineering Part A*, 18(23-24):2453–2465, 2012.
- [69] Mehdi Nikkhah, Faramarz Edalat, Sam Manoucheri, and Ali Khademhosseini. Engineering microscale topographies to control the cell–substrate interface. *Biomaterials*, 33(21):5230–5246, 2012.
- [70] Chor Yong Tay, Scott Alexander Irvine, Freddy YC Boey, Lay Poh Tan, and Subbu Venkatraman. Micro-/nano-engineered cellular responses for soft tissue engineering and biomedical applications. *Small*, 7(10):1361–1378, 2011.
- [71] Lina Altomare, N Gadegaard, L Visai, MARIA CRISTINA Tanzi, and Silvia Fare. Biodegradable microgrooved polymeric surfaces obtained by photolithography for skeletal muscle cell orientation and myotube development. *Acta biomaterialia*, 6(6):1948–1957, 2010.
- [72] Peter Molnar, Weishi Wang, Anupama Natarajan, John W Rumsey, and James J Hickman. Photolithographic patterning of c2c12 my-

- otubes using vitronectin as growth substrate in serum-free medium. *Biotechnology progress*, 23(1):265–268, 2007.
- [73] Chor Yong Tay, Mintu Pal, Haiyang Yu, Wen Shing Leong, Nguan Soon Tan, Kee Woei Ng, Subbu Venkatraman, Freddy Boey, David Tai Leong, and Lay Poh Tan. Bio-inspired micropatterned platform to steer stem cell differentiation. *Small*, 7(10):1416–1421, 2011.
  - [74] Jun Nakanishi, Tohru Takarada, Kazuo Yamaguchi, and Mizuo Maeda. Recent advances in cell micropatterning techniques for bio-analytical and biomedical sciences. *Analytical sciences*, 24(1):67–72, 2008.
  - [75] Jacinthe Gingras, Robert M Rioux, Damien Cuvelier, Nicholas A Geisse, Jeff W Lichtman, George M Whitesides, L Mahadevan, and Joshua R Sanes. Controlling the orientation and synaptic differentiation of myotubes with micropatterned substrates. *Biophysical journal*, 97(10):2771–2779, 2009.
  - [76] Joseph L Charest, Andrés J García, and William P King. Myoblast alignment and differentiation on cell culture substrates with microscale topography and model chemistries. *Biomaterials*, 28(13):2202–2210, 2007.
  - [77] Gi Hoon Yang, JiUn Lee, and GeunHyung Kim. The fabrication of uniaxially aligned micro-textured polycaprolactone struts and application for skeletal muscle tissue regeneration. *Biofabrication*, 2019.
  - [78] Lina Altomare, Mathis Riehle, Nikolaj Gadegaard, Mariacristina Tanzi, and Silvia Farè. Microcontact printing of fibronectin on a

- biodegradable polymeric surface for skeletal muscle cell orientation. *The International journal of artificial organs*, 33(8):535–543, 2010.
- [79] Rebecca M Duffy, Yan Sun, and Adam W Feinberg. Understanding the role of ecm protein composition and geometric micropatterning for engineering human skeletal muscle. *Annals of biomedical engineering*, 44(6):2076–2089, 2016.
- [80] Elena Serena, Susi Zatti, Elena Reghelin, Alessandra Pasut, Elisa Cimetta, and Nicola Elvassore. Soft substrates drive optimal differentiation of human healthy and dystrophic myotubes. *Integrative Biology*, 2(4):193–201, 2010.
- [81] Kazunori Shimizu, Hideaki Fujita, and Eiji Nagamori. Alignment of skeletal muscle myoblasts and myotubes using linear micropatterned surfaces ground with abrasives. *Biotechnology and bioengineering*, 103(3):631–638, 2009.
- [82] Peng-Yuan Wang, Hung-Te Yu, and Wei-Bor Tsai. Modulation of alignment and differentiation of skeletal myoblasts by submicron ridges/grooves surface structure. *Biotechnology and bioengineering*, 106(2):285–294, 2010.
- [83] Daniel L Yamamoto, Robert I Csikasz, Yu Li, Gunjana Sharma, Klas Hjort, Roger Karlsson, and Tore Bengtsson. Myotube formation on micro-patterned glass: intracellular organization and protein distribution in c2c12 skeletal muscle cells. *Journal of Histochemistry & Cytochemistry*, 56(10):881–892, 2008.
- [84] Jin-Ye Shen, Mary Bee-Eng Chan-Park, Zhi-Qin Feng, Vincent Chan, and Zhi-Wei Feng. Uv-embossed microchannel in biocompatible poly-

- meric film: Application to control of cell shape and orientation of muscle cells. *Journal of Biomedical Materials Research Part B: Applied Biomaterials: An Official Journal of The Society for Biomaterials, The Japanese Society for Biomaterials, and The Australian Society for Biomaterials and the Korean Society for Biomaterials*, 77(2):423–430, 2006.
- [85] Wai Yee Yeong, Haiyang Yu, Kee Pah Lim, Ka Lai Gary Ng, Yin Chiang Freddy Boey, Venkatraman S Subbu, and Lay Poh Tan. Multiscale topological guidance for cell alignment via direct laser writing on biodegradable polymer. *Tissue Engineering Part C: Methods*, 16(5):1011–1021, 2010.
- [86] Huaqiong Li, Feng Wen, Yee Shan Wong, Freddy Yin Chiang Boey, Venkatraman S Subbu, David Tai Leong, Kee Woei Ng, Gary Ka Lai Ng, and Lay Poh Tan. Direct laser machining-induced topographic pattern promotes up-regulation of myogenic markers in human mesenchymal stem cells. *Acta biomaterialia*, 8(2):531–539, 2012.
- [87] Yi Zhao, Hansong Zeng, Jin Nam, and Sudha Agarwal. Fabrication of skeletal muscle constructs by topographic activation of cell alignment. *Biotechnology and bioengineering*, 102(2):624–631, 2009.
- [88] Mainak Das, Kerry Wilson, Peter Molnar, and James J Hickman. Differentiation of skeletal muscle and integration of myotubes with silicon microstructures using serum-free medium and a synthetic silane substrate. *Nature protocols*, 2(7):1795, 2007.
- [89] Michael S Grigola, Casey L Dyck, Derin S Babacan, Danielle N Joaquin, and K Jimmy Hsia. Myoblast alignment on 2d wavy pat-

- terns: Dependence on feature characteristics and cell-cell interaction. *Biotechnology and bioengineering*, 111(8):1617–1626, 2014.
- [90] Xingyu Jiang, Shuichi Takayama, Xiangping Qian, Emanuele Ostuni, Hongkai Wu, Ned Bowden, Philip LeDuc, Donald E Ingber, and George M Whitesides. Controlling mammalian cell spreading and cytoskeletal arrangement with conveniently fabricated continuous wavy features on poly (dimethylsiloxane). *Langmuir*, 18(8):3273–3280, 2002.
- [91] Mai T Lam, Yen-Chih Huang, Ravi K Birla, and Shuichi Takayama. Microfeature guided skeletal muscle tissue engineering for highly organized 3-dimensional free-standing constructs. *Biomaterials*, 30(6):1150–1155, 2009.
- [92] Mai T Lam, Sylvie Sim, Xiaoyue Zhu, and Shuichi Takayama. The effect of continuous wavy micropatterns on silicone substrates on the alignment of skeletal muscle myoblasts and myotubes. *Biomaterials*, 27(24):4340–4347, 2006.
- [93] P Clark, GA Dunn, A Knibbs, and M Peckham. Alignment of myoblasts on ultrafine gratings inhibits fusion in vitro. *The international journal of biochemistry & cell biology*, 34(7):816–825, 2002.
- [94] Debanti Sengupta, Penney M Gilbert, Kyle J Johnson, Helen M Blau, and Sarah C Heilshorn. Protein-engineered biomaterials to generate human skeletal muscle mimics. *Advanced healthcare materials*, 1(6):785–789, 2012.
- [95] Huaqiong Li, Feng Wen, Huizhi Chen, Mintu Pal, Yuekun Lai, Allan Zijian Zhao, and Lay Poh Tan. Micropatterning extracellular matrix proteins on electrospun fibrous substrate promote human mes-

- enchymal stem cell differentiation toward neurogenic lineage. *ACS applied materials & interfaces*, 8(1):563–573, 2015.
- [96] Ting Yu, Chee Kai Chua, Chor Yong Tay, Feng Wen, Haiyang Yu, Jerry KY Chan, Mark SK Chong, David Tai Leong, and Lay Poh Tan. A generic micropatterning platform to direct human mesenchymal stem cells from different origins towards myogenic differentiation. *Macromolecular bioscience*, 13(6):799–807, 2013.
- [97] Wylie W Ahmed, Tobias Wolfram, Alexandra M Goldyn, Kristina Bruellhoff, Borja Aragüés Rioja, Martin Möller, Joachim P Spatz, Taher A Saif, Jürgen Groll, and Ralf Kemkemer. Myoblast morphology and organization on biochemically micro-patterned hydrogel coatings under cyclic mechanical strain. *Biomaterials*, 31(2):250–258, 2010.
- [98] Piyush Bajaj, Bobby Reddy Jr, Larry Millet, Chunan Wei, Pinar Zorlutuna, Gang Bao, and Rashid Bashir. Patterning the differentiation of c2c12 skeletal myoblasts. *Integrative Biology*, 3(9):897–909, 2011.
- [99] Susi Zatti, Alice Zoso, Elena Serena, Camilla Luni, Elisa Cimetta, and Nicola Elvassore. Micropatterning topology on soft substrates affects myoblast proliferation and differentiation. *Langmuir*, 28(5):2718–2726, 2012.
- [100] Brandon D Riehl, Jae-Hong Park, Il Keun Kwon, and Jung Yul Lim. Mechanical stretching for tissue engineering: two-dimensional and three-dimensional constructs. *Tissue Engineering Part B: Reviews*, 18(4):288–300, 2012.
- [101] Kathryn W Aguilar-Agon, Andrew J Capel, Neil RW Martin, Darren J Player, and Mark P Lewis. Mechanical loading stimulates hypertro-



phy in tissue-engineered skeletal muscle: Molecular and phenotypic responses. *Journal of cellular physiology*, 2019.

- [102] Jenna L Dziki, Ross M Giglio, Brian M Sicari, Derek S Wang, Riddhi M Gandhi, Ricardo Londono, Christopher L Dearth, and Stephen F Badylak. The effect of mechanical loading upon extracellular matrix bioscaffold-mediated skeletal muscle remodeling. *Tissue Engineering Part A*, 24(1-2):34–46, 2018.
- [103] Du Geon Moon, George Christ, Joel D Stitzel, Anthony Atala, and James J Yoo. Cyclic mechanical preconditioning improves engineered muscle contraction. *Tissue Engineering Part A*, 14(4):473–482, 2008.
- [104] Philipp Heher, Babette Maleiner, Johanna Prüller, Andreas Herbert Teuschl, Josef Kollmitzer, Xavier Monforte, Susanne Wolbank, Heinz Redl, Dominik Rünzler, and Christiane Fuchs. A novel bioreactor for the generation of highly aligned 3d skeletal muscle-like constructs through orientation of fibrin via application of static strain. *Acta biomaterialia*, 24:251–265, 2015.
- [105] Cristian Pablo Pennisi, Christian Gammelgaard Olesen, Mark de Zee, John Rasmussen, and Vladimir Zachar. Uniaxial cyclic strain drives assembly and differentiation of skeletal myocytes. *Tissue Engineering Part A*, 17(19-20):2543–2550, 2011.
- [106] N Nikolić, SW Görgens, GH Thoresen, V Aas, J Eckel, and K Eckardt. Electrical pulse stimulation of cultured skeletal muscle cells as a model for in vitro exercise—possibilities and limitations. *Acta Physiologica*, 220(3):310–331, 2017.

- [107] Kenneth Donnelly, Alastair Khodabukus, Andrew Philp, Louise Deldicque, Robert G Dennis, and Keith Baar. A novel bioreactor for stimulating skeletal muscle in vitro. *Tissue Engineering Part C: Methods*, 16(4):711–718, 2010.
- [108] Karin Naumann and Dirk Pette. Effects of chronic stimulation with different impulse patterns on the expression of myosin isoforms in rat myotube cultures. *Differentiation*, 55(3):203–211, 1994.
- [109] Hideaki Fujita, Taku Nedachi, and Makoto Kanzaki. Accelerated de novo sarcomere assembly by electric pulse stimulation in c2c12 myotubes. *Experimental cell research*, 313(9):1853–1865, 2007.
- [110] J Stern-Straeter, AD Bach, L Stangenberg, VT Foerster, RE Horch, GB Stark, and JP Beier. Impact of electrical stimulation on three-dimensional myoblast cultures-a real-time rt-pcr study. *Journal of Cellular and Molecular Medicine*, 9(4):883–892, 2005.
- [111] Yen-Chih Huang, Robert G Dennis, Lisa Larkin, and Keith Baar. Rapid formation of functional muscle in vitro using fibrin gels. *Journal of Applied Physiology*, 98(2):706–713, 2005.
- [112] Kazushi Ikeda, Akira Ito, Masanori Sato, Yoshinori Kawabe, and Masamichi Kamihira. Improved contractile force generation of tissue-engineered skeletal muscle constructs by igf-i and bcl-2 gene transfer with electrical pulse stimulation. *Regenerative Therapy*, 3:38–44, 2016.
- [113] Annie Brevet, Elaine Pinto, John Peacock, and Frank E Stockdale. Myosin synthesis increased by electrical stimulation of skeletal muscle cell cultures. *Science*, 193(4258):1152–1154, 1976.

- [114] Marloes LP Langelaan, Kristel JM Boonen, Kang Yuen Rosaria-Chak, Daisy WJ van der Schaft, Mark J Post, and Frank PT Baaijens. Advanced maturation by electrical stimulation: Differences in response between c2c12 and primary muscle progenitor cells. *Journal of tissue engineering and regenerative medicine*, 5(7):529–539, 2011.
- [115] Alastair Khodabukus, Lauran Madden, Neel K Prabhu, Timothy R Koves, Christopher P Jackman, Deborah M Muoio, and Nenad Bursac. Electrical stimulation increases hypertrophy and metabolic flux in tissue-engineered human skeletal muscle. *Biomaterials*, 198:259–269, 2019.
- [116] Kristel JM Boonen, Marloes LP Langelaan, Roderick B Polak, Daisy WJ van der Schaft, Frank PT Baaijens, and Mark J Post. Effects of a combined mechanical stimulation protocol: Value for skeletal muscle tissue engineering. *Journal of biomechanics*, 43(8):1514–1521, 2010.
- [117] Quinlyn A Soltow, Elizabeth H Zeanah, Vitor A Lira, and David S Criswell. Cessation of cyclic stretch induces atrophy of c2c12 myotubes. *Biochemical and biophysical research communications*, 434(2):316–321, 2013.
- [118] Hiroshi Egusa, Munemasa Kobayashi, Takuya Matsumoto, Jun-Ichi Sasaki, Shinya Uraguchi, and Hirofumi Yatani. Application of cyclic strain for accelerated skeletal myogenic differentiation of mouse bone marrow-derived mesenchymal stromal cells with cell alignment. *Tissue Engineering Part A*, 19(5-6):770–782, 2012.
- [119] P Yilgor Huri, CA Cook, DL Hutton, BC Goh, JM Gimble, DJ DiGirolamo, and Warren L Grayson. Biophysical cues enhance myoge-

- nesis of human adipose derived stem/stromal cells. *Biochemical and biophysical research communications*, 438(1):180–185, 2013.
- [120] Ashok Kumar, Ryan Murphy, Prema Robinson, LEI Wei, and Aladin M Boriek. Cyclic mechanical strain inhibits skeletal myogenesis through activation of focal adhesion kinase, rac-1 gtpase, and nf- $\kappa$ b transcription factor. *The FASEB Journal*, 18(13):1524–1535, 2004.
- [121] Sung-Ho Kook, Hyun-Jeong Lee, Wan-Tae Chung, In-Ho Hwang, Seung-Ah Lee, Beom-Soo Kim, and Jeong-Chae Lee. Cyclic mechanical stretch stimulates the proliferation of c2c12 myoblasts and inhibits their differentiation via prolonged activation of p38 mapk. *Molecules & Cells (Springer Science & Business Media BV)*, 25(4), 2008.
- [122] Courtney A Powell, Beth L Smiley, John Mills, and Herman H Vandenberg. Mechanical stimulation improves tissue-engineered human skeletal muscle. *American Journal of Physiology-Cell Physiology*, 283(5):C1557–C1565, 2002.
- [123] Takuya Matsumoto, Jun-Ichi Sasaki, Eben Alsberg, Hiroshi Egusa, Hirofumi Yatani, and Taiji Sohmura. Three-dimensional cell and tissue patterning in a strained fibrin gel system. *PloS one*, 2(11):e1211, 2007.
- [124] Hug Aubin, Jason W Nichol, Ché B Hutson, Hojae Bae, Alisha L Sieminski, Donald M Cropek, Payam Akhyari, and Ali Khademhosseini. Directed 3d cell alignment and elongation in microengineered hydrogels. *Biomaterials*, 31(27):6941–6951, 2010.
- [125] Mollie M Smoak, Albert Han, Emma Watson, Alysha Kishan, K Jane Grande-Allen, Elizabeth Cosgriff-Hernandez, and Antonios G Mikos.

- Fabrication and characterization of electrospun decellularized muscle-derived scaffolds. *Tissue Engineering Part C: Methods*, 25(5):276–287, 2019.
- [126] SY Severt, SL Maxwell, JS Bontrager, JM Leger, and AR Murphy. Mimicking muscle fiber structure and function through electromechanical actuation of electrospun silk fiber bundles. *Journal of Materials Chemistry B*, 5(40):8105–8114, 2017.
- [127] Kristin D McKeon-Fischer, Daniel P Browe, Ronke M Olabisi, and Joseph W Freeman. Poly (3, 4-ethylenedioxythiophene) nanoparticle and poly (ε-caprolactone) electrospun scaffold characterization for skeletal muscle regeneration. *Journal of Biomedical Materials Research Part A*, 103(11):3633–3641, 2015.
- [128] Ngan F Huang, Shyam Patel, Rahul G Thakar, Jun Wu, Benjamin S Hsiao, Benjamin Chu, Randall J Lee, and Song Li. Myotube assembly on nanofibrous and micropatterned polymers. *Nano letters*, 6(3):537–542, 2006.
- [129] Zheng-Ming Huang, Y-Z Zhang, M Kotaki, and S Ramakrishna. A review on polymer nanofibers by electrospinning and their applications in nanocomposites. *Composites science and technology*, 63(15):2223–2253, 2003.
- [130] Dan Li and Younan Xia. Electrospinning of nanofibers: reinventing the wheel? *Advanced materials*, 16(14):1151–1170, 2004.
- [131] Nandana Bhardwaj and Subhas C Kundu. Electrospinning: a fascinating fiber fabrication technique. *Biotechnology advances*, 28(3):325–347, 2010.

- [132] A Cai, RE Horch, and JP Beier. Nanofiber composites in skeletal muscle tissue engineering. In *Nanofiber Composites for Biomedical Applications*, pages 369–394. Elsevier, 2017.
- [133] Chris A Bashur, Linda A Dahlgren, and Aaron S Goldstein. Effect of fiber diameter and orientation on fibroblast morphology and proliferation on electrospun poly (d, l-lactic-co-glycolic acid) meshes. *Biomaterials*, 27(33):5681–5688, 2006.
- [134] Jin San Choi, Sang Jin Lee, George J Christ, Anthony Atala, and James J Yoo. The influence of electrospun aligned poly (-caprolactone)/collagen nanofiber meshes on the formation of self-aligned skeletal muscle myotubes. *Biomaterials*, 29(19):2899–2906, 2008.
- [135] Stefania A Riboldi, Maurilio Sampaolesi, Peter Neuenschwander, Giulio Cossu, and Sara Mantero. Electrospun degradable polyesterurethane membranes: potential scaffolds for skeletal muscle tissue engineering. *Biomaterials*, 26(22):4606–4615, 2005.
- [136] Yanming Wang, Haigang Shi, Jing Qiao, Ye Tian, Man Wu, Wei Zhang, Yuan Lin, Zhongwei Niu, and Yong Huang. Electrospun tubular scaffold with circumferentially aligned nanofibers for regulating smooth muscle cell growth. *ACS applied materials & interfaces*, 6(4):2958–2962, 2014.
- [137] Thomas Neumann, Stephen D Hauschka, and Joan E Sanders. Tissue engineering of skeletal muscle using polymer fiber arrays. *Tissue engineering*, 9(5):995–1003, 2003.

- [138] Alexander Huber, Andy Pickett, and Kevin M Shakesheff. Reconstruction of spatially orientated myotubes in vitro using electrospun, parallel microfibre arrays. *Eur Cell Mater*, 14:56–63, 2007.
- [139] Soumen Jana, Ashleigh Cooper, Fumio Ohuchi, and Miqin Zhang. Uniaxially aligned nanofibrous cylinders by electrospinning. *ACS applied materials & interfaces*, 4(9):4817–4824, 2012.
- [140] KJ Aviss, JE Gough, and S Downes. Aligned electrospun polymer fibres for skeletal muscle regeneration. *Eur Cell Mater*, 19(1):193–204, 2010.
- [141] Mei-Chin Chen, Yu-Chin Sun, and Yuan-Hsiang Chen. Electrically conductive nanofibers with highly oriented structures and their potential application in skeletal muscle tissue engineering. *Acta biomaterialia*, 9(3):5562–5572, 2013.
- [142] Huizhi Chen, Yuan Siang Lui, Zhen Wei Tan, Justin Yin Hao Lee, Nguan Soon Tan, and Lay Poh Tan. Migration and phenotype control of human dermal fibroblasts by electrospun fibrous substrates. *Advanced healthcare materials*, 8(9):1801378, 2019.
- [143] Jordana Gilbert-Honick, Brian Ginn, Yuanfan Zhang, Sara Salehi, Kathryn R Wagner, Hai-Quan Mao, and Warren L Grayson. Adipose-derived stem/stromal cells on electrospun fibrin microfiber bundles enable moderate muscle reconstruction in a volumetric muscle loss model. *Cell transplantation*, 27(11):1644–1656, 2018.
- [144] Phammela N Abarzúa-Illanes, Cristina Padilla, Andrea Ramos, Mauricio Isaacs, Jorge Ramos-Grez, Hugo C Olguín, and Loreto M Valenzuela. Improving myoblast differentiation on electrospun poly ( $\epsilon$ -

- caprolactone) scaffolds. *Journal of Biomedical Materials Research Part A*, 105(8):2241–2251, 2017.
- [145] AG Guex, FM Kocher, G Fortunato, E Körner, D Hegemann, TP Carrel, HT Tevaearai, and Marie-Noelle Giraud. Fine-tuning of substrate architecture and surface chemistry promotes muscle tissue development. *Acta biomaterialia*, 8(4):1481–1489, 2012.
- [146] Sook Hee Ku, Sahng Ha Lee, and Chan Beum Park. Synergic effects of nanofiber alignment and electroactivity on myoblast differentiation. *Biomaterials*, 33(26):6098–6104, 2012.
- [147] Miji Yeo and Geun Hyung Kim. Anisotropically aligned cell-laden nanofibrous bundle fabricated via cell electrospinning to regenerate skeletal muscle tissue. *Small*, 14(48):1803491, 2018.
- [148] Elizabeth M Cronin, Frederick A Thurmond, Rhonda Bassel-Duby, R Sanders Williams, Woodring E Wright, Kevin D Nelson, and Harold R Garner. Protein-coated poly (l-lactic acid) fibers provide a substrate for differentiation of human skeletal muscle cells. *Journal of Biomedical Materials Research Part A: An Official Journal of The Society for Biomaterials, The Japanese Society for Biomaterials, and The Australian Society for Biomaterials and the Korean Society for Biomaterials*, 69(3):373–381, 2004.
- [149] Matthew Richard Williamson, Eric F Adams, and Allan GA Coombes. Gravity spun polycaprolactone fibres for soft tissue engineering: interaction with fibroblasts and myoblasts in cell culture. *Biomaterials*, 27(7):1019–1026, 2006.



- [150] Nor Zahari, Ruszymah Idrus, and Shiplu Chowdhury. Laminin-coated poly (methyl methacrylate)(pmma) nanofiber scaffold facilitates the enrichment of skeletal muscle myoblast population. *International journal of molecular sciences*, 18(11):2242, 2017.
- [151] Jessica H Brown, Prativa Das, Michael D DiVito, David Ivancic, Lay Poh Tan, and Jason A Wertheim. Nanofibrous plga electrospun scaffolds modified with type i collagen influence hepatocyte function and support viability in vitro. *Acta biomaterialia*, 73:217–227, 2018.
- [152] Matthew T Wolf, Christopher L Dearth, Sonya B Sonnenberg, Elizabeth G Loba, and Stephen F Badylak. Naturally derived and synthetic scaffolds for skeletal muscle reconstruction. *Advanced drug delivery reviews*, 84:208–221, 2015.
- [153] Jianxun Ding, Jin Zhang, Jiannan Li, Di Li, Chunsheng Xiao, Haihua Xiao, Huanghao Yang, Xiuli Zhuang, and Xuesi Chen. Electrospun polymer biomaterials. *Progress in Polymer Science*, 2019.
- [154] Megane Beldjilali-Labro, Alejandro Garcia Garcia, Firas Farhat, Fahmi Bedoui, Jean-François Grosset, Murielle Dufresne, and Cécile Legallais. Biomaterials in tendon and skeletal muscle tissue engineering: current trends and challenges. *Materials*, 11(7):1116, 2018.
- [155] Jiyoung M Dang and Kam W Leong. Myogenic induction of aligned mesenchymal stem cell sheets by culture on thermally responsive electrospun nanofibers. *Advanced materials*, 19(19):2775–2779, 2007.
- [156] L Buttafoco, NG Kolkman, P Engbers-Buijtenhuijs, Andreas A Poot, Pieter J Dijkstra, I Vermes, and Jan Feijen. Electrospinning of col-

- lagen and elastin for tissue engineering applications. *Biomaterials*, 27(5):724–734, 2006.
- [157] Naoya Takeda, Kenichi Tamura, Ryo Mineguchi, Yumiko Ishikawa, Yuji Haraguchi, Tatsuya Shimizu, and Yusuke Hara. In situ cross-linked electrospun fiber scaffold of collagen for fabricating cell-dense muscle tissue. *Journal of Artificial Organs*, 19(2):141–148, 2016.
- [158] Mahsa Kheradmandi, Ebrahim Vasheghani-Farahani, Ali Ghiaseddin, and Fariba Ganji. Skeletal muscle regeneration via engineered tissue culture over electrospun nanofibrous chitosan/pva scaffold. *Journal of Biomedical Materials Research Part A*, 104(7):1720–1727, 2016.
- [159] Mengyan Li, Yi Guo, Yen Wei, Alan G MacDiarmid, and Peter I Lelkes. Electrospinning polyaniline-contained gelatin nanofibers for tissue engineering applications. *Biomaterials*, 27(13):2705–2715, 2006.
- [160] Serge Ostrovidov, Xuetao Shi, Ling Zhang, Xiaobin Liang, Sang Bok Kim, Toshinori Fujie, Murugan Ramalingam, Mingwei Chen, Ken Nakajima, Faten Al-Hazmi, et al. Myotube formation on gelatin nanofibers–multi-walled carbon nanotubes hybrid scaffolds. *Biomaterials*, 35(24):6268–6277, 2014.
- [161] Mengyan Li, Mark J Mondrinos, Milind R Gandhi, Frank K Ko, Anthony S Weiss, and Peter I Lelkes. Electrospun protein fibers as matrices for tissue engineering. *Biomaterials*, 26(30):5999–6008, 2005.
- [162] Shuming Zhang, Xi Liu, Sebastian F Barreto-Ortiz, Yixuan Yu, Brian P Ginn, Nicholas A DeSantis, Daphne L Hutton, Warren L Grayson, Fu-Zhai Cui, Brian A Korgel, et al. Creating polymer hydro-

- gel microfibres with internal alignment via electrical and mechanical stretching. *Biomaterials*, 35(10):3243–3251, 2014.
- [163] Yanheng Guo, Jordana Gilbert-Honick, Sarah M Somers, Hai-Quan Mao, and Warren L Grayson. Modified cell-electrospinning for 3d myogenesis of c2c12s in aligned fibrin microfiber bundles. *Biochemical and Biophysical Research Communications*, 2019.
- [164] Shivaprasad Manchineella, Greeshma Thrivikraman, Khadija K Khanum, Praveen C Ramamurthy, Bikramjit Basu, and T Govindaraju. Pigmented silk nanofibrous composite for skeletal muscle tissue engineering. *Advanced healthcare materials*, 5(10):1222–1232, 2016.
- [165] Xizi Dai, Khadija Kathiria, and Yen-Chih Huang. Electrospun fiber scaffolds of poly (glycerol-dodecanedioate) and its gelatin blended polymers for soft tissue engineering. *Biofabrication*, 6(3):035005, 2014.
- [166] Matthew Leung, Ashleigh Cooper, Soumen Jana, Ching-Ting Tsao, Timothy A Petrie, and Miqin Zhang. Nanofiber-based in vitro system for high myogenic differentiation of human embryonic stem cells. *Biomacromolecules*, 14(12):4207–4216, 2013.
- [167] Yong Cheol Shin, Jong Ho Lee, Linhua Jin, Min Jeong Kim, Yong-Joo Kim, Jung Keun Hyun, Tae-Gon Jung, Suck Won Hong, and Dong-Wook Han. Stimulated myoblast differentiation on graphene oxide-impregnated plga-collagen hybrid fibre matrices. *Journal of nanobiotechnology*, 13(1):21, 2015.
- [168] Miji Yeo and GeunHyung Kim. Nano/microscale topographically designed alginate/pcl scaffolds for inducing myoblast alignment and myogenic differentiation. *Carbohydrate Polymers*, page 115041, 2019.

- [169] Qifei Jing, Jia Yan Law, Lay Poh Tan, Vadim V Silberschmidt, Lin Li, and ZhiLi Dong. Preparation, characterization and properties of polycaprolactone diol-functionalized multi-walled carbon nanotube/thermoplastic polyurethane composite. *Composites Part A: Applied Science and Manufacturing*, 70:8–15, 2015.
- [170] Jiazhu Xu, Ya Xie, Hongbo Zhang, Zhaoyang Ye, and Wenjun Zhang. Fabrication of plga/mwnts composite electrospun fibrous scaffolds for improved myogenic differentiation of c2c12 cells. *Colloids and Surfaces B: Biointerfaces*, 123:907–915, 2014.
- [171] KD McKeon-Fischer, DH Flagg, and JW Freeman. Coaxial electrospun poly ( $\epsilon$ -caprolactone), multiwalled carbon nanotubes, and polyacrylic acid/polyvinyl alcohol scaffold for skeletal muscle tissue engineering. *Journal of biomedical materials research Part A*, 99(3):493–499, 2011.
- [172] Simzar Hosseinzadeh, Matin Mahmoudifard, Farzaneh Mohamadyar-Toupkanlou, Masomeh Dodel, Atena Hajarizadeh, Mahdi Adabi, and Masoud Soleimani. The nanofibrous pan-pani scaffold as an efficient substrate for skeletal muscle differentiation using satellite cells. *Bio-process and biosystems engineering*, 39(7):1163–1172, 2016.
- [173] B Chaudhuri, B Mondal, S Kumar, and SC Sarkar. Myoblast differentiation and protein expression in electrospun graphene oxide (go)-poly ( $\epsilon$ -caprolactone, pcl) composite meshes. *Materials Letters*, 182:194–197, 2016.
- [174] KD McKeon-Fischer and JW Freeman. Characterization of electrospun poly (l-lactide) and gold nanoparticle composite scaffolds for

- skeletal muscle tissue engineering. *Journal of tissue engineering and regenerative medicine*, 5(7):560–568, 2011.
- [175] Yuzhang Du, Juan Ge, Yannan Li, Peter X Ma, and Bo Lei. Biomimetic elastomeric, conductive and biodegradable polycitrate-based nanocomposites for guiding myogenic differentiation and skeletal muscle regeneration. *Biomaterials*, 157:40–50, 2018.
- [176] Huizhi Chen, Yan Peng, Shucheng Wu, and Lay Tan. Electrospun 3d fibrous scaffolds for chronic wound repair. *Materials*, 9(4):272, 2016.
- [177] Brendon M Baker, Albert O Gee, Robert B Metter, Ashwin S Nathan, Ross A Marklein, Jason A Burdick, and Robert L Mauck. The potential to improve cell infiltration in composite fiber-aligned electrospun scaffolds by the selective removal of sacrificial fibers. *Biomaterials*, 29(15):2348–2358, 2008.
- [178] Jung Bok Lee, Sung In Jeong, Min Soo Bae, Dae Hyeok Yang, Dong Nyoung Heo, Chun Ho Kim, Eben Alsberg, and Il Keun Kwon. Highly porous electrospun nanofibers enhanced by ultrasonication for improved cellular infiltration. *Tissue Engineering Part A*, 17(21-22):2695–2702, 2011.
- [179] Suk-Hee Park, Min Sung Kim, Byungjun Lee, Jean Ho Park, Hye Jin Lee, Nak Kyu Lee, Noo Li Jeon, and Kahp-Yang Suh. Creation of a hybrid scaffold with dual configuration of aligned and random electrospun fibers. *ACS applied materials & interfaces*, 8(4):2826–2832, 2016.

- [180] Jin Nam, Yan Huang, Sudha Agarwal, and John Lannutti. Improved cellular infiltration in electrospun fiber via engineered porosity. *Tissue engineering*, 13(9):2249–2257, 2007.
- [181] Rachel Lev and Dror Seliktar. Hydrogel biomaterials and their therapeutic potential for muscle injuries and muscular dystrophies. *Journal of The Royal Society Interface*, 15(138):20170380, 2018.
- [182] Yu Shrike Zhang and Ali Khademhosseini. Advances in engineering hydrogels. *Science*, 356(6337):eaaf3627, 2017.
- [183] Yeong-Jin Choi, Taek Gyoung Kim, Jonghyeon Jeong, Hee-Gyeong Yi, Ji Won Park, Woonbong Hwang, and Dong-Woo Cho. 3d cell printing of functional skeletal muscle constructs using skeletal muscle-derived bioink. *Advanced healthcare materials*, 5(20):2636–2645, 2016.
- [184] Jessica A DeQuach, Joy E Lin, Cynthia Cam, Diane Hu, Michael A Salvatore, Farah Sheikh, and Karen L Christman. Injectable skeletal muscle matrix hydrogel promotes neovascularization and muscle cell infiltration in a hindlimb ischemia model. *European cells & materials*, 23:400, 2012.
- [185] V Kroehne, I Heschel, F Schügner, D Lasrich, JW Bartsch, and Harald Jockusch. Use of a novel collagen matrix with oriented pore structure for muscle cell differentiation in cell culture and in grafts. *Journal of cellular and molecular medicine*, 12(5a):1640–1648, 2008.
- [186] Justus P Beier, Dorothee Klumpp, Markus Rudisile, Roland Dersch, Joachim H Wendorff, Oliver Bleiziffer, Andreas Arkudas, Elias Polykandriotis, Raymund E Horch, and Ulrich Kneser. Collagen ma-

- trices from sponge to nano: new perspectives for tissue engineering of skeletal muscle. *BMC biotechnology*, 9(1):34, 2009.
- [187] Marco Costantini, Stefano Testa, Ersilia Fornetti, Andrea Barbetta, Marcella Trombetta, Stefano Maria Cannata, Cesare Gargioli, and Alberto Rainer. engineering muscle networks in 3d gelatin methacryloyl hydrogels: influence of mechanical stiffness and geometrical confinement. *Frontiers in bioengineering and biotechnology*, 5:22, 2017.
- [188] Soumen Jana, Ashleigh Cooper, and Miqin Zhang. Chitosan scaffolds with unidirectional microtubular pores for large skeletal myotube generation. *Advanced healthcare materials*, 2(4):557–561, 2013.
- [189] Baolin Guo, Jin Qu, Xin Zhao, and Mengyao Zhang. Degradable conductive self-healing hydrogels based on dextran-graft-tetraaniline and n-carboxyethyl chitosan as injectable carriers for myoblast cell therapy and muscle regeneration. *Acta biomaterialia*, 84:180–193, 2019.
- [190] Juan Martin Silva Garcia, Alyssa Panitch, and Sarah Calve. Functionalization of hyaluronic acid hydrogels with ecm-derived peptides to control myoblast behavior. *Acta biomaterialia*, 84:169–179, 2019.
- [191] Mark Juhas, George C Engelmayr, Andrew N Fontanella, Gregory M Palmer, and Nenad Bursac. Biomimetic engineered muscle with capacity for vascular integration and functional maturation in vivo. *Proceedings of the National Academy of Sciences*, 111(15):5508–5513, 2014.
- [192] Johanna Prüller, Ingra Mannhardt, Thomas Eschenhagen, Peter S Zammmit, and Nicolas Figeac. Satellite cells delivered in their niche efficiently generate functional myotubes in three-dimensional cell culture. *PloS one*, 13(9):e0202574, 2018.

- [193] Woojin M Han, Shannon E Anderson, Mahir Mohiuddin, Daniela Barros, Shadi A Nakhai, Eunjung Shin, Isabel Freitas Amaral, Ana Paula Pêgo, Andrés J García, and Young C Jang. Synthetic matrix enhances transplanted satellite cell engraftment in dystrophic and aged skeletal muscle with comorbid trauma. *Science advances*, 4(8):eaar4008, 2018.
- [194] JA Passipieri, HB Baker, Mevan Siriwardane, Mary D Ellenburg, Manasi Vadhavkar, Justin M Saul, Seth Tomblyn, Luke Burnett, and George J Christ. Keratin hydrogel enhances in vivo skeletal muscle function in a rat model of volumetric muscle loss. *Tissue Engineering Part A*, 23(11-12):556–571, 2017.
- [195] HB Baker, JA Passipieri, Mevan Siriwardane, Mary D Ellenburg, Manasi Vadhavkar, Christopher R Bergman, Justin M Saul, Seth Tomblyn, Luke Burnett, and George J Christ. Cell and growth factor-loaded keratin hydrogels for treatment of volumetric muscle loss in a mouse model. *Tissue Engineering Part A*, 23(11-12):572–584, 2017.
- [196] Aline Bauer, Luo Gu, Brian Kwee, Weiwei Aileen Li, Maxence Delacherie, Adam D Celiz, and David J Mooney. Hydrogel substrate stress-relaxation regulates the spreading and proliferation of mouse myoblasts. *Acta biomaterialia*, 62:82–90, 2017.
- [197] Tanyarut Boontheeikul, Hyun-Joon Kong, and David J Mooney. Controlling alginate gel degradation utilizing partial oxidation and bimodal molecular weight distribution. *Biomaterials*, 26(15):2455–2465, 2005.
- [198] G Orive, M De Castro, S Ponce, RM Hernandez, AR Gascon, M Bosch, J Alberch, and José L Pedraz. Long-term expression of erythropoietin



- from myoblasts immobilized in biocompatible and neovascularized microcapsules. *Molecular therapy*, 12(2):283–289, 2005.
- [199] Eva Kildall Hejbøl, Jeeva Sellathurai, Prabha Damodaran Nair, and Henrik Daa Schrøder. Injectable scaffold materials differ in their cell instructive effects on primary human myoblasts. *Journal of tissue engineering*, 8:2041731417717677, 2017.
- [200] Lin Wang, Janet Shansky, Cristina Borselli, David Mooney, and Herman Vandenberg. Design and fabrication of a biodegradable, covalently crosslinked shape-memory alginate scaffold for cell and growth factor delivery. *Tissue Engineering Part A*, 18(19-20):2000–2007, 2012.
- [201] Beth E Pollot, Christopher R Rathbone, Joseph C Wenke, and Teja Guda. Natural polymeric hydrogel evaluation for skeletal muscle tissue engineering. *Journal of Biomedical Materials Research Part B: Applied Biomaterials*, 106(2):672–679, 2018.
- [202] Matthew T Wolf, Kerry A Daly, Janet E Reing, and Stephen F Badylak. Biologic scaffold composed of skeletal muscle extracellular matrix. *Biomaterials*, 33(10):2916–2925, 2012.
- [203] Matthew T Wolf, Kerry A Daly, Ellen P Brennan-Pierce, Scott A Johnson, Christopher A Carruthers, Antonio D’Amore, Shailesh P Nagarkar, Sachin S Velankar, and Stephen F Badylak. A hydrogel derived from decellularized dermal extracellular matrix. *Biomaterials*, 33(29):7028–7038, 2012.
- [204] Yeong-Jin Choi, Young-Joon Jun, Dong Yeon Kim, Hee-Gyeong Yi, Su-Hun Chae, Junsu Kang, Juyong Lee, Ge Gao, Jeong-Sik Kong, Ji-

- nah Jang, et al. A 3d cell printed muscle construct with tissue-derived bioink for the treatment of volumetric muscle loss. *Biomaterials*, 2019.
- [205] Mark Juhas and Nenad Bursac. Roles of adherent myogenic cells and dynamic culture in engineered muscle function and maintenance of satellite cells. *Biomaterials*, 35(35):9438–9446, 2014.
- [206] Ji Hyun Kim, In Kap Ko, Anthony Atala, and James J Yoo. Progressive muscle cell delivery as a solution for volumetric muscle defect repair. *Scientific reports*, 6:38754, 2016.
- [207] Raymond L Page, Christopher Malcuit, Lucy Vilner, Ina Vojtic, Sharon Shaw, Emmett Hedblom, Jason Hu, George D Pins, Marsha W Rolle, and Tanja Dominko. Restoration of skeletal muscle defects with adult human cells delivered on fibrin microthreads. *Tissue Engineering Part A*, 17(21-22):2629–2640, 2011.
- [208] Stéphane Chiron, Carole Tomczak, Alain Duperray, Jeanne Lainé, Gisèle Bonne, Alexandra Eder, Arne Hansen, Thomas Eschenhagen, Claude Verdier, and Catherine Coirault. Complex interactions between human myoblasts and the surrounding 3d fibrin-based matrix. *PloS one*, 7(4):e36173, 2012.
- [209] Sara Hinds, Weining Bian, Robert G Dennis, and Nenad Bursac. The role of extracellular matrix composition in structure and function of bioengineered skeletal muscle. *Biomaterials*, 32(14):3575–3583, 2011.
- [210] Weining Bian and Nenad Bursac. Engineered skeletal muscle tissue networks with controllable architecture. *Biomaterials*, 30(7):1401–1412, 2009.

- [211] Devin Neal, Mahmut Selman Sakar, Rashid Bashir, Vincent Chan, and Haruhiko Harry Asada. Mechanical characterization and shape optimization of fascicle-like 3d skeletal muscle tissues contracted with electrical and optical stimuli. *Tissue Engineering Part A*, 21(11-12):1848–1858, 2015.
- [212] Ai Shima, Yuya Morimoto, H Lee Sweeney, and Shoji Takeuchi. Three-dimensional contractile muscle tissue consisting of human skeletal myocyte cell line. *Experimental cell research*, 370(1):168–173, 2018.
- [213] AST Smith, S Passey, L Greensmith, V Mudera, and MP Lewis. Characterization and optimization of a simple, repeatable system for the long term in vitro culture of aligned myotubes in 3d. *Journal of cellular biochemistry*, 113(3):1044–1053, 2012.
- [214] Serge Ostrovidov, Samad Ahadian, Javier Ramon-Azcon, Vahid Hosseini, Toshinori Fujie, S Prakash Parthiban, Hitoshi Shiku, Tomokazu Matsue, Hirokazu Kaji, Murugan Ramalingam, et al. Three-dimensional co-culture of c2c12/pc12 cells improves skeletal muscle tissue formation and function. *Journal of tissue engineering and regenerative medicine*, 11(2):582–595, 2017.
- [215] Javier Ramón-Azcón, Samad Ahadian, Mehdi Estili, Xiaobin Liang, Serge Ostrovidov, Hirokazu Kaji, Hitoshi Shiku, Murugan Ramalingam, Ken Nakajima, Yoshio Sakka, et al. Dielectrophoretically aligned carbon nanotubes to control electrical and mechanical properties of hydrogels to fabricate contractile muscle myofibers. *Advanced materials*, 25(29):4028–4034, 2013.
- [216] Samad Ahadian, Javier Ramón-Azcón, Mehdi Estili, Xiaobin Liang, Serge Ostrovidov, Hitoshi Shiku, Murugan Ramalingam, Ken Naka-

- jima, Yoshio Sakka, Hojae Bae, et al. Hybrid hydrogels containing vertically aligned carbon nanotubes with anisotropic electrical conductivity for muscle myofiber fabrication. *Scientific reports*, 4:4271, 2014.
- [217] Samad Ahadian, Ramin Banan Sadeghian, Shin Yaginuma, Javier Ramón-Azcón, Yuji Nashimoto, Xiaobin Liang, Hojae Bae, Ken Nakajima, Hitoshi Shiku, Tomokazu Matsue, et al. Hydrogels containing metallic glass sub-micron wires for regulating skeletal muscle cell behaviour. *Biomaterials science*, 3(11):1449–1458, 2015.
- [218] Stephanie L Hume, Sarah M Hoyt, John S Walker, Balaji V Sridhar, John F Ashley, Christopher N Bowman, and Stephanie J Bryant. Alignment of multi-layered muscle cells within three-dimensional hydrogel macrochannels. *Acta biomaterialia*, 8(6):2193–2202, 2012.
- [219] Sung Ho Cha, Hyun Jong Lee, and Won-Gun Koh. Study of myoblast differentiation using multi-dimensional scaffolds consisting of nano and micropatterns. *Biomaterials research*, 21(1):1, 2017.
- [220] Ruonan Dong, Xin Zhao, Baolin Guo, and Peter X Ma. Biocompatible elastic conductive films significantly enhanced myogenic differentiation of myoblast for skeletal muscle regeneration. *Biomacromolecules*, 18(9):2808–2819, 2017.
- [221] Apoorva S Salimath and Andrés J García. Biofunctional hydrogels for skeletal muscle constructs. *Journal of tissue engineering and regenerative medicine*, 10(11):967–976, 2016.
- [222] Ling Wang, Yaobin Wu, Baolin Guo, and Peter X Ma. Nanofiber yarn/hydrogel core-shell scaffolds mimicking native skeletal muscle

- tissue for guiding 3d myoblast alignment, elongation, and differentiation. *ACS nano*, 9(9):9167–9179, 2015.
- [223] Claudia Fuoco, Maria Lavinia Salvatori, Antonella Biondo, Keren Shapira-Schweitzer, Sabrina Santoleri, Stefania Antonini, Sergio Bernardini, Francesco Saverio Tedesco, Stefano Cannata, Dror Seliktar, et al. Injectable polyethylene glycol-fibrinogen hydrogel adjuvant improves survival and differentiation of transplanted mesoangioblasts in acute and chronic skeletal-muscle degeneration. *Skeletal muscle*, 2(1):24, 2012.
- [224] Chieh Mei, Chih-Wei Chao, Che-Wei Lin, Shing Tak Li, Kuan-Han Wu, Kai-Chiang Yang, and Jiashing Yu. Three-dimensional spherical gelatin bubble-based scaffold improves the myotube formation of h9c2 myoblasts. *Biotechnology and bioengineering*, 2019.
- [225] Francesca Gattazzo, Carmelo De Maria, Alessandro Rimessi, Silvia Donà, Paola Braghetta, Paolo Pinton, Giovanni Vozzi, and Paolo Bonaldo. Gelatin–genipin-based biomaterials for skeletal muscle tissue engineering. *Journal of Biomedical Materials Research Part B: Applied Biomaterials*, 106(8):2763–2777, 2018.
- [226] Wei Wang, Ming Fan, Li Zhang, Shu-hong Liu, Liang Sun, and Cheng-yue Wang. Compatibility of hyaluronic acid hydrogel and skeletal muscle myoblasts. *Biomedical materials*, 4(2):025011, 2009.
- [227] Carlo Alberto Rossi, Marina Flaibani, Bert Blaauw, Michela Pozzobon, Elisa Figallo, Carlo Reggiani, Libero Vitiello, Nicola Elvassore, and Paolo De Coppi. In vivo tissue engineering of functional skeletal muscle by freshly isolated satellite cells embedded in a photopolymerizable hydrogel. *The FASEB Journal*, 25(7):2296–2304, 2011.

- [228] Kevin J De France, Kevin G Yager, Katelyn JW Chan, Brandon Corbett, Emily D Cranston, and Todd Hoare. Injectable anisotropic nanocomposite hydrogels direct in situ growth and alignment of myotubes. *Nano letters*, 17(10):6487–6495, 2017.
- [229] Michiel W Pot, Kaeuis A Faraj, Alaa Adawy, Willem JP van Enckevort, Herman TB van Moerkerk, Elias Vlieg, Willeke F Daamen, and Toin H van Kuppevelt. Versatile wedge-based system for the construction of unidirectional collagen scaffolds by directional freezing: practical and theoretical considerations. *ACS applied materials & interfaces*, 7(16):8495–8505, 2015.
- [230] Mokit Chau, Kevin J De France, Bernd Kopera, Vanessa R Machado, Sabine Rosenfeldt, Laura Reyes, Katelyn JW Chan, Stephan Förster, Emily D Cranston, Todd Hoare, et al. Composite hydrogels with tunable anisotropic morphologies and mechanical properties. *Chemistry of Materials*, 28(10):3406–3415, 2016.
- [231] Daming Wang, Frederik Romer, Louise Connell, Claudia Walter, Eduardo Saiz, Sheng Yue, Peter D Lee, David S McPhail, John V Hanna, and Julian R Jones. Highly flexible silica/chitosan hybrid scaffolds with oriented pores for tissue regeneration. *Journal of Materials Chemistry B*, 3(38):7560–7576, 2015.
- [232] Kazuya Furusawa, Shoichi Sato, Jyun-ichi Masumoto, Yohei Hanazaki, Yasuyuki Maki, Toshiaki Dobashi, Takao Yamamoto, Akimasa Fukui, and Naoki Sasaki. Studies on the formation mechanism and the structure of the anisotropic collagen gel prepared by dialysis-induced anisotropic gelation. *Biomacromolecules*, 13(1):29–39, 2011.

- [233] Xinxin Zhao, Yuan Siang Lui, Caleb Kai Chuen Choo, Wan Ting Sow, Charlotte Liwen Huang, Kee Woei Ng, Lay Poh Tan, and Joachim Say Chye Loo. Calcium phosphate coated keratin–pcl scaffolds for potential bone tissue regeneration. *Materials Science and Engineering: C*, 49:746–753, 2015.
- [234] Lucy A Bosworth, Lesley-Anne Turner, and Sarah H Cartmell. State of the art composites comprising electrospun fibres coupled with hydrogels: a review. *Nanomedicine: Nanotechnology, Biology and Medicine*, 9(3):322–335, 2013.
- [235] Soumen Jana, Matthew Leung, Julia Chang, and Miqin Zhang. Effect of nano-and micro-scale topological features on alignment of muscle cells and commitment of myogenic differentiation. *Biofabrication*, 6(3):035012, 2014.
- [236] S Deepthi, K Jeevitha, M Nivedhitha Sundaram, KP Chennazhi, and R Jayakumar. Chitosan–hyaluronic acid hydrogel coated poly (caprolactone) multiscale bilayer scaffold for ligament regeneration. *Chemical Engineering Journal*, 260:478–485, 2015.
- [237] Rishma Shah, Jonathan C Knowles, Nigel P Hunt, and Mark P Lewis. Development of a novel smart scaffold for human skeletal muscle regeneration. *Journal of tissue engineering and regenerative medicine*, 10(2):162–171, 2016.
- [238] Ying Yang, Ian Wimpenny, and Mark Ahearne. Portable nanofiber meshes dictate cell orientation throughout three-dimensional hydrogels. *Nanomedicine: Nanotechnology, Biology and Medicine*, 7(2):131–136, 2011.

- [239] Wei Zhu, Haitao Cui, Benchaa Boualam, Fahed Masood, Erin Flynn, Raj D Rao, Zhi-Yong Zhang, and Lijie Grace Zhang. 3d bioprinting mesenchymal stem cell-laden construct with core-shell nanospheres for cartilage tissue engineering. *Nanotechnology*, 29(18):185101, 2018.
- [240] Anni Sorkio, Lothar Koch, Laura Koivusalo, Andrea Deiwick, Susanna Miettinen, Boris Chichkov, and Heli Skottman. Human stem cell based corneal tissue mimicking structures using laser-assisted 3d bioprinting and functional bioinks. *Biomaterials*, 171:57–71, 2018.
- [241] Yuxiao Lai, Ye Li, Huijuan Cao, Jing Long, Xinluan Wang, Long Li, Cairong Li, Qingyun Jia, Bin Teng, Tingting Tang, et al. Osteogenic magnesium incorporated into plga/tcp porous scaffold by 3d printing for repairing challenging bone defect. *Biomaterials*, 197:207–219, 2019.
- [242] Yu Shrike Zhang, Andrea Arneri, Simone Bersini, Su-Ryon Shin, Kai Zhu, Zahra Goli-Malekabadi, Julio Aleman, Cristina Colosi, Fabio Busignani, Valeria Dell’Erba, et al. Bioprinting 3d microfibrous scaffolds for engineering endothelialized myocardium and heart-on-a-chip. *Biomaterials*, 110:45–59, 2016.
- [243] Pei Zhuang, Alfred Xuyang Sun, Jia An, Chee Kai Chua, and Sing Yian Chew. 3d neural tissue models: From spheroids to bioprinting. *Biomaterials*, 154:113–133, 2018.
- [244] Amir K Miri, Akbar Khalilpour, Berivan Cecen, Sushila Maharjan, Su Ryon Shin, and Ali Khademhosseini. Multiscale bioprinting of vascularized models. *Biomaterials*, 198:204–216, 2019.
- [245] Bagrat Grigoryan, Samantha J Paulsen, Daniel C Corbett, Daniel W Sazer, Chelsea L Fortin, Alexander J Zaita, Paul T Greenfield,



- Nicholas J Calafat, John P Gounley, Anderson H Ta, et al. Multi-vascular networks and functional intravascular topologies within bio-compatible hydrogels. *Science*, 364(6439):458–464, 2019.
- [246] Serge Ostrovidov, Sahar Salehi, Marco Costantini, Kasinan Suthiwanich, Majid Ebrahimi, Ramin Banan Sadeghian, Toshinori Fujie, Xuetao Shi, Stefano Cannata, Cesare Gargioli, et al. 3d bioprinting in skeletal muscle tissue engineering. *Small*, page 1805530, 2019.
- [247] Sean V Murphy and Anthony Atala. 3d bioprinting of tissues and organs. *Nature biotechnology*, 32(8):773, 2014.
- [248] Wei Long Ng, Jia Min Lee, Wai Yee Yeong, and May Win Naing. Microvalve-based bioprinting—process, bio-inks and applications. *Bio-materials science*, 5(4):632–647, 2017.
- [249] Miaomiao Zhou, Bae Hoon Lee, Yu Jun Tan, and Lay Poh Tan. Microbial transglutaminase induced controlled crosslinking of gelatin methacryloyl to tailor rheological properties for 3d printing. *Biofabrication*, 11(2):025011, 2019.
- [250] Miaomiao Zhou, Bae Hoon Lee, and Lay Poh Tan. A dual crosslinking strategy to tailor rheological properties of gelatin methacryloyl. *International Journal of Bioprinting*, 3(2):130–137, 2017.
- [251] Ji Hyun Kim, Young-Joon Seol, In Kap Ko, Hyun-Wook Kang, Young Koo Lee, James J Yoo, Anthony Atala, and Sang Jin Lee. 3d bioprinted human skeletal muscle constructs for muscle function restoration. *Scientific reports*, 8, 2018.
- [252] Miji Yeo and GeunHyung Kim. Three-dimensional microfibrillar bundle structure fabricated using an electric field-assisted/cell printing

- process for muscle tissue regeneration. *ACS Biomaterials Science & Engineering*, 4(2):728–738, 2018.
- [253] WonJin Kim and GeunHyung Kim. A functional bioink and its application in myoblast alignment and differentiation. *Chemical Engineering Journal*, 2019.
- [254] Tyler K Merceron, Morgan Burt, Young-Joon Seol, Hyun-Wook Kang, Sang Jin Lee, James J Yoo, and Anthony Atala. A 3d bioprinted complex structure for engineering the muscle–tendon unit. *Biofabrication*, 7(3):035003, 2015.
- [255] Hyun-Wook Kang, Sang Jin Lee, In Kap Ko, Carlos Kengla, James J Yoo, and Anthony Atala. A 3d bioprinting system to produce human-scale tissue constructs with structural integrity. *Nature biotechnology*, 34(3):312, 2016.
- [256] Miji Yeo, Hyeongjin Lee, and Geun Hyung Kim. Combining a micro/nano-hierarchical scaffold with cell-printing of myoblasts induces cell alignment and differentiation favorable to skeletal muscle tissue regeneration. *Biofabrication*, 8(3):035021, 2016.
- [257] WonJin Kim, Minseong Kim, and Geun Hyung Kim. 3d-printed biomimetic scaffold simulating microfibril muscle structure. *Advanced Functional Materials*, 28(26):1800405, 2018.
- [258] Marco Costantini, Stefano Testa, Pamela Mozetic, Andrea Barbetta, Claudia Fuoco, Ersilia Fornetti, Francesco Tamiro, Sergio Bernardini, Wojciech Jaroszewicz, Jakub and, et al. Microfluidic-enhanced 3d bioprinting of aligned myoblast-laden hydrogels leads to functionally

- organized myofibers in vitro and in vivo. *Biomaterials*, 131:98–110, 2017.
- [259] Kuen Yong Lee, Martin C Peters, Kenneth W Anderson, and David J Mooney. Controlled growth factor release from synthetic extracellular matrices. *Nature*, 408(6815):998, 2000.
- [260] Jonathan M Grasman, Michelle J Zayas, Raymond L Page, and George D Pins. Biomimetic scaffolds for regeneration of volumetric muscle loss in skeletal muscle injuries. *Acta biomaterialia*, 25:2–15, 2015.
- [261] Cristina Borselli, Hannah Storrie, Frank Benesch-Lee, Dmitry Shvartsman, Christine Cezar, Jeff W Lichtman, Herman H Vandenberg, and David J Mooney. Functional muscle regeneration with combined delivery of angiogenesis and myogenesis factors. *Proceedings of the National Academy of Sciences*, 107(8):3287–3292, 2010.
- [262] EA Silva and David J Mooney. Spatiotemporal control of vascular endothelial growth factor delivery from injectable hydrogels enhances angiogenesis. *Journal of Thrombosis and Haemostasis*, 5(3):590–598, 2007.
- [263] Bridget M Deasy, Joseph M Feduska, Thomas R Payne, Yong Li, Fabrisia Ambrosio, and Johnny Huard. Effect of vegf on the regenerative capacity of muscle stem cells in dystrophic skeletal muscle. *Molecular Therapy*, 17(10):1788–1798, 2009.
- [264] Elliott Hill, Tanyarut Boontheekul, and David J Mooney. Regulating activation of transplanted cells controls tissue regeneration. *Proceedings of the National Academy of Sciences*, 103(8):2494–2499, 2006.

- [265] Cristina Borselli, Christine A Cezar, Dymitri Shvartsman, Herman H Vandenburgh, and David J Mooney. The role of multifunctional delivery scaffold in the ability of cultured myoblasts to promote muscle regeneration. *Biomaterials*, 32(34):8905–8914, 2011.
- [266] Andrea García-Lizarribar, Xiomara Fernández-Garibay, Ferran Velasco-Mallorquí, Albert G Castaño, Josep Samitier, and Javier Ramon-Azcon. Composite biomaterials as long-lasting scaffolds for 3d bioprinting of highly aligned muscle tissue. *Macromolecular bio-science*, 18(10):1800167, 2018.
- [267] Wafaa Arab, Sakandar Rauf, Ohoud Al-Harbi, and Charlotte AE Hauser. Novel ultrashort self-assembling peptide bioinks for 3d culture of muscle myoblast cells. *Int. J. Bioprint.*, 4:129, 2018.
- [268] Xiaofeng Cui, Guifang Gao, and Yongjun Qiu. Accelerated myotube formation using bioprinting technology for biosensor applications. *Biotechnology letters*, 35(3):315–321, 2013.
- [269] Pei Zhuang, Wei Long Ng, Jia An, Chee Kai Chua, and Lay Poh Tan. Layer-by-layer ultraviolet assisted extrusion-based (uae) bioprinting of hydrogel constructs with high aspect ratio for soft tissue engineering applications. *PloS one*, 14(6):e0216776, 2019.
- [270] Chee Kai Chua and Wai Yee Yeong. *Bioprinting: principles and applications*, volume 1. World Scientific Publishing Co Inc, 2014.
- [271] Chee Kai Chua and Kah Fai Leong. *3D Printing and Additive Manufacturing: Principles and Applications (with Companion Media Pack) of Rapid Prototyping Fifth Edition*. World Scientific Publishing Company, 2017.

- [272] Wei Long Ng, Shuai Wang, Wai Yee Yeong, and May Win Naing. Skin bioprinting: impending reality or fantasy? *Trends in Biotechnology*, 34(9):689–699, 2016.
- [273] Wei Long Ng, Jovina Tan Zhi Qi, Wai Yee Yeong, and May Win Naing. Proof-of-concept: 3d bioprinting of pigmented human skin constructs. *Biofabrication*, 10(2):025005, 2018.
- [274] Ramya Bhuthalingam, Pei Qi Lim, Scott Alexander Irvine, Animesh Agrawal, Priyadarshini S Mhaisalkar, Jia An, Chee Kai Chua, and Subbu Venkatraman. A novel 3d printing method for cell alignment and differentiation. *International Journal of Bioprinting*, 1(1):57–65, 2015.
- [275] Nazia Mehrban, Gui Zhen Teoh, and Martin Anthony Birchall. 3d bioprinting for tissue engineering: Stem cells in hydrogels. *International journal of bioprinting*, 2(1), 2016.
- [276] Wei Long Ng, Min Hao Goh, Wai Yee Yeong, and May Win Naing. Applying macromolecular crowding to 3d bioprinting: fabrication of 3d hierarchical porous collagen-based hydrogel constructs. *Biomaterials science*, 6(3):562–574, 2018.
- [277] Jeffrey J Rice, Mikaël M Martino, Laura De Laporte, Federico Tortelli, Priscilla S Briquez, and Jeffrey A Hubbell. Engineering the regenerative microenvironment with biomaterials. *Advanced healthcare materials*, 2(1):57–71, 2013.
- [278] Guoyou Huang, Lin Wang, ShuQi Wang, Yulong Han, Jinhui Wu, Qiancheng Zhang, Feng Xu, and Tian Jian Lu. Engineering three-

- dimensional cell mechanical microenvironment with hydrogels. *Bio-fabrication*, 4(4):042001, 2012.
- [279] Haiyang Yu, Chor Yong Tay, Mintu Pal, Wen Shing Leong, Huaqiong Li, Hai Li, Feng Wen, David Tai Leong, and Lay Poh Tan. A bio-inspired platform to modulate myogenic differentiation of human mesenchymal stem cells through focal adhesion regulation. *Advanced healthcare materials*, 2(3):442–449, 2013.
- [280] Chor Yong Tay, Cheng Gee Koh, Nguan Soon Tan, David Tai Leong, and Lay Poh Tan. Mechanoregulation of stem cell fate via micro-/nano-scale manipulation for regenerative medicine. *Nanomedicine*, 8(4):623–638, 2013.
- [281] Fu-Yu Hsieh, Hsin-Hua Lin, and Shan-hui Hsu. 3d bioprinting of neural stem cell-laden thermoresponsive biodegradable polyurethane hydrogel and potential in central nervous system repair. *Biomaterials*, 71:48–57, 2015.
- [282] Falguni Pati, Jinah Jang, Dong-Heon Ha, Sung Won Kim, Jong-Won Rhie, Jin-Hyung Shim, Deok-Ho Kim, and Dong-Woo Cho. Printing three-dimensional tissue analogues with decellularized extracellular matrix bioink. *Nature communications*, 5:3935, 2014.
- [283] Ratima Suntornnond, Edgar Yong Sheng Tan, Jia An, and Chee Kai Chua. A mathematical model on the resolution of extrusion bioprinting for the development of new bioinks. *Materials*, 9(9):756, 2016.
- [284] Ibrahim T Ozbolat and Monika Hospodiuk. Current advances and future perspectives in extrusion-based bioprinting. *Biomaterials*, 76:321–343, 2016.

- [285] Wei Long Ng, Wai Yee Yeong, and May Win Naing. Polyelectrolyte gelatin-chitosan hydrogel optimized for 3d bioprinting in skin tissue engineering. *International Journal of Bioprinting*, 2(1), 2016.
- [286] Wei Long Ng, Wai Yee Yeong, and May Win Naing. Potential of bioprinted films for skin tissue engineering. 2014.
- [287] Rachel Elizabeth Saunders and Brian Derby. Inkjet printing biomaterials for tissue engineering: bioprinting. *International Materials Reviews*, 59(8):430–448, 2014.
- [288] Christopher Chi Wai Tse, Shea Shin Ng, Jonathan Stringer, Sheila MacNeil, John W Haycock, and Patrick J Smith. Utilising inkjet printed paraffin wax for cell patterning applications. 2016.
- [289] Wei Long Ng, Wai Yee Yeong, and May Win Naing. Polyvinylpyrrolidone-based bio-ink improves cell viability and homogeneity during drop-on-demand printing. *Materials*, 10(2):190, 2017.
- [290] Lothar Koch, Ole Brandt, Andrea Deiwick, and Boris N Chichkov. Laser-assisted bioprinting at different wavelengths and pulse durations with a metal dynamic release layer: A parametric study. *International Journal of Bioprinting 3 (2017), Nr. 1*, 3(1):42–53, 2017.
- [291] Hang Lin, Dongning Zhang, Peter G Alexander, Guang Yang, Jian Tan, Anthony Wai-Ming Cheng, and Rocky S Tuan. Application of visible light-based projection stereolithography for live cell-scaffold fabrication with designed architecture. *Biomaterials*, 34(2):331–339, 2013.

- [292] Jos Malda, Jetze Visser, Ferry P Melchels, Tomasz Jüngst, Wim E Hennink, Wouter JA Dhert, Jürgen Groll, and Dietmar W Hutmacher. 25th anniversary article: engineering hydrogels for biofabrication. *Advanced materials*, 25(36):5011–5028, 2013.
- [293] Nasim Annabi, Ali Tamayol, Jorge Alfredo Uquillas, Mohsen Akbari, Luiz E Bertassoni, Chaenyung Cha, Gulden Camci-Unal, Mehmet R Dokmeci, Nicholas A Peppas, and Ali Khademhosseini. 25th anniversary article: Rational design and applications of hydrogels in regenerative medicine. *Advanced materials*, 26(1):85–124, 2014.
- [294] Amit Panwar and Lay Poh Tan. Current status of bioinks for micro-extrusion-based 3d bioprinting. *Molecules*, 21(6):685, 2016.
- [295] Tae-Sik Jang, Hyun-Do Jung, Houwen Matthew Pan, Win Tun Han, Shenyang Chen, and Juha Song. 3d printing of hydrogel composite systems: Recent advances in technology for tissue engineering. *International Journal of Bioprinting*, 4(1), 2018.
- [296] Sarah Bertlein, Gabriella Brown, Khoon S Lim, Tomasz Jungst, Thomas Boeck, Torsten Blunk, Joerg Tessmar, Gary J Hooper, Tim BF Woodfield, and Juergen Groll. Thiol–ene clickable gelatin: a platform bioink for multiple 3d biofabrication technologies. *Advanced Materials*, 29(44):1703404, 2017.
- [297] Shahid M Naseer, Amir Manbachi, Mohamadmahdi Samandari, Philipp Walch, Yuan Gao, Yu Shrike Zhang, Farideh Davoudi, Wesley Wang, Karen Abrinia, Jonathan M Cooper, et al. Surface acoustic waves induced micropatterning of cells in gelatin methacryloyl (gelma) hydrogels. *Biofabrication*, 9(1):015020, 2017.



- [298] Zongjie Wang, Zhenlin Tian, Fredric Menard, and Keekyoung Kim. Comparative study of gelatin methacrylate hydrogels from different sources for biofabrication applications. *Biofabrication*, 9(4):044101, 2017.
- [299] Kan Yue, Grissel Trujillo-de Santiago, Mario Moisés Alvarez, Ali Tamayol, Nasim Annabi, and Ali Khademhosseini. Synthesis, properties, and biomedical applications of gelatin methacryloyl (gelma) hydrogels. *Biomaterials*, 73:254–271, 2015.
- [300] Alberto Sensini, Chiara Gualandi, Luca Cristofolini, Gianluca Tozzi, Manuela Dicarlo, Gabriella Teti, Monica Mattioli-Belmonte, and Maria Letizia Focarete. Biofabrication of bundles of poly (lactic acid)-collagen blends mimicking the fascicles of the human achille tendon. *Biofabrication*, 9(1):015025, 2017.
- [301] Henrike Stratesteffen, Marius Köpf, Franziska Kreimendahl, Andreas Blaeser, Stefan Jockenhoevel, and Horst Fischer. Gelma-collagen blends enable drop-on-demand 3d printability and promote angiogenesis. *Biofabrication*, 9(4):045002, 2017.
- [302] Nicole Diamantides, Louis Wang, Tylar Pruiksma, Joseph Siemiatkoski, Caroline Dugopolski, Sonya Shortkroff, Stephen Kennedy, and Lawrence J Bonassar. Correlating rheological properties and printability of collagen bioinks: the effects of riboflavin photocrosslinking and ph. *Biofabrication*, 9(3):034102, 2017.
- [303] Vivian HM Mouser, Ferry PW Melchels, Jetze Visser, Wouter JA Dhert, Debby Gawlitta, and Jos Malda. Yield stress determines bioprintability of hydrogels based on gelatin-methacryloyl and gellan gum for cartilage bioprinting. *Biofabrication*, 8(3):035003, 2016.

- [304] Wei Zhu, Brent T Harris, and Lijie Grace Zhang. Gelatin methacrylamide hydrogel with graphene nanoplatelets for neural cell-laden 3d bioprinting. In *Engineering in Medicine and Biology Society (EMBC), 2016 IEEE 38th Annual International Conference of the*, pages 4185–4188. IEEE, 2016.
- [305] Su Ryon Shin, Claudio Zihlmann, Mohsen Akbari, Pribpandao Asawes, Louis Cheung, Kaizhen Zhang, Vijayan Manoharan, Yu Shrike Zhang, Mehmet Yükksekaya, Kai-tak Wan, et al. Reduced graphene oxide-gelma hybrid hydrogels as scaffolds for cardiac tissue engineering. *Small*, 12(27):3677–3689, 2016.
- [306] Ali Navaei, Harpinder Saini, Wayne Christenson, Ryan Tanner Sullivan, Robert Ros, and Mehdi Nikkhah. Gold nanorod-incorporated gelatin-based conductive hydrogels for engineering cardiac tissue constructs. *Acta biomaterialia*, 41:133–146, 2016.
- [307] Wanjun Liu, Marcel A Heinrich, Yixiao Zhou, Ali Akpek, Ning Hu, Xiao Liu, Xiaofei Guan, Zhe Zhong, Xiangyu Jin, Ali Khademhosseini, et al. Extrusion bioprinting of shear-thinning gelatin methacryloyl bioinks. *Advanced healthcare materials*, 6(12):1601451, 2017.
- [308] Janet R Xavier, Teena Thakur, Prachi Desai, Manish K Jaiswal, Nick Sears, Elizabeth Cosgriff-Hernandez, Roland Kaunas, and Akhilesh K Gaharwar. Bioactive nanoengineered hydrogels for bone tissue engineering: a growth-factor-free approach. *ACS nano*, 9(3):3109–3118, 2015.
- [309] Daniela F Coutinho, Shilpa V Sant, Hyeongho Shin, João T Oliveira, Manuela E Gomes, Nuno M Neves, Ali Khademhosseini, and Rui L

- Reis. Modified gellan gum hydrogels with tunable physical and mechanical properties. *Biomaterials*, 31(29):7494–7502, 2010.
- [310] Ferry PW Melchels, Wouter JA Dhert, Dietmar W Hutmacher, and Jos Malda. Development and characterisation of a new bioink for additive tissue manufacturing. *Journal of Materials Chemistry B*, 2(16):2282–2289, 2014.
- [311] Hyeongho Shin, Bradley D Olsen, and Ali Khademhosseini. The mechanical properties and cytotoxicity of cell-laden double-network hydrogels based on photocrosslinkable gelatin and gellan gum biomacromolecules. *Biomaterials*, 33(11):3143–3152, 2012.
- [312] Mehdi Kazemzadeh-Narbat, Jeroen Rouwkema, Nasim Annabi, Hao Cheng, Masoumeh Ghaderi, Byung-Hyun Cha, Mansi Aparnathi, Akbar Khalilpour, Batzaya Byambaa, Esmail Jabbari, et al. Engineering photocrosslinkable bicomponent hydrogel constructs for creating 3d vascularized bone. *Advanced healthcare materials*, 6(10):1601122, 2017.
- [313] Robert M Silverstein and G Clayton Bassler. Spectrometric identification of organic compounds. *Journal of Chemical Education*, 39(11):546, 1962.
- [314] Liliang Ouyang, Rui Yao, Shuangshuang Mao, Xi Chen, Jie Na, and Wei Sun. Three-dimensional bioprinting of embryonic stem cells directs highly uniform embryoid body formation. *Biofabrication*, 7(4):044101, 2015.
- [315] Marta Cavo, Marco Fato, Leonardo Peñuela, Francesco Beltrame, Roberto Raiteri, and Silvia Scaglione. Microenvironment complex-

- ity and matrix stiffness regulate breast cancer cell activity in a 3d in vitro model. *Scientific reports*, 6:35367, 2016.
- [316] Joséphine Lantoine, Thomas Grevesse, Agnes Villers, Geoffrey Delhay, Camille Mestdagh, Marie Versaevel, Danahe Mohammed, Céline Bruyere, Laura Alaimo, Stéphanie P Lacour, et al. Matrix stiffness modulates formation and activity of neuronal networks of controlled architectures. *Biomaterials*, 89:14–24, 2016.
- [317] Michal Bartnikowski, R Mark Wellard, Maria Woodruff, and Travis Klein. Tailoring hydrogel viscoelasticity with physical and chemical crosslinking. *Polymers*, 7(12):2650–2669, 2015.
- [318] Jun Yin, Mengling Yan, Yancheng Wang, Jianzhong Fu, and Hairui Suo. 3d bioprinting of low-concentration cell-laden gelatin methacrylate (gelma) bioinks with a two-step cross-linking strategy. *ACS applied materials & interfaces*, 10(8):6849–6857, 2018.
- [319] Cristina Colosi, Su Ryon Shin, Vijayan Manoharan, Solange Massa, Marco Costantini, Andrea Barbetta, Mehmet Remzi Dokmeci, Mariella Dentini, and Ali Khademhosseini. Microfluidic bioprinting of heterogeneous 3d tissue constructs using low-viscosity bioink. *Advanced materials*, 28(4):677–684, 2016.
- [320] Hitomi Shirahama, Bae Hoon Lee, Lay Poh Tan, and Nam-Joon Cho. Precise tuning of facile one-pot gelatin methacryloyl (gelma) synthesis. *Scientific reports*, 6:31036, 2016.
- [321] Jinlin Jiang, Donna S Woulfe, and Eleftherios T Papoutsakis. Shear enhances thrombopoiesis and formation of microparticles that induce

- megakaryocytic differentiation of stem cells. *Blood*, 124(13):2094–2103, 2014.
- [322] Huijun Li, Sijun Liu, and L Lin. Rheological study on 3d printability of alginate hydrogel and effect of graphene oxide. *Int. J. Bioprinting*, 2(2):54–66, 2016.
- [323] Zihao Xu, Zhuqing Li, Shan Jiang, and Kaitlin M Bratlie. Chemically modified gellan gum hydrogels with tunable properties for use as tissue engineering scaffolds. *ACS omega*, 3(6):6998–7007, 2018.
- [324] Xin Zhao, Qi Lang, Lara Yildirim, Zhi Yuan Lin, Wenguo Cui, Nasim Annabi, Kee Woei Ng, Mehmet R Dokmeci, Amir M Ghaemmaghami, and Ali Khademhosseini. Photocrosslinkable gelatin hydrogel for epidermal tissue engineering. *Advanced healthcare materials*, 5(1):108–118, 2016.
- [325] Nicole Diamantides, Caroline Dugopolski, Eric Blahut, Stephen Kennedy, and Lawrence J Bonassar. High density cell seeding affects the rheology and printability of collagen bioinks. *Biofabrication*, 11(4):045016, 2019.
- [326] Shahzad Ather, KG Harding, and SJ Tate. Wound management and dressings. In *Advanced textiles for wound care*, pages 1–22. Elsevier, 2019.
- [327] Monica Puri Sikka and Vinay Kumar Midha. The role of biopolymers and biodegradable polymeric dressings in managing chronic wounds. In *Advanced Textiles for Wound Care*, pages 463–488. Elsevier, 2019.

- [328] Hossein Derakhshandeh, Sara Saheb Kashaf, Fariba Aghabaglou, Ian O Ghanavati, and Ali Tamayol. Smart bandages: the future of wound care. *Trends in biotechnology*, 36(12):1259–1274, 2018.
- [329] Yi Cao, Yu Gong, Liangliang Liu, Yiwei Zhou, Xin Fang, Cao Zhang, Yining Li, and Juan Li. The use of human umbilical vein endothelial cells (huvecs) as an in vitro model to assess the toxicity of nanoparticles to endothelium: a review. *Journal of Applied Toxicology*, 37(12):1359–1369, 2017.
- [330] Johanna Andersson, Anna Ström, Tobias Gebäck, and Anette Larsson. Dynamics of capillary transport in semi-solid channels. *Soft matter*, 13(14):2562–2570, 2017.
- [331] Caroline Rhim, Dorothy A Lowell, Mary C Reedy, Dorothy H Slentz, Sarah J Zhang, William E Kraus, and George A Truskey. Morphology and ultrastructure of differentiating three-dimensional mammalian skeletal muscle in a collagen gel. *Muscle & Nerve: Official Journal of the American Association of Electromyography and Clinical Neurophysiology*, 36(1):71–80, 2007.